Lattice Boltzmann Methods in Interfacial Wave Modelling

James Maxwell Buick

Doctor of Philosophy

The University of Edinburgh

1997

Abstract

An immiscible, binary fluid lattice Boltzmann model is described and its associated equations of motion are given. It is seen that the lattice Boltzmann scheme is totally isotropic and that it does not suffer from the problems of noisy results and a lack of Galilean invariance which plagued its predecessor: the lattice gas model. The incorporation of a body force into the lattice Boltzmann technique is considered. A method which introduces the body force directly into the governing equation is proposed and is seen to have the desired effect without destroying the Galilean invariance of the original model and without introducing any dependency on the grid orientation.

The immiscible, binary fluid model, with the body force incorporated, is applied to simulate interfacial waves between the two fluids. The model parameters allow the interface thickness, the fluid viscosity, the gravitational strength and the relative density of the two fluids to be varied. The wavelength of the wave can also be set during the wave initialisation. Standing waves are simulated for a wide range of the variable parameters and progressive waves for a subset of the parameters. The results are seen to compare well with linear wave theory. When compared with available experimental results the behaviour is seen to be similar.

Acknowledgements

I would like to thank my supervisor, Clive Greated, for his suggestions and support. I would also like to thank Paul Stansell for numerous useful discussions and for proof reading this thesis; Roger Kingdon for his help and encouragement; Alastair Martin for his insight into internal waves and for allowing me to reproduce some of his results; and Edinburgh Parallel Computing Centre (EPCC) for allowing me time on the Connection Machine CM200.

The financial support of SERC is gratefully acknowledged.

Table of Contents

List of Figures

List of Tables

Chapter 1

Introduction

1.1 The Study of Fluid Motion

Fluid motion can take a variety of forms ranging from simple flows such as laminar flow in a pipe, to more complex flows such as vortex shedding behind cylinders, wave motion and turbulence. It incorporates both liquid and gaseous flows. Many of the different flow situations have been examined experimentally, however it is advantageous to develop a numerical model capable of simulating the many flow structures experienced in the motion of different fluids.

Fluid motion is governed by the continuity equation

$$\frac{\partial \rho}{\partial t} + \nabla \cdot (\rho \boldsymbol{u}) \tag{1.1}$$

and the Navier-Stokes equation

$$\frac{\partial \boldsymbol{u}}{\partial t} + \boldsymbol{u} \cdot \nabla \boldsymbol{u} = -\frac{1}{\rho}\nabla p + \nu \nabla^2 + \zeta \nabla(\nabla \cdot \boldsymbol{u}) \tag{1.2}$$

for a fluid with velocity $\boldsymbol{u}$, density ρ, pressure p, kinematic shear viscosity ν and kinematic bulk viscosity ζ. The Navier-Stokes equation is a second-order partial differential equation which has no known analytic solution except for a small number of special cases. With the advent of computer technology attempts have been made at producing numerical simulations of fluid flows.

1.2 Numerical Methods in Fluid Study

Computational fluid dynamics (CFD) has developed mainly around using numerical techniques to solve the Navier-Stokes equation (1.2) and the continuity equation (1.1) or an equation derived from them. Another approach which has proved less popular is the molecular dynamics approach.

Numerical Solutions of the Navier-Stokes Equation

The most popular method in CFD is the numerical solution of the Navier-Stokes equation (1.2). Given the Navier-Stokes equation and a set of suitable boundary conditions it is possible to solve on a grid using the standard numerical techniques. This works well for simple flows, however more complex problems frequently require a more complex approach. There are many standard texts on numerical methods in fluids including Roach [1] and Conner and Brebbia [2].

Molecular Dynamics

One obvious way to simulate a fluid on a computer is to model the individual molecules which make up the fluid. Then, provided the inter-molecular interactions are modelled correctly, the system should behave as a fluid [3]. Different situations can be modelled by changing the average energy of the molecules and their separation.

The main disadvantage with such an approach is that large computer resources are required, many simulations taking hours to evolve a fraction of a second [4]. The system must be updated in small time-steps, the new position and velocity of all particles being calculated, at every time-step, from a knowledge of their previous position and velocity, taking into account any external forces which are acting on them. Any particles which collided during the previous time-step have to be identified and their new trajectories calculated. This can be restrictively

time consuming when considering even a very small volume of fluid. Even when a gas is being considered where there are fewer molecules and a larger time-step can be used, because of the longer mean free path of the molecules, the number of molecules which can be considered is severely limited.

Lattice Gas Modelling

Over the past ten years, a new method for the computer simulation of fluids has been developed: the lattice gas model [5]. Instead of considering a large number of individual molecules, the molecular dynamics approach, a much smaller number of fluid 'particles' are considered. A fluid 'particle' is a large group of molecules which although much larger than a molecule is still considerably smaller then the smallest length scale of the simulation. This reduces the amount of data which needs to be stored since large simulations can be performed using less than one million 'particles'. This is justified on the grounds that the macroscopic properties do not depend directly on the microscopic behaviour of the fluid. This can be seen in low Mach flows where, provided the Reynolds number is the same, experiments carried out in a water tank and a wind tunnel produce the same results. These two fluids have different microscopic structures, but they both exhibit the same macroscopic features. In a lattice gas model the 'particles' are restricted to move on the links of a regular underlying grid and the motion evolves in discrete time-steps. The conservation laws are incorporated into update rules which are applied at each discrete time.

A lattice gas model in which the state of the fluid needs to be known only at the lattice sites and only at discrete times can run much faster on a computer than a molecular dynamics simulation. The lattice gas model has another big advantage over molecular simulation since all the collisions occur at the same time. This is a particular advantage if the simulation is being run on a parallel computer. These two time saving advantages of the lattice gas model allow simulations of a significantly large scale to be performed.

Lattice Boltzmann Models

The lattice Boltzmann model has evolved from the lattice gas model. There are a number of difficulties with the lattice gas approach to fluid modelling; various modifications have been made to overcome these difficulties and the outcome is the lattice Boltzmann model. As the name suggests this technique involves simulating the Boltzmann equation

$$\frac{\partial f}{\partial t} + \boldsymbol{c} \cdot \frac{\partial f}{\partial \boldsymbol{r}} + \boldsymbol{F} \cdot \frac{\partial f}{\partial \boldsymbol{c}} = \Omega(f) \tag{1.3}$$

where $\Omega(f)$ is a 'collision' function, $\boldsymbol{F}(\boldsymbol{r}, t)$ is the body force per unit mass, $\boldsymbol{c}(\boldsymbol{r}, t)$ is the particle velocity and $f(\boldsymbol{r}, \boldsymbol{c}, t)$ is the distribution function. The distribution function is a statistical parameter from which the macroscopic properties of the fluid can be found. The simulation of the Boltzmann equation is performed on a regular lattice and the forms of the collision function Ω is taken to be the BGK [6] collision operator which was fist considered to represent collisions in the non-discrete Boltzmann equation. The computation reflects the evolution from the lattice gas model. The model is updated in the same manner as the lattice gas model except that now, instead of considering individual particles to be travelling along the links, it is the distribution function which is evolved. The lattice Boltzmann model has the advantages associated with the lattice gas model but all the lattice gas difficulties have been overcome. Thus the lattice Boltzmann model is an ideal tool in fluid simulation.

1.3 Wave Modelling

A major area of study, both experimental, theoretical and computational, within fluid dynamics is wave motion. This includes the study of surface gravity waves, which occur at the free surface between a liquid phase and a gaseous phase, and internal gravity waves which can either be interfacial, occurring at the interface between two fluids of the same phase, or can occur within a stratified fluid where a density gradient is produced by an external influence. Internal waves occur

in both liquid and gaseous phases. Numerical studies of wave motion have followed the traditional route, common to most numerical problems, of solving the differential equation describing the motion subject to a set of boundary and initial conditions. A major problem when applying this to gravity waves is that a boundary condition needs to be applied at the interface at which the waves are propagating. The interface can be either the free-surface between a liquid and a gas or an internal interface between two fluids with the same phase. Either way the boundary conditions need to be applied at a boundary which is changing as the simulation develops. This can become even more complicated if wave breaking is being considered when the surface becomes a multi-valued function of the horizontal co-ordinates. This problem does not occur is a lattice gas or a lattice Boltzmann model exhibiting some form of fluid separation. Wave simulations have been performed [7] using a lattice gas model, however they were subject to the problems inherent in all lattice gas model. The results did however suggest that a lattice Boltzmann model, which overcomes the lattice gas problems, could be a useful tool in the study of wave motion.

1.4 Aims

The main aims of this thesis are:

1. To examine the existing lattice Boltzmann models for multi-fluid simulation, in the literature, and asses their suitability for modelling interfacial internal waves.

2. To investigate the introduction of a body force into the lattice Boltzmann scheme.

3. To test the two-component fluid model, which is selected for the simulations, with the body force incorporated to insure that the model is Galilean invari-

ant and independent of the underlying lattice.

4. To use the lattice Boltzmann model incorporating the body force to simulate interfacial waves for a range of model and wave parameters.

5. To compare the results of the simulations with the theoretical predictions and with existing experimental results.

1.5 Notation

A full list of the notation used in this thesis is given in appendix A. When a symbol has more than one meaning the most common one is given first. Greek indices will be used to refer to components and summation over repeated indices will be implicit. Roman indices will be used as labels and no summation will be implicit over repeated indices.

1.6 Preview

In chapter 2 the concept of a distribution function is considered and the derivation and theory of the classical Boltzmann equation are discussed. Different forms of the collision function and their effect on the equilibrium distribution function are also considered. A brief outline of the derivation of the equations of motions is also given.

In chapter 3 the concept of a lattice gas model is explained and a full description of the technique is given. A square grid model is described briefly, as are the three hexagonal grid models which have been used most commonly in two-dimensional simulations. A summary of Frisch's derivation [8] of the equations of the model is

presented and their implications on the lattice gas model considered. The development of multi-fluid models is also considered. The strengths and weaknesses of the lattice gas approach are discussed.

In chapter 4 an account of the development of the lattice Boltzmann model, from the lattice gas technique, is given and the similarity with the classical Boltzmann equation is shown. A lattice Boltzmann model for a totally isotropic and Galilean invariant fluid, from the literature, is presented which satisfies the exact continuity equation and Navier-Stokes equation correct to second-order in the expansion parameter and the velocity. Multi-fluid lattice Boltzmann models are also discussed briefly and the model which will be used in the subsequent chapters is described in detail. At the end of the chapter a number of simulation results for the chosen model, which have been performed elsewhere, are repeated to highlight some of the important features of the model.

In chapter 5 the inclusion of a body force in the lattice Boltzmann scheme is investigated. A number of methods suggested in the literature are considered and a new method is proposed which includes the body force directly in the Boltzmann equation. This method is compared with the other techniques and is tested to ensure it is independent of the underlying grid orientation. The immiscible binary fluid of Orlandini *et al.* [9] with a body force incorporated is tested for Galilean invariance.

In chapter 6 the equations describing interfacial wave motion are presented. These are all well established in the literature.

In chapter 7 the immiscible, binary fluid model of Orlandini *et al.* [9] is combined with the gravitational interactions described in chapter 5. A method for initialising standing interfacial waves is described and the results obtained from numerous simulations are presented. The results are compared with the theoretical predictions given in chapter 6.

In chapter 8 the model implemented in chapter 7 is used to simulate progressive interfacial waves. The progressive waves are initialised using the information obtained in chapter 7 about the density and velocity profiles. The resulting progressive wave simulations are presented and compared with experimental results obtained elsewhere [10]. A brief discussion of the experimental technique is also given.

Chapter 2

The Boltzmann Equation

In this chapter the ideas underlying the Boltzmann description of a fluid system are described. The classical Boltzmann equation is derived and the macroscopic quantities of mass, velocity and energy are defined in terms of the distribution function which describes the fluid. It is shown that the Boltzmann description of the fluid satisfies the fluid conservation equations. The form of the collision function is reviewed for a rare fluid, in which only binary collisions are considered, and for a simplified collision operator. An outline of the derivation of the Navier-Stokes equation and a discussion of the equilibrium distribution are given for the binary collision model.

2.1 The Classical Boltzmann Equation

A statistical description of a system can be made in terms of the distribution function $f(\boldsymbol{r}, \boldsymbol{c}, t)$ [11,12,13] where $f(\boldsymbol{r}, \boldsymbol{c}, t)$ is defined such that $f(\boldsymbol{r}, \boldsymbol{c}, t)\mathrm{d}\boldsymbol{r}\mathrm{d}\boldsymbol{c}$ is the number of molecules at time t positioned between $\boldsymbol{r}$ and $\boldsymbol{r} + \mathrm{d}\boldsymbol{r}$ which have velocities in the range $\boldsymbol{c} \to \boldsymbol{c} + \mathrm{d}\boldsymbol{c}$.

Consider a gas in which an external force $m\boldsymbol{F}$ acts and assume initially that no collisions take place between the gas molecules. In time $\mathrm{d}t$ the velocity $\boldsymbol{c}$ of any molecule will change to $\boldsymbol{c} + \boldsymbol{F}\mathrm{d}t$ and its position $\boldsymbol{r}$ will change to $\boldsymbol{r} + \boldsymbol{c}\mathrm{d}t$.

Thus the number of molecules $f(\boldsymbol{r},\boldsymbol{c},t)\mathrm{d}\boldsymbol{r}\mathrm{d}\boldsymbol{c}$ is equal to the number of molecules $f(\boldsymbol{r}+\boldsymbol{c}\mathrm{d}t,\boldsymbol{c}+\boldsymbol{F}\mathrm{d}t,t+\mathrm{d}t)\mathrm{d}\boldsymbol{r}\mathrm{d}\boldsymbol{c}$, that is to say,

$$f(\boldsymbol{r}+\boldsymbol{c}\mathrm{d}t,\boldsymbol{c}+\boldsymbol{F}\mathrm{d}t,t+\mathrm{d}t)\mathrm{d}\boldsymbol{r}\mathrm{d}\boldsymbol{c}-f(\boldsymbol{r},\boldsymbol{c},t)\mathrm{d}\boldsymbol{r}\mathrm{d}\boldsymbol{c}=0. \tag{2.1}$$

If, however, collisions do occur between the molecules there will be a net difference between the number of molecules $f(\boldsymbol{r}+\boldsymbol{c}\mathrm{d}t,\boldsymbol{c}+\boldsymbol{F}\mathrm{d}t,t+\mathrm{d}t)\mathrm{d}\boldsymbol{r}\mathrm{d}\boldsymbol{c}$ and the number of molecules $f(\boldsymbol{r},\boldsymbol{c},t)\mathrm{d}\boldsymbol{r}\mathrm{d}\boldsymbol{c}$. This can be written [11] $\Omega(f)\mathrm{d}\boldsymbol{r}\mathrm{d}\boldsymbol{c}\mathrm{d}t$ where $\Omega(f)$ is the collision operator. This gives the following equation describing the evolution of the distribution function:

$$f(\boldsymbol{r}+\boldsymbol{c}\mathrm{d}t,\boldsymbol{c}+\boldsymbol{F}\mathrm{d}t,t+\mathrm{d}t)\mathrm{d}\boldsymbol{r}\mathrm{d}\boldsymbol{c}-f(\boldsymbol{r},\boldsymbol{c},t)\mathrm{d}\boldsymbol{r}\mathrm{d}\boldsymbol{c}=\Omega(f)\mathrm{d}\boldsymbol{r}\mathrm{d}\boldsymbol{c}\mathrm{d}t. \tag{2.2}$$

Dividing equation (2.2) by $\mathrm{d}t\mathrm{d}\boldsymbol{r}\mathrm{d}\boldsymbol{c}$ and letting $\mathrm{d}t\to 0$ gives the Boltzmann equation [11,12]

$$\partial_t f+c_\alpha\partial_\alpha f+F_\alpha\partial_{c\alpha}f=\Omega(f) \tag{2.3}$$

where

$$\partial_t=\frac{\partial}{\partial t},\quad \partial_\alpha=\frac{\partial}{\partial \boldsymbol{r}_\alpha},\quad \partial_{c\alpha}=\frac{\partial}{\partial \boldsymbol{c}_\alpha}. \tag{2.4}$$

The fluid density ρ, velocity $\boldsymbol{u}$ and internal energy e can be found from the distribution function f as follows [11]:

$$\rho(\boldsymbol{r},t)=\int mf(\boldsymbol{r},\boldsymbol{c},t)\mathrm{d}\boldsymbol{c}$$

$$\rho(\boldsymbol{r},t)\boldsymbol{u}(\boldsymbol{r},t)=\int m\boldsymbol{c}f(\boldsymbol{r},\boldsymbol{c},t)\mathrm{d}\boldsymbol{c} \tag{2.5}$$

$$\rho(\boldsymbol{r},t)e(\boldsymbol{r},t)=\frac{1}{2}\int mu_0^2 f(\boldsymbol{r},\boldsymbol{c},t)\mathrm{d}\boldsymbol{c}$$

where m is the molecular mass and $\boldsymbol{u}_0$ is the peculiar velocity $\boldsymbol{u}_0\stackrel{\text{def}}{=}\boldsymbol{c}-\boldsymbol{u}$, the particle velocity with respect to the fluid flow. The internal energy can be shown [11] to be

$$e=\frac{3}{2m}k_BT \tag{2.6}$$

where T is the temperature and k_B is Boltzmann's constant.

Any solution of Boltzmann's equation (2.3) requires that an expression is found for the collision operator $\Omega(f)$. Without knowing the form of $\Omega(f)$ there are however several properties which can be deduced. If the collision is to conserve mass, momentum and energy it is required that

$$\int \begin{bmatrix} 1 \\ \boldsymbol{c} \\ c^2 \end{bmatrix} \Omega(f) \mathrm{d}\boldsymbol{c} = 0. \tag{2.7}$$

The terms ψ_i, $i = 0, ..., 4$ where $\psi_0 = 1$, $\psi_1 = c_1$, $\psi_2 = c_2$, $\psi_3 = c_3$ and $\psi_4 = c^2$ are frequently called the elementary collision invariants since $\int \psi_i \Omega(f) \mathrm{d}\boldsymbol{c} = 0$ [12]. Any linear combination of the ψ_i terms is also a collision invariant.

2.1.1 The Conservation Equations

The continuity equations can be derived by multiplying Boltzmann's equation (2.3) by ψ_i, $i = 0, ..., 4$ and integrating over $\mathrm{d}\boldsymbol{c}$. We note from equation (2.7) that the integral of $\psi_i \Omega(f)$ is zero and that

$$\int \frac{\partial f}{\partial c_\alpha} \mathrm{d}\boldsymbol{c} = 0,$$

$$\int c_\beta \frac{\partial f}{\partial c_\alpha} \mathrm{d}\boldsymbol{c} = -\int \delta_{\alpha\beta} f \mathrm{d}\boldsymbol{c} = -\frac{\rho}{m} \delta_{\alpha\beta}, \; . \tag{2.8}$$

$$\frac{1}{2} \int c^2 \frac{\partial f}{\partial c_\alpha} \mathrm{d}\boldsymbol{c} = -\int c_\alpha f \mathrm{d}\boldsymbol{c} = -\frac{\rho}{m} u_\alpha.$$

The results in equation (2.8) can be seen by integrating by parts and by noting that $\lim_{\boldsymbol{c} \to \infty} (\psi_i f) = 0$ since the integrals defined in equation (2.5) must converge [12]. We also note that $\boldsymbol{r}$, $\boldsymbol{c}$ and t are independent variables and so $\boldsymbol{c}$ commutes with $\partial_{\boldsymbol{r}}$ and ∂_t. We are therefor considering

$$\int \partial_t \psi_i f \mathrm{d}\boldsymbol{c} + \int \partial_\alpha c_\alpha \psi_i f \mathrm{d}\boldsymbol{c} + F_\alpha \int \partial_{c\alpha} \psi_i f \mathrm{d}\boldsymbol{c} = 0. \tag{2.9}$$

Consider first the case $i = 0$. Multiplying by m and using equation (2.5) this gives the continuity equation

$$\partial_t \rho + \partial_\alpha \rho u_\alpha = 0. \tag{2.10}$$

When $i = 1$, 2, and 3 we get

$$\partial_t \rho u_\beta + \partial_\alpha \Pi_{\alpha\beta} = \rho F_\beta \tag{2.11}$$

where $\Pi_{\alpha\beta} = \int m c_\alpha c_\beta f \mathrm{d}\boldsymbol{c}$. Expressing the molecular velocity $\boldsymbol{c}$ in terms of the fluid velocity $\boldsymbol{u}$ and the peculiar velocity $\boldsymbol{u}_0$ we can write

$$\Pi_{\alpha\beta} = \int m u_\alpha u_\beta f \mathrm{d}\boldsymbol{c} + \int m u_{0\alpha} u_{0\beta} f \mathrm{d}\boldsymbol{c}. \tag{2.12}$$

The first term in equation (2.12) is simply $\rho u_\alpha u_\beta$ and the second term is the pressure tensor $P_{\alpha\beta}$ [13]. Thus we have the Euler equation

$$\partial_t(\rho u_\beta) + \partial_\alpha(\rho u_\alpha u_\beta + P_{\alpha\beta}) = \rho F_\beta. \tag{2.13}$$

Similarly, when $i = 4$, we get the conservation of energy equation [12,13],

$$\partial_t \left[\rho\left(\frac{1}{2}u^2 + e\right)\right] + \partial_{r\alpha}\left[\rho u_\alpha\left(\frac{1}{2}u^2 + e\right) + P_{\alpha\beta}u_\beta + q_\alpha\right] = \rho F_\alpha u_\alpha, \tag{2.14}$$

where $\boldsymbol{q}$ is the heat flux [12],

$$q_\alpha = \frac{1}{2}\int c_\alpha c^2 f \mathrm{d}\boldsymbol{r}. \tag{2.15}$$

2.1.2 The Collision Function

The form of the collision function $\Omega(f)$ can be found [11,12,14] by assuming that the gas has a low density so only binary collisions need be considered. It is also assumed that the molecules are completely uncorrelated before the collision, this assumption is called 'molecular chaos'. With these assumptions the collision function is given by [11,12,14]

$$\Omega(f) = \int\int (f' f'_* - f f_*) g \sigma(\theta, g) \mathrm{d}\Omega \mathrm{d}\boldsymbol{c}_* \tag{2.16}$$

where $\boldsymbol{c}'$ and $\boldsymbol{c}'_*$ are the velocities of the two particles before a collision, $\boldsymbol{c}$ and $\boldsymbol{c}_*$ are their velocities after the collision, $f' = f(\boldsymbol{r}, \boldsymbol{c}', t)$, $f'_* = f(\boldsymbol{r}, \boldsymbol{c}'_*, t)$, $f = f(\boldsymbol{r}, \boldsymbol{c}, t)$, $f_* = f(\boldsymbol{r}, \boldsymbol{c}_*, t)$, g is the magnitude of the particles relative velocity before the collision, $\mathrm{d}\Omega$ is the solid angle the particles are scattered into,

$$\mathrm{d}\Omega = \sin(\theta)\mathrm{d}\theta\mathrm{d}\phi, \tag{2.17}$$

and $\sigma(g,\theta)$ is the differential cross section in the centre of mass reference frame,

$$\sigma(g,\theta) = \frac{b(g,\theta)}{\sin(\theta)}\frac{\mathrm{d}b}{\mathrm{d}\theta}, \tag{2.18}$$

where b and θ are the impact parameter and the scattering angle respectively in the centre of mass reference frame, as defined in figure 2–1, ϕ is the azimuthal angle.

FIGURE 2–1: Two particles (of equal mass) before and after a collision in the centre of mass reference frame. The impact parameter b and the angle θ are shown.

2.2 Boltzmann's H-Theorem

Boltzmann's equation describes the evolution of molecules in a rare gas. If no external forces are present ($\boldsymbol{F} = 0$) then, after a long time, the gas should reach an equilibrium state. This can be seen [14,11] by considering the function

$$H(t) = \int f \ln f \mathrm{d}\boldsymbol{c}. \tag{2.19}$$

Differentiating equation (2.19) with respect to time we get

$$\partial_t H = \int (1 + \ln f)\partial_t f \mathrm{d}\boldsymbol{c}. \tag{2.20}$$

Substituting $\partial_t f$ from equation (2.3), with $\boldsymbol{F} = 0$, and using equation (2.16) we get

$$\partial_t H = -\int [(c_\alpha \partial_{r\alpha} f)(\ln f + 1)]\,\mathrm{d}\boldsymbol{c} + \int\int\int (f' f'_* - f f_*) g\sigma (\ln f + 1)\mathrm{d}\Omega \mathrm{d}\boldsymbol{c}_* \mathrm{d}\boldsymbol{c}. \tag{2.21}$$

Now, following [14], consider the first term on the right hand side of equation (2.21). Since $\boldsymbol{c}$ and $\boldsymbol{r}$ are independent variables we can write $c_\alpha \partial_{r\alpha} f$ as $\partial_{r\alpha} f c_\alpha$ and using Gauss's theorem we can write

$$\int [c_\alpha \partial_{r\alpha} f(\ln f + 1)]\, \mathrm{d}\boldsymbol{c} = \int (\ln f + 1) f \boldsymbol{c} \cdot \mathrm{d}\boldsymbol{s} \tag{2.22}$$

where $\mathrm{d}\boldsymbol{s}$ is the surface enclosing the volume $\mathrm{d}\boldsymbol{c}$. Now $\lim_{\boldsymbol{c}\to\infty}(f\psi_i) = 0$ so the first term on the right-hand side of equation (2.21) vanishes. This leaves

$$\partial_t H = \int\int\int g\sigma(f'f'_* - ff_*)(\ln f + 1)\mathrm{d}\Omega \mathrm{d}\boldsymbol{c}_* \mathrm{d}\boldsymbol{c}. \tag{2.23}$$

Now consider the reverse of the collision: particles with velocity $\boldsymbol{c}$ and $\boldsymbol{c}_*$ colliding and moving off with velocities $\boldsymbol{c}'$ and $\boldsymbol{c}'_*$. For this collision we have

$$\partial_t H = \int\int\int g\sigma(f'f'_* - ff_*)(\ln f_* + 1)\mathrm{d}\Omega \mathrm{d}\boldsymbol{c}_* \mathrm{d}\boldsymbol{c} \tag{2.24}$$

since $\mathrm{d}\boldsymbol{c}\mathrm{d}\boldsymbol{c}_* = \mathrm{d}\boldsymbol{c}'\mathrm{d}\boldsymbol{c}'_*$. Summing equations (2.23) and (2.24) and dividing by two gives

$$\partial_t H = \frac{1}{2}\int\int\int g\sigma(f'f'_* - ff_*)(\ln f + \ln f_* + 2)\mathrm{d}\Omega \mathrm{d}\boldsymbol{c}_* \mathrm{d}\boldsymbol{c}. \tag{2.25}$$

Changing the dummy variables $\boldsymbol{c} \leftrightarrow \boldsymbol{c}'$ and $\boldsymbol{c}_* \leftrightarrow \boldsymbol{c}'_*$ we get

$$\partial_t H = \frac{1}{2}\int\int\int g\sigma(f'f'_* - ff_*)(-\ln f' - \ln f'_* - 2)\mathrm{d}\Omega \mathrm{d}\boldsymbol{c}_* \mathrm{d}\boldsymbol{c}. \tag{2.26}$$

Finally summing equations (2.25) and (2.26) and dividing by two gives

$$\partial_t H = \frac{1}{4}\int\int\int g\sigma(f'f'_* - ff_*) \ln \frac{ff_*}{f'f'_*} \mathrm{d}\Omega \mathrm{d}\boldsymbol{c}_* \mathrm{d}\boldsymbol{c}. \tag{2.27}$$

Now $(f'f'_* - ff_*)\ln(ff_*/f'f'_*) \leq 0$ and all the other terms in the integrand of equation (2.27) are positive so

$$\partial_t H \leq 0. \tag{2.28}$$

This means that H can never increase and is known as Boltzmann's H-theorem. It can also be shown that H is bounded below [11]. We know that $\int f c^2 \mathrm{d}^2\boldsymbol{c}$ converges because the total energy of the molecules must converge. Thus either H converges or $-\ln f \to \infty$ more rapidly than c^2 as $\boldsymbol{c} \to \infty$. In the later case $f \to 0$ more rapidly than $\exp(-c^2)$ which implies that H converges. Since H can never increase

but tends to a finite limit the finite limit must correspond to $\partial_t H = 0$. This is only possible, see equation (2.27), if

$$f' f'_* = f f_*. \tag{2.29}$$

This condition is known as detailed balance [11] and can be expressed equivalently as

$$\ln f' + \ln f'_* = \ln f + \ln f_*. \tag{2.30}$$

Thus if $\overline{f}$ is the equilibrium distribution then $\ln \overline{f}$ is a collision invariant and so must be of the form

$$\ln \overline{f} = \sum_i \alpha_i \psi_i \quad i = 0, 1, ..., 4 \tag{2.31}$$

where ψ_i are the collision invariants defined below equation (2.7) and α_i are constants. This can be re-written [11]

$$\ln \overline{f} = \ln(\alpha'_0) - \alpha'_4 \frac{1}{2} m \left\{ \left[c_1 - \left(\frac{\alpha'_1}{\alpha'_4} \right) \right]^2 + \left[c_2 - \left(\frac{\alpha'_2}{\alpha'_4} \right) \right]^2 + \left[c_3 - \left(\frac{\alpha'_3}{\alpha'_4} \right) \right]^2 \right\} \tag{2.32}$$

where $\alpha'_0 = \exp(\alpha_0)$, $\alpha'_1 = \alpha_1/m$, $\alpha'_2 = \alpha_2/m$, $\alpha'_3 = \alpha_3/m$ and $\alpha'_4 = 2\alpha_4/m$. With $\boldsymbol{C} = \boldsymbol{c} - \boldsymbol{\alpha}'/\alpha'_4$ where $\boldsymbol{\alpha}' = (\alpha'_1, \alpha'_2, \alpha'_3)$ we can write

$$\overline{f} = \alpha'_0 e^{-\alpha'_4 \frac{1}{2} m C^2} \tag{2.33}$$

This is the Maxwell distribution function for a gas [11,12,14] and it describes the equilibrium state of the distribution function f. The form of the constants can be found by substituting equation (2.33) into equation (2.5) to give the more common form of the Maxwell distribution function [11,12]

$$\overline{f} = \frac{\rho}{m} \left(\frac{m}{2\pi k_B T} \right)^{3/2} \exp \left[\frac{-m(\boldsymbol{c} - \boldsymbol{u})^2}{2 k_B T} \right]. \tag{2.34}$$

The H-theorem states that the distribution function f must tend towards its equilibrium state $\overline{f}$. The entropy $S(t)$ of the system (which is a non-decreasing function of time) is given by [11,14]

$$S(t) = -k_B H(t). \tag{2.35}$$

2.3 The Chapman-Enskog Method

The Navier-Stokes equation can be derived from the Boltzmann equation using a Chapman-Enskog expansion. Only a brief outline of the method will be given here since the same procedure can be applied, in a much more straightforward manner, to the simplified lattice Boltzmann equation in which we are mainly interested. A full derivation of the Navier-Stokes equation using the Chapman-Enskog expansion will be given in section 4.2.3 for the lattice Boltzmann equation. Details of the Chapman-Enskog method for the classical Boltzmann equation can be found in [11]. The Chapman Enskog expansion parameter is the Knudsen number, ϵ, defined as

$$\epsilon = \frac{\lambda}{l} \tag{2.36}$$

where λ is the mean free path of the molecules and l is a typical macroscopic length. The derived equations will only be valid if the Knudsen number is small. By analysing the time and length scales involved in the Boltzmann equation [13], ϵ can be introduced into the Boltzmann equation:

$$\partial_t f + c_\alpha \partial_\alpha f + F_\alpha \partial_{c\alpha} f = \frac{1}{\epsilon}\Omega(f). \tag{2.37}$$

Setting

$$f = \sum_{n=0}^{\infty} \epsilon^n f^{(n)} \tag{2.38}$$

we look for solutions of equation (2.37) such that

$$\begin{aligned} \int m f^{(n)} \begin{bmatrix} 1 \\ c \\ u_0^2 \end{bmatrix} \mathrm{d}\boldsymbol{c} &= \begin{bmatrix} \rho \\ \rho \boldsymbol{u} \\ 3\frac{\rho}{m} k_B T \end{bmatrix} \quad \text{for} \quad n = 0 \\ \int m f^{(n)} \begin{bmatrix} 1 \\ c \\ u_0^2 \end{bmatrix} \mathrm{d}\boldsymbol{c} &= 0 \qquad\qquad \text{for} \quad n \geq 1. \end{aligned} \tag{2.39}$$

The zeroth order them $f^{(0)}$ is taken to be the local Maxwell-Boltzmann distribution $\overline{f}$ and $f^{(n)}$, for $n \geq 1$, are chosen so they have no contribution to the moments

expressed in equation (2.39). The first-order solution can be found by considering $O(1/\epsilon)$ which gives the Euler equation of section 2.1.1 [11,13]. The second-order solution, found by considering $O(\epsilon^0)$, requires a knowledge of the collision operator and can be shown [11] to give the Navier-Stokes equation when the binary collision function is used.

2.4 The Single Relaxation Model

The Boltzmann equation detailed above describes the evolution of the distribution function f of a fluid. The fluid density, momentum and energy can then be found from the distribution function by considering the appropriate integral. In theory this appears straightforward, however in practice it can be difficult because of the complicated form of the collision term Ω. A large amount of the detail of the two-body interaction, which is contained in the Boltzmann collision operator, is unlikely to influence significantly the values of the macroscopic quantities. It is therefor assumed [12] that $\Omega(f)$ can be replaced by a simplified collision operator which retains only the qualitative and average properties of the actual collision operator. Any replacement collision function must satisfy the conservation of mass, momentum and energy expressed by equation (2.7). Such an operator is based on the idea of a single relaxation time and can be written [6]

$$\Omega(f) = -\frac{f(\boldsymbol{r},\boldsymbol{c},t) - \overline{f}(\boldsymbol{r},\boldsymbol{c},t)}{\tau} \tag{2.40}$$

where $\overline{f}(\boldsymbol{r},\boldsymbol{c},t)$ is the local Maxwell-Boltzmann equilibrium distribution, given by equation (2.34), and τ is the 'relaxation time' which is of the order of the time between collisions. This model is frequently called the BGK model after Bhatnagar, Gross and Krook [6] who first introduced it.

2.5 The Boltzmann Equation for a High Density Fluid

Some attempts have been made to generalise the Boltzmann equation to incorporate fluids with a higher density by writing the collision function as $\Omega_2(ff) + \Omega_3(fff) + \Omega_4(ffff) + ...$ where $\Omega_2(ff)$ is the binary collision operator discussed above and $\Omega_3, \Omega_4, ...$ describe triple, quadruple, ... collisions. This was not successful since the terms $\Omega_n, \quad n \geq 4$ were found to diverge [15]. Thus the classical Boltzmann equation described here can only be applied to a low density gas.

2.6 Summary

We have seen that a fluid can be described in terms of its distribution function $f(\boldsymbol{r}, \boldsymbol{c}, t)$, a function of position, molecular velocity and time. The evolution of the distribution function is governed by the Boltzmann equation and the macroscopic fluid density, velocity and energy can all be found, at any time, from this distribution function. If we are dealing with a rare fluid where the number of molecular collisions is small, and so the majority of the collisions are binary, an expression can be found for the molecular collision function $\Omega(f)$. Using this expression the gas can be shown to satisfy the Navier-Stokes equation and explicit expressions can be found for the transport coefficients. An H-theorem can also be proved, using the binary collision function, which states that the distribution function tends towards an equilibrium state which satisfies a Maxwell-Boltzmann distribution. We have also seen that the complex form of the collision function can be replaced by a BGK function which depends only on a single relaxation time. The H-theorem and the derivation of the Navier-Stokes equation and the transport coefficients are only valid for a rare gas where the number of non-binary collisions is negligible.

Chapter 3

The Lattice Gas Model

In this chapter the lattice gas model is examined. The basic single species models are described as are the attempts at multi-fluid simulations. The derivation of the lattice gas Navier-Stokes equation [8] is outlined and the differences between it and the true Navier-Stokes equation are discussed.. The application of the lattice gas model is also considered.

3.1 Definition of a Lattice Gas Model

Lattice gas models belong to the class of cellular automata and are used for simulating fluid systems. A cellular automata consists of a lattice whose sites, the intersection points of the lattice, can take a finite number of states. The automaton evolves in discrete time steps; the state of each site at any time is determined by its own state and the state of a set of neighbouring sites at the previous time step.

3.2 Development of the Lattice Gas Model

It is assumed that the macroscopic behaviour of a fluid does not depend directly on the detailed microscopic behaviour. This is similar to the BGK assumption in the classical Boltzmann theory, see section 2.4. Thus in general any system which satisfies the continuity equation (1.1) and the Navier-Stokes equation (1.2) can be used to model a fluid, the detail of the microscopic behaviour is not important. A cellular automata approach to modelling the microscopic behaviour has the advantage that it can be implemented efficiently and quickly on a computer. The fluid properties are incorporated into the update rules.

3.2.1 The HPP Model

The first lattice gas model was introduced by Hardy, Pomeau and de Pazzis (HPP) [16,17] . The particles are restricted to travel on the links $\boldsymbol{e}_i$, $i = 1, .., 4$, of a square lattice, where $\boldsymbol{e}_i = \sin[\frac{\pi}{2}(i-1)]\,\boldsymbol{i} + \cos[\frac{\pi}{2}(i-1)]\,\boldsymbol{j}$, see figure 3–1. Each particle travels at unit speed so it moves from one lattice site to a neighbouring site in each time step. An exclusion rule is applied so that only one particle is allowed to travel in each direction along a link. This means that a maximum of four particles can arrive at any site at any time step. When particles arrive at a site they collide according to the collision rules shown in figure 3–2: at any site where there is an incoming configuration shown in the left hand column the particles collide to give the outgoing configuration shown in the right hand column. If the incoming configuration is not shown on the left-hand side of figure 3–2 then the particles continue travelling in a straight line. It can easily be seen from these collision rules that both the number of particles and the momentum at each site is conserved and thus the total particle number and total momentum are also conserved. It has been shown [8] that viscous dissipation is anisotropic due to the underlying square grid and so it is necessary to use a different underlying grid in any simulation of fluid flow.

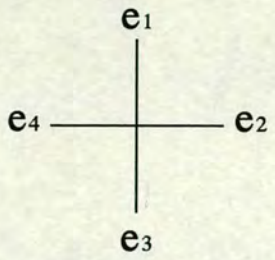

FIGURE 3–1: The square grid used in the HPP model.

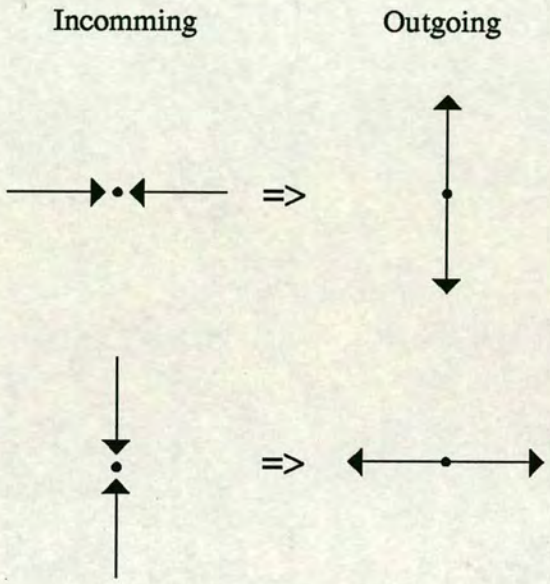

FIGURE 3–2: The collision rules for the HPP model. The left hand column shows the incoming configurations and the right hand column shows the corresponding outgoing configurations after the collision.

3.2.2 The FHP Models

In 1986 Frisch Hasslacher and Pomeau (FHP) [5] introduced a lattice gas model based on a hexagonal grid. The six link directions $\boldsymbol{e}_i$ $i = 1, .., 6$, shown in figure 3–3, are $\boldsymbol{e}_i = \cos(\frac{\pi_1}{3} - \frac{\pi}{6})\,\boldsymbol{i} + \sin(\frac{\pi_1}{3} - \frac{\pi}{6})\,\boldsymbol{j}$. As with the HPP model each of the particles travels with unit speed and an exclusion principle is applied allowing only one particle to travel in each direction along a link. Rest particles can also be introduced into the model. A rest particle remains at rest at a site, link $\boldsymbol{e}_0$, but is able to take part in a collision with particles arriving at the site. A set of collision rules on a hexagonal lattice is shown in figure 3–4 where the small filled circles represent the lattice site and the large empty circles represent a rest particle at the

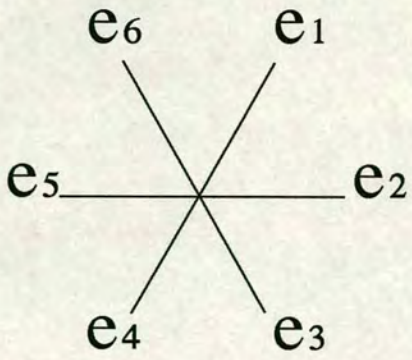

FIGURE 3–3: The hexagonal grid used in the FHP model.

site. The full set of collisions can be obtained by combining the collisions of figure 3–4 with the collisions found by rotating the particles through multiples of $\pi/3$ and considering the collision duals, formed by swapping the full and empty links. As in figure 3–2 the left hand column represents the possible incoming configurations. The right hand column represents the outgoing configurations, however now there may be a choice between two different possible outcomes; when this happens one of the choices is picked at random. Again, it can be clearly seen that each individual rule conserve both particle number and momentum at each site.

The FHP-I Model

The simplest of the FHP models is the FHP-I [8] in which there are no rest particles. The particles collide according to rules (a) and (b) in figure 3–4, that is 3 binary head-on collisions of type (a) and two triple collisions of type (b). That gives a total of 5 collisions out of the 64 possible in-states.

The FHP-II Model

This model introduces a rest particle and allows the particles to collide according to the following rules [8]: the five FHP-I collisions, type (a) and (b); six rest particle creation collisions , type (c); six rest particle destruction collisions, type (d) and also the five FHP-I rules with a spectator rest particle, an example of

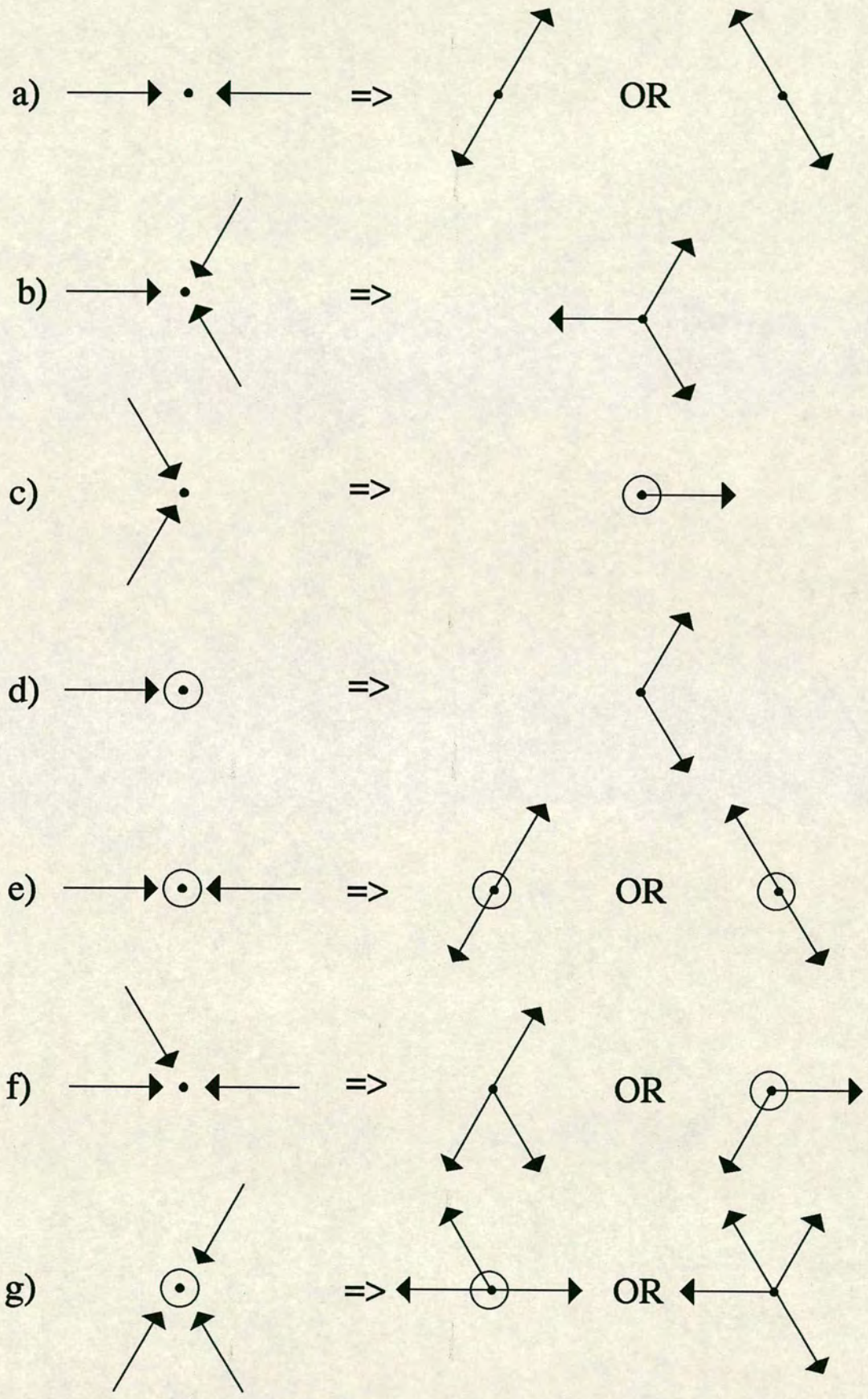

FIGURE 3–4: A set of collision rules for the FHP model. The sites are represented by the small filled circles and rest particles are represented by the large empty circles.

which is collision (e). This gives 22 possible interactions out of a possible total of 128.

The FHP-III Model

FHP-III [8] is an extension of FHP-II which allows all collisions which conserve mass and momentum at each site. There are 76 possible collisions: 15 two-particle collisions of type (a), (c) and (d); 23 three-particle collisions of type (b), (e) and (f); 23 four-particle collisions and 15 five-particle collisions. The four- and five-particle collisions are the dual of the three- and two-particle collisions respectively. The dual of a collision is found by adding particles to the empty links and removing particles from the links which were originally filled. Example (g) is the dual of example (f). There are a total of 18 collisions of type (f) which can be considered to be collisions of type (a) or (c) with a spectator particle (a particle which does not take part in the collision and which continues travelling in a straight line). The two possible outcomes of collision (f) arise from these two different ways of viewing the collision. The one restriction which is commonly applied to the FHP-III model is that collisions (b) and (e) are not interchangeable, that is the (e) in-state can not collide to give the (b) out-state even though this conserves mass and momentum. This restriction do not affect the properties of the model but simplifies its implementation since it restricts the maximum possible number of out-states, for each in-state, to two. The FHP-III collision at non boundary sites are reproduced in full in appendix B.

Other FHP Models

The models described above are the main ones in use, it is, however, possible to produce any number of variants. For example the FHP-I rules could be increased to include the duals of the existing rules [8]. Any number of rest particles could be added [18]. Models have also been used where the two out-states do not occur with equal probability [19].

3.2.3 Three-Dimensional Models

An obvious extension to the lattice gas model is to expand it to three-dimensions. However, it has been found that three-dimensional lattices do not have enough symmetry to ensure macroscopic isotropy [5,20]. This has been overcome [20] by introducing a multi-speed model on a cubic lattice.

The Multi-Speed Model on a Cubic Lattice

The Multi-Speed Model was introduced by d'Humières *et al.* [20]. It uses a regular cubic lattice and has particles travelling with three different velocities: zero, unity and $\sqrt{2}$. Such a lattice is shown in figure 3–5. The rest particles remain stationary

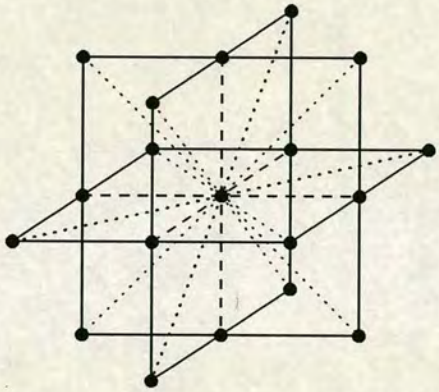

FIGURE 3–5: A cubic lattice. The solid lines show the planes $x = 0, y = 0$ and $z = 0$ through the sites which are represented by solid dots. The central site is connected to its six nearest neighbours by the dashed links, and to its twelve next-nearest neighbours by the dotted links

at the sites, the unit velocity particles travel to the nearest neighbours along the dashed links and the $\sqrt{2}$ velocity particles travel to the next-nearest neighbours along the dotted links. The collision rules conserve mass and momentum at each site: two particles approaching head on collide and move off at right angles (as in the HPP model but here there are two possible outcomes, one of which is picked at random), two unit speed particles colliding at right angles produce a rest particle and a $\sqrt{2}$ particle travelling so as to conserve momentum. Conversely, when a $\sqrt{2}$ particle and a rest particle collide two unit speed particles are produced.

3.3 Boundaries in the Model

Boundaries can be introduced into the model by initially labelling certain of the lattice sites. Different collision rules are then applied at these sites by the collision operator. No-slip conditions are introduced at a boundary by forcing any particle colliding with the boundary to return along the link on which it approached [21]. Figure 3–6 shows the no-slip boundary conditions for the HPP and FHP models for particles approaching a horizontal boundary.

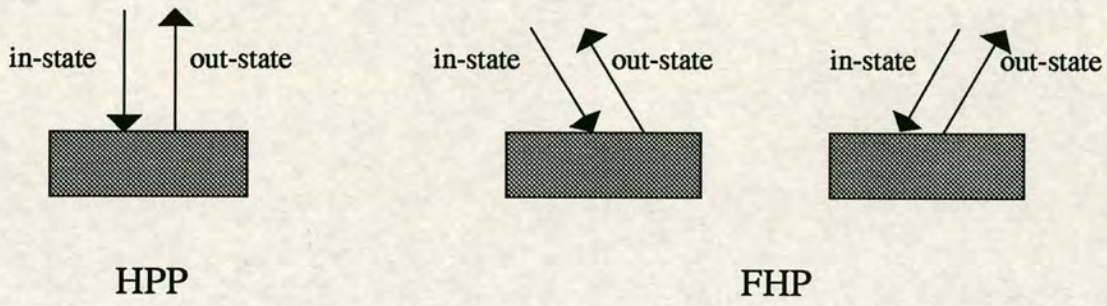

FIGURE 3–6: No-Slip boundary conditions at a horizontal boundary for the HPP and FHP models.

3.4 Updating the Lattice

At the start of each time step the particles at each site collide according to the particular collision rules for the model being used - the collision stage. After the collision stage each particle travels in a straight line along one of the lattice links, unless it is a rest particle, until it arrives at the next link - the streaming stage. The particles arriving at their new sites then collide at the beginning of the next time step. Figure 3–7 shows the evolution of particles colliding and streaming on a square lattice according to the HPP collision rules. Note that although the exclusion principle allows only one particle to travel along each link direction two particles travelling in opposite directions are allowed on the same link, these

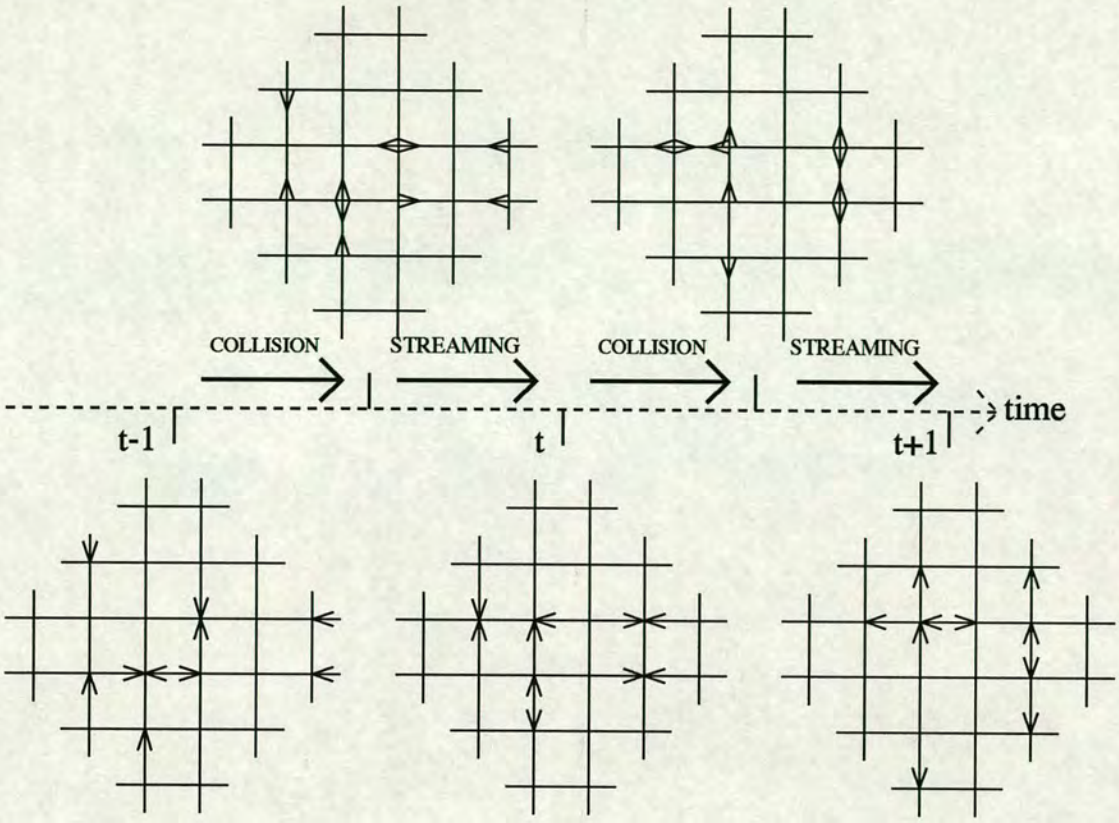

FIGURE 3–7: The evolution of particles on a portion of a square lattice from time $t-1$ to time $t+1$.

particles pass each other during the streaming stage without colliding. As well as considering the discrete space of the lattice sites time is also considered as being discrete. Each particle jumps from its position at time $t-1$ to its position at time t where it collides instantaneously before jumping to its new position at time $t+1$.

3.5 Equations for the Lattice Gas Model

The derivation of the microscopic and macroscopic equations for a lattice gas model which are outlined below were first derived by Frisch *et al.* [8] where the general case of a D-dimensional lattice is considered. Here a brief review of the method and the significant results are presented for a two-dimensional lattice. Frisch *et al.* [8] only considers a model without rest particles although results for other models are given.

3.5.1 Definitions

Consider a two-dimensional regular lattice where $\boldsymbol{r}$ is the position vector of any site. The lattice has b distinct links $\boldsymbol{e}_i$. Any particle travelling on link $\boldsymbol{e}_i$, $i = 1, ..., b$ moves from one site to a neighbouring site in unit time and so has velocity $\boldsymbol{e}_i$.

We label the occupation numbers of the links at a site $\boldsymbol{r}$ at time t by $n_i(t, \boldsymbol{r})$, $i = 1, ..., b$ where

$$n_i(t, \boldsymbol{r}) = \begin{cases} 1 & \text{if } \boldsymbol{e}_i \text{ is occupied} \\ 0 & \text{otherwise.} \end{cases} \tag{3.1}$$

The density and velocity, ρ and $\boldsymbol{u}$ are defined

$$\begin{aligned} \rho &= \sum_i n_i \\ \rho u_\alpha &= \sum_i n_i e_{i\alpha}. \end{aligned} \tag{3.2}$$

We also define the collision function

$$\Delta_i(n) = \begin{cases} 1 & \text{if a particle added to link } \boldsymbol{e}_i \\ 0 & \text{if there is no change to link } \boldsymbol{e}_i \\ -1 & \text{if a particle is removed from link } \boldsymbol{e}_i \end{cases} \tag{3.3}$$

The collision function describes the change in $n_i(t, \boldsymbol{r})$ during a collision at time t at site $\boldsymbol{r}$.

The mass and momentum must be conserved by the collision function at each site. This can be expressed

$$\sum_i n_i(t+1, \boldsymbol{r} + \boldsymbol{e}_i) = \sum_i n_i(t, \boldsymbol{r}), \tag{3.4}$$

$$\sum_i \boldsymbol{e}_i n_i(t+1, \boldsymbol{r} + \boldsymbol{e}_i) = \sum_i \boldsymbol{e}_i n_i(t, \boldsymbol{r}). \tag{3.5}$$

The particles on the lattice are updated according to a time evolution operator which can be described as the convolution

$$\mathcal{E} = \mathcal{S} \circ \mathcal{C} \tag{3.6}$$

where $\mathcal{C}$ describes the collision operator and $\mathcal{S}$ the streaming operator.

Each collision can be considered to be the transition from an in-state $s = s_1, s_2, ..., s_b$ at time t^- just before the collision to an out-state $s' = s'_1, s'_2, ..., s'_b$ at t^+ just after the collision. We can assign a probability $A(s \to s') \geq 0$ to be the probability that an in-state s collides to give an out-state s'. The collision rules are said to satisfy detailed balance if

$$A(s \to s') = A(s' \to s) \tag{3.7}$$

and semi-detailed balance if

$$\sum_s A(s \to s') = 1, \quad \forall s'. \tag{3.8}$$

The FHP models described here satisfy semi-detailed balance but not detailed balance.

3.5.2 Microdynamical Equations

Frisch *et al.* [8] use a probabilistic approach which is traditional in statistical mechanics. Thus they consider the mean population

$$N_i(t, \boldsymbol{r}) = \langle n_i(t, \boldsymbol{r}) \rangle, \tag{3.9}$$

the mean density

$$\rho(t, \boldsymbol{r}) = \sum_i N_i(t, \boldsymbol{r}), \tag{3.10}$$

the mean mass current

$$\boldsymbol{J}(t, \boldsymbol{r}) = \sum_i \boldsymbol{e}_i N_i(t, \boldsymbol{r}) \tag{3.11}$$

and the mean velocity

$$\boldsymbol{u}(t,\boldsymbol{r}) = \boldsymbol{J}(t,\boldsymbol{r})/\rho(t,\boldsymbol{r}). \tag{3.12}$$

Note that the mean density and mass current are defined to be the mean quantities per site, and *not* per unit area as they normally are in the real world. Frisch *et al.* [8] have found a steady state equilibrium solution for the mean population,

$$\overline{N}_i = f(h(\rho,\boldsymbol{u}) + \boldsymbol{q}(\rho,\boldsymbol{u})\cdot\boldsymbol{e}_i), \tag{3.13}$$

where f is the Fermi-Dirac function

$$f(x) \stackrel{\text{def}}{=} \frac{1}{1+e^x}, \tag{3.14}$$

$\overline{N}_i$ is the equilibrium mean population and h and $\boldsymbol{q}$ are Lagrange multipliers which depend on the mean density ρ and the mean velocity $\boldsymbol{u}$ through equations (3.9) - (3.12). Note that although the solution is independent of the transition probabilities $A(s \to s')$ Frisch's proof requires that A satisfies semi-detailed balance: equation (3.8). The Fermi-Dirac distribution for the equilibrium state of the mean population is obtained because there is an exclusion principle applied to the lattice gas model: only one particle is allowed on any link at any time-step.

Explicit solutions for h and $\boldsymbol{q}$ are only known for special cases, such as when $\boldsymbol{u} = \boldsymbol{0}$ where $N_i = \rho/6$ is clearly a solution. Expressions for h and $\boldsymbol{q}$ can be found in the limit of small $\boldsymbol{u}$ by expanding equation (3.13) about the zero velocity case to give

$$\overline{N}_i(\rho,\boldsymbol{u}) = \frac{\rho}{6} + \frac{2\rho}{6}e_{i\alpha}u_\alpha + \rho G(\rho)Q_{i\alpha\beta}u_\alpha u_\beta + O(u^3) \tag{3.15}$$

where

$$G(\rho) = \frac{1}{3}\frac{(6-2\rho)}{(6-\rho)} \tag{3.16}$$

and

$$Q_{i\alpha\beta} = e_{i\alpha}e_{i\beta} - \frac{1}{2}\delta_{\alpha\beta}. \tag{3.17}$$

This restricts us to using speeds u which are small compared to c_s, the speed of sound in the model. Given a solution for $\boldsymbol{u} = \boldsymbol{0}$ it is not possible to use a Galilean transformation to find the solution for non-zero $\boldsymbol{u}$ because the solution found here

only applies in an inertial frame in which the underlying grid is at rest. This lack of Galilean invariance is an important feature of the model and can lead to problems when the model is implemented.

It can also be shown [22] that the lattice gas model obeys an H-theorem. This states that the mean population must tend towards the equilibrium mean population $\overline{N}_i$.

3.5.3 Macrodynamical Equations

We now have equation (3.15) giving an equilibrium solution for the mean occupation numbers of the links. Ensemble averaging the conservation equations (3.4) and (3.5) gives the conservation equations for the mean occupation numbers

$$\sum_i N_i(t+1, \boldsymbol{r}+\boldsymbol{e}_i) = \sum_i N_i(t, \boldsymbol{r}), \tag{3.18}$$

$$\sum_i \boldsymbol{c}_i N_i(t+1, \boldsymbol{r}+\boldsymbol{e}_i) = \sum_i \boldsymbol{c}_i N_i(t, \boldsymbol{r}). \tag{3.19}$$

In order to derive the macrodynamical equations it is assumed [8] that the actual mean population $N_i(t, \boldsymbol{r})$ is close to the equilibrium population, described in equation (3.15), which we will now call $N_i^{(0)}$. The population is expanded in terms of a small parameter ϵ:

$$N_i(t, \boldsymbol{r}) = N_i^{(0)} + \epsilon N_i^{(1)}(t, \boldsymbol{r}) + \epsilon^2 N_i^{(2)}(t, \boldsymbol{r}) + O(\epsilon^3), \tag{3.20}$$

where we assume that $N_i^{(1)}$ and $N_i^{(2)}$ do not contribute to the mean density or momentum. The derivatives are also expanded in terms of the same parameter [8]

$$\begin{aligned} \partial_t &= \epsilon \partial_{1t} + \epsilon^2 \partial_{2t} + \ldots \\ \partial_{\boldsymbol{r}} &= \epsilon \partial_{1\boldsymbol{r}} \end{aligned} \tag{3.21}$$

and a Chapman-Enskog expansion performed up to second-order in ϵ and $\boldsymbol{u}$. To first-order in ϵ this gives

$$\partial_t \rho + \partial_\beta(\rho u_\beta) = 0 \tag{3.22}$$

and

$$\partial_t(\rho u_\alpha) + \partial_\beta \Pi_{\alpha\beta} = 0 \tag{3.23}$$

where Π is the first-order approximation to the momentum flux tensor, and is given by

$$\begin{aligned} \Pi_{\alpha\beta} &= \textstyle\sum_i e_{i\alpha} e_{i,\beta} N_i^{(0)} \\ &= \tfrac{1}{2}\rho\delta_{\alpha\beta} + \rho G(\rho) T_{\alpha\beta\gamma\delta} u_\gamma u_\delta + O(u^4) \end{aligned} \tag{3.24}$$

where

$$T_{\alpha\beta\gamma\delta} = \sum_i e_{i\alpha} e_{i\beta} Q_{i\gamma\delta}. \tag{3.25}$$

Expanding to the next order in ϵ and combining the second-order solutions with equations (3.22) and (3.23) we get the continuity equation

$$\partial_t \rho + \partial_\beta(\rho u_\beta) = 0 \tag{3.26}$$

and

$$\partial_t(\rho u_\alpha) + \partial_\beta \Pi_{\alpha\beta} = \partial_\beta S_{\alpha\beta}, \tag{3.27}$$

where

$$S_{\alpha\beta} = \nu(\rho)[\partial_\alpha(\rho u_\beta) + \partial_\beta(\rho u_\alpha) - \delta_{\alpha\beta}\partial_\gamma(\rho u_\gamma)] \tag{3.28}$$

and the kinematic viscosity $\nu(\rho)$ is a function of density. The viscosity has been calculated by Frisch [8] using the Boltzmann approximation and also by Hénon [23], by considering the particle motion on the grid. The viscosity is found to be model dependent as well as density dependent, the values for the FHP-I, FHP-II and FHP-III models are

$$\frac{1}{12}\frac{1}{d(1-d)^3} - \frac{1}{8}, \tag{3.29}$$

$$\frac{1}{28}\frac{1}{d(1-d)^3}\frac{1}{1-4d/7} - \frac{1}{8} \tag{3.30}$$

and

$$\frac{1}{28}\frac{1}{d(1-d)}\frac{1}{1-8d(1-d)/7} - \frac{1}{8} \tag{3.31}$$

respectively. Here d is the mean density per link given by $\rho/6$ for FHP-I and $\rho/7$ for FHP-II and FHP-III were rest particles are allowed.

3.5.4 Isotropy of the Model

Equation (3.27) is not fully isotropic, due to the tensor $T_{\alpha\beta\gamma\delta} = \sum_i e_{i\alpha}e_{i\beta}(e_{i\gamma}e_{i\delta} - \frac{1}{2}\delta_{\gamma\delta})$. Clearly the isotropy of this tensor will depend on the velocity vectors $\boldsymbol{e}_i$. Frisch *et al.* [8] show that for the FHP models the velocity vectors are such that equation (3.27) is isotropic. This means that the underlying rotation group of the hexagonal lattice is sufficiently symmetric to allow us to model an isotropic fluid. Hexagonal grids are generally used in lattice gas simulations because they are the simplest lattice for which the fluid is isotropic.

3.6 The Navier-Stokes Equation

Equation (3.26) is the continuity equation for a real fluid. Equation (3.27) is similar to the Navier-Stokes equation for a real fluid. We need to see if a fluid satisfying (3.27) satisfies the Navier-Stokes equation.

The equations for lattice gas hydrodynamics are only valid for $u \ll c_s$, the speed of sound of the model, since we have assumed this in their derivation. In this regime we can follow the approach of Frisch *et al.* [8] and consider the density to have a constant value ρ_0. The density is, however, allowed to fluctuate where it appears in the pressure term. This gives

$$\partial_\alpha u_\alpha = 0 \tag{3.32}$$

and

$$\partial_t u_\alpha + g(\rho_0)u_\beta\partial_\beta u_\alpha = -\frac{1}{\rho_0}\partial_\alpha\left(p - p_0 g(\rho_0)u^2\right) + \nu(\rho_0)\partial_{\beta\beta}u_\alpha, \tag{3.33}$$

for $p = \rho c_s^2$, $p_0 = \rho_0 c_s^2$ and $g(\rho) = \frac{1}{2}\frac{b-2\rho}{b-\rho}$.

This equation differs from the standard Navier-Stokes equation in the following ways:

1. the nonlinear term is multiplied by a model and density-dependent function, $g(\rho_0)$;

2. the viscosity is a function of density;

3. the pressure term has an extra term which is dependent on the density and the velocity.

It is possible to re-scale certain variables in equation (3.33) and to redefine the pressure in order to produce the Navier-Stokes equation. This can be done in two ways:

1. Following Frisch *et al.* [8] define

$$t^* = g(\rho_0)t, \tag{3.34}$$

$$\nu^*(\rho_0) = \frac{\nu(\rho_0)}{g(\rho_0)}, \tag{3.35}$$

and

$$p^* = \frac{1}{g(\rho_0)}\left(p - p_0 g(\rho_0)\frac{u^2}{c^2}\right). \tag{3.36}$$

2. Alternatively, following Wolfram [24], we can set

$$\tilde{\boldsymbol{u}} = g(\rho_0)\boldsymbol{u} \tag{3.37}$$

and

$$\tilde{p} = g(\rho_0)\left(p - p_0 g(\rho_0)\frac{u^2}{c^2}\right). \tag{3.38}$$

In both cases equation (3.33) gives the Navier-Stokes equation in the rescaled variables

$$\partial_{t^*} u_\alpha + u_\beta \partial_\beta u_\alpha = -\frac{1}{\rho_0}\partial_\alpha p^* + \nu^*(\rho_0)\partial_{\beta\beta} u_\alpha \tag{3.39}$$

and

$$\partial_t \tilde{u}_\alpha + \tilde{u}_\beta \partial_\beta \tilde{u}_\alpha = -\frac{1}{\rho_0}\partial_\alpha \tilde{P} + \nu(\rho_0)\partial_{\beta\beta}\tilde{u}_\alpha. \tag{3.40}$$

For both scalings we can define the Reynolds number for lattice gas simulations to be

$$Re = \frac{UL}{\nu^*(\rho_0)} = \frac{\tilde{U}\,L}{\nu(\rho_0)} = \frac{ULg(\rho_0)}{\nu(\rho_0)}, \tag{3.41}$$

where U and L are representative velocity and length scales of the flow and ν is the kinematic viscosity.

3.7 Units of Measurement in a Lattice Gas Model

When measurements are made from a lattice gas simulation it must be in terms of standard units which are fundamental to the lattice gas model. The basic unit of time is one time-step, the basic unit of length is a lattice unit (lu) which is the distance between two neighbouring sites on the grid. The basic unit of mass is the mass of a particle which is taken to be unity. Other quantities, such as velocity, are measured in units derived from these basic units, velocity being measured in lattice units per time-step. The Reynolds number, which is a dimensionless quantity, can be calculated from equation (3.41) and the simulation compared to a flow in the real world with the same Reynolds number.

As stated above the basic length scale is the lattice unit (lu), the distance between two neighbouring sites. It is sometimes convenient when describing the grid to refer to the number of sites in each direction. Thus a 512 by 512 grid is a grid with 512 sites in each direction, the grid is 512 by 443 lu since the separation between rows of sites is $\sqrt{3}/2$ lu.

3.8 Obtaining Macroscopic Quantities

The density and momentum at each site are defined in equation (3.2) as the sum of the occupation numbers at a site and the sum of the occupation number multiplied by its velocity. This allows the density and velocity to be calculated at each site. The density and velocity found in this way are very noisy and need to be averaged. In section 3.5.2 the mean density and velocity are found by taking ensemble averages. In practice it is usually more convenient to average over a region of the grid. This region must be small compared to the typical length scale of the flow being simulated. The larger the region, or averaging cell, the less noisy the results will be. The size of a cell is, however, restricted by the limits imposed

on the overall grid size by computer memory and time restrictions. Typically a cell will be no smaller than 16 by 16 sites. Figure 3–8 shows four averaging cells (here

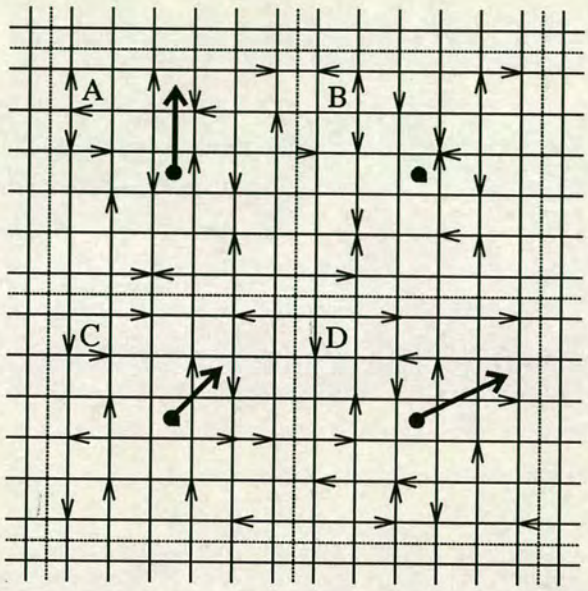

FIGURE 3–8: An example of averaging on a section of a square lattice with four averaging cells, shown by the dashed lines, superimposed over the grid. The individual particles are represented by the small arrows and the average velocities by the large arrows. The details of the different velocities and densities are shown in table 3–1.

shown as 6 by 6 sites for convenience) on a portion of a square lattice. Table 3–1 shows the microscopic details of the total number of particles M_i on each of the links $\boldsymbol{e}_i$ in each cell and the total number of particles in each cell, M. Also shown in the table are the details of the averaged velocity $\boldsymbol{u}$ and the averaged density ρ. The angle θ is the angle between the averaged velocity direction and the x-axis (the direction of $\boldsymbol{e}_2$). Note that the density is defined to be the mean number of particles per site *not* the mean number of particles per unit volume. Even after averaging over a large cell the results can still by noisy. Ensemble averaging is often used as well as cell averaging in an attempt to further reduce the noise.

3.9 Binary Fluid Models

In this section we examine models which have been proposed to simulate two fluids of the same phase within the lattice gas scheme.

Cell	M_1	M_2	M_3	M_4	M	ρ (lu)	u_x (lu)	u_y (lu)	$\lvert\boldsymbol{u}\rvert$ (lu)	θ (deg)
A	6	3	4	3	16	16/36	0	$2/\rho$	$2/\rho$	90
B	5	3	5	3	16	16/36	0	0	0	$\sim$
C	4	4	3	3	14	14/36	$1/\rho$	$1/\rho$	$\sqrt{2}/\rho$	45
D	4	5	3	3	15	15/36	$2/\rho$	$1/\rho$	$\sqrt{5}/\rho$	26.5

TABLE 3–1: The total number of particles M_i on link $\boldsymbol{e}_i$, the x and y components of the averaged velocity $\boldsymbol{u}$, its magnitude and inclination from link $\boldsymbol{e}_2, \theta$, the total number of particles M and the average density ρ for the four averaging cells shown in figure 3–8.

3.9.1 Introduction to Models with Coloured Particles

When using a lattice gas model it is possible to distinguish between the individual 'particles' by labelling them. Little can be gained from watching just one tagged particle since it will travel at constant speed along the lattice links and may well be travelling in a different direction to the mean flow. In lattice gas models it is necessary to consider the average behaviour of a number of particles; tagging particles can only give useful information about a flow if a significant percentage of the particles are tagged. The simplest example of tagged flow is when the particles are considered to be of two types or colours. In this case the particles are initially labelled either 'red' or 'blue', say, and the evolution of both fluids can be seen, along with any interactions between the fluids. The idea of using two different particles in a lattice gas model was first introduced by Clavin *et al.* [25]. The model has also been extended to allow three different particle types [26,27].

3.9.2 Properties of Colour Models

It is important that the mass of each fluid should remain constant in such a simulation. Thus we must add the conservation of colour equations

$$\begin{aligned} \textstyle\sum_i n_i^{(r)}(\boldsymbol{r}+\boldsymbol{e}_i, t+1) &= n_i^{(r)}(\boldsymbol{r}, t) \\ \textstyle\sum_i n_i^{(b)}(\boldsymbol{r}+\boldsymbol{e}_i, t+1) &= n_i^{(b)}(\boldsymbol{r}, t) \end{aligned} \tag{3.42}$$

to the conservation of mass and momentum equations (3.4) and (3.5). Here $n_i^{(r)}$ and $n_i^{(b)}$ are the occupation numbers for red and blue particles on link $\boldsymbol{e}_i$. We can define $C(\boldsymbol{r},t)$ to be the colour density given by

$$C(\boldsymbol{r},t) = \sum_i n_i^{(r)}(\boldsymbol{r},t) - n_i^{(b)}(\boldsymbol{r},t). \tag{3.43}$$

Equation (3.42) represents the only restriction on the colour of the particles. There is no constraint imposed, after a collision, as to which of the particles at any site should be of which colour. The available colour is re-assigned arbitrarily amongst the particles at each site after a collision. Thus if three particles, one red and two blue, arrive at a site and collide then after the collision one particle is randomly labelled red and the other two blue.

3.9.3 Surface Tension in a Binary Fluid Model

Two methods have been proposed and implemented to produce surface tension between the two coloured fluids.

The Reactive Model

The reactive surface tension model was proposed by Clavin *et al.* [25] and it involves particles changing from one particle type to the other if they cross the boundary between fluids. This is done by allowing the reactions

$$R + R + B \rightarrow R + R + R \tag{3.44}$$

and

$$R + B + B \rightarrow B + B + B \tag{3.45}$$

at every site containing three particles. Here R and B represent a red and a blue particle respectively. On average the same number of each interaction should take place and so the total number of particles of each colour should be conserved. Other than this reaction the particles interact according to the normal FHP rules. The coloured particle being assigned randomly amongst the out-state configuration after the collision.

The Colour-Field Model

The colour-field surface tension model was devised by Rothman *et al.* [28]. Let $C_i(\boldsymbol{r},t)$, the colour density of link $\boldsymbol{e}_i$ at time t and site $\boldsymbol{r}$ on a grid, be given by

$$C_i(\boldsymbol{r},t) = n_i^{(r)}(\boldsymbol{r},t) - n_i^{(b)}(\boldsymbol{r},t), \tag{3.46}$$

the difference between the number of red and blue particles on the link. Due to the exclusion principle C_i can take the values -1, 0 and 1. The colour density at a site, defined by equation (3.43), is given by

$$C(\boldsymbol{r},t) = \sum_i C_i(\boldsymbol{r},t). \tag{3.47}$$

The local colour flux $\boldsymbol{q}[s^{(r)}(\boldsymbol{r},t), s^{(b)}(\boldsymbol{r},t)]$ is given by

$$\boldsymbol{q}[s^{(r)}(\boldsymbol{r},t), s^{(b)}(\boldsymbol{r},t)] = \sum_i C_i(\boldsymbol{r},t)\boldsymbol{e}_i \tag{3.48}$$

and is the difference between the red momentum and the blue momentum at site $\boldsymbol{r}$ at time t where the site is in state $s = s^{(r)} + s^{(b)}$, the sum of the red and blue states. The local colour gradient $\boldsymbol{f}(\boldsymbol{r},t)$ is given by

$$\boldsymbol{f}(\boldsymbol{r},t) = \sum_i \boldsymbol{e}_i \sum_j C_j(\boldsymbol{r}+\boldsymbol{e}_i,t), \tag{3.49}$$

which is the microscopic gradient of the colour density $C(\boldsymbol{r},t)$. The work $W(s^{(r)}, s^{(b)})$ performed by the flux against the gradient is

$$W(s^{(r)}, s^{(b)}) = -\boldsymbol{f}\cdot\boldsymbol{q}(s^{(r)}, s^{(b)}). \tag{3.50}$$

The out-state of any FHP interaction $s^{(r)} \rightarrow s'^{(r)}, s^{(b)} \rightarrow s'^{(b)}$ is then chosen such that

$$W(s'^{(r)}, s'^{(b)}) = \min_{s''^{(r)}, s''^{(b)}} W(s''^{(r)}, s''^{(b)}) \tag{3.51}$$

where $s''^{(r)}, s''^{(b)}$ are all the possible collision outcomes.

3.10 Liquid-Gas Lattice Gas Models

The following liquid-gas model was first proposed to induce phase separation in a lattice gas by Appert and Zaleski [29]. The interaction was further developed in reference [30]. The interactions act to separate the fluid into two phases of considerably different densities, a liquid phase and a gaseous phase.

3.10.1 The Interactions

Figure 3–9 shows the basic interactions acting along the $\boldsymbol{e}_2$ direction on two sites a distance R apart. The interaction can take place only if there are particles travelling in *both* the directions indicated by the solid arrows and if there are *no* particles travelling in the direction of either of the dashed arrows. If this is the case the particles are flipped from the solid link to the dashed link. These five basic interactions are also applied along the $\boldsymbol{e}_1$ and $\boldsymbol{e}_3$ directions.

3.10.2 Implementation of the Interactions

Let $\mathcal{J}_i^{(x)}$, $x \in \{a, b, c, d, e\}$, $i \in \{1, 2, 3\}$ be the operator which implements interaction x, from figure 3–9, along direction $\boldsymbol{e}_i$. If the interaction cannot take place the operator $\mathcal{J}_i^{(x)}$ defaults to the identity operator $\mathcal{I}$ leaving the particles unchanged. If we define the operators

$$\mathcal{J}^{(x)} \stackrel{\text{def}}{=} \mathcal{J}_j^{(x)} \circ \mathcal{J}_k^{(x)} \circ \mathcal{J}_l^{(x)}, \quad x \in \{a, b, c, d, e\}, \tag{3.52}$$

where j,k,l are a random ordering or 1,2,3, then we can define an overall interaction operator

$$\mathcal{J} \stackrel{\text{def}}{=} \mathcal{J}^{(a)} \circ \mathcal{J}^{(b)} \circ \ldots\ldots \circ \mathcal{J}^{(e)}. \tag{3.53}$$

The evolution operator, first introduced in section 3.5.1, can now be re-written

$$\mathcal{E} = \mathcal{S} \circ \mathcal{J} \circ \mathcal{C}. \tag{3.54}$$

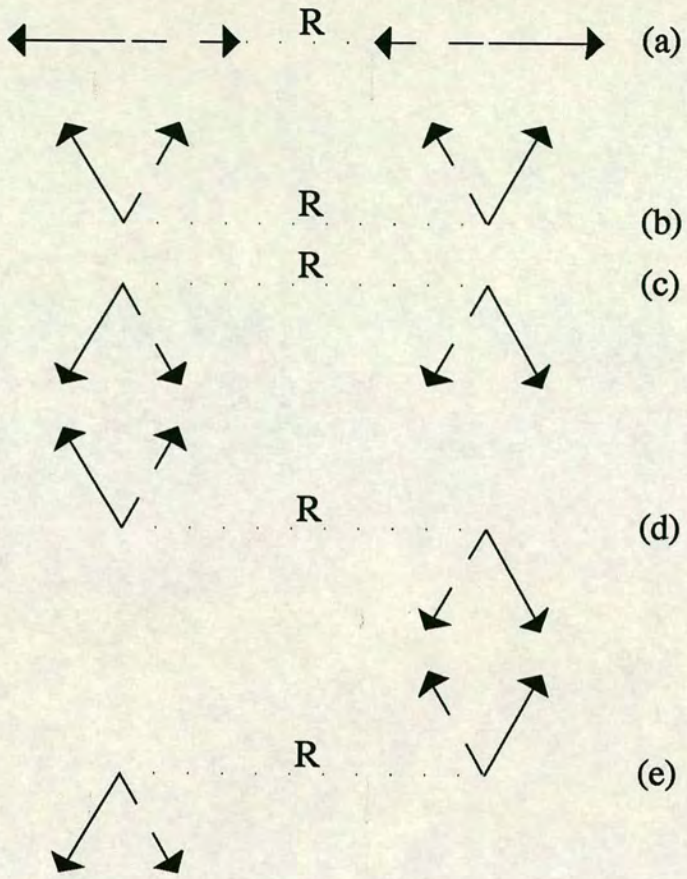

FIGURE 3–9: The basic long-range interactions acting in the direction of $\boldsymbol{e}_2$. Particles at sites R lattice units apart are flipped from the solid link directions to the dashed directions provided there is initially a particle in both the solid links and no particles in either of the dashed links.

3.11 Lattice Gas Simulations

All the lattice gas models have been used to simulate many different flow situations. These include single fluid simulation such as Poiseuille flow in a pipe [31]; Von Karman street formation behind a flat plate [32,33,19]; flow over a step [34]; vortex shedding behind various objects inserted in a steady flow [35]; jet simulation [35]; injected flow from a pipe into a transverse flow [36] and multiple fluid simulations such as the Kelvin-Helmholtz instability [25].

3.11.1 Drawbacks of the Lattice Gas Approach

There are a number of problems with the lattice gas technique.

Lack of Galilean Invariance

The most significant problem is the lack of Galilean invariance. This appears in the equations of motion as the non-unity density dependent term $g(\rho)$. The correct Navier-Stokes equation can be recovered using a scaling technique, see section 3.6, for a single fluid simulation, however for a multi-fluid simulation the scaling procedure will introduce a g factor into the diffusion equation [37,19]. Thus two fluids can not be correctly modelled in a Galilean invariant system. Some attempts have been made to devise collision rules which achieve $g(\rho) = 1$ [19,18] however g remains a function of the density and so the model is only Galilean invariant at one density and can not be used if there is any density variation involved in the simulation. In a single species model the scaling techniques can be used to overcome the lack of Galilean invariance but even here the density must be constant because the viscosity and the pressure are both functions of the density. This severely limits the application of the lattice gas model.

Noisy Results

The lattice gas simulations tend to be very noisy. This is overcome, to some extent, by averaging the density and velocity over a cell, typically containing at least 16 by 16 sites. The results of such averaging are still significantly noisy and frequently much larger cells are used and ensemble averaging is also employed. The cellular automaton structure of the lattice gas model makes it suitable for parallel computer implementation. If, however, a significant amount of averaging is required before acceptable results are obtained this can more than outweigh any advantages the model has when computer resources are considered. For example consider a simulation which requires cell averaging in 32 by 32 cells and ensemble averaging over 10 simulations. This evolves using a grid with 1024 times larger than the

resolution required and running the same simulation, with different random seeds, 10 times. This is clearly wasteful of computer resources.

Large Collision Matrices

The number of possible collisions which must be considered at each time-step can also prove computationally restrictive. When a three-dimensional model is being used there are 2^{24} possible in-states and out-states which need to be considered.

Non-Physical Phase Separation

The binary fluid and liquid-gas models suffer from the lack of Galilean invariance discussed earlier. They have the further drawback that the surface tension and phase separation are produced in an arbitrary manner. The rules appear to produce the desired effect but they have no underlying physical basis.

3.12 Summary

We have examined the lattice gas model. There are a number of different variants but they all consider the evolution of fluid particles on a regular lattice. The particle distribution tends to an equilibrium which is described by the Fermi-Dirac distribution. The model has been seen to satisfy the continuity equation and an equation similar to the Navier-Stokes equation. The lattice gas Navier-Stokes equation differs from the standard Navier-Stokes equation through the inclusion of a density dependent function $g(\rho)$ and an additional term, added to the pressure term, which is a function of density and velocity. The viscosity of a lattice gas fluid is also a function of density. The $g(\rho)$ term, which represents the lack of Galilean invariance, can be removed from the lattice gas Navier-Stokes equation using a scaling technique, however the density dependence remains. Multi-fluid models have also been discussed. It has been seen that the lattice gas model is capable of simulating a binary fluid mixture and a liquid-gas. The lack of Galilean invariance

can *not* be overcome by the scaling technique for such a model and the unphysical density dependence can cause problems, particularly in a liquid-gas model where there is a large density difference across the simulation. Listed below are some of the main features of the models.

Exclusion Principle

An exclusion principle is applied to each of the links, allowing only one particle to travel in each direction along any of the links. The number of rest particles, when they are allowed, is also limited to one in most models. This leads to the Fermi-Dirac distribution of the equilibrium population.

Galilean Invariance

The lack of Galilean invariance appears in the equations of motion through the factor $g(\rho)$. There are Galilean invariant models in which $g(\rho) = 1$. This is achieved in the FHP model by changing the probability with which a rest particle is created and destroyed [19] or by adding a large number of extra rest particles [18]. Scaling techniques can also be used to eliminate the lack of Galilean invariance, see section 3.6, for a single species model. Whichever method is used to restore Galilean invariance the model must be run at a constant density. Galilean invariant models have the disadvantage that they achieve $g = 1$ by relaxing semi-detailed balance which is assumed in the derivation of the equilibrium distribution function.

Conservables

All the models conserve the density $\sum_{i=0}^{b} n_i$ and momentum $\sum_{i=1}^{b} \mathbf{e}_i n_i$ during the collision stage at each site, where b is the number of links in the model and $n_0 = 0$ for a model with no rest particles.

Isotropy

All the FHP models exhibit isotropy. This is clearly crucial since any dependence on the orientation of the underlying grid would render the model unusable.

Results for the FHP Models

There are several model-dependent quantities involved in lattice gas modelling. They were found by Frisch *et al.* [8] and are reproduces in table 3–2 for the most common FHP models. Table 3–2 gives the mean density, ρ_0; the speed of sound, c_s; the 'g-factor' which re-scales the nonlinear term in the Navier-Stokes equation,

	FHP-I	FHP-II	FHP-III
ρ_0	$6d$	$7d$	$7d$
c_s	$\frac{1}{\sqrt{2}}$	$\sqrt{\frac{3}{7}}$	$\sqrt{\frac{3}{7}}$
g	$\frac{1}{2}\frac{1-2d}{1-d}$	$\frac{7}{12}\frac{1-2d}{1-d}$	$\frac{7}{12}\frac{1-2d}{1-d}$
ν	$\frac{1}{12}\frac{1}{d(1-d)^3}-\frac{1}{8}$	$\frac{1}{28}\frac{1}{d(1-d)^3}\frac{1}{1-4d/7}-\frac{1}{8}$	$\frac{1}{28}\frac{1}{d(1-d)}\frac{1}{1-8d(1-d)/7}-\frac{1}{8}$
ζ	0	$\frac{1}{98}\frac{1}{d(1-d)^4}-\frac{1}{28}$	$\frac{1}{98}\frac{1}{d(1-d)}\frac{1}{1-2d(1-d)}-\frac{1}{28}$

TABLE 3–2: Results for the FHP models

g; the kinematic shear viscosity, ν; and the kinematic bulk viscosity, ζ; as functions of the mean density per site, d.

Chapter 4

The Lattice Boltzmann Model

The lattice Boltzmann model has evolved from the lattice gas model. In this chapter we outline the changes which have been made to the lattice gas formulation in order to overcome the problems associated with it. The accumulation of these alterations has resulted in the lattice Boltzmann model. This is described in detail for a single species fluid and it is shown that the correct form of the equilibrium distribution will ensure that the model is isotropic and Galilean invariant. Multi-fluid models are also considered with particular attention to the immiscible, binary fluid model of Orlandini *et al.* [9]. At the end of the chapter a number of simulation results using the Orlandini model are shown. These repeat results already presented [9,38] and act to demonstrate some important features of the model and to test the model implementation.

4.1 Development of the Lattice Boltzmann Model

While lattice gas models have had some success in simulating fluid behaviour they have a number of draw backs. One of these is the noise which is inherent in a lattice gas model. This is due to the limited number of sites over which the averaging takes placer to find the macroscopic variables ρ and $\rho\boldsymbol{u}$. Another problem is the number of states which need to be considered during the collision stage. For a two-dimensional model such as the FHP-III this is fairly small since each in-state

has a maximum of two possible outcomes and a look-up table with 2×2^7 entries is required. For a three-dimensional simulation a table as large as $2^{24} \times 2^{24}$ may be required. The Galilean invariance problem is a major draw back of the lattice gas scheme. It can be overcome using a scaling technique for single fluid flows with a slowly varying density. This is not possible for multi-phase simulations. The density-dependence of the transport coefficients is another feature of the lattice gas models which restricts their use to constant density situations.

4.1.1 Lattice Boltzmann Model for the Ensemble Averaged Distribution Function

The problem with the noise in the lattice gas model has been overcome by the development of the first Lattice Boltzmann model [39] which replaces the Boolean lattice variables $n_i(\boldsymbol{r}, t)$ with there ensemble averaged quantities $f_i(\boldsymbol{r}, t)$ where $f_i(\boldsymbol{r}, t) = \langle n_i(\boldsymbol{r}, t) \rangle$. The averaged quantities $f_i(\boldsymbol{r}, t)$ are now real functions in the range $0 \leq f_i \leq 1$ and the average mass and momentum are given (see equations (3.9)–(3.12)) by

$$\rho(\boldsymbol{r}, t) = \sum_i f_i(\boldsymbol{r}, t) \tag{4.1}$$

and

$$\rho(\boldsymbol{r}, t)\boldsymbol{u}(\boldsymbol{r}, t) = \sum_i f_i(\boldsymbol{r}, t)\boldsymbol{e}_i \tag{4.2}$$

The evolution of f, the distribution function, is found by ensemble averaging the lattice gas collision function,

$$f_i(\boldsymbol{r} + \boldsymbol{r}_i, t + 1) - f_i(\boldsymbol{r}, t) = \langle \Omega_i(n) \rangle. \tag{4.3}$$

4.1.2 The Linear Collision Operator

The use of the above lattice Boltzmann equation removes the statistical noise from the lattice simulations. The collision operator $\Omega_i(f) = \langle \Omega_i(n) \rangle$ still depends on the 2^m Boolean input and output states, where $m = b$ for a model with b

links and no 'rest-particles' and $m = b + 1$ for a model with rest-particles. For a Boltzmann simulation based on the two-dimensional FHP-III model $\Omega_i(f)$ is a $2^7 \times 2^7$ matrix, for a face-centred-hypercubic (FCHC) model, used in three-dimensional simulations, $\Omega_i(f)$ is a $2^{24} \times 2^{24}$ matrix. Clearly the computational requirements for handling such a matrix can be limiting. The size of the matrix can be greatly reduced [40] by expanding the distribution function

$$f_i = \overline{f_i} + f_i^* \tag{4.4}$$

where $\overline{f_i}$ is the equilibrium value of the distribution function and $f_i^* \ll \overline{f_i}$ is the non-equilibrium part. Expanding the collision operator about the equilibrium distribution gives

$$\Omega_i(f_i) = \Omega_i(\overline{f_j}) + \sum_j f_j^* \Omega_{ij} + O((f_i^*)^2) \tag{4.5}$$

where

$$\Omega_{ij} = \left. \frac{\partial \Omega_i}{\partial f_j} \right|_{f_j = \overline{f_j}} \tag{4.6}$$

Thus, since $\Omega_i(\overline{f_i}) = 0$, the lattice Boltzmann equation can be written [40]

$$f_i(\boldsymbol{r} + \boldsymbol{r}_i, t+1) - f_i(\boldsymbol{r}, t) = \sum_j \Omega_{ij}(f_j - \overline{f_j}) \tag{4.7}$$

Here Ω_{ij} is the linearised collision matrix and is an $m \times m$ matrix, a considerable reduction from the $2^m \times 2^m$ matrix $\Omega_i(f)$. The value of the individual elements of Ω_{ij} still depends on the form of the lattice gas collision rules.

4.1.3 The Enhanced Collision Rules

The form of the collision operator can be further simplified by considering the form of Ω_{ij} to depend not on a set of collisions but on the isotropy of the model and the conservation constraints [41]. Consider first the elements $\Omega_{ij} \quad i, j = 1, .., b$ which describe the change in the distribution function f_i which is induced by a unit change in f_j during the collision. Due to the isotropy of the model Ω_{ij} must depend only on the angle between $\boldsymbol{e}_i$ and $\boldsymbol{e}_j$ which, for a hexagonal grid, must be one of four angle: $0^0, 60^0, 120^0$ and 180^0. Thus there are only four independent

elements in Ω_{ij}. If 'rest-particles' are also allowed two new independent variables must also be included in $\Omega_{ij} \quad i,j = 0,..,b$, one to account for the influence of 'rest particles' on themselves (Ω_{00}) and one to account for the influence of 'rest particles' on moving 'particles' (Ω_{0i} and $\Omega_{i0} \quad i \neq 0$) [41]. Thus for a hexagonal lattice with 'rest particles'

$$\Omega_{ij} = \begin{bmatrix} c & b & b & b & b & b & b \\ b & a_0 & a_{60} & a_{120} & a_{180} & a_{120} & a_{60} \\ b & a_{60} & a_0 & a_{60} & a_{120} & a_{180} & a_{120} \\ b & a_{120} & a_{60} & a_0 & a_{60} & a_{120} & a_{180} \\ b & a_{180} & a_{120} & a_{60} & a_0 & a_{60} & a_{120} \\ b & a_{120} & a_{180} & a_{120} & a_{60} & a_0 & a_{60} \\ b & a_{60} & a_{120} & a_{180} & a_{120} & a_{60} & a_0 \end{bmatrix} \tag{4.8}$$

where a_θ are the matrix elements linking directions which intersect at an angle θ and b and c are elements linking 'rest particles' to moving 'particles' and to themselves respectively. The number of independent variables can be further reduced by considering the conservation of mass (the sum of each column of the matrix equation (4.8) $= 0$) and the conservation of momentum [41]

$$\begin{aligned} 6b + c &= 0 \\ a_0 + 2a_{60} + 2a_{120} + a_{180} + b &= 0 \\ a_0 + a_{60} - a_{120} - a_{180} &= 0. \end{aligned} \tag{4.9}$$

The collision rules described by this greatly reduced collision matrix are referred to as the enhanced collision rules. The eigenvectors for the matrix $\Omega_{ij} \quad i,j = 0,...,b$ can be calculated. For a two-dimensional hexagonal grid with $b = 6$ there are three distinct non-zero eigenvalues

$$\begin{aligned} \lambda &= 6(a_0 + a_{60}) + 2b \\ \sigma &= -6(a_0 + 2a_{60}) - 3b \\ \tau &= -7b. \end{aligned} \tag{4.10}$$

The first eigenvalue can then be associated with the viscosity [41,8] to give

$$\nu = -\frac{1}{4}\left(\frac{1}{\lambda} + \frac{1}{2}\right) \tag{4.11}$$

where $-2 < \lambda \leq 0$. Such a model can be shown [41,42] to satisfy the Navier-Stokes equation with the additional $g(\rho)$ factor and with the viscosity given by equation (4.11).

4.1.4 The Single Relaxation Time Lattice Boltzmann Model

The collision operator Ω_{ij} can be further simplified [43] by assuming that the particle distribution function relaxes to its equilibrium state at a constant rate

$$\left.\frac{\partial \Omega_i}{\partial f_j}\right|_{f_j=\overline{f_j}} = -\frac{1}{\tau}\delta_{ij} \tag{4.12}$$

which gives a collision term

$$\Omega_i = \frac{-1}{\tau}(f_i - \overline{f}_i). \tag{4.13}$$

A lattice Boltzmann equation with this collision operator is called a lattice BGK equation because of its similarity to the classical BGK Boltzmann operator [6]. With the introduction of this single relaxation parameter and the comparison with the classical Boltzmann equation the form of the equilibrium distribution was also compared. In the classic model the equilibrium distribution is a Maxwell-Boltzmann distribution [11], while in the earlier lattice Boltzmann models, which have been considered to be an evolution of the lattice gas models, a Fermi-Dirac distribution is used. This originates in the constraint that only one particle is allowed on each of the lattice links. This constraint was applied to simplify the computation, it allowed the state of each link to be described by a Boolean variable and limited the number of collisions which could take place. There is no physical requirement for such a constraint. The single relaxation time model described here is inspired by the classical Boltzmann BGK model described in section 2.4. Using the lattice BGK approach and selecting an equilibrium distribution such that the correct macroscopic equations are satisfied, rather than adopting the lattice gas equilibrium distribution, the lattice Boltzmann model is found to satisfy (to second-order in the velocity and the Knudsen number) the continuity equation and the exact Navier-Stokes equation without the $g(\rho)$ term [44,45,46]. This will be shown in section 4.2.

4.2 An Isotropic, Galilean Invariant BGK Model

Here we derive an equilibrium distribution which is intrinsically isotropic and Galilean invariant. The continuity equation and the Navier-Stokes equation are then derived from the single relaxation time lattice Boltzmann equation by performing a Chapman-Enskog expansion and considering the conservation of mass and momentum. The method followed will be the same as in reference [47], however here we consider a hexagonal lattice rather than a square one.

4.2.1 The Equilibrium Distribution

First we expand the equilibrium distribution $\overline{f}_i$ up to second-order in the velocity $O(u^2)$:

$$\overline{f}_i(\boldsymbol{u}) = \overline{f}_i(0)\left(1 + Au_\alpha e_{i\alpha} + Bu_\alpha u_\alpha + Cu_\alpha u_\beta e_{i\alpha} e_{i\beta}\right), \tag{4.14}$$

where

$$\begin{aligned} \overline{f}_i(0) &= \overline{f}^0 \quad i = 0 \\ \overline{f}_i(0) &= \overline{f}^* \quad i = 1, 2, ..., 6. \end{aligned} \tag{4.15}$$

The coefficients $A, B, C, \overline{f}^0$ and $\overline{f}^*$ need to be found, subject to isotropy and Galilean invariance, in order to obtain the required equilibrium distribution (to accuracy $O(u^2)$). The isotropy conditions required on the second- and fourth-order tensors [47,48] can be explicitly introduced by defining n_2 and n_4:

$$\sum_i \overline{f}_i(0) e_{i\alpha} e_\beta = n_2 \delta_{\alpha\beta} \tag{4.16}$$

and

$$\sum_i \overline{f}_i(0) e_{i\alpha} e_\beta e_{i\gamma} e_{i\delta} = n_4(\delta_{\alpha\beta}\delta_{\gamma\delta} + \delta_{\alpha\gamma}\delta_{\beta\delta} + \delta_{\alpha\delta}\delta_{\beta\gamma}). \tag{4.17}$$

The sum of the equilibrium distribution multiplied by an odd number of $\boldsymbol{e}_i$'s is zero. Considering $\alpha = \beta = x$ in equation (4.16) and $\alpha = \beta = \gamma = \delta = x$ in equation (4.17) gives

$$n_2 = 3\overline{f}^* \tag{4.18}$$

and

$$n_4 = \frac{3}{4}\overline{f}^*. \tag{4.19}$$

Combining these we see that

$$n_2 = 4n_4. \tag{4.20}$$

We now consider the Galilean invariance requirement. If M_j is the jth moment,

$$M_j(\boldsymbol{u}) = \sum_i (\boldsymbol{u} - \boldsymbol{e}_i)^j \overline{f}_i(\boldsymbol{u}), \tag{4.21}$$

then we require [47,48]

$$M_j(\boldsymbol{u}) = M_j(0), \quad j = 0, 1, 2, 3. \tag{4.22}$$

The zeroth moment is

$$M_0(\boldsymbol{u}) = \sum_i \overline{f}_i(0)\left(1 + Au_\alpha e_{i\alpha} + Bu_\alpha u_\alpha + Cu_\alpha u_\beta e_{i\alpha} e_{i\beta}\right). \tag{4.23}$$

Considering terms $O(u^2)$ and using the isotropy condition, equation (4.16), we get

$$\rho B + n_2 C = 0. \tag{4.24}$$

The first moment is

$$M_1(\boldsymbol{u}) = \sum_i (\boldsymbol{u} - \boldsymbol{e}_i)\overline{f}_i(0)\left(1 + Au_\alpha e_{i\alpha} + Bu_\alpha u_\alpha + Cu_\alpha u_\beta e_{i\alpha} e_{i\beta}\right). \tag{4.25}$$

Considering terms $O(u)$ and using the isotropy condition, equation (4.16), gives

$$\rho - n_2 A = 0. \tag{4.26}$$

The second moment is

$$M_2(\boldsymbol{u})_{\gamma\delta} = \sum_i (\boldsymbol{u} - \boldsymbol{e}_i)_\gamma (\boldsymbol{u} - \boldsymbol{e}_i)_\delta \overline{f}_i(0)\left(1 + Au_\alpha e_{i\alpha} + Bu_\alpha u_\alpha + Cu_\alpha u_\beta e_{i\alpha} e_{i\beta}\right). \tag{4.27}$$

Collecting terms of second-order in $\boldsymbol{u}$ gives

$$u_\gamma u \delta\rho - An_2 u_\gamma u_\delta - An_2 u_\gamma u_\delta + Bn_2 \delta_{\gamma\delta} u_\alpha u_\alpha + n_4 C u_\alpha u_\alpha \delta_{\gamma\delta} + n_4 C u_\gamma u_\delta + n_4 C u_\gamma u_\delta = 0. \tag{4.28}$$

Considering separately the terms $O(u_\gamma u_\delta)$ and $O(u^2\delta_{\gamma\delta})$ we get

$$\rho - 2An_2 + 2n_4C = 0 \tag{4.29}$$

and

$$Bn_2 + Cn_4 = 0. \tag{4.30}$$

The third moment is

$$M_3(\boldsymbol{u})_{\gamma\delta\epsilon} = \sum_i (\boldsymbol{u}-\boldsymbol{e}_i)_\gamma (\boldsymbol{u}-\boldsymbol{e}_i)_\delta (\boldsymbol{u}-\boldsymbol{e}_i)_\epsilon \overline{f}_i(0)\,(1 + Au_\alpha e_{i\alpha} + Bu_\alpha u_\alpha + Cu_\alpha u_\beta e_{i\alpha} e_{i\beta})\,. \tag{4.31}$$

Collecting terms $O(u\delta)$ gives

$$(u_\gamma\delta_{\delta\epsilon} + u_\delta\delta_{\gamma\epsilon} + u_\epsilon\delta_{\gamma\delta})(n_2 - An_4) = 0. \tag{4.32}$$

This gives the final condition

$$n_2 - An_4 = 0. \tag{4.33}$$

Solving equations (4.20), (4.24), (4.26), (4.29), (4.30) and (4.33) gives $n_2 = \rho/4, n_4 = \rho/16, A = 4, B = -2$ and $C = 8$. The value of $\overline{f^*} = \rho/12$ is found from equation (4.18) and $\overline{f^0} = \rho/2$ is obtained by considering the sum of the distribution functions

$$\rho = \sum_i f_i = \overline{f^0} + 6\overline{f^*}. \tag{4.34}$$

Thus we have the following equilibrium distribution for a two-dimensional lattice Boltzmann model which, by construction, must be isotropic and Galilean invariant.

$$\overline{f}_i(\boldsymbol{u}) = \overline{f}_i(0)\,(1 + 4u_\alpha e_{i\alpha} - 2u_\alpha u_\alpha + 8u_\alpha u_\beta e_{i\alpha} e_{i\beta}) \tag{4.35}$$

where

$$\begin{aligned} \overline{f}_i(0) &= \frac{\rho}{2} \quad i = 0 \\ \overline{f}_i(0) &= \frac{\rho}{12} \quad i = 1, 2, ..., 6 \end{aligned} \tag{4.36}$$

4.2.2 The Conservation Equations

The derivation of the continuity equation and the Navier-Stokes equation from the equilibrium distribution is normally carried out using a Chapman-Enskog expansion, following the lattice gas derivation of Frisch [8]. This is shown below for a model, first used by Chen *et al.* [45], which is for a D-dimensional grid with b links where the particle speed is $|\boldsymbol{e}_i| = c$.

Useful Relations

Before considering the model we note some useful relations [24,38].

$$\sum_i e_{i\alpha} = 0 \tag{4.37}$$

$$\sum_i e_{i\alpha} e_{i\beta} = \frac{c^2 b}{D} \delta_{\alpha\beta} \tag{4.38}$$

$$\sum_i e_{i\alpha} e_{i\beta} e_{i\gamma} = 0 \tag{4.39}$$

$$\sum_i e_{i\alpha} e_{i\beta} e_{i\gamma} e_{i\beta} = \frac{c^4 b}{D(D+2)} (\delta_{\alpha\beta}\delta_{\gamma\delta} + \delta_{\alpha\gamma}\delta_{\beta\delta} + \delta_{\alpha\gamma}\delta_{\beta\delta}) \tag{4.40}$$

$$\sum_i e_{i\alpha} e_{i\beta} e_{i\gamma} e_{i\delta} e_{i\epsilon} = 0 \tag{4.41}$$

Basic Model

Consider the following model:

$$f_i(\boldsymbol{r} + \boldsymbol{e}_i, t+1) - f_i(\boldsymbol{r}, t) = \Omega_i(\boldsymbol{r}, t) \tag{4.42}$$

where the collisions are performed by a single relaxation time BGK operator

$$\Omega_i(\boldsymbol{r}, t) = -\frac{1}{\tau} \left[f_i(\boldsymbol{r}, t) - \overline{f}_i(\boldsymbol{r}, t) \right]. \tag{4.43}$$

The equilibrium distribution function is

$$\overline{f}_i(\boldsymbol{r}, t) = E_i(\rho, \boldsymbol{u}) \tag{4.44}$$

where

$$E_i(\rho, \boldsymbol{u}) = \begin{cases} \rho\left(\dfrac{1-d_0}{b} + \dfrac{D}{c^2 b}\boldsymbol{e}_i \cdot \boldsymbol{u} + \dfrac{D(D+2)}{2c^4 b}(\boldsymbol{e}_i \cdot \boldsymbol{u})^2 - \dfrac{Du^2}{2c^2 b}\right), & i = 1, .., b \\ \rho\left(d_0 - \dfrac{u^2}{c^2}\right), & i = 0, \end{cases} \tag{4.45}$$

d_0 is a constant, $\rho = \sum_i f_i$ and $\rho u_\alpha = \sum_i f_i e_{i\alpha}$. This reduces to the isotropic, Galilean invariant, two-dimensional equilibrium distribution derived in section 4.2.1 when $D = 2, b = 6$ and $d_0 = 1/2$. Using this equilibrium distribution and equations (4.37)–(4.41) we see that

$$\sum_i \overline{f}_i = \rho, \tag{4.46}$$

$$\sum_i \overline{f}_i e_{i\alpha} = \rho u_\alpha, \tag{4.47}$$

$$\sum_i \overline{f}_i e_{i\alpha} e_{i\beta} = \frac{\rho(1-d_0)c^2}{D}\delta_{\alpha\beta} + \rho u_\alpha u_\beta \tag{4.48}$$

and

$$\sum_i \overline{f}_i e_{i\alpha} e_{i\beta} e_{i\gamma} = \frac{\rho c^2}{D+2}(u_\alpha \delta_{\beta\gamma} + u_\beta \delta_{\alpha\gamma} + u_\gamma \delta_{\alpha\beta}). \tag{4.49}$$

4.2.3 Chapman-Enskog Expansion

To perform the Chapman-Enskog expansion we must first Taylor expand equation (4.42):

$$\begin{aligned} & f_i(\boldsymbol{r} + \boldsymbol{e}_i, t+1) - f_i(\boldsymbol{r}, t) \\ & \simeq \left[\partial_t + e_{i\alpha}\partial_\alpha + \frac{1}{2}e_{i\alpha}\partial_\alpha(e_{i\beta}\partial_\beta + \partial_t) + \frac{1}{2}\partial_t(e_{i\alpha}\partial_\alpha + \partial_t)\right] f_i(\boldsymbol{r}, t). \end{aligned} \tag{4.50}$$

Expanding the population functions and the time and space derivatives in terms of the Knudsen number,

$$\begin{aligned} f_i &= f_i^{(0)} + \epsilon f_i^{(1)} + \epsilon^2 f_i^{(2)} + ... \\ \partial_t &= \epsilon\partial_{1t} + \epsilon^2\partial_{2t} + ... \\ \partial_{\boldsymbol{r}} &= \epsilon\partial_{1\boldsymbol{r}}, \end{aligned} \tag{4.51}$$

and using equation (4.50) we can perform an Chapman-Enskog expansion. Substituting equation (4.51) into equations (4.42), (4.43) and (4.50) gives

$$\left\{\left(\epsilon\partial_{1t}+\epsilon^2\partial_{2t}\right)+e_{i\alpha}\epsilon\partial_{1\alpha}+\frac{1}{2}e_{i\alpha}\epsilon\partial_{1\alpha}\left[e_{i\beta}\epsilon\partial_{1\beta}+\left(\epsilon\partial_{1t}+\epsilon^2\partial_{2t}\right)\right]\right.$$

$$\left.+\frac{1}{2}\left(\epsilon\partial_{1t}+\epsilon^2\partial_{2t}\right)\left[e_{i\alpha}\epsilon\partial_{1\alpha}+\left(\epsilon\partial_{1t}+\epsilon^2\partial_{2t}\right)\right]\right\} \tag{4.52}$$

$$\times\left(f_i^{(0)}+\epsilon f_i^{(1)}+\epsilon^2 f_i^{(2)}\right)=-\frac{1}{\tau_\rho}\left(f_i^{(0)}+\epsilon f_i^{(1)}+\epsilon^2 f_i^{(2)}-\overline{f}_i\right).$$

The notation $(\partial_{1}\boldsymbol{r})_\alpha=\partial_{1\alpha}$ has been used. The zeroth-order approximation, $f_i^{(0)}$, is taken to be the equilibrium distribution: $f_i^{(0)}=\overline{f}_i$. The conservation of mass and momentum require that $\sum_i f_i^{(a)}=\sum_i f_i^{(a)}e_{i\alpha}=0 \quad a=1,2$. To first-order in ϵ equation (4.52) is

$$\partial_{1t}f_i^{(0)}+\partial_{1\alpha}e_{i\alpha}f_i^{(0)}=-\frac{1}{\tau}f_i^{(1)}. \tag{4.53}$$

Summing equation (4.53), using equations (4.46) and (4.47), gives

$$\partial_{1t}\rho+\partial_{1\alpha}\rho u_\alpha=0. \tag{4.54}$$

Multiply equation (4.53) by $e_{i\beta}$ we get

$$\partial_{1t}e_{i\beta}f_i^{(0)}+\partial_{1\alpha}e_{i\beta}e_{i\alpha}f_i^{(0)}=-\frac{1}{\tau}f_i^{(1)}e_{i\beta}. \tag{4.55}$$

Summing this, using equations (4.47) and (4.48), gives

$$\partial_{1t}\rho u_\beta+\partial_{1\alpha}\rho u_\alpha u_\beta=-\partial_{1\alpha}\left[\frac{\rho(1-d_0)}{D}c^2\delta_{\alpha\beta}\right]. \tag{4.56}$$

To second-order in ϵ we get

$$\partial_{2t}f_i^{(0)}+\partial_{1t}f_i^{(1)}+\partial_{1\alpha}e_{i\alpha}f_i^{(1)}+\frac{1}{2}\partial_{1t}(\partial_{1t}f_i^{(0)}+\partial_{1\alpha}e_{i\alpha}f_i^{(0)})$$

$$+\frac{1}{2}\partial_{1\alpha}(\partial_{1t}e_{i\alpha}f_i^{(0)}+\partial_{1\beta}e_{i\beta}e_{i\alpha}f_i^{(0)})=-\frac{1}{\tau}f_i^{(2)}. \tag{4.57}$$

Summing equation (4.57) over i, we see that terms two and three are zero due to the conservation of mass and momentum and terms four and five are zero by equations (4.54) and (4.56). This leaves

$$\partial_{2t}\rho=0. \tag{4.58}$$

Multiplying equation (4.57) by $e_{i\gamma}$ and summing over i gives

$$\sum_i \Big\{ \partial_{2t} e_{i\gamma} f_i^{(0)} + \partial_{1t} e_{i\gamma} f_i^{(1)} + \partial_{1\alpha} e_{i\gamma} e_{i\alpha} f_i^{(1)} + \frac{1}{2}\partial_{1t}(\partial_{1t} e_{i\gamma} f_i^{(0)} + \partial_{1\alpha} e_{i\gamma} e_{i\alpha} f_i^{(0)})$$

$$+\frac{1}{2}\partial_{1\alpha}(\partial_{1t} e_{i\alpha} e_{i\gamma} f_i^{(0)} + \partial_{1\beta} e_{i\gamma} e_{i\beta} e_{i\alpha} f_i^{(0)}) = -\frac{1}{\tau} f_i^{(2)} e_{i\gamma} \Big\}. \tag{4.59}$$

The second term is zero by the definition of $f_i^{(1)}$ while the fourth term is zero by equations (4.56). The fifth term is given by equations (4.48) and (4.49). The third term can be found by considering equations (4.53) multiplied by $\partial_{1\beta} e_{i\beta} e_{i\gamma}$ and summed over i giving, to order $O(u)$,

$$\sum_i \partial_{1\alpha} e_{i\alpha} e_{i\gamma} f_i^{(1)}$$

$$= -\tau \left\{ \frac{(1-d_0)c^2}{D} \partial_{1t}\partial_{1\alpha}\rho\delta_{\alpha\gamma} + \partial_{1\alpha}\partial_{1\beta}\frac{\rho c^2}{D+2}\left[u_\alpha\delta_{\beta\gamma} + u_\beta\delta_{\alpha\gamma} + u_\gamma\delta_{\alpha\beta}\right] \right\}. \tag{4.60}$$

So we get, using equation (4.54) to convert time derivatives into spatial derivatives,

$$\partial_{2t}\rho u_\gamma = \nu\partial_{1\alpha}\partial_{1\alpha}\rho u_\gamma + \partial_{1\gamma}(\zeta\partial_{1\alpha}\rho u_\alpha) \tag{4.61}$$

where $\nu = c^2(\tau - 1/2)/(D+2)$ and $\zeta = (\tau - 1/2)[2c^2/(D+2) - c^2(1-d_0)/D]$ are the kinematic shear and bulk viscosities. Summing the first- and second-order density and momentum equations and recombining the derivatives gives the continuity equation,

$$\partial_t\rho + \partial_\alpha\rho u_\alpha = 0 \tag{4.62}$$

and the Navier-Stokes equation

$$\partial_t\rho u_\alpha + \partial_\beta\rho u_\beta u_\alpha = -\partial_\beta\left[\frac{\rho(1-d_0)}{D}c^2\delta_{\alpha\beta}\right] + \nu\partial_\beta\partial_\beta\rho u_\alpha + \partial_\alpha\zeta\partial_\beta\rho u_\beta. \tag{4.63}$$

4.3 Boundaries in a Lattice Boltzmann Model

As with the lattice gas model, see section 3.3, a boundary can be introduced to a lattice Boltzmann model by selecting the grid sites where the boundary is to be set and evolving the fluid in a different manner at these sites. The effect the boundary has on the fluid depends on how the distribution functions are treated at these sites.

4.3.1 Bounce Back Boundary Conditions

The initial approach to simulating a boundary was to follow the FHP method and reflect all distribution functions, at the boundary sites, back along the links they arrived on. Averaging the velocity at the boundary, before and after a collision, gives the required boundary condition $\langle \boldsymbol{u} \rangle = 0$. Further consideration of this method [21] has shown that sites adjacent to the boundary sites 'see' a flow at the boundary with the same magnitude but opposite direction. It is pointed out by Cornubert *et al.* [21] that this form of boundary collision can better simulates a no-slip boundary at the centre of the links, half way between a boundary site and an adjacent non-boundary site. The bounce back boundary collisions were further modified by Ziegler [49] who considered the boundary to be coincident with the boundary sites. At these boundary sites, after the propagation, the distribution functions on the links interior to the boundary are set equal to the distribution functions on the 'opposite' exterior links. The 'opposite' link being the link in the opposite direction. Thus at a wall parallel to the direction $\boldsymbol{e}_2$, as in figure 3–6, the distribution function approaching the boundary on link $\boldsymbol{e}_4$ (interior to the wall) is set equal to the distribution function $\boldsymbol{e}_1$ (exterior to the wall). These modified boundary conditions are seen to simulate a no-slip boundary more accurately than the standard bounce back rules when applied to Poiseuille flow [49]. Bounce back boundary conditions only give first-order accuracy [21,50] and it can be shown [51] that the standard bounce back conditions produce a wall velocity which is a function of the relaxation parameter τ and is only zero for $\tau = 1$.

4.3.2 Higher-Order Boundary Conditions

A Finite Difference Method

A second-order boundary condition has been proposed by Skordos [52]. This involves a finite-difference scheme which requires the velocity gradient to be known or calculated at the boundary. If the velocity gradient is known at the boundary the boundary conditions produce good accuracy, however this method can only be applied if the velocity distribution is already known. When the velocity gradient is not know it can be calculated using first- or second-order asymmetric differences. Both methods produce good accuracy but neither are as accurate as the exact gradient method [52]. As expected the second-order scheme is more accurate than the first-order, however both of the difference methods are unstable at high values of the 'computational Mach number', $\Delta t/\Delta r$, the second-order method being less stable than the first-order. This method has the disadvantage that it rejects the simplicity of the lattice Boltzmann method at the boundaries and instead requires a finite-difference approach.

Dirichlet Boundary Conditions

The boundary conditions in any fluid simulation are expressed either in terms of the fluid velocity at the boundary or the velocity gradient at the boundary. These are called Dirichlet and Neumann boundary conditions. A method for imposing a Dirichlet boundary condition, for a fixed boundary, to a lattice Boltzmann fluid is devised by Noble *et al.* [51,50] for a hexagonal and a square grid. The boundary conditions developed by Noble *et al.* [51] are for a general velocity applied at a boundary parallel to $\boldsymbol{e}_2$. The same approach can be applied to any boundary but the details have still to be worked out [51]. Here we consider the simplified situation of a non-slip boundary parallel to $\boldsymbol{e}_2$. The velocity at the boundary is to be zero. Consider a site at the 'boundary' which has fluid above it and a solid wall below it. This is shown in figure 4–1 where the sites are labelled 'fluid sites' is they are in the body of the fluid, 'boundary sites' if they are at the boundary and 'wall sites' if they are in the body of the boundary. The distribution functions

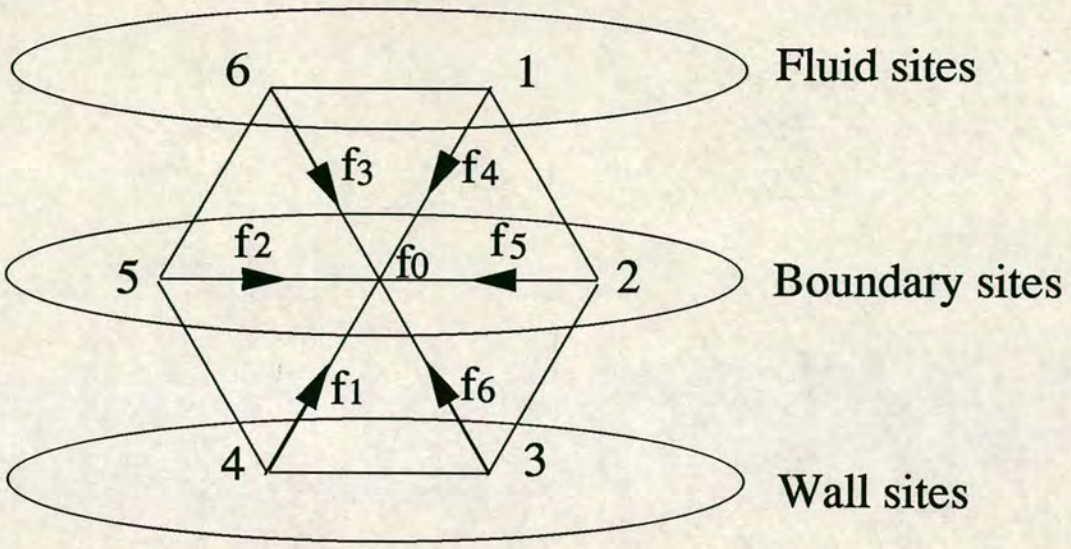

FIGURE 4–1: A site on a boundary with the fluid above and the solid wall below and its six nearest neighbours. The six distribution functions approaching the site during the propagation stage are shown as is f_0 the 'rest-particle' distribution function.

approaching the boundary site during the propagation stage are shown. These are the distribution functions of the neighbouring sites at the previous time-step $f_i = f_i(\boldsymbol{r} - \boldsymbol{e}_i, t-1)$. Fluid is allowed within the boundary sites but not the wall sites so the distribution functions f_0, f_2, f_3, f_4 and f_5 are non-zero. Functions f_1 and f_6 are zero and need to be specified so that the boundary condition can be applied at the site [51]. The boundary condition is $u_x = u_y = 0$:

$$\begin{aligned} f_1 + 2f_2 + f_3 - f_4 - 2f_5 - f_6 &= 0 \\ f_1 - f_2 - f_3 + f_6 &= 0. \end{aligned} \tag{4.64}$$

These can be solved for f_1 and f_6, which become f_4 and f_3 respectively at the next time step. These are required in calculating the new equilibrium distribution at the site.

Defining f_1 and f_6 in this way means that the density, the sum of all the distribution functions, is also a calculated quantity. This is different from the standard bounce back boundary conditions where the density is a conserved quantity. Here the density, and hence the pressure, at the boundary is calculated by the algorithm

to be correct for the desired boundary condition. This is an important feature of the model as it is a necessary feature of the boundary conditions [51,52].

Other schemes have also been considered [53,54,55]. These are concerned with modelling particle suspensions where the boundary is frequently moving. Here we are only concerned with a stationary boundary.

4.4 Binary-Fluid and Liquid-Gas Lattice Boltzmann Models

A number of different approaches have been considered for modelling two similar binary fluids or a liquid-gas combination using the lattice Boltzmann technique. These methods are described below along with their strengths and weaknesses.

4.4.1 Colour Model

The first model proposed for simulating immiscible, binary fluids [56] is based on the colour lattice gas model of Rothman and Keller [28]. As in the lattice gas model a colour gradient $\boldsymbol{f}(\boldsymbol{r})$ is defined

$$\boldsymbol{f}(\boldsymbol{r}) = \sum_i \sum_j \boldsymbol{e}_j \left[f_j^{(r)}(\boldsymbol{r} + \boldsymbol{e}_i) - f_j^{(b)}(\boldsymbol{r} + \boldsymbol{e}_i) \right] \tag{4.65}$$

where $f_i^{(r)}$ and $f_i^{(b)}$ are the distribution functions of the red and blue fluids respectively on link i. The distribution function of the whole fluid on link i, f_i, is the sum of the two colour distribution functions

$$f_i = f_i^{(r)} + f_i^{(b)}. \tag{4.66}$$

An angle θ_f is also defined

$$\theta_f = \tan^{-1}\left(\frac{f_y}{f_x}\right). \tag{4.67}$$

The fluid is then evolved in the following manner.

1. The fluid distribution function is found for each link at each site: $f_i = f_i^{(r)} + f_i^{(b)}$.

2. The total fluid distribution function f_i is collided, but not propagated, according to the lattice Boltzmann equation

$$f_i'(\boldsymbol{r}, t) - f_i(\boldsymbol{r}, t) = \Omega_i \tag{4.68}$$

to give the new fluid distribution function f'.

3. At all sites were $|\boldsymbol{f}| > \epsilon$, where ϵ is a small number, the distribution function is perturbed to an alternative value $f''(\boldsymbol{r}, t)$ such that

$$f''(\boldsymbol{r}, t) = f'(\boldsymbol{r}, t) + A\,|\boldsymbol{f}| \cos\left[2(\theta_i - \theta_f)\right] \tag{4.69}$$

where θ_i is the angle $\boldsymbol{e}_i$ makes with the x-axis and A is a constant which sets the strength of the surface tension. If $|\boldsymbol{f}| < \epsilon$ then $f'' = f'$.

4. The new distribution functions for the red and blue fluid, $f_i'^{(r)}$ and $f_i'^{(b)}$ are then found by solving the maximisation problem

$$W(f_i'^{(r)}, f_i'^{(b)}) = \max_{f_i''^{(r)}, f_i''^{(b)}} W(f_i''^{(r)}, f_i''^{(b)}) \tag{4.70}$$

where

$$W(f_i''^{(r)}, f_i''^{(b)}) = \left[\sum_i (f_i''^{(r)} - f_i''^{(b)})\boldsymbol{e}_i\right] \cdot \boldsymbol{f} \tag{4.71}$$

and $f_i''^{(r)}$ and $f_i''^{(b)}$ are all possible functions which satisfy the conservation of mass

$$f_i''^{(r)} + f_i''^{(b)} = f_i'' \tag{4.72}$$

and the conservation of colour

$$\sum_i f_i''^{(r)} = \sum_i f_i^{(r)}. \tag{4.73}$$

5. The red and blue distribution functions are then propagated along the lattice

$$f_i^{(r)}(\boldsymbol{r} + \boldsymbol{e}_i, t+1) = f_i'^{(r)}(\boldsymbol{r}, t) \tag{4.74}$$

and

$$f_i^{(b)}(\boldsymbol{r} + \boldsymbol{e}_i, t+1) = f_i'^{(b)}(\boldsymbol{r}, t). \tag{4.75}$$

The collision term Ω in equation (4.68) will depend on the lattice Boltzmann model being used. In reference [56] a collision term similar to the linearised collision operator [40,41] is employed. A single relaxation time lattice Boltzmann model has also be used [57,58]. The surface tension produced in this manner can be shown [56] to satisfy Laplace's equation.

4.4.2 Miscible Binary Fluid

Another model was proposed by Flekkøy [59]. This model simulates two miscible fluids moving on the same grid. There is no interaction between the two fluids and so there is no state in which the fluids are immiscible. A brief description of the model is given for completeness. In this model the total density $\rho = \rho_r + \rho_b$ and the difference in densities, $\Delta\rho = \rho_r - \rho_b$ are used. Two lattice Boltzmann equations are defined

$$\begin{aligned} f_i(\boldsymbol{r} + \boldsymbol{e}_i, t+1) - f_i(\boldsymbol{r}, t) &= -\frac{1}{\tau_\nu}\left[f_i(\boldsymbol{r}, t) - \overline{f}_i(\boldsymbol{r}, t)\right] \\ \Delta_i(\boldsymbol{r} + \boldsymbol{e}_i, t+1) - \Delta_i(\boldsymbol{r}, t) &= -\frac{1}{\tau_D}\left[\Delta_i(\boldsymbol{r}, t) - \overline{\Delta}_i(\boldsymbol{r}, t)\right], \end{aligned} \tag{4.76}$$

where τ_ν and τ_D are relaxation parameters which determine the viscosity ν and the diffusion coefficient D. For a hexagonal lattice the equilibrium distributions are defined

$$\overline{f}_i = \frac{\rho}{6}(1 + u_\alpha e_{i\alpha} + GQ_{i\alpha\beta}u_\alpha u_\beta) \tag{4.77}$$

and

$$\overline{\Delta}_i = \frac{\rho}{6}(i + u_\alpha e_{i\alpha}), \tag{4.78}$$

where the density ρ, the momentum ρu_α and the density difference $\Delta\rho$ are defined

$$\rho = \sum_i f_i, \quad \rho u_\alpha = \sum_i f_i e_{i\alpha}, \quad \Delta\rho = \sum_i \Delta_i. \tag{4.79}$$

The tensor $Q_{i\alpha\beta}$ is defined

$$Q_{i\alpha\beta} = e_{i\alpha}e_{i\beta} - c_s^2\delta_{\alpha\beta}, \tag{4.80}$$

where $c_s = 1/\sqrt{2}$ is the FHP speed of sound and $G = 4.5$ is a non-Galilean invariant factor. With these definitions the model can be shown [59] to satisfy the convection-diffusion equation

$$(\partial_t + u_\alpha e_{i\alpha})\Delta\rho = D(\partial_\alpha\partial_\alpha\Delta\rho - \frac{1}{c_s^2}u_\alpha u_\beta\partial_\alpha\partial_\beta\Delta\rho) \tag{4.81}$$

and the Navier-Stokes equation

$$\partial_t u_\alpha + u_\beta\partial_\beta u_\alpha = -\frac{1}{\rho}\partial_\alpha p + \nu\partial_\beta\partial_\beta u_\alpha, \tag{4.82}$$

where the diffusion coefficient, the viscosity and the pressure are given by

$$D_0 = -c_s^2\left(\tau_D + \frac{1}{2}\right), \tag{4.83}$$

$$\nu = -\frac{1}{4}\left(\tau_\nu + \frac{1}{2}\right) \tag{4.84}$$

and

$$p = \frac{1}{2}\rho(1 - u^2). \tag{4.85}$$

4.4.3 The Local Interaction Model

Shan *et al.* [60,61,62] consider a fluid with S different components on a regular lattice with b links in D-dimensional space. The direction of the b links are given by the vectors $\boldsymbol{e}_i$, $i = 1, ...b$ and each link has length unity. The distribution functions of the S components on link $\boldsymbol{e}_i$ at site $\boldsymbol{r}$ at time t is given by $f_i^a(\boldsymbol{r}, t)$, $i = 0, ..., b$, $a = 1, ..., S$ and is described by the Boltzmann equations

$$f_i^a(\boldsymbol{r} + \boldsymbol{e}_i, t+1) - f_i^a(\boldsymbol{r}, t) = \Omega_i^a(\boldsymbol{r}, t); \quad a = 1, .., S. \tag{4.86}$$

The collision term Ω_i^a has the form

$$\Omega_i^a(\boldsymbol{r}, t) = -\frac{1}{\tau_a}\left[f_i^a(\boldsymbol{r}, t) - \overline{f}_i^a(\boldsymbol{r}, t)\right] \tag{4.87}$$

where each component has a single relaxation time τ_a. Here $\overline{f}_i^a(\boldsymbol{r}, t)$ is the equilibrium distribution of the ath component on link $\boldsymbol{e}_i$ at site $\boldsymbol{r}$ at time t and is given

by $\overline{f}_i^a(\boldsymbol{r},t) = E_i(\rho_a, \boldsymbol{u}_a^*)$ where $\rho_a = \sum_i f_i^a$ and $\boldsymbol{u}_a^*$ is the 'equilibrium' velocity of the ath component which has still to be defined,

$$E_i(\rho,\boldsymbol{u}) = \begin{cases} \rho\left(\dfrac{1-d_0}{b} + \dfrac{D}{c^2 b}\boldsymbol{e}_i\cdot\boldsymbol{u} + \dfrac{D(D+2)}{2c^4 b}(\boldsymbol{e}_i\cdot\boldsymbol{u})^2 - \dfrac{Du^2}{2c^2 b}\right), & i = 1,..,b \\ \\ n\left(d_0 - \dfrac{u^2}{c^2}\right), & i = 0 \end{cases}, \tag{4.88}$$

and d_0 is a positive constant. If we set $\boldsymbol{u}_a^*$ to a common value $\boldsymbol{u}'$ for each component,

$$\boldsymbol{u}' = \sum_a \frac{\rho_a \boldsymbol{u}_a}{\tau_a} \Big/ \sum_a \frac{\rho_a}{\tau_a}, \tag{4.89}$$

then the equilibrium distribution in equation (4.88) is simply that of S ideal gases, see equation (4.45). To incorporate inter-component interactions Shan *et al.* [60] introduce a nonlocal interaction with potential

$$V(\boldsymbol{r},\boldsymbol{r}') = \sum_a \sum_{\overline{a}} G_{a\overline{a}}(\boldsymbol{r},\boldsymbol{r}')\psi_a(\boldsymbol{r})\psi_{\overline{a}}(\boldsymbol{r}'), \tag{4.90}$$

where $G_{\sigma\overline{a}}(\boldsymbol{r},\boldsymbol{r}')$ is a Green's function and ψ_a, the 'effective mass', is a function of the density of the ath component, ρ_a. G is restricted to act only on nearest neighbours and so can be simplified to

$$G_{a\overline{a}}(\boldsymbol{r},\boldsymbol{r}') = \begin{cases} 0, & |\boldsymbol{r}-\boldsymbol{r}'| > 1 \\ \mathcal{G}_{a\overline{a}}, & |\boldsymbol{r}-\boldsymbol{r}'| = 1. \end{cases} \tag{4.91}$$

The force acting on the ath component can be found, by summing over all the components and all the neighbouring sites, and is

$$\boldsymbol{F}_a = -\psi_a(\boldsymbol{r}) \sum_i \sum_{\overline{a}} \mathcal{G}_{a\overline{a}}(\boldsymbol{r},\boldsymbol{r}')\psi_{\overline{a}}(\boldsymbol{r}+\boldsymbol{e}_i)\boldsymbol{e}_i. \tag{4.92}$$

The rate of change of momentum of the ath component induced at each site by the additional interactions is given by

$$\frac{\mathrm{d}\boldsymbol{P}_a}{\mathrm{d}t}(\boldsymbol{r}) = \boldsymbol{F}_a(\boldsymbol{r}) \tag{4.93}$$

This momentum change can be combined with the momentum change of each component due to the collisions at each site. This gives the equilibrium velocity

$$\rho_a \boldsymbol{u}_a^* = \rho_a \boldsymbol{u}' + \tau_a \boldsymbol{F}_a. \tag{4.94}$$

Combining equations (4.86) and (4.87) and summing over all directions gives

$$\sum_i [f_i^a(\boldsymbol{r}+\boldsymbol{e_i},t+1)-f_i^a(\boldsymbol{r},t)] = \sum_i -\frac{1}{\tau_a}\left[f_i^a(\boldsymbol{r},t)-\overline{f}_i^a(\boldsymbol{r},t)\right]. \tag{4.95}$$

Substituting the expression for $\overline{f}_i^a = E_i(\rho_a, \boldsymbol{u}_a^*)$ given in equation (4.88) we see that

$$\sum_i [f_i^a(\boldsymbol{r}+\boldsymbol{e_i},t+1)-f_i^a(\boldsymbol{r},t)] = 0. \tag{4.96}$$

The change in momentum at each site is found by combining equations (4.86) and (4.87), multiplying by $\boldsymbol{e}_i$ and summing over all components and all directions,

$$\sum_a \sum_i [f_i^a(\boldsymbol{r}+\boldsymbol{e_i},t+1)-f_i^a(\boldsymbol{r},t)]\,\boldsymbol{e}_i = \Delta\boldsymbol{P}(\boldsymbol{r}) \tag{4.97}$$

where $\Delta\boldsymbol{P}$ is given by

$$\Delta\boldsymbol{P} = -\sum_a \frac{1}{\tau_a}\rho\boldsymbol{u}' + \sum_a \frac{1}{\tau_a}\rho\boldsymbol{u}_a^* = \sum_a \boldsymbol{F}_a \tag{4.98}$$

The conservation of mass, equation (4.96), and the momentum equation,

$$\sum_a \sum_i [f_i^a(\boldsymbol{r}+\boldsymbol{e_i},t+1)-f_i^a(\boldsymbol{r},t)]\,\boldsymbol{e}_i = \sum_a \boldsymbol{F}_a, \tag{4.99}$$

can be Taylor expanded and a Chapman-Enskog expansion performed. This gives the 'diffusion' equation [62]

$$\begin{aligned}\partial_t\rho_a + \partial_\alpha\rho_a u_\alpha = -\tau_a\partial_\alpha F_\alpha + \left(\tau_a-\frac{1}{2}\right)\partial_\alpha\left[\frac{(1-d_0)}{D}\partial_\alpha\rho_a - \frac{\rho_a}{\rho}\partial_\alpha p\right] \\ +\partial_\alpha\frac{\rho_a}{\rho}\left[\sum_a \tau_a F_{a\alpha} + \frac{\partial_\alpha p}{\rho}\sum_a \tau_a\rho_a + \frac{1}{2}\sum_a F_{a\alpha} - \frac{(1-d_0)}{D}\sum_a \tau_a\partial_\alpha\rho_a\right]\end{aligned} \tag{4.100}$$

and the Navier-Stokes equation [62,60,44]

$$\partial_t(\rho u_\alpha + \partial_\beta(\rho u_\alpha u_\beta) = -\partial_\alpha p + \partial_\beta[\nu\partial_\beta(\rho u_\alpha)] + \partial_\alpha[\zeta\partial_\beta(\rho u_\beta)] \tag{4.101}$$

where the kinematic shear viscosity is $\nu = (\sum_a \tau_a - 1/2)/(D+2)$, the bulk viscosity is $\zeta = d_0(\sum_a \tau_a - 1/2)/D$, the pressure is $p = [(1-d_0)\rho + \sum_{a\bar{a}} \mathcal{G}_{a\bar{a}}\psi_a\psi_{\bar{a}}b/2]/D$ and $\boldsymbol{u}$ is defined by

$$\rho\boldsymbol{u} = \sum_a \sum_i f_i^a \boldsymbol{e}_i + \frac{1}{2}\sum_a \boldsymbol{F}_a, \tag{4.102}$$

and is the average of the fluid velocity before and after the inter-particle force acts. Summing equation (4.100) over a gives the usual continuity equation for the whole fluid

$$\partial_t \rho + \partial_\alpha \rho u_\alpha = 0 \tag{4.103}$$

as expected. It can also be shown [62] that for a two component system with $\tau_1 = \tau_2$ the following diffusion equation is satisfied,

$$\frac{\mathrm{D}\xi}{\mathrm{D}t} = \frac{1 - d_0}{D}\left(\tau - \frac{1}{2}\right)\nabla^2 \xi, \tag{4.104}$$

where ξ is a function of the deviation of the density from its equilibrium value. A binary fluid can be simulated using this model when $S = 2$. If the effective mass $\psi(\rho)$ and the strength of the inter-component interaction $\mathcal{G}$ are suitably chosen the two components are observed to separate [60]. One component forms circular drops inside the other component and the density difference across the boundary of the drops is seen to obey Laplace's Law. When $S = 1$ a single component fluid is modelled. This fluid is seen to phase separate into a liquid and gaseous phase with surface tension between the two phases, again for a suitable choice of ψ and $\mathcal{G}$ [61]. Full details of the properties of the binary fluid model and the liquid-gas model are given in references [60,62] and [60,61] respectively.

4.4.4 The Free Energy Model

The models proposed by Orlandini *et al.* and Swift *et al.* [9,63,38] for simulating binary fluids and liquid-gas fluids are described here. The binary fluid model will be described in detail while the similar liquid-gas model will only be mentioned briefly since it is based on similar principles.

Binary Fluid Model

Rather than considering the densities of the two fluids, ρ_r and ρ_b, the total density, $\rho = \rho_r + \rho_b$, and the density difference or order parameter, $\Delta\rho = \rho_r - \rho_b$, are considered. Two distribution functions f_i and Δ_i are then used to describe the population of ρ and $\Delta\rho$ respectively on each of the i links. The evolution of

both distribution functions are governed by the single relaxation time Boltzmann equations:

$$f_i(\boldsymbol{r}+\boldsymbol{e}_i, t+\Delta t) - f_i(\boldsymbol{r}, t) = -\frac{1}{\tau_\rho}(f_i - \overline{f_i}) \tag{4.105}$$

and

$$\Delta_i(\boldsymbol{r}+\boldsymbol{e}_i, t+\Delta t) - \Delta_i(\boldsymbol{r}, t) = -\frac{1}{\tau_\Delta}(\Delta_i - \overline{\Delta_i}). \tag{4.106}$$

The equilibrium distributions $\overline{f_i}$ and $\overline{\Delta_i}$ take the general form

$$\overline{f_i} = \begin{cases} A + Be_{i\alpha}u_\alpha + Cu^2 + Du_\alpha u_\beta e_{i\alpha}e_{i\beta} + F_\alpha e_{i\alpha} + G_{\alpha\beta}e_{i\alpha}e_{i\beta}, & i = 1, 2, ..., 6 \\ A_0 + C_0 u^2, & i = 0 \end{cases} \tag{4.107}$$

and

$$\overline{\Delta_i} = \begin{cases} a + be_{i\alpha}u_\alpha + cu^2 + du_\alpha u_\beta e_{i\alpha}e_{i\beta} + f_\alpha e_{i\alpha} + g_{\alpha\beta}e_{i\alpha}e_{i\beta}, & i = 1, 2, ..., 6 \\ a_0 + c_0 u^2, & i = 0. \end{cases} \tag{4.108}$$

The coefficients $A, A_0, ..., G_{\alpha\beta}$ and $a, a_0, ..., g_{\alpha\beta}$ are chosen to satisfy the following equations. The equilibrium distribution must satisfy the conservation of mass and momentum equations:

$$\sum_i \overline{f_i} = \rho,$$

$$\sum_i \overline{f_i} e_{i\alpha} = \rho u_\alpha, \tag{4.109}$$

$$\sum_i \overline{\Delta_i} = \Delta\rho,$$

while the higher moments of $\overline{f_i}$ and $\overline{\Delta_i}$ are defined

$$\sum_i \overline{f_i} e_{i\alpha}e_{i\beta} = P_{\alpha\beta} + \rho u_\alpha u_\beta,$$

$$\sum_i \overline{\Delta_i} e_{i\alpha} = \Delta\rho u_i, \tag{4.110}$$

$$\sum_i \overline{\Delta_i} e_{i\alpha}e_{i\beta} = \Gamma\Delta\mu\delta_{\alpha\beta} + \Delta\rho u_\alpha u_\beta$$

so that the resulting continuum equations have the correct form for a binary fluid [9,64]. Here Γ is the mobility and $\Delta\mu$ is the chemical-potential difference between

the two components. The pressure tensor $P_{\alpha\beta}$ and the chemical potential $\Delta\mu$ determine the thermodynamical properties of the model and are determined by the free energy [9,38,14,65]. Orlandini *et al.* [9] choose the free energy describing the simplest possible binary fluid; two ideal gases with a repulsive interaction energy. This corresponds to a free energy [9,38]

$$\Psi = \int \mathrm{d}^2\boldsymbol{r} \left\{ \psi(\Delta\rho, \rho, T) + \frac{\kappa}{2}(\nabla\rho)^2 + \frac{\kappa}{2}(\nabla\Delta\rho)^2 \right\} \tag{4.111}$$

where T is the temperature,

$$\psi(\Delta\rho, \rho, T)$$

$$= \frac{\Lambda}{4}\left(1 + \frac{\Delta\rho^2}{\rho^2}\right) - T\rho + \frac{T}{2}(\rho + \Delta\rho)\log\left(\frac{\rho + \Delta\rho}{2}\right) + \frac{T}{2}(\rho - \Delta\rho)\log\left(\frac{\rho - \Delta\rho}{2}\right), \tag{4.112}$$

κ is the interfacial energy and Λ measures the strength of the interaction. For $T < \Lambda/2$ the mixture separates into two phases. With this definition of the free energy the chemical potential and the pressure tensor are given by [9,38,14,65]

$$\Delta\mu(\Delta\rho, \rho, T) = -\lambda\frac{\Delta\rho}{\rho} + T\log\left(\frac{1 + \Delta\rho/\rho}{1 - \Delta\rho/\rho}\right) - \kappa\nabla^2(\Delta\rho), \tag{4.113}$$

and

$$P_{\alpha\beta} = p_0\delta_{\alpha\beta} + \kappa\partial_\alpha\rho\partial_\beta\rho + \kappa\partial_\alpha\Delta\rho\partial_\beta\Delta\rho \tag{4.114}$$

were

$$p_0 = \rho T - \frac{\kappa}{2}(\rho\nabla^2\rho + \Delta\rho\nabla^2\Delta\rho) - \frac{\kappa}{2}(|\nabla\rho|^2 + |\nabla\Delta\rho|^2). \tag{4.115}$$

Liquid-Gas Model

A similar approach was also employed in the development of a liquid-gas model [63,38]. Only one component is present in the model and the free energy is chosen to be the free energy of a Van-der-Walls fluid [63,65].

$$\Psi = \int \mathrm{d}^2\boldsymbol{r} \left\{ \psi(T, \rho) + \frac{\kappa}{2}(\nabla\rho)^2 \right\}, \tag{4.116}$$

where

$$\psi(T, \rho) = \rho T \ln\left(\frac{\rho}{1 - b\rho}\right) - a\rho^2 \tag{4.117}$$

and a and b are constants determining the strength of the interaction. With this definition of the free energy and the same definitions for the moments of f_i, see equations (4.109) and (4.110), an equilibrium distribution function, with the same form as equation (4.107), can be found [63,38].

4.4.5 The Distribution Functions and the Equations of Motion for a Binary Fluid

Solving for the Distribution Functions

Substituting the distribution functions, equations (4.107) and (4.108) into the constraint equations (4.109) and (4.110) and using equations (4.37) – (4.41) we can find the coefficients.

The conservation of mass, $\sum_i \overline{f}_i = \rho$, gives

$$A_0 + C_0 u^2 + 6A + 6Cu^2 + 3Du^2 + 3G_{\alpha\beta}\delta_{\alpha\beta} = \rho. \tag{4.118}$$

Considering the coefficients of $u^0$and u^2 separately we see

$$A_0 + 6A + 3G_{\alpha\alpha} \tag{4.119}$$

and

$$C_0 + 6C + 3D = 0. \tag{4.120}$$

The conservation of momentum, $\sum_i \overline{f}_i e_{i\alpha} = \rho u_\alpha$, gives

$$3Bu_\alpha + 3F_\alpha = \rho u_\alpha. \tag{4.121}$$

Considering the coefficients of u^0 and u^1 we find

$$F_\alpha = 0 \tag{4.122}$$

and

$$B = \frac{\rho}{3}. \tag{4.123}$$

The constraint $\sum_i \overline{f}_i e_{i\alpha} e_{i\beta} = P_{\alpha\beta} + \rho u_\alpha u_\beta$ gives

$$3A\delta_{\alpha\beta} + 3Cu^2\delta_{\alpha\beta} + \frac{3}{4}Du^2\delta_{\alpha\beta} + \frac{3}{2}Du_\alpha u_\beta + \frac{3}{4}G_{\gamma\gamma}\delta_{\alpha\beta} + \frac{3}{2}G_{\alpha\beta} =$$

$$\left\{\rho T - \frac{\kappa}{2}(\rho\nabla^2\rho + \Delta\rho\nabla^2\Delta\rho) - \frac{\kappa}{2}\left[\left(\frac{\partial\rho}{\partial x}\right)^2 + \left(\frac{\partial\rho}{\partial y}\right)^2 + \left(\frac{\partial\Delta\rho}{\partial x}\right)^2 + \left(\frac{\partial\Delta\rho}{\partial y}\right)^2\right]\right\}\delta_{\alpha\beta}$$

$$+ \kappa\left[\frac{\partial\rho}{\partial x_\alpha}\frac{\partial\rho}{\partial x_\beta} + \frac{\partial\Delta\rho}{\partial x_\alpha}\frac{\partial\Delta\rho}{\partial x_\beta}\right] + \rho u_\alpha u_\beta. \tag{4.124}$$

Setting $\alpha = \beta = x$ and considering the coefficients of $u_x u_x$ and $u_y u_y$ gives

$$3C + \frac{3}{4}D + \frac{3}{2}D = \rho \tag{4.125}$$

and

$$3C + \frac{3}{4}D = 0 \tag{4.126}$$

respectively which can be solved to find

$$C = -\frac{\rho}{6} \tag{4.127}$$

and

$$D = \frac{2\rho}{3}. \tag{4.128}$$

Considering the coefficient of u^0 for the two cases $\alpha = \beta = x$ and $\alpha = \beta = y$ gives

$$3A + \frac{3}{4}G_{xx} + \frac{3}{4}Gyy + \frac{3}{2}G_{xx} = \rho T - \frac{\kappa}{2}(\rho\nabla^2\rho + \Delta\rho\nabla^2\Delta\rho)$$

$$-\frac{\kappa}{2}\left[\left(\frac{\partial\rho}{\partial x}\right)^2 + \left(\frac{\partial\rho}{\partial y}\right)^2 + \left(\frac{\partial\Delta\rho}{\partial x}\right)^2 + \left(\frac{\partial\Delta\rho}{\partial y}\right)^2\right] + \kappa\left[\left(\frac{\partial\rho}{\partial x}\right)^2 + \left(\frac{\partial\Delta\rho}{\partial x}\right)^2\right] \tag{4.129}$$

and

$$3A + \frac{3}{4}G_{xx} + \frac{3}{4}Gyy + \frac{3}{2}G_{yy} = \rho T - \frac{\kappa}{2}(\rho\nabla^2\rho + \Delta\rho\nabla^2\Delta\rho)$$

$$-\frac{\kappa}{2}\left[\left(\frac{\partial\rho}{\partial x}\right)^2 + \left(\frac{\partial\rho}{\partial y}\right)^2 + \left(\frac{\partial\Delta\rho}{\partial x}\right)^2 + \left(\frac{\partial\Delta\rho}{\partial y}\right)^2\right] + \kappa\left[\left(\frac{\partial\rho}{\partial y}\right)^2 + \left(\frac{\partial\Delta\rho}{\partial y}\right)^2\right] \tag{4.130}$$

which have solution

$$G_{xx} = -G_{yy} = \frac{\kappa}{3}\left[\left(\frac{\partial\rho}{\partial x}\right)^2 - \left(\frac{\partial\rho}{\partial y}\right)^2 + \left(\frac{\partial\Delta\rho}{\partial x}\right)^2 - \left(\frac{\partial\Delta\rho}{\partial y}\right)^2\right] \tag{4.131}$$

and

$$A = \frac{1}{3}\left[\rho T - \frac{\kappa}{2}(\rho\nabla^2\rho + \Delta\rho\nabla^2\Delta\rho)\right]. \tag{4.132}$$

The coefficient of u^0 with $\alpha = x, \beta = y$ gives directly

$$G_{xy} = \frac{2\kappa}{3}\left(\frac{\partial\rho}{\partial x}\frac{\partial\rho}{\partial y} + \frac{\partial\Delta\rho}{\partial x}\frac{\partial\Delta\rho}{\partial y}\right). \tag{4.133}$$

The values of A_0 and C_0 can now be found from equations (4.119) and (4.120) to be

$$A_0 = \rho - 2\left[\rho T - \frac{\kappa}{2}(\rho\nabla^2\rho + \Delta\rho\nabla^2\Delta\rho)\right] \tag{4.134}$$

and

$$C_0 = -\rho. \tag{4.135}$$

The constraints $\sum_i \overline{\Delta_i} = \Delta\rho$ and $\sum_i \overline{\Delta_i} e_{i\alpha} = \Delta u_i$ give

$$a_0 + 6a + 3g_{\alpha\beta}\delta_{\alpha\beta} = \Delta\rho, \tag{4.136}$$

$$c_0 + 6c + 3d = 0, \tag{4.137}$$

$$f_\alpha = 0 \tag{4.138}$$

and

$$b = \frac{\Delta\rho}{3} \tag{4.139}$$

in the same way as equations (4.119), (4.120), (4.122) and (4.123).

The constraint $\sum_i \overline{\Delta_i} e_{i\alpha} e_{i\beta} = \Gamma\Delta\mu\delta_{\alpha\beta} + \Delta\rho u_\alpha u_\beta$ gives

$$3a\delta_{\alpha\beta} + 3cu^2\delta_{\alpha\beta} + \frac{3}{4}du^2\delta_{\alpha\beta} + \frac{3}{2}du_\alpha u_\beta + \frac{3}{4}g_{\gamma\gamma}\delta_{\alpha\beta} + \frac{3}{2}g_{\alpha\beta} = \Gamma\Delta\mu\delta_{\alpha\beta} + \Delta\rho u_\alpha u_\beta. \tag{4.140}$$

The coefficient of u^0 with $\alpha = \beta = x$ and $\alpha = \beta = y$ gives

$$3a + \frac{3}{4}(g_{xx} + g_{yy}) + \frac{3}{2}g_{xx} = \Gamma\Delta\mu \tag{4.141}$$

and

$$3a + \frac{3}{4}(g_{xx} + g_{yy}) + \frac{3}{2}g_{yy} = \Gamma\Delta\mu. \tag{4.142}$$

These have solution

$$g_{xx} = g_{yy} = 0 \tag{4.143}$$

and

$$a = \frac{\Gamma\Delta\mu}{3}. \tag{4.144}$$

Setting $\alpha = x$ and $\beta = y$ gives

$$g_{xy} = 0. \tag{4.145}$$

The coefficient of $u_\alpha u_\beta$ gives

$$d = \frac{2}{3}\Delta\rho \tag{4.146}$$

when $\alpha = x$ and $\beta = y$. Setting $\alpha = x$ and $\beta = x$ and substituting the expression found for d in equation (4.146) gives

$$c = -\frac{1}{6}\Delta\rho. \tag{4.147}$$

Finally we find the value of a_0 and c_0 from equations (4.136) and (4.137):

$$a_0 = \Delta\rho - 2\Gamma\Delta\mu \tag{4.148}$$

and

$$c_0 = -\Delta\rho. \tag{4.149}$$

This gives all the coefficients in equations (4.107) and (4.108).

The Equations of Motion for a Binary Fluid

It now must be shown that any binary mixture with these equilibrium distributions satisfies the correct hydrodynamic equations. This is done here using the standard Chapman-Enskog method. A similar expansion approach is employed in reference [38] using a perturbation parameter Δt, the time between collisions. Equations (4.105) and (4.106) can be Taylor expanded:

$$\begin{aligned} & f_i(\boldsymbol{r} + \boldsymbol{e}_i, t+1) - f_i(\boldsymbol{r}, t) \\ & \simeq \left[\partial_t + e_{i\alpha}\partial_\alpha + \frac{1}{2}e_{i\alpha}\partial_\alpha(e_{i\beta}\partial_\beta + \partial_t) + \frac{1}{2}\partial_t(e_{i\alpha}\partial_\alpha + \partial_t)\right] f_i(\boldsymbol{r}, t). \end{aligned} \tag{4.150}$$

and

$$\begin{aligned}&\Delta_i(\boldsymbol{r}+\boldsymbol{e}_i,t+1)-\Delta_i(\boldsymbol{r},t)\\&\simeq\left[\partial_t+e_{i\alpha}\partial_\alpha+\frac{1}{2}e_{i\alpha}\partial_\alpha(e_{i\beta}\partial_\beta+\partial_t)+\frac{1}{2}\partial_t(e_{i\alpha}\partial_\alpha+\partial_t)\right]\Delta_i(\boldsymbol{r},t).\end{aligned}\tag{4.151}$$

Expanding the distribution functions and the time and space derivatives:

$$\begin{aligned}f_i&=f_i^{(0)}+\epsilon f_i^{(1)}+\epsilon^2 f_i^{(2)}+\ldots\\\Delta_i&=\Delta_i^{(0)}+\epsilon\Delta_i^{(1)}+\epsilon^2\Delta_i^{(2)}+\ldots\\\partial_t&=\epsilon\partial_{1t}+\epsilon^2\partial_{2t}+\ldots\\\partial_{\boldsymbol{r}}&=\epsilon\partial_{1\boldsymbol{r}}\end{aligned}\tag{4.152}$$

and using equations (4.150) and (4.151) we can perform a Chapman-Enskog expansion. Substituting equation (4.152) into equations (4.150) and (4.151) gives

$$\begin{aligned}&\left\{\left(\epsilon\partial_{1t}+\epsilon^2\partial_{2t}\right)+e_{i\alpha}\epsilon\partial_{1\alpha}+\frac{1}{2}e_{i\alpha}\epsilon\partial_{1\alpha}\left[e_{i\beta}\epsilon\partial_{1\beta}+\left(\epsilon\partial_{1t}+\epsilon^2\partial_{2t}\right)\right]\right.\\&\left.+\frac{1}{2}\left(\epsilon\partial_{1t}+\epsilon^2\partial_{2t}\right)\left[e_{i\alpha}\epsilon\partial_{1\alpha}+\left(\epsilon\partial_{1t}+\epsilon^2\partial_{2t}\right)\right]\right\}\\&\times\left(f_i^{(0)}+\epsilon f_i^{(1)}+\epsilon^2 f_i^{(2)}\right)=-\frac{1}{\tau_\rho}\left(f_i^{(0)}+\epsilon f_i^{(1)}+\epsilon^2 f_i^{(2)}-\overline{f}_i\right)\end{aligned}\tag{4.153}$$

and

$$\begin{aligned}&\left\{\left(\epsilon\partial_{1t}+\epsilon^2\partial_{2t}\right)+e_{i\alpha}\epsilon\partial_{1\alpha}+\frac{1}{2}e_{i\alpha}\epsilon\partial_{1\alpha}\left[e_{i\beta}\epsilon\partial_{1\beta}+\left(\epsilon\partial_{1t}+\epsilon^2\partial_{2t}\right)\right]\right.\\&\left.+\frac{1}{2}\left(\epsilon\partial_{1t}+\epsilon^2\partial_{2t}\right)\left[e_{i\alpha}\epsilon\partial_{1\alpha}+\left(\epsilon\partial_{1t}+\epsilon^2\partial_{2t}\right)\right]\right\}\\&\times\left(\Delta_i^{(0)}+\epsilon\Delta_i^{(1)}+\epsilon^2\Delta_i^{(2)}\right)=-\frac{1}{\tau_\Delta}\left(\Delta_i^{(0)}+\epsilon\Delta_i^{(1)}+\epsilon^2\Delta_i^{(2)}-\overline{\Delta}_i\right).\end{aligned}\tag{4.154}$$

It is still require that the total mass and momentum and the mass of each component are conserved at each site. This is achieved, to second-order, if the zeroth-order expansion of the distribution functions are equal to their equilibrium values and if

$$\sum_i f_i^{(a)}=0,\quad\sum_i f_i^{(a)}e_{i\alpha}=0,\quad\sum_i\Delta_i^{(a)}=0,\quad a=1,2.\tag{4.155}$$

To first-order in ϵ equation (4.153) is

$$\partial_{1t} f_i^{(0)} + e_{i\alpha}\partial_{1\alpha} f_i^{(0)} = -\frac{1}{\tau_\rho} f_i^{(1)}. \tag{4.156}$$

Summing equation (4.156) over i gives the first-order continuity equation for the total population:

$$\partial_{1t}\rho + \partial_{1\alpha}\rho u_\alpha = 0. \tag{4.157}$$

Multiplying equation (4.156) by $e_{i\beta}$ and summing over i gives the first-order continuity equation for the fluid momentum:

$$\partial_{1t}\rho u_\beta + \partial_{1\alpha} P_{\beta\alpha} + \partial_{1\alpha}\rho u_\alpha u_\beta = 0. \tag{4.158}$$

Similarly equation (4.154) to first-order in ϵ is

$$\partial_{1t}\Delta_i^{(0)} + e_{i\alpha}\partial_{1\alpha}\Delta_i^{(0)} = -\frac{1}{\tau_\Delta}\Delta_i^{(1)}. \tag{4.159}$$

Summing over i gives the first-order convection-diffusion equation

$$\partial_{1t}\Delta\rho + \partial_{1\alpha}\Delta\rho u_\alpha = 0. \tag{4.160}$$

To second-order in ϵ equation (4.153) is

$$\begin{aligned} &\partial_{1t} f_i^{(1)} + \partial_{2t} f_i^{(0)} + e_{i\alpha}\partial_{1\alpha} f_i^{(1)} \\ &+\frac{1}{2}\partial_{1t}(\partial_{1t} + e_{i\alpha}\partial_{1\alpha}) f_i^{(0)} + \frac{1}{2} e_{i\alpha}\partial_{1\alpha}(\partial_{1t} + e_{i\beta}\partial_{1\beta}) f_i^{(0)} = -\frac{1}{\tau_\rho} f_i^{(2)}. \end{aligned} \tag{4.161}$$

The first and third terms sum to zero by equation (4.155) and the fourth and fifth terms also sum to zero as in equations (4.157) and (4.158) respectively. Thus summing equation (4.161) we obtain the second-order continuity equation for the whole fluid:

$$\partial_{2t}\rho = 0. \tag{4.162}$$

Combining this with the first-order equation (4.157) and recombining the derivatives we get the continuity equation for the whole fluid

$$\partial_t\rho + \partial_\alpha\rho u_\alpha = 0. \tag{4.163}$$

Multiplying equation (4.161) by $e_{i\gamma}$ and summing over i gives

$$\partial_{2t}\rho u_\gamma + \sum_i e_{i\gamma}e_{i\alpha}\partial_{1\alpha}f_i^{(1)} + \frac{1}{2}\partial_{1t}\partial_{1\alpha}(P_{\gamma\alpha} + \rho u_\gamma u_\alpha) + \frac{1}{2}\sum_i e_{i\alpha}e_{i\beta}e_{i\gamma}\partial_{1\alpha}\partial_{1\beta}f_i^{(0)} = 0. \tag{4.164}$$

To find expressions for the two summations in equation (4.164) consider first

$$e_{i\alpha}e_{i\beta}e_{i\gamma}\partial_{i\beta}\partial_{i\gamma}f_i^{(0)} = \partial_{1\beta}\partial_{1\gamma}e_{i\alpha}e_{i\beta}e_{i\gamma}\left(A + Be_{i\delta}u_\delta + Cu^2 + Du_\delta u_\epsilon e_{i\delta}e_{i\epsilon} + G_{\delta\epsilon}e_{i\delta}e_{i\epsilon}\right). \tag{4.165}$$

With $B = \rho/3$ and the sum of all terms containing an odd number of $\boldsymbol{e}_i$s being zero this gives

$$\sum_i e_{i\alpha}e_{i\beta}e_{i\gamma}\partial_{i\beta}\partial_{i\gamma}f_i^{(0)} = \frac{1}{4}\partial_{1\beta}\partial_{1\beta}\rho u_\alpha + \frac{1}{2}\partial_{1\alpha}\partial_{1\beta}\rho u_\beta. \tag{4.166}$$

Next consider equation (4.156) multiplied by $e_{i\gamma}e_{i\beta}\partial_{1\beta}$ and summed over i:

$$\sum_i \partial_{i\beta}f_i^{(1)}e_{i\gamma}e_{i\beta} = -\tau_\rho\left[\partial_{1t}\partial_{1\beta}(P_{\gamma\beta} + \rho u_\gamma u_\beta) + \frac{1}{4}\partial_{1\beta}\partial_{1\beta}\rho u_\gamma + \frac{1}{2}\partial_{1\gamma}\partial_{1\beta}\rho u_\beta\right]. \tag{4.167}$$

Substituting equations (4.166) and (4.167) into equation (4.164) gives

$$\partial_{2t}\rho u_\alpha = \left(\tau_\rho - \frac{1}{2}\right)\left\{\frac{1}{4}\partial_{1\beta}\partial_{1\beta}u_\alpha + \frac{1}{2}\partial_{1\alpha}\partial_{1\beta}u_\beta + [\partial_{1t}\partial_{1\beta}(P_{\alpha\beta} + \rho u_\alpha u_\beta)]\right\}. \tag{4.168}$$

We are dealing here with terms $O(\epsilon^2)$ so, since $\boldsymbol{u}$ is also small, we can neglect terms $O(u^2)$. From the definition of $P_{\alpha\beta}$, equations (4.114) and (4.115), we also see that, neglecting higher-order derivatives, we can write $P_{\alpha\beta} = p_0$ [38]. We can now re-write the term in square brackets in equation (4.168)

$$\partial_{1t}\partial_{1\beta}(P_{\alpha\beta} + \rho u_\alpha u_\beta) \simeq \partial_{1t}\partial_{1\beta}p_0 = \partial_{1\beta}\frac{\partial p_0}{\partial\rho}\partial_{1t}\rho. \tag{4.169}$$

Using the expression for $\partial_{1t}\rho$ from equation (4.157) we can combine equations (4.158) and (4.168) to obtain the Navier-Stokes equation

$$\partial_t\rho u_\alpha + \partial_\beta\rho u_\alpha u_\beta = -\partial_\alpha p_0 + \nu\partial_\beta\partial_\beta\rho u_\alpha + \partial_\alpha\zeta\partial_\beta\rho u_\beta \tag{4.170}$$

where

$$\nu = \frac{2\tau_\rho - 1}{8}, \quad \zeta = \left(\tau_\rho - \frac{1}{2}\right)\left(\frac{1}{2} - \frac{\partial p_0}{\partial n}\right). \tag{4.171}$$

To second-order in ϵ equation (4.154) is

$$\partial_{1t}\Delta_i^{(1)} + \partial_{2t}\Delta_i^{(0)} + e_{i\alpha}\partial_{1\alpha}\Delta_i^{(1)} + \frac{1}{2}\partial_{1t}(\partial_{1t} + e_{i\alpha}\partial_{1\alpha})\Delta_i^{(0)}\frac{1}{2}e_{i\alpha}\partial_{1\alpha}(\partial_{1t} + e_{i\alpha}\partial_{1\alpha})\Delta_i^{(0)}$$

$$= -\frac{1}{\tau_\Delta}\Delta_i^{(2)}. \tag{4.172}$$

Summing over i and noting that the first and fourth terms are zero we can write

$$\partial_{2t}\Delta\rho + \sum_i e_{i\alpha}\partial_{1\alpha}\Delta_i^{(1)} + \frac{1}{2}\partial_{1\alpha}\partial_{1t}\Delta\rho u_\alpha + \frac{1}{2}\partial_{1\alpha}\partial_{1\alpha}\Gamma\Delta\mu + \frac{1}{2}\partial_{1\alpha}\partial_{1\beta}\Delta\rho u_{1\alpha}u_{1\beta} = 0. \tag{4.173}$$

Multiplying equation (4.159) by $e_{i\alpha}\partial_{1\alpha}$ and summing over i we find the term $\sum_i e_{i\alpha}\partial_{1\alpha}\Delta_i^{(1)}$:

$$\sum_i e_{i\alpha}\partial_{1\alpha}\Delta_i^{(1)} = -\tau_\Delta(\partial_{1t}\partial_{1\alpha}\Delta\rho u_\alpha + \partial_{1\alpha}\partial_{1\beta}\Gamma\Delta\mu\delta_{\alpha\beta} + \partial_{1\alpha}\partial_{1\beta}\Delta\rho u_\alpha u_\beta). \tag{4.174}$$

Substituting this into equation (4.173) we get

$$\partial_{2t}\Delta\rho = \left(\tau_\Delta - \frac{1}{2}\right)(\partial_{1\alpha}\partial_{1\alpha}\Gamma\Delta\mu + \partial_{1t}\partial_{1\alpha}\Delta\rho u_\alpha) \tag{4.175}$$

where as before we have neglected terms smaller than $O(\epsilon^2 u)$. Finally we can express $\partial_{1t}\Delta\rho u_\alpha$ as $\partial_{1t}[(\Delta\rho/\rho) \times (\rho u_\alpha)]$ [38] and perform the differentiation on both the terms in brackets:

$$\partial_{1\alpha}\partial_{1t}\Delta\rho u_\alpha = \partial_{1\alpha}\left[\rho u_\alpha \partial_{1t}\left(\frac{\Delta\rho}{\rho}\right)\right] + \partial_{1\alpha}\left[\frac{\Delta\rho}{\rho}\partial_{1t}(\rho u_\alpha)\right]. \tag{4.176}$$

Replacing the time derivatives with spatial derivatives using equations (4.157), (4.158) and (4.160) and, as before, neglecting terms $O(u^2)$ gives

$$\partial_{1\alpha}\partial_{1t}\Delta\rho u_\alpha = P_{\alpha\beta} \tag{4.177}$$

for the final term in equation (4.175). Combining equation (4.175) with equation (4.160) and neglecting terms of order $O(\epsilon^2 u^2)$ we obtain the convection-diffusion equation

$$\partial_t\Delta\rho + \partial_\alpha\Delta\rho u_\alpha = \Gamma\theta\partial_\beta\partial_\beta\Delta\mu - \theta\partial_\alpha\left(\frac{\Delta\rho}{\rho}\partial_\beta P_{\alpha\beta}\right) \tag{4.178}$$

where

$$\theta = \left(\tau_\Delta - \frac{1}{2}\right). \tag{4.179}$$

The Navier-Stokes equation for the liquid-gas model follows [63,38] in the same manner as the Navier-Stokes equation for the binary fluid. The kinematic and bulk viscosities have the same τ dependence as equation (4.171).

4.4.6 Model Selection

The miscible binary fluid proposed by Flekkøy [59] is not suited to our aim of applying the lattice Boltzmann model to interfacial waves since we require two immiscible fluids. It also has a non-Galilean invariant factor associated with it. The colour model [56] and the local interaction model [60] both simulate immiscible fluids. In the colour model the fluid separation is driven by the local 'colour' differences between the fluids. The method used involves maximising the scalar product of the colour gradient and the colour flux. This does indeed produce an interface between the two fluids and Laplace's law is seen to be obeyed. This colour based scheme does not directly mimic the physics of phase separation since there is no consideration of the thermodynamics of the process. This means that although the fluids separate there is no guarantee that they separate an a manner akin to a real fluid. The approach of Shan *et al.* [60] is based on the assumption that phase separation is produced by microscopic interactions on the scale of the lattice sites. This interaction introduces a momentum change into the Boltzmann equation. This model has also been shown to facilitate phase separation, however, like the colour model there is no certainty that the microscopic interactions are in fact mimicking real phase separation. The free energy model [9,63,38] does consider the thermodynamics of the problem. The approach to equilibrium is governed by the free energy which enters the model through the equilibrium distribution function. The model therefore simulates the phase separation of a real fluid mixture. Unfortunately the liquid-gas model is not Galilean invariant so its application is limited. The binary fluid model, on the other hand, does not suffer from a lack of Galilean invariance and is isotropic [38]. This makes it a suitable choice for the interfacial wave simulations considered in chapters 7 and 8.

4.5 Implementation of the Free Energy Binary Model

The binary fluid model of Orlandini *et al.* [9] was implemented on the Connection Machine CM-200 at Edinburgh University. To illustrate some of the important features of the model and to test the implementation a number of simulations, previously presented in references [9,38], were performed. The parameters Λ and Γ where set to $\Lambda = 1.1$ and $\Gamma = 0.1$ throughout. These are the values which were used in references [9,38].

Fluid Separation

For temperatures $T < \Lambda/2$ the fluid was seen to separate into two immiscible fluids as described in [9,38]. This is illustrated in figure 4–2 which shows the value of the order parameter $\Delta\rho$ for $\kappa = 0.1$ and $T = 0.4$ on a 128 by 128 site grid. The shading is proportional to $\Delta\rho$ with black represents $\Delta\rho < -0.4$ and light grey represents $\Delta\rho > 0.4$. Initially the fluid is completely mixed with $\rho = 1$ everywhere and $\Delta\rho$ set randomly to a value in the range $(-1/70 < \Delta\rho < 1/70)$. After 1,000 time-steps the fluid has begun to separate into small regions of each fluid although the value of $|\Delta\rho|$ is smaller than its final value in each fluid. After 2,000 time-steps the fluid has separated into many small areas of one fluid within the other. At this stage $|\Delta\rho|$ has almost reached its final value although there is some variation within each fluid. By 4,000 time steps $|\Delta\rho|$ is constant in each fluid. For times greater than 2,000 time-steps the small areas of fluid move around slowly and collide with each other to produce larger areas. The size of the interface is about ten lattice steps but can be altered by changing the interfacial energy κ [9].

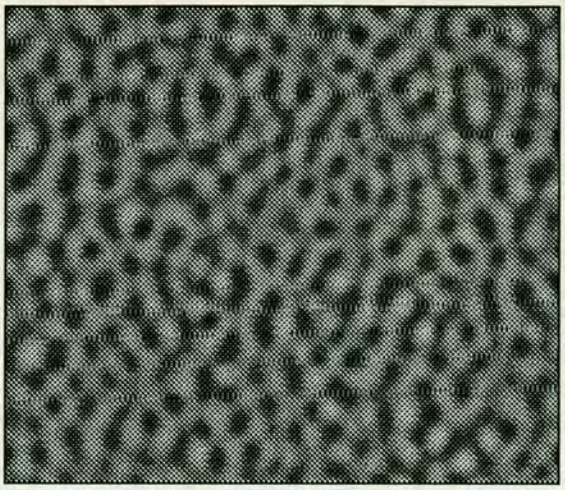

Figure 4–2–a: t=1,000

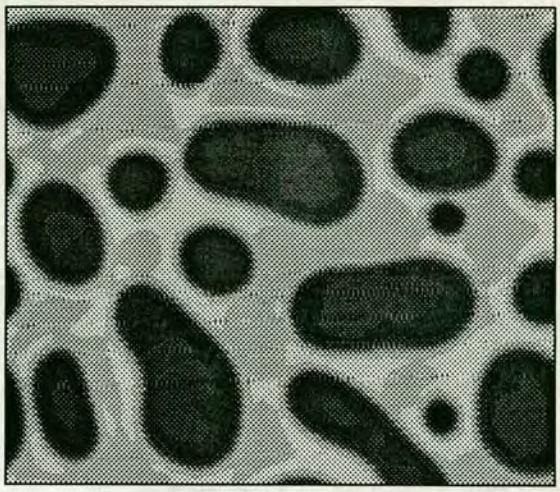

Figure 4–2–b: t=2,000

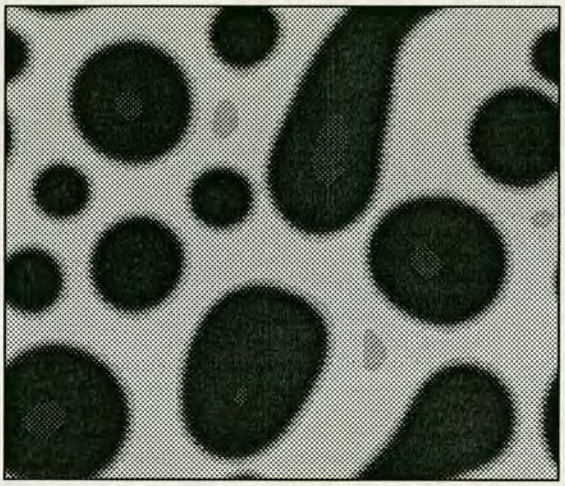

Figure 4–2–c: t=3,000

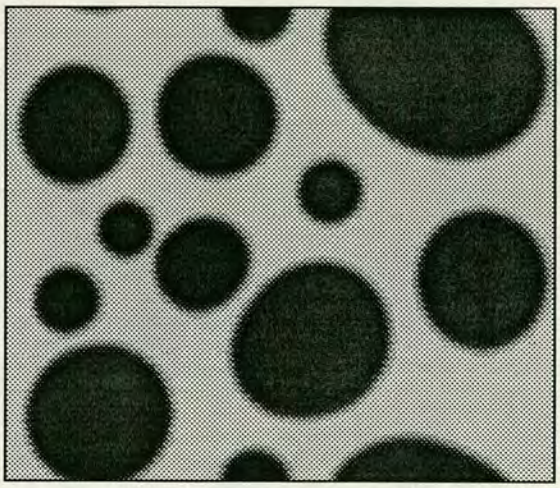

Figure 4–2–d: t=4,000

Figure 4–2–e: t=5,000

Figure 4–2–f: t=6,000

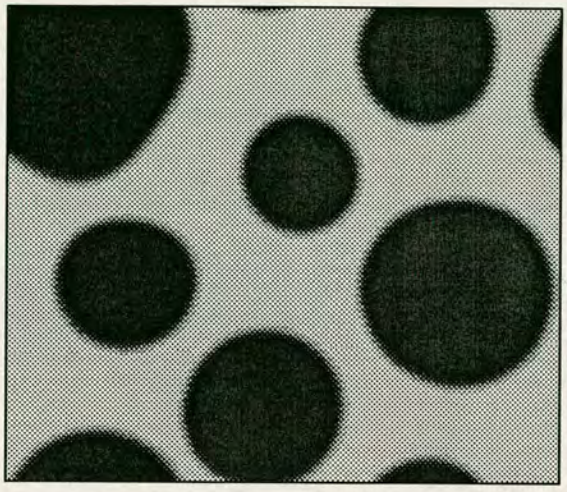

Figure 4–2–g: t=7,000

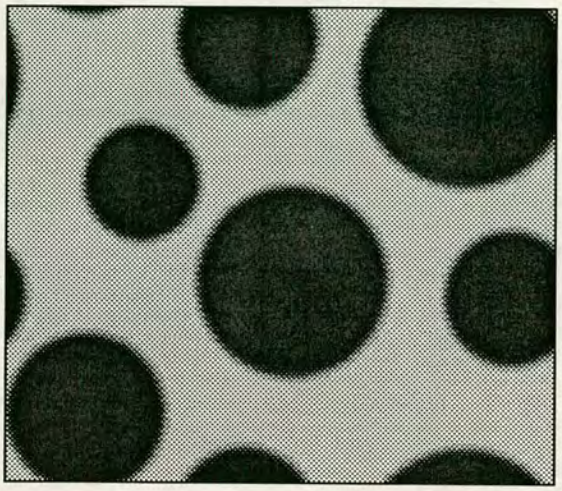

Figure 4–2–h: t=13,000

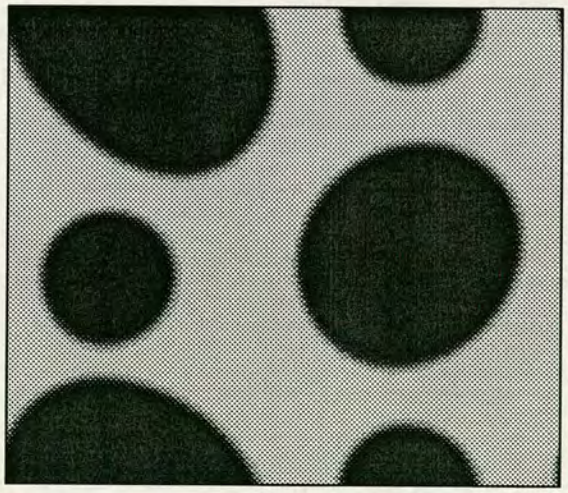

Figure 4–2–i: t=25,000

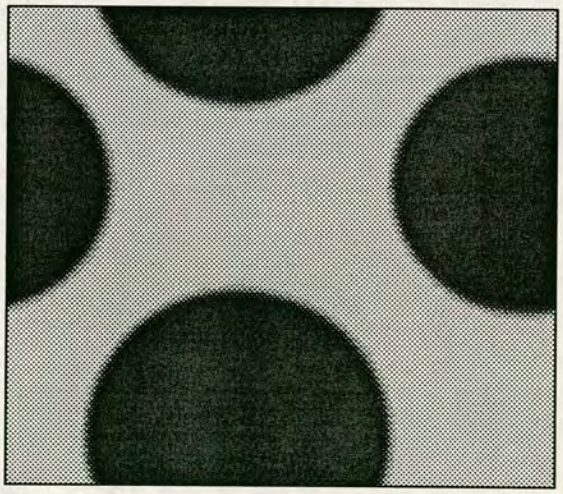

Figure 4–2–j: t=44,000

FIGURE 4–2: The separation of the two immiscible fluids for a temperature $T = 0.4$. The value of $\Delta\rho$ is shown where black represents $\Delta\rho < -0.4$, light grey represents $\Delta\rho > 0.4$ and intermediate shades of grey represent areas where $|\Delta\rho| \leq 0.4$ and there is a mixture of the two fluids.

Bubble Equilibrium

A 'circular' bubble, of radius 32 grid points, was initialised at the centre of a 128 by 128 grid. The fluid density was set at $\rho = 1$ everywhere with $\Delta\rho = -0.42$ inside the bubble and $\Delta\rho = 0.42$ elsewhere. The fluids were then allowed to evolve for 10,000 time-steps. The density and the order parameter were measured along a line through the centre of the inner fluid parallel to the y-axis (perpendicular to $\boldsymbol{e}_2$) and are shown in figures 4–3 and 4–4 respectively at selected times. The relaxation times used were $\tau_\rho = 1.0$ and $\tau_\Delta = \tau_*$. The relaxation time τ_* is $\tau_\Delta = 0.789$ which is the value at which the model is Galilean invariant [9,38]. This initialisation differs from the final state in four ways. The order parameter has changed from its initial value of $\Delta\rho = \pm 0.42$ to its expected value of 0.50. The initially interface width of one lattice unit has increased to about ten lattice units. The shape of the inner fluid has changed from an ellipse with semi-major and semi-minor axis of 32 lu and $32 \times \sqrt{3}/2$ lu to a circle with radius $\simeq 30$ lu. The final density is slightly larger in the inner fluid than the outer fluid. The small change in the density occurs everywhere within the first 1,000 time-steps with only a small change in the shape of the interface occurring at subsequent times. The larger change in the order parameter takes 10,000 time-steps to reach the areas furthest from the interface. The movement of the inner fluid from an ellipse to a circle is achieved within the 10,000 time steps.

The Density and Order Parameter at the Interface

A bubble with radius 20 lu was initialised at the centre of a 64 by 64 site grid and allowed to reach equilibrium. The fluid density and the order parameter are plotted in figures 4–5 and 4–6 respectively for $\kappa = 0.1$, 0.01 and 0.001. Figure 4–5 shows a small decrease, of less than 1%, in the fluid density across the interface. The width of this decrease is about 10 lu when $\kappa = 0.1$, 5 lu when $\kappa = 0.01$ and 3 lu when $\kappa = 0.001$. There is also a small difference between the fluid density inside and outside the bubble. The difference is about 0.2% when $\kappa = 0.1$ and much smaller for the smaller values of κ. The change in $\Delta\rho$, the order parameter, across the

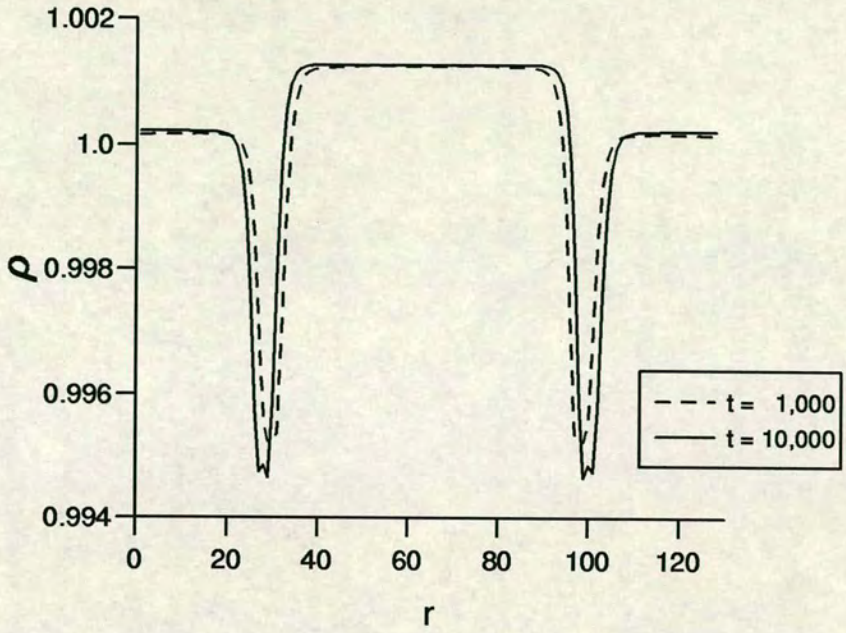

FIGURE 4–3: The density ρ as a function of r the distance from the edge of the grid. The density is plotted along a line through the centre of the inner fluid parallel to the y-axis (perpendicular to $\boldsymbol{e}_2$).

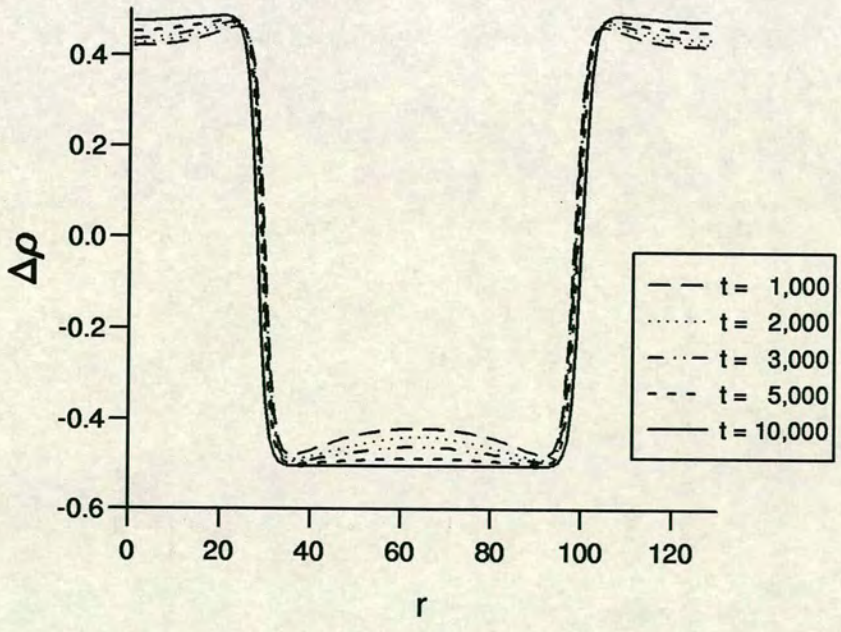

FIGURE 4–4: The order parameter $\Delta\rho$ plotted against r the distance from the edge of the grid. The order parameter is plotted along a line through the centre of the inner fluid parallel to the y-axis (perpendicular to $\boldsymbol{e}_2$).

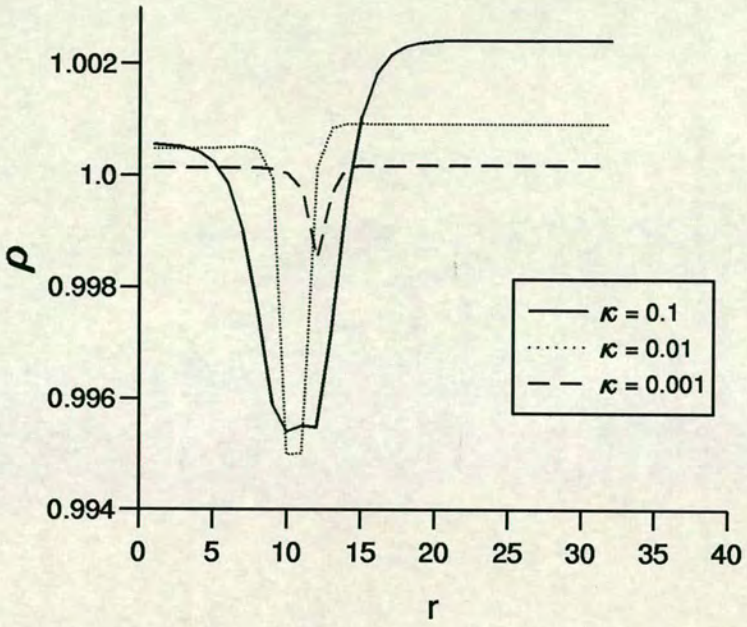

FIGURE 4–5: The density, along a line through the centre of a bubble, as a function of r The centre of the bubble is at $r = 32$. The density profile across the interface can be seen for three values of the interfacial energy κ.

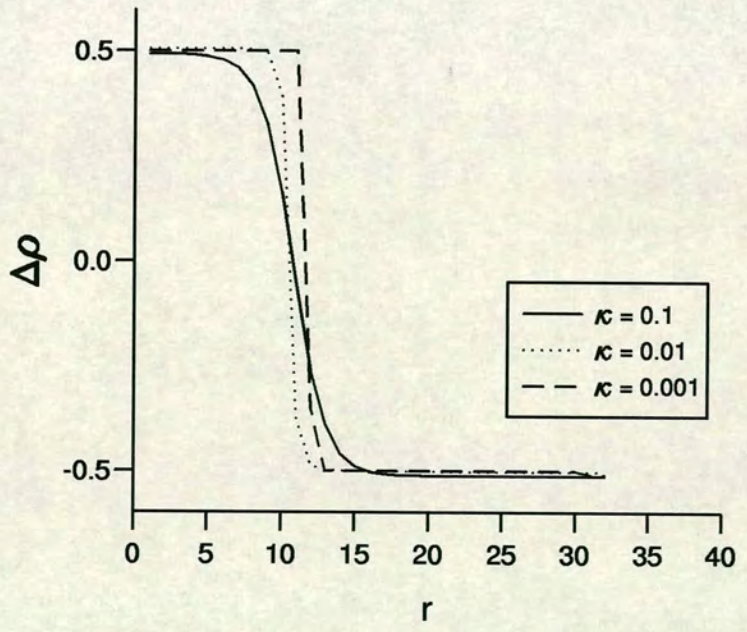

FIGURE 4–6: The order parameter, along a line through the centre of a bubble, as a function of r. The centre of the bubble is at $r = 32$. The change in the order parameter across the interface can be seen for three values of the interfacial energy κ.

interface shows a gradual smooth change when $\kappa = 0.1$ with an interface width of about 10 lu. The lower values of κ show a much sharper change occurring over a few lattice units. The results displayed in figures 4–5 and 4–6 are consistent with the similar results in [9,38].

Isotropy

To investigate the isotropy of the model a bubble of fluid with $\Delta\rho = -0.5$ was initialised inside a fluid with $\Delta\rho = 0.5$. The fluid density was $\rho = 1.0$. This was done on a 64 by 64 grid and the radius of the circle was 13 lu. The lattice was then allowed to evolved for 10,000 time-steps and the centre of mass $\boldsymbol{r}_{\mathrm{CM}}$ of the bubble found. Figure 4–7 shows the value of $\Delta\rho$ of each point on the grid plotted

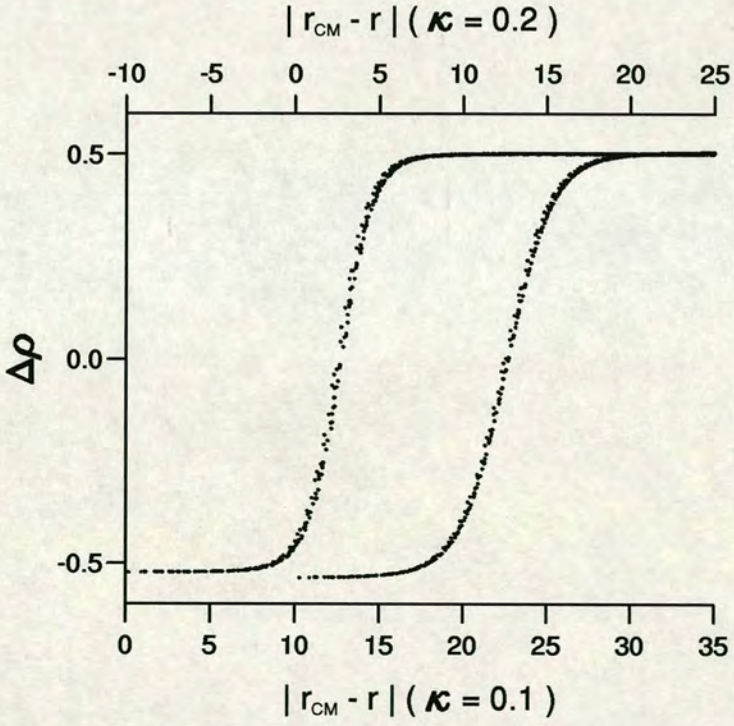

FIGURE 4–7: The value of $\Delta\rho$ at all points on the grid as a function of the points distance from the centre of mass of the bubble $|\boldsymbol{r}_{\mathrm{CM}} - \boldsymbol{r}|$. Results are shown for $\kappa = 0.1$ and 0.2, the results for $\kappa = 0.2$ are displaced by ten lu with respect to the results for $\kappa = 0.1$

against the distance of the point from the centre of mass. The results lie on, or very close to, a single curve for each value of κ showing that the model is, at

worst, very close in isotropic. These results agree with similar results obtained elsewhere for the model [38]. It can also be seen from figure 4–7 that the interface is larger for $\kappa = 0.2$ than it is for $\kappa = 0.1$. Figure 4–8 also shows the approximate

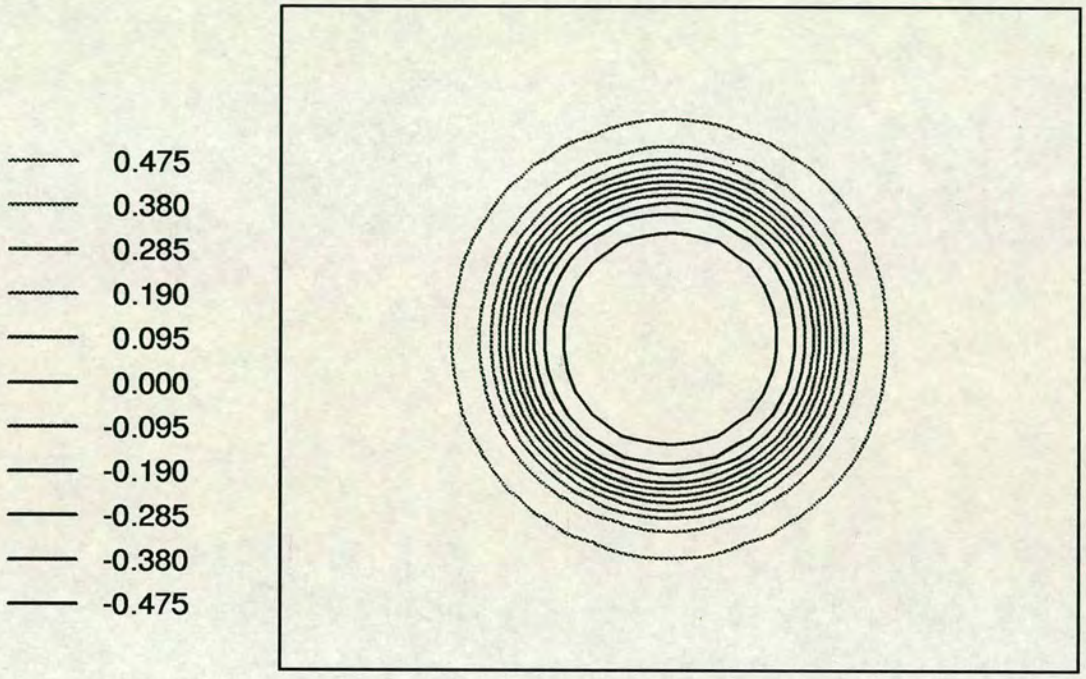

FIGURE 4–8: Contour plot of $\Delta\rho$ when $\kappa = 0.1$

isotropy of the model when $\kappa = 0.1$. A contour plot of $\Delta\rho$ shows contours which are very close to circular. There is no evidence of a departure from isotropy or of the underlying hexagonal grid.

Galilean Invariance

This model can be shown to be Galilean invariant [38]. This will be shown in section 5.3 for the binary fluid model with a gravitational interaction present.

4.6 Summary

The lattice Boltzmann model has been reviewed: from its initial use to overcome some of the difficulties with the lattice gas model, to the latest state of the art multi-fluid models. It has been seen that the lattice Boltzmann model has overcome the problems associated with the lattice gas model. The immiscible binary fluid model of Orlandini *et al.* [9] has been described in detail and some features of the model have been demonstrated by simulation.

Chapter 5

Gravity in a Lattice Boltzmann Model

In this chapter different methods are considered for introducing a body force, in this case gravity, into a lattice Boltzmann model. A new method is proposed which introduces the body force directly into the lattice Boltzmann equation. This is compared with the method of Martys *et al.* [66]. It is shown that when the new body force rules are incorporated into an isotropic model the body force acts independently of the grid orientation. It is also shown that when the body force is introduced into the Galilean invariant, binary model of Orlandini *et al.* [9] the resulting model is also Galilean invariant.

5.1 Introducing Gravity

In many fluid simulations gravity plays an important role. Here we consider five methods for introducing a body force into the lattice Boltzmann model.

5.1.1 The Classic Boltzmann Equation

The Boltzmann equation for a fluid with a body force $\boldsymbol{F}$ is

$$\partial_t f + c_\alpha \partial_{r\alpha} f + F_\alpha \partial_{c\alpha} f = \Omega(f) \tag{5.1}$$

where $f(\boldsymbol{c}, \boldsymbol{r}, t)\mathrm{d}\boldsymbol{c}\mathrm{d}\boldsymbol{r}$ is the number of molecules at time t with velocities in the range $\boldsymbol{c} \to \boldsymbol{c} + \mathrm{d}\boldsymbol{c}$ and position in the range $\boldsymbol{r} \to \boldsymbol{r} + \mathrm{d}\boldsymbol{r}$. The difference between

the Boltzmann equation when there is no body force present and when there is a body force is an extra term: $F_\alpha \partial_{c\alpha} f$. In the lattice Boltzmann equation we are looking to add a similar term to incorporate a body force. Since, however, the velocity of all the 'particles' is constant in the lattice Boltzmann model we can not simply introduce a term with exactly the same form but must instead introduce a term which will modify the fluid momentum.

5.1.2 Combining the Gravity Term and the Pressure Tensor

The Navier-Stokes equation

$$\frac{D\boldsymbol{u}}{Dt} = -\frac{1}{\rho}\nabla p + \nu\nabla^2\boldsymbol{u} + \zeta\nabla(\nabla\cdot\boldsymbol{u}) + \frac{\boldsymbol{F}}{\rho} \tag{5.2}$$

can be written

$$\frac{D\boldsymbol{u}}{Dt} = -\frac{1}{\rho_0}\nabla P + \nu\nabla^2\boldsymbol{u} + \zeta\nabla(\nabla\cdot\boldsymbol{u}) + \frac{\delta\rho}{\rho_0}\boldsymbol{g} \tag{5.3}$$

where $P = p + \rho_0\Phi$, $\boldsymbol{F} = \rho\boldsymbol{g}$, $\boldsymbol{g} = -\nabla\Phi$ and $\rho = \rho_0 + \delta\rho$. If $\delta\rho = 0$ then equation (5.3) is the same as equation (5.2) without a body force but with a modified pressure. Following this approach we can re-define the equilibrium distribution:

$$E_i(\rho,\boldsymbol{u}) = \begin{cases} \rho\left(\dfrac{1-d_0}{b} + \dfrac{\Phi D}{bc^2} + \dfrac{D}{c^2 b}\boldsymbol{e}_i\cdot\boldsymbol{u} + \dfrac{D(D+2)}{2c^4 b}(\boldsymbol{e}_i\cdot\boldsymbol{u})^2 - \dfrac{Du^2}{2c^2 b}\right), & i = 1,b \\ \rho\left(d_0 - \dfrac{\Phi D}{c^2} - \dfrac{u^2}{c^2}\right), & i = 0. \end{cases} \tag{5.4}$$

Using this expression for the equilibrium distribution and performing the Chapman-Enskog expansion, as in section 4.2.3, equations (4.46), (4.47) and (4.49) remain unchanged and equation (4.48) becomes

$$\sum_i \overline{f}_i e_{i\alpha} e_{i\beta} = \frac{\rho(1-d_0)c^2}{D}\delta_{\alpha\beta} + \rho u_\alpha u_\beta + \rho\Phi\delta_{\alpha\beta}. \tag{5.5}$$

Equations (4.54) and (4.58), the first- and second-order density equations, will therefore remain unchanged. Equation (4.56), the first-order momentum equation, has the same form except the pressure term on the right hand side, $\rho(1 -$

$d_0)c^2\delta_{\alpha\beta}/D$, has an additional term, $+\rho\Phi\delta_{\alpha\beta}$, which can remain where it is to give a modified pressure or be separated from the pressure term to give a separate force term, $-\nabla\Phi\rho$. Equation (4.61), the second-order momentum equation, has the same form as before except now $\zeta = (\tau - 1/2)[2c^2/(D+2) - c^2(1-d_0)/D - \rho\Phi\delta_{\alpha\beta}]$ giving an altered bulk viscosity. This method has the disadvantage that it requires the density to be constant, that is $\delta\rho = 0$. Thus it could only be applied if Φ is small enough that there is only a negligible change in ρ with depth.

5.1.3 Adding a Force Term to Equation (4.47)

In reference [63] Swift *et al.* suggested that a force, which changes the momentum, can be introduced by changing equation (4.47) to

$$\sum_i \overline{f}_i e_{i\alpha} = \rho u_\alpha - F_\alpha. \tag{5.6}$$

If this approach is taken, then the extra term must be included in the equations of motion. For example, the first-order density equation, equation (4.54), will become

$$\partial_{1t}\rho + \partial_{1\alpha}(\rho u_\alpha + F_\alpha) = 0. \tag{5.7}$$

Thus again this method can only be used if the term F_α is negligible small. The form of the terms $\sum_i f^{(a)} e_{i\alpha} \quad a = 0, 1, 2$ would also need to be considered.

5.1.4 Calculating the Equilibrium Distribution with an Altered Velocity

Gravity can be introduced into the model following a method similar to the local interaction method of section 4.4.3 but considering the momentum change to be caused by a body force rather than an inter-particle force [66]. If a gravitational force $\boldsymbol{F}$ is acting then at every time-step there is a change of momentum $\Delta\boldsymbol{P} = \boldsymbol{F}$. To incorporate this into the model we let the equilibrium distribution be given by

$$\overline{f}_i(\boldsymbol{r}, t) = E(\rho, \boldsymbol{u}^*) \tag{5.8}$$

where

$$\rho \boldsymbol{u}^* = \rho \boldsymbol{u} + \tau \boldsymbol{F}. \tag{5.9}$$

Here $\boldsymbol{u}$ is defined, as before, by $\rho u_\alpha = \sum_i f_i(\boldsymbol{r}, t) e_{i\alpha}$ the sum of the product of the distribution function before a collision and the lattice vector. Combining equations (4.42) and (4.43) and summing over i gives

$$\sum_i \{f_i(\boldsymbol{r} + \boldsymbol{e}_i, t+1) - f_i(\boldsymbol{r}, t)\} = -\frac{1}{\tau}[\rho - \rho] = 0. \tag{5.10}$$

Multiplying by $e_{i\beta}$ before summing gives

$$\sum_i e_{i\beta} \{f_i(\boldsymbol{r} + \boldsymbol{e}_i, t+1) - f_i(\boldsymbol{r}, t)\} = -\frac{1}{\tau}[\rho u_\beta - \rho u_\beta^*] = F_\beta \tag{5.11}$$

as in equation (4.99). Finally we define the fluid momentum $\rho \boldsymbol{v}$ to be the average of the momentum before the collision, $\rho \boldsymbol{u}$, and the momentum after the collision, $\rho \boldsymbol{u} + \boldsymbol{F}$:

$$\rho v_\alpha = \rho u_\alpha + \frac{1}{2} F_\alpha. \tag{5.12}$$

Now we can perform a Chapman-Enskog expansion of the left-hand sides of equations (5.10) and (5.11) using $E(\rho, \boldsymbol{v})$ as the first-order approximation $f^{(0)}$. Now $\sum_i f_i^{(0)} = 0$ and $\sum_i f_i^{(0)} e_{i\alpha} = \rho v_\alpha$ so we require

$$\sum_i f_i^{(1)} = 0 \tag{5.13}$$

and

$$\sum_i f_i^{(1)} e_{i\alpha} = -\frac{1}{2} F_\alpha. \tag{5.14}$$

This gives the left hand sides of equations (4.53), (4.55), (4.57) and (4.59) as before. The right hand sides are $0, F_\beta, 0$ and 0 respectively. Summing these equations (where now $f^{(0)} = E(\rho, \boldsymbol{v})$) we get

$$\partial_{1t} \rho + \partial_{1\alpha} \rho v_\alpha = 0. \tag{5.15}$$

and

$$\partial_{1t} \rho v_\beta + \partial_{1\alpha} \rho v_\alpha v_\beta = -\partial_{1\alpha} \left[\frac{\rho(1 - d_0)}{D} c^2 \delta_{\alpha\beta} \right] + F_\beta. \tag{5.16}$$

for the first two equations. Summing the left hand side of equation (4.57) we see that the second and fourth terms are zero as before, the third term is $-\partial_{1\alpha}F_\alpha/2$ by equation (5.14) and the fifth term is $\partial_{1\alpha}F_\alpha/2$ by equation (5.16). This gives

$$\partial_{2t}\rho = 0. \tag{5.17}$$

Summing the left hand side of equation (4.59) we similarly see that the second and fourth terms cancel and the remaining terms give equation (4.61), the second-order momentum equation, with $\boldsymbol{u}$ replaced by $\boldsymbol{v}$. Note that the third term of equation (4.59) is still given by equation (4.60) with $\boldsymbol{u}$ replaced by $\boldsymbol{v}$. Consider the first-order expansion of equations (4.42) and (4.43):

$$\epsilon\partial_{1t}f_i^{(0)} + \epsilon\partial_{1\beta}e_{i\beta}f_i^{(0)} = -\frac{1}{\tau}[f_i^{(0)} + \epsilon f_i^{(1)} - \overline{f}_i], \tag{5.18}$$

where $f_i^{(0)} = E(\rho, \boldsymbol{v})$ and $\overline{f}_i = E(\rho, \boldsymbol{u}^*)$. Multiplying equation (5.18) by $\partial_{1\alpha}e_{i\alpha}e_{i\gamma}$ and summing over i and noting that to first-order in the velocity

$$\sum_i e_{i\alpha}e_{i\gamma}f_i^{(0)} = \sum_i e_{i\alpha}e_{i\gamma}\overline{f}_i \tag{5.19}$$

we get

$$\begin{aligned}&\sum_i \partial_{1\alpha}e_{i\alpha}e_{i\gamma}f_i^{(1)} \\ &= -\tau\left\{\frac{(1-d_0)c^2}{D}\partial_{1t}\partial_{1\alpha}\rho\delta_{\alpha\gamma} + \partial_{1\alpha}\partial_{1\beta}\frac{\rho c^2}{D+2}[v_\alpha\delta_{\beta\gamma} + v_\beta\delta_{\alpha\gamma} + v_\gamma\delta_{\alpha\beta}]\right\}\end{aligned} \tag{5.20}$$

as before. Combining the first- and second-order equations we get the continuity equation (4.62) in terms of the fluid velocity $\boldsymbol{v}$ and the Navier-Stokes equation

$$\partial_t\rho v_\alpha + \partial_\beta\rho v_\beta v_\alpha = -\partial_\beta\left[\frac{\rho(1-d_0)}{D}c^2\delta_{\alpha\beta}\right] + \nu\partial_\beta\partial_\beta\rho v_\alpha + \partial_\alpha\zeta\partial_\beta\rho v_\beta + F_\alpha. \tag{5.21}$$

This is the same as equation (4.63) in terms of the fluid velocity $\boldsymbol{v}$ with the additional force term F_α which comes from equation (5.16).

5.1.5 Adding an Additional Term to the Boltzmann Equation

Consider the Boltzmann equation,

$$f_i(\boldsymbol{r} + \boldsymbol{e}_i, t+1) - f_i(\boldsymbol{r}, t) = \Omega_i(\boldsymbol{r}, t), \tag{5.22}$$

where

$$\Omega_i(\boldsymbol{r},t) = -\frac{1}{\tau}\left[f_i(\boldsymbol{r},t) - \overline{f}_i(\boldsymbol{r},t)\right] + \frac{D}{bc^2}F_\alpha e_{i\alpha}, \tag{5.23}$$

and $\boldsymbol{u}$ and $\overline{f}_i$ are defined in the usual way: $\rho u_\alpha = \sum_i f_i e_{i\alpha}$ and $\overline{f}_i = E(\rho, \boldsymbol{u})$. Summing equation (5.23) over i gives

$$\sum_i \{f_i(\boldsymbol{r}+\boldsymbol{e}_i, t+1) - f_i(\boldsymbol{r},t)\} = -\frac{1}{\tau}[\rho - \rho] = 0. \tag{5.24}$$

Multiplying by $e_{i\alpha}$ before summing gives

$$\sum_i \{f_i(\boldsymbol{r}+\boldsymbol{e}_i, t+1) - f_i(\boldsymbol{r},t)\} = -\frac{1}{\tau}[\rho u_\alpha - \rho u_\alpha] + F_\alpha = F_\alpha. \tag{5.25}$$

Defining, as before, the fluid momentum through $\rho v_\alpha = \rho u_\alpha + \frac{1}{2}F_\alpha$ we get the same equations as in section 5.1.4.

The equation equivalent to equation (4.60) has an additional term $\frac{D}{bc^2}F_\alpha e_{i\alpha}$, however, when this is multiplied by $\partial_{1\alpha} e_{i\alpha} e_{i\gamma}$ and summed over i it sums to zero by equation (4.39). We therefore obtain the same expression for $\sum_i \partial_{1\alpha} f_i^{(1)} e_{i\alpha} e_{i\gamma}$ as we did in section 5.1.4. Thus we again obtain the continuity equation (4.62) in terms of the fluid velocity $\boldsymbol{v}$ and the Navier-Stokes equation (5.21).

5.1.6 Review of Methods

The first two methods can only be used if the body force is so small that its effect is negligible, so neither is suited to modelling a phenomena where gravity is important. The two methods described in sections 5.1.4 and 5.1.5 give the same equations of motion, however they are different. The method described in section 5.1.4 shall be called method (1) and the method described in section 5.1.5 method (2). The difference between the lattice Boltzmann operators $\Omega_1 - \Omega_2$ for models 1 and 2, acting on the same distribution function f_i is

$$\frac{\rho}{\tau}\left\{\left[\frac{2u_\alpha \tau F_\beta}{\rho} + \frac{\tau^2 F_\alpha F_\beta}{\rho^2}\right]\frac{D(D+2)e_{i\alpha}e_{i\beta}}{2c^4 b} - \frac{D}{2c^2 b}\left[\frac{2u_\alpha \tau F_\alpha}{\rho} + \frac{\tau^2 F_\alpha F_\alpha}{\rho^2}\right]\right\} \quad i = 1, b$$

$$-\frac{\rho}{\tau}\left(\frac{2\tau F_\alpha u_\alpha}{\rho c^2} - \frac{\tau^2 F_\alpha F_\alpha}{\rho^2 c^2}\right) \quad i = 0. \tag{5.26}$$

The difference contains terms $O(uF/\rho)$ and $O\left((F/\rho)^2\right)$. During the implementation $u \ll c_s$, the speed of sound and $F/\rho = g \ll 1$. Thus, in general, the difference expressed in equation (5.26) will be small. Although F/ρ is small it can still produce a significant effect. The difference expressed in equation (5.26) being small does not imply that $\delta\rho$ is negligible in equation (5.3) or that F_α in equation (5.7) is negligible.

In section 5.1.4 the additional force affects the updated distribution function, $f_i(\boldsymbol{r} + \boldsymbol{e}_i, t+1)$, on each link, $i = 0, ..7$. In section 5.1.5 the updated distribution function is altered, by the additional term, by an amount proportional to $F_\alpha e_{i\alpha}$. This means that f_0 is not changed (f_0 will, however, be updated according to the standard collision operator). If a hexagonal grid, with links 2 and 5 horizontal, is used then neither f_2 or f_5 will be changed by the additional term. If the grid is orientated so that f_2 and f_5 are vertical then the additional term will affect $f_1, ..., f_6$ and it will have a larger effect on f_2 and f_5 than it will on the others. A change in some of the f_i terms at one time-step will propagate through to all the f_i terms at the next time-step.

5.2 Model Implementation

The two models described in sections 5.1.4 and 5.1.5 were both implemented so that the affect they have on a fluid simulation could be observed and any differences between the models could be considered. In all the simulations, unless stated otherwise, we will use $\tau = 0.9$ and $\boldsymbol{F} = 0.001\rho\boldsymbol{e}_z$. This value of $\boldsymbol{F}$ is larger than any value used in subsequent wave simulations. A single-species model was implemented using the isotropic, Galilean invariant equilibrium distribution derived in section 4.2.1. An immiscible binary fluid was implemented using the free energy model described in section 4.4.4.

5.2.1 Density Gradient

A world was initialised on a 64 by 64 grid with zero velocity and $\rho = 4$. A boundary was placed at the bottom ($z = 0$) of the grid, which also acted as a boundary at the top, continuous boundary conditions were applied at the other two edges. Gravity was then applied using method (1) and method (2) and the density measured every 1,000 time-steps along a vertical line through the middle of the grid. The results are shown in figure 5–1 at times 1,000, 2,000, 3,000, 4,000, and 5,000 time-steps when gravity is applied using method (2). The density profile is seen to 'oscillate' about its final position for several thousand time-steps before reaching its final state. It is clear from figure 5–1 that during this time the distribution is not symmetric about the mid-height. After 10,000 time-steps the density at each point is within 0.07% of its final value, at this time the density distribution is found to lie on the same distribution as that for $t = 3,000$ time-steps in figure 5–1 and so is not included for clarity.

The two methods, method (1) and method (2), were compared by looking at the difference in the density, $\delta\rho = |\rho^{(1)} - \rho^{(2)}|$, at different heights above the boundary. Here $\rho^{(1)}$ and $\rho^{(2)}$ are the density when method (1) and method (2) are used

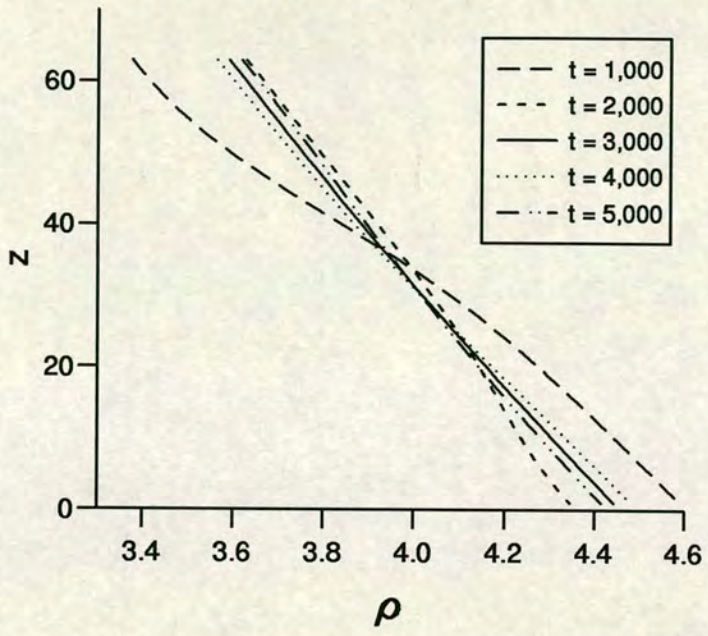

FIGURE 5–1: Density as a function of height at selected times when gravity is applied using method (2).

respectively. The results are shown in figure 5–2 at times 1,000 4,000 and 10,000 time-steps. The size of the density difference is small compared to the mean density of 4 and is seen to decrease with time. After 1,000 time-steps it has a maximum value of 1×10^{-3}, only 0.025% of the mean density, at subsequent times the difference is always smaller. The shape of the graphs shown in figure 5–2 are typical of the shape of all the results obtained. Consider either method applied to an infinite fluid with the same initial density at each site. There is no density change induced at any of the sites by the gravitational force. On our finite grid a small difference will occur at sites adjacent to the boundary and these will propagate through the fluid. The difference in the update rules at these sites account for the small variations observed here, which are negligibly small, and for the shape of the curves in figure 5–2. Thus both method (1) and method (2) are producing the same effect. This is to be expected since they both satisfy the same equations of motion.

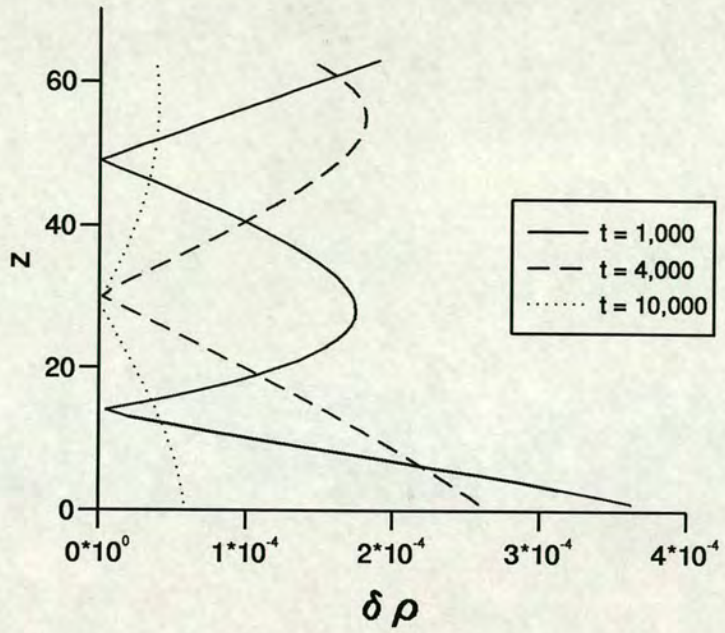

FIGURE 5–2: The difference in density between method (1) and method (2) as a function of height at selected times.

5.2.2 Model Comparison

Method (1) and method (2) both produce similar results, however method (2) is preferred for use in the rest of the simulations. This is because the body force appears in a natural manner: as an extra term in the governing equation. In method (1) the body force is produced by considering the equilibrium distribution, not of the actual fluid but of a fluid with a non-physical 'equilibrium velocity'. The model tests described in sections 5.2.3, 5.2.4 and 5.3 and the interfacial wave simulations in chapters 7 and 8 will all have gravity implemented using method (2).

5.2.3 Grid Orientation

It is important to insure that the model is independent of the grid orientation, particularly since, as discussed is section 5.1.6, the orientation of the grid can affect the change in each distribution function and whether four or six of the seven distribution functions are changed. As noted in section 5.1.6 a change in some of

the f_i at one time-step will produce a change in all the f_i at the next time-step. The dependence on the grid orientation was tested using a 64 by 64 grid which was set up with the x-axis along the direction of $\boldsymbol{e}_2$. A new set of perpendicular axis x' and y' were defined so that the x-axis and the x'-axis intersect at an angle, θ. A square box 40 lu by 40 lu was then superimposed on the grid, the edges of the square being parallel to the directions of the x'- and y'-axis. All points outside this square where then defined as boundary sites. This is shown in figure 5–3. The non-boundary sites inside the 40 by 40 lu tilted square were filled with par-

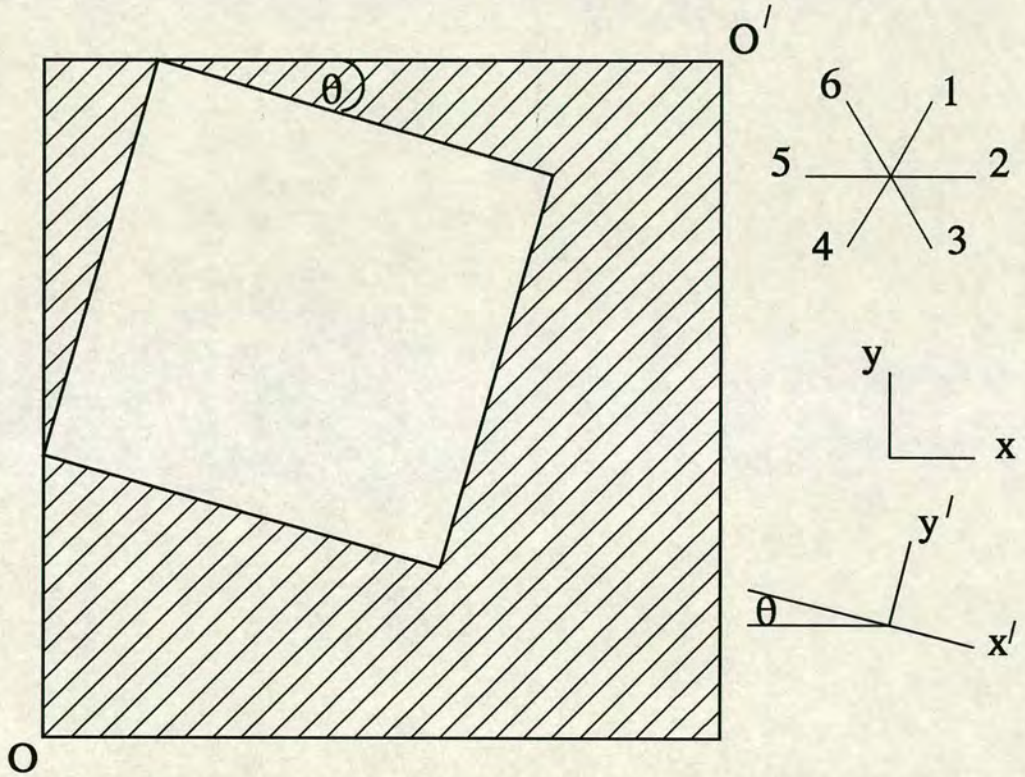

FIGURE 5–3: A box, at angle θ to the x-axis, superimposed on the regular grid and the co-ordinate systems. The hashed area is filled with boundary sites.

ticles with $\rho = 4$ and velocity zero and gravity was applied in the direction of the $-y'$-axis. Thus the vertical direction $\boldsymbol{e}_z$ is in the direction of the y'-axis. This was done for $\theta = 0°$, $18°$, $36°$, $54°$, $72°$ and $90°$. The density variation with height was then found in the following ways:

When $\theta = 0^o$ the density was measured in a horizontal line (parallel to the y-axis) above the boundary, as was done in the previous section. Density values were found at heights with separation $\sqrt{3}/2$ lu.

When $\theta = 90^o$ the density was measure in a horizontal line (parallel to the x-axis). Density values were found at heights with separation 1 lu.

When $\theta = 18^o$, 36^o, 54^o and 72^o the horizontal direction (parallel to the y'-axis) does not lie along a grid direction. The following method was used to find the density at given heights above the boundary.

1. Let a be in index labelling the data points.

2. Calculate the gradient, m, of a line through the origin O, see figure 5–3, parallel to the y'-axis.

3. Start at the origin O with co-ordinates $(x, y) = (0, 0)$.

4. Given a point calculate its distance from the origin, d.

5. Calculate the gradient m_1 of the line $((0,0),(x+1,y))$ and gradient m_2 of the line $((0,0),(x+1/2,y+\sqrt{3}/2))$.

6. Move to the point $(x+1, y)$ if m_1 is closer to m or to the point $(x+1/2, y+\sqrt{3}/2)$ of m_2 is closer to m.

7. If the density at the point is zero (the point is a boundary site) then let $D = d$.

8. If the density is non-zero (the point is a non-boundary site) retrieve a set of values $z_a = d - D$ and $\rho_a = \rho$.

9. Repeat steps 4 – 8 until there are no points left.

This gives a set of data z_a, ρ_a for $a = 1, 2, ..., N$ where the value of N depends on the angle θ. This is illustrated in figure 5–4 where the thick solid line represents

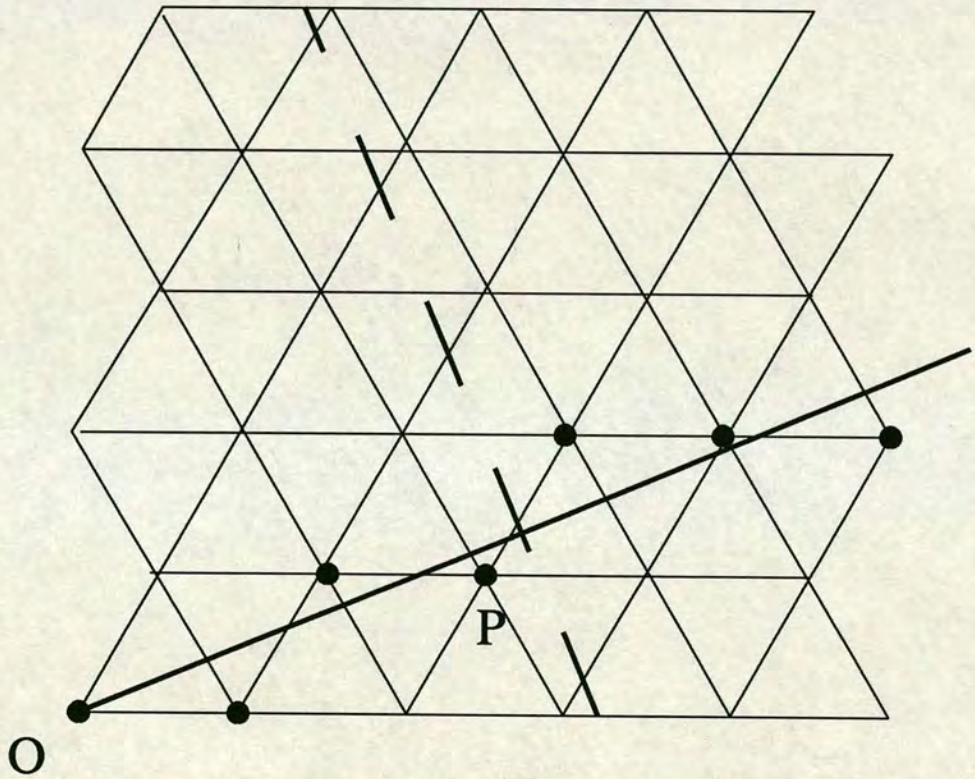

FIGURE 5–4: Part of the hexagonal grid is shown. The thick solid line represents the line through O with gradient m, the thick dashed line represents the 'bottom' boundary and the solid dots represent the sites which are considered as lying nearest to the thick solid line. Point P is the last of these point which is still within the boundary.

the line through O with gradient m, the thick dashed line represents the 'bottom' boundary and the solid dots represent the sites which are considered as lying nearest to the thick solid line. Point P is the last of these point which is within the boundary so the distance D is the length of OP. For some values of θ the line parallel to the y'-axis, passing through O', see figure 5–3, also passes through the

fluid and the density at various heights above the boundary can be found along this line. Similar results were obtained for both methods confirming that the angle of the box and the angle at which gravity is acting are consistent.

Results

All the results show good agreement with each other. Figure 5–5 shows the results

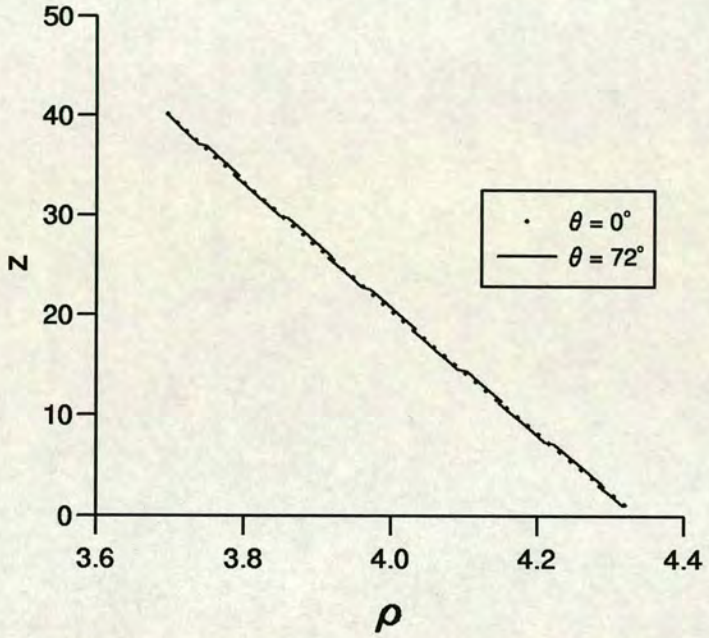

FIGURE 5–5: The equilibrium density as a function of height when $\theta = 0^o$ (points) and $\theta = 72^o$ (line).

for two angles, $\theta = 0^o$ and $\theta = 72^o$ when gravity is implemented using method (2). The results for $\theta = 72^o$ are seen to lie on either side of the results for $\theta = 0^o$ The cross over between these lines corresponds to the points, shown in figure 5–4, moving from one side of the solid line to the other. This effect was also noticed on the other results for smaller θ but to a lesser extent. There is also a small error introduced because the point P is not exactly on the boundary. Clearly these errors are relatively small, all the results lie within one lattice unit of each other. A closer comparison can be made between the results for $\theta = 0^o$ and $\theta = 90^o$ because the exact height above the boundary is know. To do this the results for $\theta = 0^o$ were linearly interpolated to find the density at integer lattice-step separations. These

were then compared to the results for $\theta = 90^o$ and their difference $\delta\rho$ is plotted in figure 5–6. The difference between the results is always less than 0.04%, the

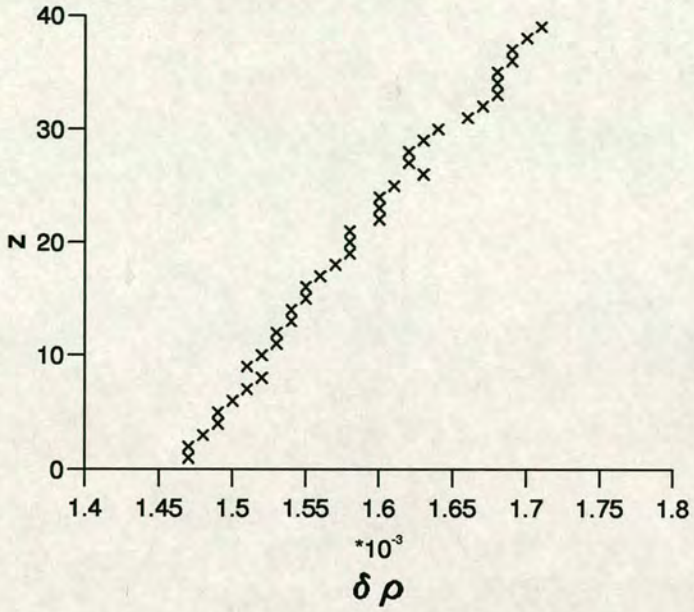

FIGURE 5–6: The equilibrium density difference $\delta\rho$ between the results for $\theta = 0^o$ and $\theta = 90^o$ as a function of height.

difference depending on the height above the boundary. This is probably due to the box not being exactly square, its dimensions are 40 by $46 \times \sqrt{3}/2$ lu which is 40 by 39.8 lu, a difference of 0.5%.

5.2.4 Gravitational Strength

Single Species Model

Gravity was imposed on a single-species fluid using method (2). The initial density of the fluid was $\rho_0 = 1.0$ and the fluid was evolved for 10,000 time-steps with $\tau = 200.0$ to ensure that the fluid reaches its equilibrium state. Figure 5–7 shows the density variation with depth when $g = 0.001$. The density gradient is slowly increasing with depth. The shape of the curve shown in figure 5–7 is consistent with the expected exponential variation of the density with depth. The variation of the density gradient with depth is a function of the gravitational strength, when

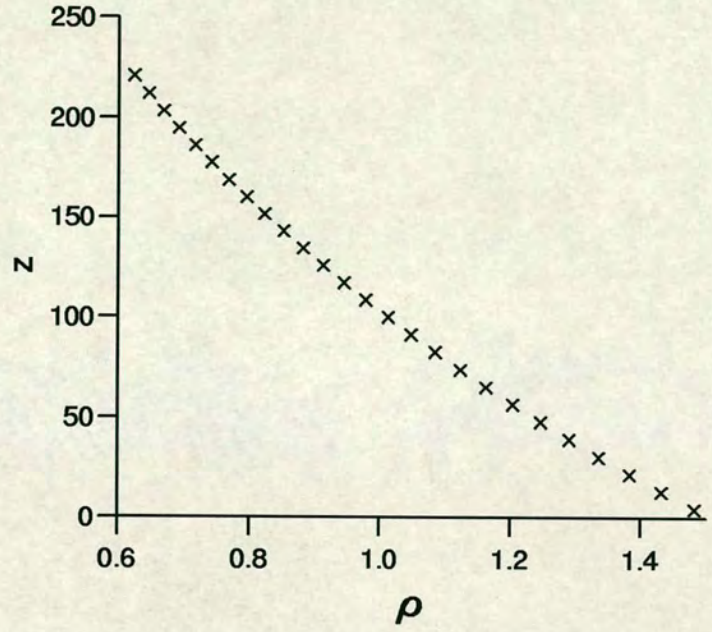

FIGURE 5–7: Density as a function of depth for a fluid with $\rho_0 = 1.0$, $\tau = 200.0$ and $g = 0.001$ after 10,000 time-steps.

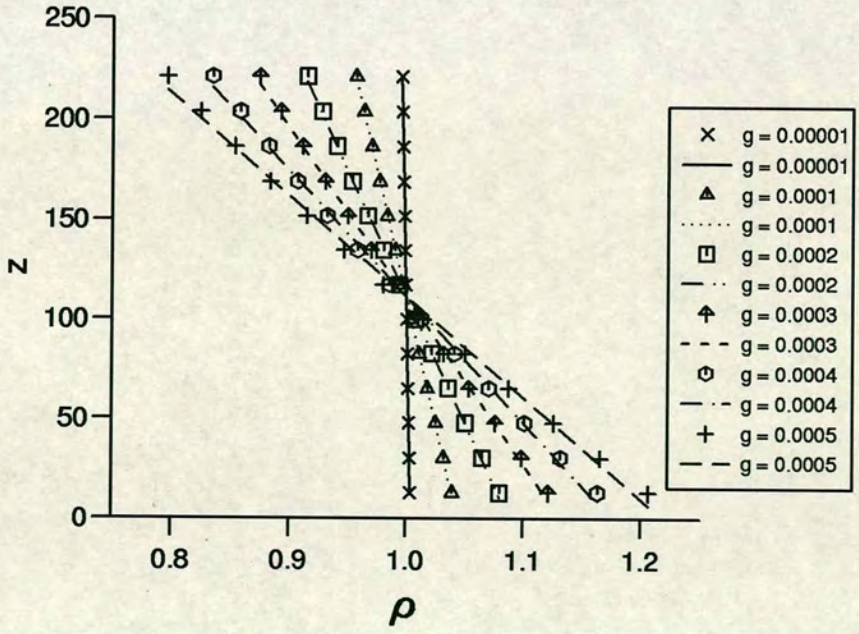

FIGURE 5–8: The density as a function of depth for a fluid with $\rho_0 = 1.0$ and $\tau = 200.0$ after 10,000 time-steps when $g = 0.00001$, 0.0001, 0.0002, 0.0003, 0.0004 and 0.0005. The markers show the results of the simulations and the lines are the best-fit straight lines through the points.

the gravitational strength is less than 0.005 the density gradient can be considered as being constant over the range of depths we are considering. Figure 5–8 shows the density variation with depth for a range of gravitational strengths and the best-fit straight line through the points. Even for the largest value of $g = 0.0005$ the linear approximation appears to fit well. The linear density gradient is shown in figure 5–9 for a range of values of g less than 0.0005. Clearly the density gradient is proportional to the gravitational strength g. It is important to remember that these results show that the density gradient is approximately linear over the depths we are considering. The actual form of the density gradient is an exponential, as suggested by figure 5–7. This can be seen in figure 5–10 which shown the linear density gradients plotted against g, as in figure 5–9, but for an initial uniform density of 4.0. The density gradients shown in figure 5–10 are four times the gradients shown in figure 5–9.

We have seen that, provided the gravitational strength and the fluid depth are small, the density gradient is approximately linear and is proportional to g. For larger values of g, where the gradient can no-longer be considered linear, we would still expect the density gradient to be proportional to the gravitational strength.

Immiscible Binary Fluid

An immiscible binary fluid was initialised with the two fluids separated by a horizontal interface. The upper fluid has $\Delta\rho$ negative. Gravity was applied to both fluids with strength $\rho g = ((sg_1(\rho - \Delta\rho) + sg_2(\rho + \Delta\rho))/2$ using method (2), where $sg_1 < sg_2$. At temperature $T = 0.5$ we have seen that $|\rho/\Delta\rho| \simeq 2$ in the absence of gravity. Figure 5–11 shows the value of the modulus of the ratio $\rho/\Delta\rho$ at different depths for the immiscible fluid when $sg_1 = 0.0001$ and $sg_2 = 0.0002$. At the interface the value of $|\rho/\Delta\rho|$ is different from 2.0 by no more than 4%, away from the interface the ratio appears constant with depth, and hence also with density.

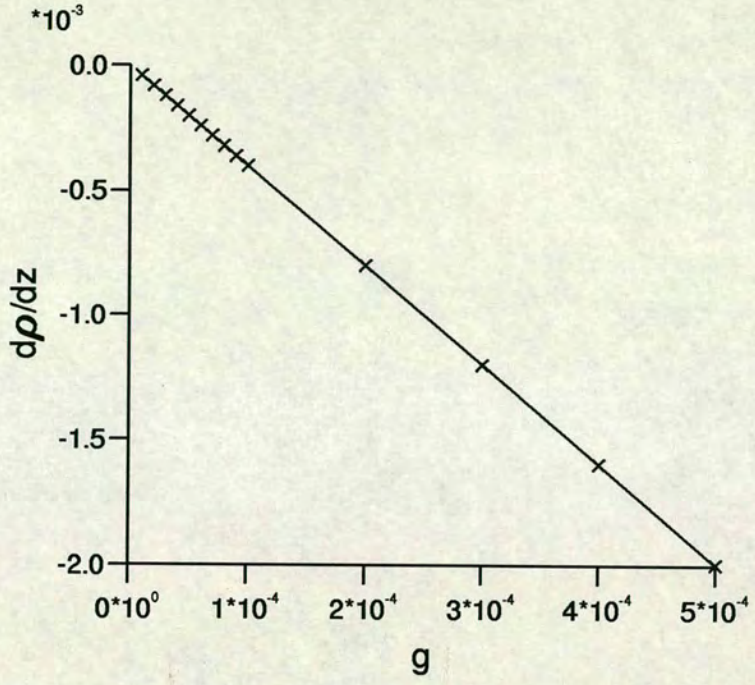

FIGURE 5–9: The linear density gradient as a function of the gravitational strength g for an initial density $\rho_0 = 1.0$.

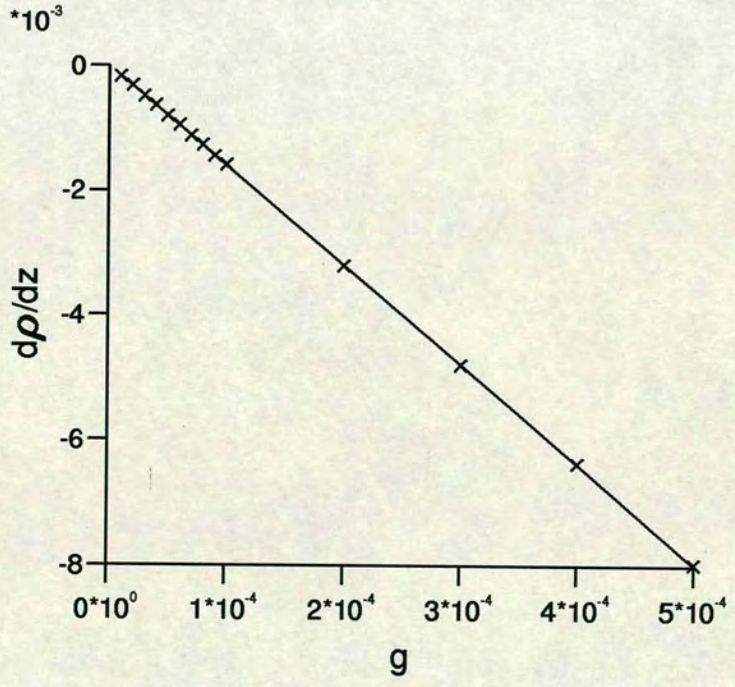

FIGURE 5–10: The linear density gradient as a function of the gravitational strength g for an initial density $\rho_0 = 4.0$.

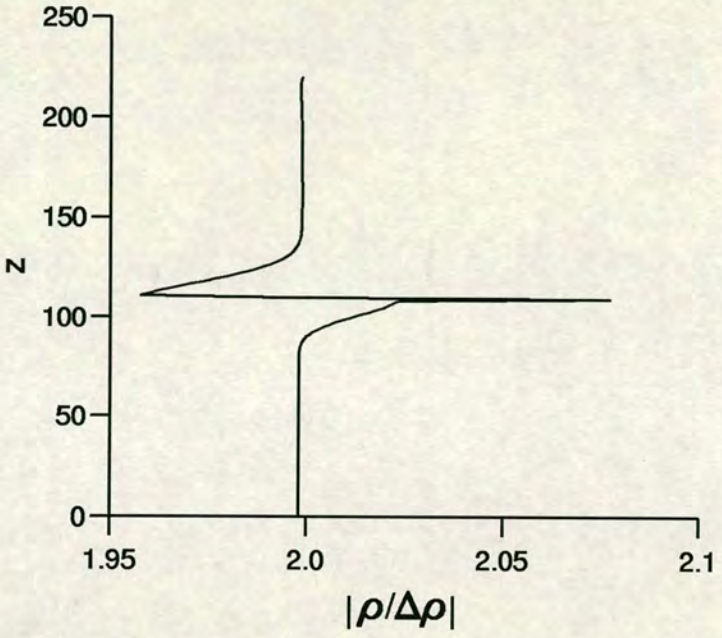

FIGURE 5–11: The modulus of the ratio $\rho/\Delta\rho$ as a function of depth when gravity is applied to a binary fluid with a horizontal interface between the fluids. Gravity was applied with $sg_1 = 0.0001$ and $sg_2 = 0.0002$.

Thus the value of g in both fluids is given by

$$g_1 = sg_1(1 + 1/2) + sg_2(1 - 1/2))/2$$
$$g_2 = sg_1(1 - 1/2) + sg_2(1 + 1/2))/2. \tag{5.27}$$

Figures 5–12 and 5–13 show the variation in density with depth for a immiscible fluid for two different sets of values sg_1 and sg_2. The values are shown in table 5–1 as are the values of g_1, g_2 and the expected gradients m_1 and $m_2 = \mathrm{d}\rho/\mathrm{d}z$

case	sg_1	sg_2	g_1	g_2	m_1	m_2
(a)	1×10^{-4}	2×10^{-4}	2.5×10^{-4}	3.5×10^{-4}	-4.33×10^{-4}	-6.06×10^{-4}
(b)	5.0×10^{-5}	5.5×10^{-5}	1.025×10^{-4}	1.075×10^{-4}	-1.78×10^{-4}	-1.86×10^{-4}

TABLE 5–1: The values of sg_1 and sg_2 used in case (a) and (b) in figure 5–12. Also shown is the expected gradient m_1 and m_2 across the two fluids. This is found by calculating g_1 and g_2, the values of the acceleration due to gravity in the two fluids, using equation (5.27) and then finding the expected density gradients m_1 and m_2 from the results obtained for the single species fluid which are displayed in figure 5–9.

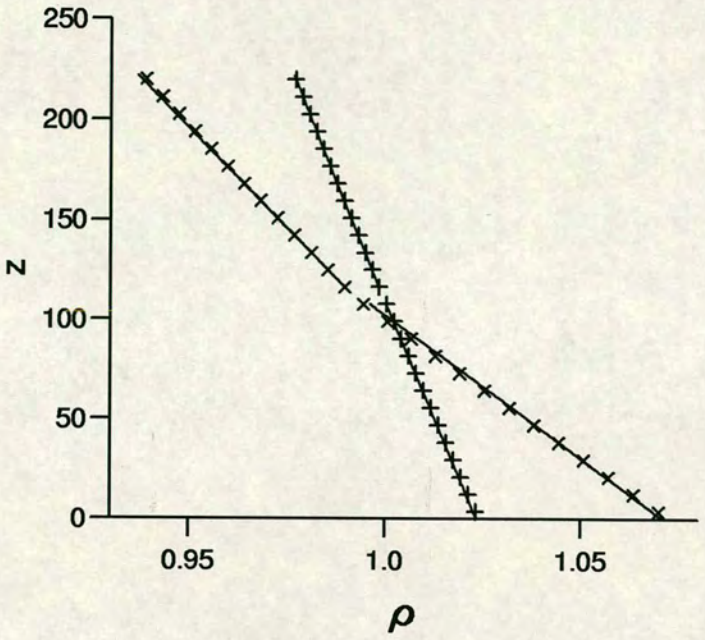

FIGURE 5–12: The density as a function of depth for case (a) (x) and case (b) (+) shown in table 5–1. Also shown are straight lines with the gradients shown in table 5–1.

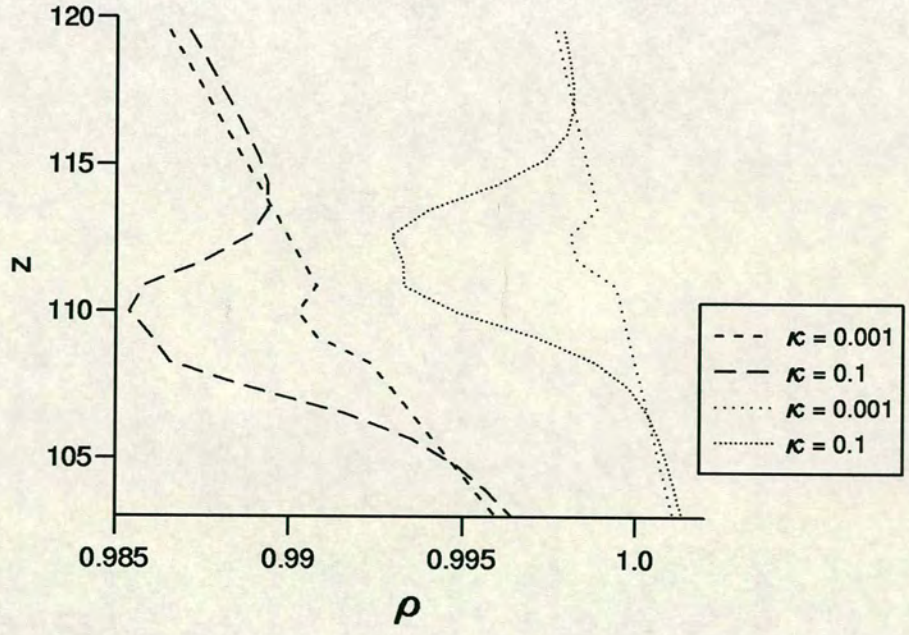

FIGURE 5–13: The density as a function of depth close to the interface for case (a) (dashed lines) and case (b) (dotted lines) for $\kappa = 0.1$ and 0.001.

in the upper and lower fluids respectively. Straight lines with these gradients are also shown in figure 5–12. The agreement between the actual gradients and the predicted gradients is good and reinforces the use of equation (5.27) is calculating g_1 and g_2. The details of the density close to the interface are shown in figure 5–13 for two different values of κ. The results for case (a) are shown by the dashed lines and the results for case (b) are shown by the dotted lines. It can be seen that, as before, the density is reduced slightly across the interface and that the interface is larger for $\kappa = 0.1$. Away from the interface the results for $\kappa = 0.001$ and $\kappa = 0.1$ are virtually indistinguishable.

5.3 Galilean Invariance

To test the Galilean invariance of the model a drop of radius $\simeq 60$ lattice units was initialised at the centre of a 128 by 128 grid with the whole fluid moving with speed u_x in the x-direction and with gravity acting in the z-direction with strength $g = 0.0005$. The bubble was then allowed to equilibrate for a number of different values of the relaxation time associated with the order parameter, τ_Δ. The fluid relaxation parameter τ_ρ was set to 1.1 throughout. The ratio of a_z, the drop diameter in the z-direction, to a_x, the diameter in the x-direction, is shown in figure 5–14. When $\tau_\Delta = \tau_*$ the radio is independent of u_x as observed elsewhere [38] in the absence of gravity. For other values of τ_Δ the ratio is dependent on u_x and the model is not Galilean invariant, the further τ_Δ is from τ_* the worse the lack of Galilean invariance is. The ratio of the two diameters appears independent of the velocity when $\tau_\Delta = \tau_*$ and is slightly smaller than unity. The difference from unity is due to the density gradient across the drop. This does not affect the Galilean invariance because the free energy binary-fluid model is Galilean invariant [38] for all densities and the transport coefficients are independent of density. The constant value of a_z/a_x shows that this model, incorporating the gravitational interaction, is, at worst, very close to Galilean invariant provided $\tau_\Delta = \tau_*$.

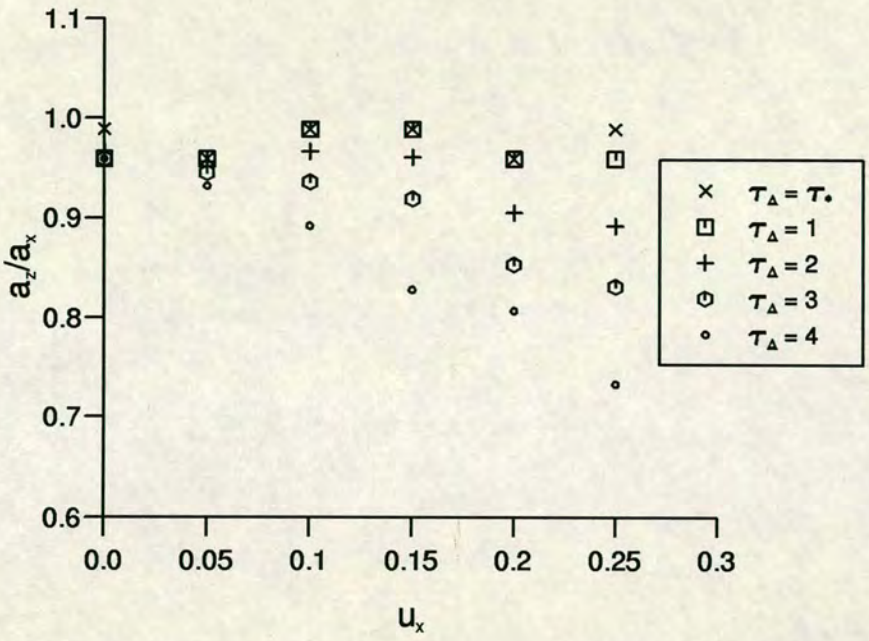

FIGURE 5–14: Equilibrium shape of a fluid drop in a system moving with constant speed u_x along the x-direction when gravity is applied with strength $g = 0.0005$ in the z-direction. Results are shown for a number of different values of the relaxation time τ_Δ of the order parameter. The ratio of the diameters in the z- and x-direction a_z/a_x is plotted.

5.4 Summary

We have seen that a body force, such as gravity, can be incorporated into the lattice Boltzmann model. A method has been proposed which incorporates the body force into the lattice Boltzmann equation. This method is seen to produce very similar results to the method proposed by Martys *et al.* [66]. The new method is preferred because it introduces the gravitational term directly into the governing equation in a straight forward manner. The implementation of the new method is also shown to be independent of the underlying grid. When the body force is applied to the binary fluid model [9] the resulting model has been shown to be, at worst, very close to Galilean invariant for the correct choice of the relaxation parameter τ_Δ.

Chapter 6

The Equations of Internal Wave Motion

In this chapter a summary of the equations governing internal wave motion is presented. Initially wave propagation at a sharp interface, between two non-viscous fluids, will be considered and the equations describing the wave motion derived. Two fluids with a finite smooth interface will also be considered and the effect of the finite interface on the equations of motion discussed. The fluid viscosity will also be examined and its effect on the frequency, the damping of interfacial waves and the velocity profile will be found. Finally the equations for standing waves will be found from the progressive wave solutions.

6.1 The Potential Density

The density of a fluid is a function of the pressure p, temperature T and, for a liquid, the salinity χ, defined as the proportion by mass of the dissolved salts [67]. Consider a particle at height z, where the density is $\rho(z)$, in a fluid with no temperature or salinity variation. The pressure at height z is given by the hydrostatic pressure equation [67]

$$\frac{\mathrm{d}p(z)}{\mathrm{d}z} = -\rho(z)g. \tag{6.1}$$

If the particle moves slightly to height $z + \xi$ then the pressure acting on the particle and the fluid density will change to $p(z+\xi)$ and $\rho(z+\xi)$ respectively and

the particle will remain in equilibrium. When we are considering internal waves we are concerned, not with the actual density, but with the excess or potential density defined [68,69] as the density the fluid would have if compressed adiabatically, with constant salinity, to a reference pressure p_0. This can be expressed [69]

$$\rho_{\text{pot}} = \rho - \int_{p_0}^{p} \left(\frac{\partial \rho}{\partial p}\right)_{\chi S} \mathrm{d}p \tag{6.2}$$

where S is the entropy. This means that a fluid which has a density gradient produced solely by gravity has ρ_{pot} constant and no internal wave motion will occur. In practice internal waves only occur when there is a change in temperature or a change in salinity with depth.

6.2 Inviscid Wave Equations

Before considering the effects of viscosity we review the interfacial wave equations for an inviscid fluid.

6.2.1 The Two-Layer Model

Gravity wave motion between immiscible, homogeneous, incompressible fluids can, provided any disturbances are small, be described by linear wave theory an a manner analogous to linear surface waves [67,70,71]. Consider two fluids of depth h_1 and h_2 with densities ρ_1 and ρ_2, $\rho_1 < \rho_2$, separated by a sharp interface. Let the origin be at the interface with the x-coordinate horizontal and the z-coordinate vertically upwards. If the fluids are irrotational then they can be described in terms of a velocity potential ϕ such that the velocity $\boldsymbol{u}_0 = (u_0, w_0)$ is given by

$$u_0 = \frac{\partial \phi}{\partial x}, \qquad w_0 = \frac{\partial \phi}{\partial z}. \tag{6.3}$$

Let the velocity potential be ϕ_1 for $0 < z < h_1$ and ϕ_2 for $0 > z > -h_2$. Now, the fluid velocity must satisfy the continuity equation so the velocity potential must satisfy the Laplace equation

$$\frac{\partial^2 \phi}{\partial x^2} + \frac{\partial^2 \phi}{\partial z^2} = 0. \tag{6.4}$$

We now consider the interface to be perturbed by a small amount $z = \eta(x,t)$ where the perturbation is assumed to be a plane monochromatic wave with frequency ω_0, wavenumber k and amplitude a:

$$\eta = ae^{i(kx-\omega_0 t)} \tag{6.5}$$

where a is the deformation amplitude and where it is understood that it is the real part of η which is of interest. The following boundary conditions apply to the fluids.

1. The is no vertical motion at the bed,

$$\frac{\partial \phi_2}{\partial z} = 0\Big|_{z=-h_2}. \tag{6.6}$$

2. Any surface motion produced by the internal waves is negligible and the surface can be considered as a solid boundary,

$$\frac{\partial \phi_1}{\partial z} = 0\Big|_{z=h_1}. \tag{6.7}$$

3. At the interface the horizontal velocity in both fluids must be the same as the $\partial\eta/\partial t$. Using the linear approximation that all disturbances are small this can be applied at $z = 0$,

$$\begin{aligned} \frac{\partial \eta}{\partial t} &= \frac{\partial \phi_1}{\partial z}\Big|_{z=0}, \\ \frac{\partial \eta}{\partial t} &= \frac{\partial \phi_2}{\partial z}\Big|_{z=0}. \end{aligned} \tag{6.8}$$

4. At the interface the Bernoulli equation must be satisfied. If we assume that the waves are being driven solely by gravity and that the pressure difference across the interface is negligible then this can be expressed,

$$\rho_1\left(\frac{\partial \phi_1}{\partial t}\Big|_{z=0} + g\eta\right) = \rho_2\left(\frac{\partial \phi_2}{\partial t}\Big|_{z=0} + g\eta\right). \tag{6.9}$$

To solve the Laplace equation we look for wave solutions of the form

$$\phi_i = A_i Z_i(z) e^{i(kx-\omega_0 t)}, \quad i = 1,2 \tag{6.10}$$

where A is an amplitude term and $Z(z)$ describes the z-dependence of the solution. Substituting equation (6.10) into the Laplace equation gives

$$\frac{\partial^2 Z_i}{\partial z} - k^2 Z_i = 0 \tag{6.11}$$

which has solution, subject to the boundary conditions equations (6.6) and (6.7),

$$\begin{aligned} Z_1 &= \cosh[k(z - h_1)] \\ Z_2 &= \cosh[k(z + h_2)]. \end{aligned} \tag{6.12}$$

Substituting equations (6.10) into the boundary conditions (6.8) and using the expressions for Z_i we find the amplitudes A_i in terms of the deformation amplitude a:

$$\begin{aligned} A_1 &= \frac{i\omega_0 a}{k \sinh(kh_1)}, \\ A_2 &= -\frac{i\omega_0 a}{k \sinh(kh_2)}. \end{aligned} \tag{6.13}$$

Substituting equations (6.10) into equation (6.9) and using the expressions for A_i and Z_i gives the dispersion relation

$$\frac{\omega_0^2 \rho_1}{k \tanh(kh_1)} + \frac{\omega_0^2 \rho_2}{k \tanh(kh_2)} - (\rho_2 - \rho_1) g = 0. \tag{6.14}$$

If the interface is far from the bed and the free surface so that $\tanh(kh_1) \simeq 1$ and $\tanh(kh_2) \simeq 1$ this can be written in a form analogous to the dispersion relation for surface waves

$$\omega_0^2 = g' k \tag{6.15}$$

where g' is the reduced gravity and is defined by

$$g' \stackrel{\text{def}}{=} \frac{(\rho_2 - \rho_1)}{(\rho_2 + \rho_1)} g. \tag{6.16}$$

The velocity can be found by differentiating the velocity potential and taking the real part:

$$\begin{aligned} u_0 &= -\frac{\omega_0 a \cosh[k(z - h_1)]}{\sinh(kh_1)} \cos(kx - \omega_0 t), \quad 0 < z < h_1 \\ u_0 &= +\frac{\omega_0 a \cosh[k(z + h_2)]}{\sinh(kh_2)} \cos(kx - \omega_0 t), \quad 0 > z > -h_2 \\ w_0 &= -\frac{\omega_0 a \sinh[k(z - h_1)]}{\sinh(kh_1)} \sin(kx - \omega_0 t), \quad 0 < z < h_1 \\ w_0 &= \frac{\omega_0 a \sinh[k(z + h_2)]}{\sinh(kh_2)} \sin(kx - \omega_0 t), \quad 0 > z > -h_2. \end{aligned} \tag{6.17}$$

6.2.2 Continuous Density Variation

The equations in the preceding section describe interfacial waves at a sharp interface between two immiscible fluids. The density has a discontinuity at the interface taking a value ρ_1 at $z = 0^+$ and ρ_2 at $z = 0^-$. In many situations this model may have some shortcomings since there will normally be a small, but finite, region around the interface where the density changes smoothly from ρ_1 to ρ_2. To investigate this phenomenon we will look at the theory for internal waves in a fluid with a continuously varying density and then find the solutions for our desired density distribution. Following references [69,71] the Sturm-Liouville equation will be derived which can then be solved numerically for the required density distribution.

Here we assume, as in the two-fluid case, that the fluid is incompressible, irrotational and homogeneous. We also make the Boussinesq approximation. This assumes that density variations are small and can be neglected in so far as they affect inertia, but retained in the buoyancy terms where they appear in combination with gravity. The density is given by $\rho = \overline{\rho} + \rho'$ where $\overline{\rho}(z)$ is the mean density and $\rho'(x, z, t)$ is the density fluctuation due to waves motion. Now the continuity and Navier-Stokes equations are

$$\begin{aligned} &\frac{\partial \rho}{\partial t} + \frac{\partial(\rho u)}{\partial x} + \frac{\partial(\rho w)}{\partial z} = 0 \\ &\frac{\partial u}{\partial t} + u\frac{\partial u}{\partial x} + w\frac{\partial u}{\partial z} = -\frac{1}{\rho}\frac{\partial p}{\partial x} \\ &\frac{\partial w}{\partial t} + u\frac{\partial w}{\partial x} + w\frac{\partial w}{\partial z} = -\frac{1}{\rho}\frac{\partial p}{\partial z} - g. \end{aligned} \tag{6.18}$$

Since the fluid is assumed to be incompressible we can also write

$$\frac{\partial u}{\partial x} + \frac{\partial w}{\partial z} = 0. \tag{6.19}$$

Substituting $\rho(x, z, t) = \overline{\rho}(z) + \rho'(x, z, t)$ into equation (6.18) and assuming, as before, that the velocities are small and that ρ' is also small so we can neglect

second-order terms in ρ', u, w and their derivatives, we get

$$\begin{aligned} &\frac{\partial \rho'}{\partial t} + w\frac{\partial \overline{\rho}}{\partial z} = 0 \\ &\overline{\rho}\frac{\partial u}{\partial t} + \frac{\partial p}{\partial x} = 0 \\ &\overline{\rho}\frac{\partial w}{\partial t} + w\frac{\partial p}{\partial z} + (\overline{\rho} + \rho')g = 0. \end{aligned} \tag{6.20}$$

Differentiating the second of these equations with respect to z and the third with respect to x and noting that $\partial\overline{\rho}/\partial x = 0$ we get

$$\begin{aligned} -\frac{\partial^2 p}{\partial x \partial z} &= \overline{\rho}\frac{\partial}{\partial t}\left(\frac{\partial u}{\partial z}\right) + \frac{\partial u}{\partial t}\frac{\partial \overline{\rho}}{\partial z}, \\ -\frac{\partial^2 p}{\partial x \partial z} &= \overline{\rho}\frac{\partial}{\partial t}\left(\frac{\partial w}{\partial x}\right) + g\frac{\partial \rho'}{\partial x}. \end{aligned} \tag{6.21}$$

Equating the two terms for $\partial^2 p/\partial x \partial z$ and differentiating with respect to t and x yields

$$\overline{\rho}\frac{\partial^2}{\partial t^2}\left(\frac{\partial^2 u}{\partial x \partial z} - \frac{\partial^2 w}{\partial x \partial x}\right) - g\frac{\partial^2}{\partial x^2}\frac{\partial \rho'}{\partial t} = -\frac{\partial \overline{\rho}}{\partial z}\frac{\partial^3 u}{\partial t^2 \partial x}. \tag{6.22}$$

Finally we can apply the Boussinesq approximation and set the right hand side of equation (6.22) to zero since variations in the density are only important when they occur in combination with gravity. Now from equations (6.20) and (6.19) we have $\partial u/\partial x = -\partial w/\partial z$ and $\partial \rho'/\partial t = -w\partial\overline{\rho}/\partial z$. Thus equation (6.22) can be re-written in terms of the mean density $\overline{\rho}$ and the z-component of velocity w as

$$\overline{\rho}\frac{\partial^2}{\partial t^2}\left(\frac{\partial^2 w}{\partial x \partial z} + \frac{\partial^2 w}{\partial x \partial x}\right) - g\frac{\partial^2 w}{\partial x^2}\frac{\partial \overline{\rho}}{\partial z} = 0. \tag{6.23}$$

We look for solutions of equation (6.23) of the form

$$w = \mathcal{W}(z)e^{i(kx-\omega t)} \tag{6.24}$$

which when substituted into equation (6.23) gives

$$\frac{\mathrm{d}}{\mathrm{d}z}\left[P(z)\frac{\mathrm{d}\mathcal{W}(z)}{\mathrm{d}z}\right] + [Q(z) + ER(z)]\,\mathcal{W}(z) = 0, \tag{6.25}$$

where $P(z) = 1$, $\quad Q(z) = -k^2$, $\quad E = 1/c^2$ where $c = \omega/k$ is the wave celerity and $R(z) = N^2(z)$ where $N(z)$ is the Brunt-Väisälä frequency,

$$N^2(z) = -\frac{g}{\overline{\rho}}\frac{\partial \overline{\rho}}{\partial z}. \tag{6.26}$$

Equation (6.25) is the Sturm-Liouville equation and it can not, in general, be solved analytically. It is however known [72] that, provided $P(z) > 0$, $Q(z) \leq 0$ and $R(z) > 0$, the Sturm-Liouville equation has an infinite number of real, positive eigen-value solutions $E = E_0, E_1, E_2, ...$ each with eigen-functions $\mathcal{W}_n, n = 0, 1, 2, ...$ Each of the eigen-functions $\mathcal{W}_n(z)$ having n+1 extremes in the z-range in which ρ is defined. For each mode (n=0, 1, ...) there is a unique relationship between the celerity, $c = \sqrt{1/E_n}$ and the wave number k, this relationship is referred to as the dispersion relation of that mode. If we now write the x-velocity in the same form

$$u = \mathcal{U} e^{i(kx - \omega t)} \tag{6.27}$$

then, from the incompressibility equation (6.19), we find

$$\frac{\mathrm{d}\mathcal{W}(z)}{\mathrm{d}z} = -ik\mathcal{U}(z). \tag{6.28}$$

If we define

$$\rho = \begin{cases} \rho_1 & z > \dfrac{l}{2} \\ \rho_1 + \dfrac{(\rho_2 - \rho_1) \times (\frac{l}{2} - z)}{l} & \dfrac{l}{2} \geq z \geq -\dfrac{l}{2} \\ \rho_2 & z < -\dfrac{l}{2} \end{cases} \tag{6.29}$$

then

$$\frac{\partial \rho}{\partial z} = \begin{cases} \dfrac{(\rho_2 - \rho_1)}{l} & -\dfrac{l}{2} \leq z \leq \dfrac{l}{2} \\ 0 & \text{otherwise.} \end{cases} \tag{6.30}$$

This density distribution is similar to that of the two-layer model except now the interface is no longer sharp but has a finite size l. The density changes linearly from ρ_1 to ρ_2 across the interface. The lowest mode ($n = 0$) gives a similar motion to the two-layer model while the higher modes give perturbations to the motion within the interfacial region l. To demon straight the difference between the two models

the Sturm-Liouville equation was solved [73] for $\lambda = 512$, $\rho_2 = 2\rho_1$, $g = 0.00015$, $a = 20\sqrt{3}/2$, $h_1 = h_2 = 108$ and $l = 5$. These are of a similar order to the values used later in the lattice Boltzmann simulations. The velocities and wave frequency were also calculated from equations (6.15) - (6.17) for the two-layer model. The z-velocity was found to be virtually the same at all depths for the two models. The x-velocity was also almost identical except in the interface region. The difference between the velocities predicted by the two models is shown in figure 6–1. The

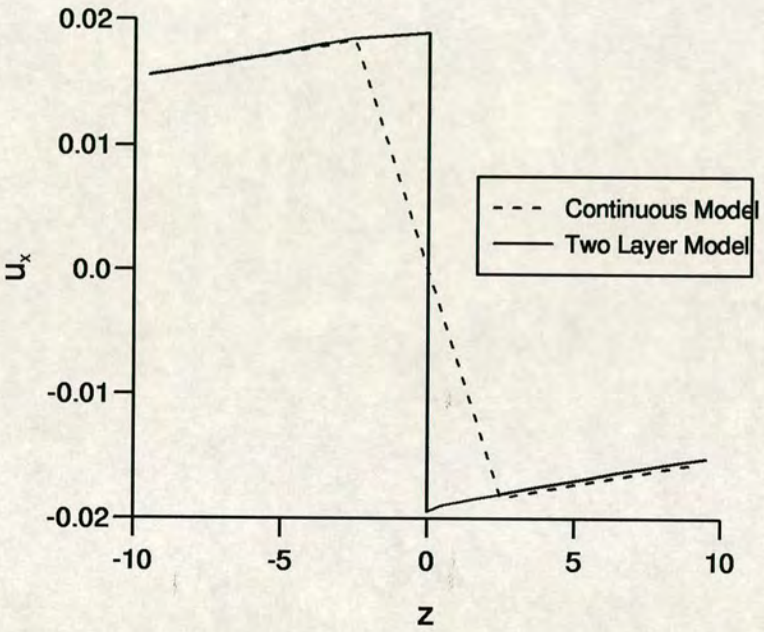

FIGURE 6–1: The x-velocity predicted by the two-layer model and the continuous model in the region of the interface.

values of the frequency ω_0, calculated for the two-layer model and the continuous model were 1.108×10^{-3} and 1.081×10^{-3} respectively, a difference of about 2.5%.

6.3 Waves in a Viscous Fluids

We now turn our attention to wave motion in a viscous fluid.

6.3.1 Frequency and Damping Parameter

Consider internal wave motion between two viscous fluids separated by a sharp interface. This can be considered [74] in a manner similar to the treatment of surface waves [75,76]. If the fluids are viscous then the equations of motion can be written:

$$\begin{aligned} \frac{\partial u}{\partial t} &= -\frac{1}{\rho}\frac{\partial p}{\partial x} + \nu\nabla^2 u, \\ \frac{\partial w}{\partial t} &= -\frac{1}{\rho}\frac{\partial p}{\partial z} + \nu\nabla^2 w, \\ \frac{\partial u}{\partial x} &+ \frac{\partial w}{\partial z} = 0. \end{aligned} \tag{6.31}$$

For the two-fluid system these have solutions [75,74]

$$\begin{aligned} u_i &= \frac{\partial \phi_i}{\partial x} + \frac{\partial \psi_i}{\partial z}, \\ u_i &= \frac{\partial \phi_i}{\partial x} - \frac{\partial \psi_i}{\partial z}, \end{aligned} \tag{6.32}$$

where

$$\begin{aligned} \phi_1 &= A_1 e^{-kz} e^{i(kx-\sigma t)} \quad & \phi_2 &= A_2 e^{kz} e^{i(kx-\sigma t)}, \\ \psi_1 &= H_1 e^{-m_1 z} e^{i(kx-\sigma t)} \quad & \psi_2 &= H_2 e^{m_2 z} e^{i(kx+\sigma t)} \end{aligned} \tag{6.33}$$

and

$$m_i^2 = k^2 + \frac{\sigma}{\nu_i} \tag{6.34}$$

where ν_i is the viscosity of fluid i, $i = 1, 2$. The boundary conditions at the interface are:

1. The continuity of the velocities across the interface

$$u_1|_{z=0} = u_2|_{z=0}, \quad w_1|_{z=0} = w_2|_{z=0}; \tag{6.35}$$

2. The continuity of stresses p_{xz} and p_{zz} across the interface

$$\left(\frac{(p_1)_{zz}}{\rho_1}\right)\Bigg|_{z=0} = \left(\frac{(p_2)_{zz}}{\rho_2}\right)\Bigg|_{z=0}, \quad \left(\frac{(p_1)_{xz}}{\rho_1\nu_1}\right)\Bigg|_{z=0} = \left(\frac{(p_2)_{zz}}{\rho_2\nu_2}\right)\Bigg|_{z=0}. \tag{6.36}$$

The stress terms are [75]

$$\frac{p_{zz}}{\rho} = -\frac{p}{\rho} + 2\nu\frac{\partial w}{\partial z}, \quad \frac{p_{xz}}{\rho\nu} = \left(\frac{\partial u}{\partial z} + \frac{\partial w}{\partial x}\right), \tag{6.37}$$

where p is given by the Bernoulli equation

$$\frac{p}{\rho} = -\frac{\partial\phi}{\partial t} - g\eta. \tag{6.38}$$

For an infinite fluid A_i and H_i can be eliminated by the interface boundary conditions to give the 'frequency' equation [74]

$$\sigma = \pm\left\{\left[\frac{gk(\rho_2-\rho_1)}{(\rho_2+\rho_1)}\right]^{\frac{1}{2}} - \left[\frac{gk(\rho_2-\rho_1)}{(\rho_2+\rho_1)}\right]^{\frac{1}{4}}\frac{\sqrt{2}k\rho_2\rho_1\sqrt{\nu_2\nu_1}}{(\rho_2+\rho_1)(\rho_2\sqrt{\nu_2}+\rho_1\sqrt{\nu_1})}\right\}$$

$$+i\left\{\left[\frac{gk(\rho_2-\rho_1)}{(\rho_2+\rho_1)}\right]^{\frac{1}{4}}\frac{\sqrt{2}k\rho_2\rho_1\sqrt{\nu_2\nu_1}}{(\rho_2+\rho_1)(\rho_2\sqrt{\nu_2}+\rho_1\sqrt{\nu_1})} + 2k^2\frac{\nu_2^2\rho_2^3+\nu_1^2\rho_1^3}{(\rho_2+\rho_1)(\rho_2\sqrt{\nu_2}+\rho_1\sqrt{\nu_1})^2}\right\}. \tag{6.39}$$

For a single fluid ($\rho_2 = 0, \nu_2 = 0$) this reduces to

$$\sigma = \pm\sqrt{(gk)} + 2i\nu_1k^2 \tag{6.40}$$

which is the expression for the frequency and the proportional damping of a surface wave [67]. Expressing σ in the form $\sigma = \pm(\omega_0 - \omega') - i\alpha$, where ω_0 is the frequency of an inviscid wave, and considering two fluids with the same viscosity

$$\nu_1 = \nu_2 = \nu \tag{6.41}$$

and with densities given by

$$\rho_1 = \rho, \quad \rho_2 = f\rho, \tag{6.42}$$

a series expansion, in terms of $\sqrt{\nu}$, can be made for σ [74]. To order $O(\nu)$ the solution is [74]

$$\omega' = (\omega_0)^{1/2}\frac{\sqrt{2}kf\sqrt{\nu}}{(1+f)^2} \tag{6.43}$$

and

$$\alpha = (\omega_0)^{1/2}\frac{\sqrt{2}kf\sqrt{\nu}}{(1+f)^2} + \frac{2k^2(1+f^3)\nu}{(1+f)^3}. \tag{6.44}$$

The interfacial disturbance is now given by

$$\eta = ae^{-\alpha t}e^{i(kx-\omega t)} \tag{6.45}$$

where $\omega = \omega_0 - \omega'$. Thus the frequency (and hence also the celerity $c = \omega/k$) is reduced by an amount ω' from the inviscid solution and the wave amplitude a is replaced by a decaying exponential: $a\exp(-\alpha t)$. In many situations ω' and α are small and of a similar size. In such situations the frequency is only altered slightly from its inviscid value however the damping term $\exp(-\alpha t)$ can produce a large effect when accumulated over large times. As noted by Harrison [74] his solution is an expansion in $\sqrt{\nu}$ correct to order $O(\nu)$ and also a series expansion in k correct to order $O(k^2)$. This solution is in agreement with the solution of Johns [77] which was found by considering separate solutions inside and outside the boundary layer, in a manner akin to the treatment of the velocities in section 6.3.2, and matching the two solutions. The solution of Johns [77] is only to first-order in $\sqrt{\nu}$.

6.3.2 Wave Velocities

The linearised Navier-Stokes equation permits the velocity to be split into a potential part, $\boldsymbol{u}_0 = \nabla\phi$, and a rotational part, $\boldsymbol{U} = (U, W)$ [78,79,77,80,81]. The solution for $\boldsymbol{u}_0$ is simply the inviscid solution which has already been given in equation (6.17). To find the rotational velocity we note [81,80] that provided

$$\epsilon_i = \frac{\omega^2}{g}\left(\frac{\nu_i}{\omega}\right)^{1/2} \tag{6.46}$$

is small in both fluids; the motion is essentially irrotational except near viscous boundary layers which are of thickness $(\nu_i/\omega)^{1/2}$ and which occur at solid boundaries and at the interface. Thus we look for solutions for $\boldsymbol{U}$ which satisfy the Navier-Stokes equation for the rotational part of the velocity,

$$\frac{\partial \boldsymbol{U}_i}{\partial t} = \nu_i\nabla^2\boldsymbol{U}_i, \tag{6.47}$$

and the appropriate boundary conditions. We only consider solutions which have a significant value in the boundary layer and a negligible value outside the boundary layer. Since we expect [79,80] that W_i will be an order of magnitude smaller then U_i we will solve for U_i, the component in the direction of wave propagation. The solution for W_i can then be found by integrating U_i [80]. Looking first at the area of the interface we consider solutions of the form [78,80]

$$\begin{aligned} U_1 &= C_1 \exp\left[-(1+i)\left(\frac{\sigma}{2\nu_1}\right)^{1/2} z\right] e^{i(kx-\sigma t)} \\ U_2 &= C_2 \exp\left[(1+i)\left(\frac{\sigma}{2\nu_2}\right)^{1/2} z\right] e^{i(kx-\sigma t)}. \end{aligned} \tag{6.48}$$

Now consider the boundary conditions at the interface

1. The conservation of horizontal velocity at the interface requires

$$\left(\frac{\partial \phi_1}{\partial x} + U_1 = \frac{\partial \phi_2}{\partial x} + U_2\right)\Bigg|_{z=0}. \tag{6.49}$$

2. Conservation of the stress p_{xz} across the interface requires

$$\left(\rho_1 \nu_1 \frac{\partial U_1}{\partial z} = \rho_2 \nu_2 \frac{\partial U_2}{\partial z}\right)\Bigg|_{z=0}. \tag{6.50}$$

Substituting the velocities, equation (6.48), into the boundary conditions, equations (6.49) and (6.50) gives

$$\begin{aligned} C_1 &= -f' \frac{ik(A_1 Z_1^0 - A_2 Z_2^0)}{1+f'}, \\ C_2 &= \frac{ik(A_1 Z_1^0 - A_2 Z_2^0)}{1+f'} \end{aligned} \tag{6.51}$$

where $Z_i^0 = Z_i(z)|_{z=0}$ and $f' = (\rho_2/\rho_1)(\nu_2/\nu_1)^{1/2}$.

Next consider the fluid adjacent to the solid boundaries. We look for solutions, for the rotational velocity close to the boundary layer, of the form [78,80]

$$U_1' = C_1' \exp\left[(1+i)\left(\frac{\sigma}{2\nu_1}\right)^{1/2}(z-h_1)\right] e^{i(kx-\sigma t)},$$
$$U_2' = C_2' \exp\left[-(1+i)\left(\frac{\sigma}{2\nu_2}\right)^{1/2}(z+h_2)\right] e^{i(kx-\sigma t)}. \tag{6.52}$$

Substituting these into the no-slip boundary condition

$$\left(\frac{\partial \phi_1}{\partial x} + U_1'\right)\Big|_{z=h_1} = 0,$$
$$\left(\frac{\partial \phi_2}{\partial x} + U_2'\right)\Big|_{z=-h_2} = 0 \tag{6.53}$$

gives the constants

$$C_1' = -ikA_1 Z_1^{h_1}, \qquad C_2' = -ikA_2 Z_2^{-h_2}. \tag{6.54}$$

The final solution for $\boldsymbol{u}$ can be found by summing all the horizontal velocity terms. In doing this we neglect α in terms $(\omega - i\alpha)$ except where it appears in an exponential multiplied by t, which can be large. This gives

$$u_1 = \frac{a\omega}{\sinh(kh)} e^{-\alpha t}\Big\{-\cosh[k(z-h)]\cos(kx-\omega t)$$
$$+\frac{2f}{(1+f)}\cosh(kh)\cos\left[kx-\omega t-\left(\tfrac{\omega}{2\nu}\right)^{\frac{1}{2}} z\right]\exp\left[-\left(\tfrac{\omega}{2\nu}\right)^{\frac{1}{2}} z\right] \tag{6.55}$$
$$+\cos[kx-\omega t+\left(\tfrac{\omega}{2\nu}\right)^{\frac{1}{2}}(z-h)\Big]\exp\left[\left(\tfrac{\omega}{2\nu}\right)^{\frac{1}{2}}(z-h)\right]\Big\}$$

and

$$u_2 = \frac{a\omega}{\sinh(kh)} e^{-\alpha t}\Big\{\cosh[k(z+h)]\cos(kx-\omega t)$$
$$-\frac{2}{(1+f)}\cosh(kh)\cos\left[kx-\omega t+\left(\tfrac{\omega}{2\nu}\right)^{\frac{1}{2}} z\right]\exp\left[\left(\tfrac{\omega}{2\nu}\right)^{\frac{1}{2}} z\right] \tag{6.56}$$
$$-\cos\left[kx-\omega t-\left(\tfrac{\omega}{2\nu}\right)^{\frac{1}{2}}(z+h)\right]\exp\left[-\left(\tfrac{\omega}{2\nu}\right)^{\frac{1}{2}}(z+h)\right]\Big\}$$

where we have set $h_1 = h_2 = h$ and $\nu_1 = \nu_2 = \nu$. Note that the total velocity can be taken as the sum of the three velocity terms, equations (6.17), (6.48) and

(6.52) since the rotational velocities must be negligible far from their respective boundary layers. The first term in both equation (6.55) and equation (6.56) is the inviscid solution and the second and third terms are the rotational corrections at the interface and the solid boundaries respectively. The vertical velocity can be found from the continuity equation and is

$$w_1 = -\int_{-h}^{0} \frac{\partial u_1}{\partial x} \mathrm{d}z - \int_{0}^{z} \frac{\partial u_1}{\partial x} \mathrm{d}z \tag{6.57}$$

and

$$w_2 = -\int_{-h}^{z} \frac{\partial u_1}{\partial x} \mathrm{d}z. \tag{6.58}$$

It can easily be seen that integrating the first term in equations (6.55) and (6.56) gives the inviscid solution w_0. The integral of the second and third terms are smaller than the original terms by a factor $k\sqrt{(2\nu/\omega)}$ and so give only a very small correction term. Figures 6–2 and 6–3 show the different components of the horizontal and vertical velocities for a wave with amplitude $20\sqrt{3}/2$, $\omega = 1 \times 10^{-3}$, $f = 1.4$, $\lambda = 256$ and $h_1 = h_2 = 128\sqrt{3}/2$. The solid line in figure 6–2 shows the irrotational velocity which has a discontinuity at $z = 0$ and is symmetric under a rotation of π about $(z = 0, u = 0)$. The magnitude of the irrotational velocity is maximum at $z = 0$. The dashed line is the sum of the irrotational velocity and the rotational component at the interface. This velocity distribution changes continuously from its smallest value slightly below $z = 0$ to its maximum value slightly above $z = 0$. In most of the boundary layer the rotational velocity has the opposite sign to the irrotational velocity and a smaller magnitude. Thus it has the effect of reducing the velocity from its inviscid value. At the outer region of the boundary layer, where the rotational component is small but not negligible, the sign of the rotational component is the same as the irrotational component and so the combined velocity is larger than the inviscid velocity. Further from the interface the rotational component becomes negligible and the solid and dashed lines appear to merge. The velocity represented by the dashed line is not symmetric about $(z = 0, u = 0)$. This is due to the ratio C_1/C_2 being f and not unity. The dotted line represents the final solution for the velocity incorporating the rotational components at the interface and the solid boundaries. It is coincidental with the dashed line except close to the solid boundaries at the top and bottom of the

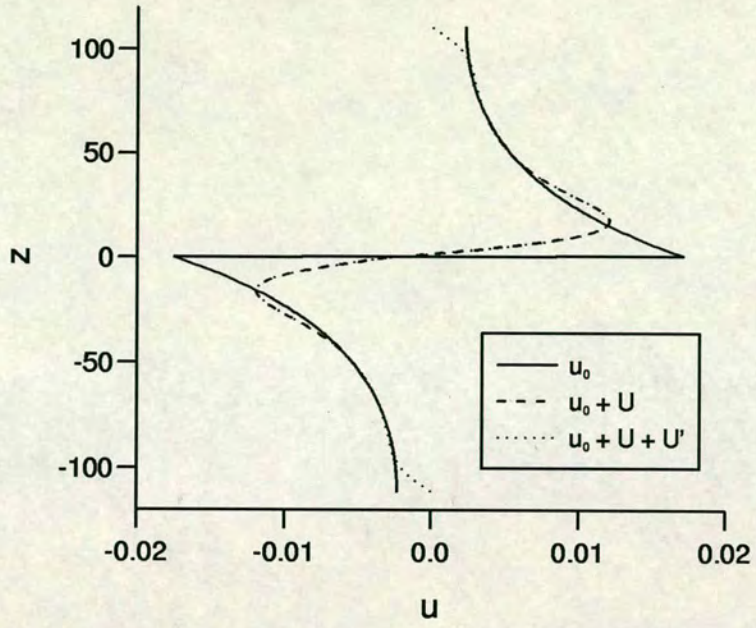

FIGURE 6–2: The irrotational horizontal velocity, u_0; the sum of the irrotational velocity and the rotational velocity from the interfacial boundary layer, $u_0 + U$; and the full solution for the horizontal velocity including the irrotational component at the solid boundary, U'. The velocities are calculate for an interfacial wave with amplitude $20\sqrt{3}/2, \omega = 1 \times 10^{-3}, f = 1.4, \lambda = 256$ and $h_1 = h_2 = 128\sqrt{3}/2$.

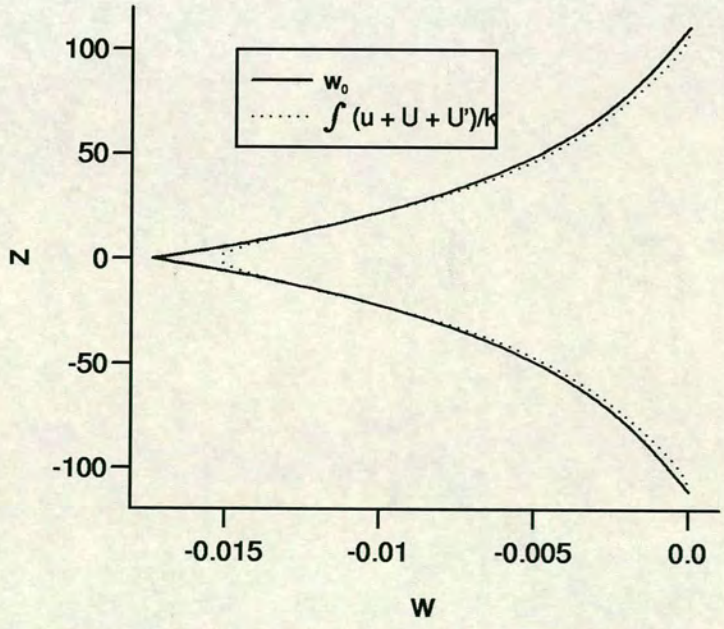

FIGURE 6–3: The irrotational vertical velocity w_0 and the full viscous solution. The velocities are calculate for an interfacial wave with amplitude $20\sqrt{3}/2, \omega = 1 \times 10^{-3}, f = 1.4, \lambda = 256$ and $h_1 = h_2 = 128\sqrt{3}/2$.

wave. Here, as with the rotational velocity at the interface, the sign of U' is opposite to the sign of u close to the boundary, where its magnitude is largest. In this region the rotational component acts to reduce the magnitude of the total velocity, reducing it to zero on the boundary where the two components have the same magnitude. Further from the boundary there is a region where the signs are the same and the rotational component adds to the magnitude of the horizontal velocity. The magnitude of the rotational component is small here and the effect is not as obvious in figure 6–2 as it is near the interface. This is because $|u_0|$ is increasing away from the solid boundary but it is decreasing away from the interface. There is much less difference between the inviscid vertical velocity and the viscous vertical velocity shown in figure 6–3. The main difference is near the interface where the magnitude of the velocity is maximum. The magnitude of the viscous solution is slightly smaller and slightly more rounded at $z = 0$.

6.4 Standing Waves

All the expressions above are for progressive waves travelling, with celerity $c = \omega/k$, in the positive x-direction. For each situation considered the real part of the interface has the form

$$\eta = \mathcal{A}(t)\cos(kx - \omega t) \tag{6.59}$$

and the velocity has the form (where we are now considering only the real part)

$$\begin{aligned} u &= \mathcal{A}(t)\mathcal{B}(z)\cos(kx - \omega t + \mathcal{D}z) \\ w &= \mathcal{A}(t)\mathcal{C}(z)\sin(kx - \omega t) \end{aligned} \tag{6.60}$$

where $\mathcal{A}, \mathcal{B}$ and $\mathcal{C}$ are also functions of the frequency and wavenumber and $\mathcal{D}$ may be zero. The corresponding expressions for a standing wave can be found by considering the superposition of two waves travelling in opposite directions with the same frequency and with half the amplitude ($\mathcal{A}(t)/2$). These two waves have

interfaces and velocities given by

$$\eta_a = \frac{\mathcal{A}(t)}{2}\cos(kx - \omega t) \qquad \eta_b = \frac{\mathcal{A}(t)}{2}\cos(kx + \omega t)$$

$$u_a = \frac{\mathcal{A}(t)\mathcal{B}(z)}{2}\cos(kx - \omega t + \mathcal{D}z) \quad u_b = -\frac{\mathcal{A}(t)\mathcal{B}(z)}{2}\cos(kx + \omega t + \mathcal{D}z) \tag{6.61}$$

$$w_a = \frac{\mathcal{A}(t)\mathcal{C}(z)}{2}\sin(kx - \omega t) \qquad w_b = \frac{\mathcal{A}(t)\mathcal{C}(z)}{2}\sin(kx + \omega t).$$

The interface η_s and the velocities u_s and w_s of the corresponding standing wave are the sum of the two progressive waves:

$$\eta_s = \mathcal{A}\cos(kx)\cos(\omega t)$$

$$u_s = \mathcal{A}\mathcal{B}\sin(kx + \mathcal{D})\sin(\omega t) \tag{6.62}$$

$$w_s = \mathcal{A}\mathcal{C}\cos(kx)\sin(\omega t).$$

Thus if a progressive wave is damped at a rate α: $\mathcal{A} = ae^{-\alpha t}$ then a standing wave will be damped at the same rate. The ratio of the interface amplitude to the amplitudes of the horizontal and vertical velocities, $\mathcal{B}$ and $\mathcal{C}$ respectively, are the same for progressive and standing waves as is the frequency. The x and t dependence are different.

6.5 Summary

The theoretical expressions describing the velocity, frequency and damping parameter in terms of the wavelength, the interface width and the fluid depths have been presented. This has been done for an inviscid two-layer fluid, an inviscid fluid with a constantly changing density and a viscous two-layer fluid.

Chapter 7

Interfacial Standing Wave Simulations

It has been seen in chapters 4 and 5 that a lattice Boltzmann model can be used to simulate two immiscible binary fluids and that a gravitational interaction can be introduced into the lattice Boltzmann scheme. It has been shown that the immiscible, binary fluid model of Orlandini *et al.* [9] is isotropic and that the gravitational interactions are independent of the grid orientation. The combination of the two is, at worst, very close to Galilean invariant for the correct choice of τ_Δ. This model is therefore suitable for modelling interfacial waves.

7.1 The density Gradient, the Potential Density, the Relative Density and the Gravitational Strength

In chapter 4 the fluid density was defined $\rho = \sum_i f_i$. In chapter 5 gravity was applied and the density became a function of depth, The gradient $\partial\rho/\partial z$ was found to be proportional to the gravitational strength g_i in fluid i. This density gradient it produced solely by gravity so the potential density ρ_{pot} is constant in each fluid. In chapter 6 the equations describing interfacial wave motion were in terms of f, the ratio of the potential densities. If we consider two fluids with

the same density, $\rho_1 = \rho_2 = \rho$, and apply gravity to fluid 1 with strength g_1 and to fluid 2 with strength g_2, then the ratio of the body forces, $\rho_1 g_1 / \rho_2 g_2$, is g_1/g_2. This is the same as the ratio for two fluids with densities ρ_1 and $\rho_2 = (g_2/g_1)\rho_1$ when gravity act equally, with strength g, in each. Thus when we apply gravity with strength g_1 in fluid 1 and g_2 in fluid 2 it is equivalent to simulating two fluids with relative densities g_2/g_1 in a constant gravitational field. When the interface occurs close to the centre of the grid g is taken to be $(g_1 + g_2)/2$.

7.2 Standing Wave Initialisation

The ability of the model to simulate interfacial waves was investigated using standing waves. These were initialised on grids with the same number of grid points in the horizontal and vertical directions, the grid being orientated as shown in figure 3–3. The grid was initialised with $\rho = 1.0$ and divided into two by a horizontal line near the centre. The line was either taken to be at the centre of the grid or, when a large gravitational force was being applied, near the centre with the bottom section slightly larger than the top. The order parameter $\Delta\rho$ was set to +0.5 above the line and to -0.5 below the line. A solid boundary was set at the bottom and top of the fluid and continuous boundary conditions applied at the other edges. The boundary conditions were applied at the solid boundary using the boundary conditions of Noble *et al.* [51] discussed in section 4.3.2. The fluid was then allowed to evolve with $\tau_\rho = 200.0$ for 8,000 time-steps. This allows the fluids to reach an equilibrium state where the density gradient in each fluid is established. The height of the interface between the two fluids was then found, this is the mean water level (mwl). A sinusoidal interface was enforced between the fluids about the previous interface, as shown in figure 7–1, and the sign of $\Delta\rho$ was switched in regions A and B. The coordinate system is also shown in figure 7–1. The sinusoidal interface has a wavelength equal to the length of the grid and an amplitude of $20\sqrt{3}/2$. Using this initialisation method the density gradients are set correctly and any initial y-velocity, produced by the creation of these gradients, has been damped, by the high viscosity, to a negligible magnitude. The shape of

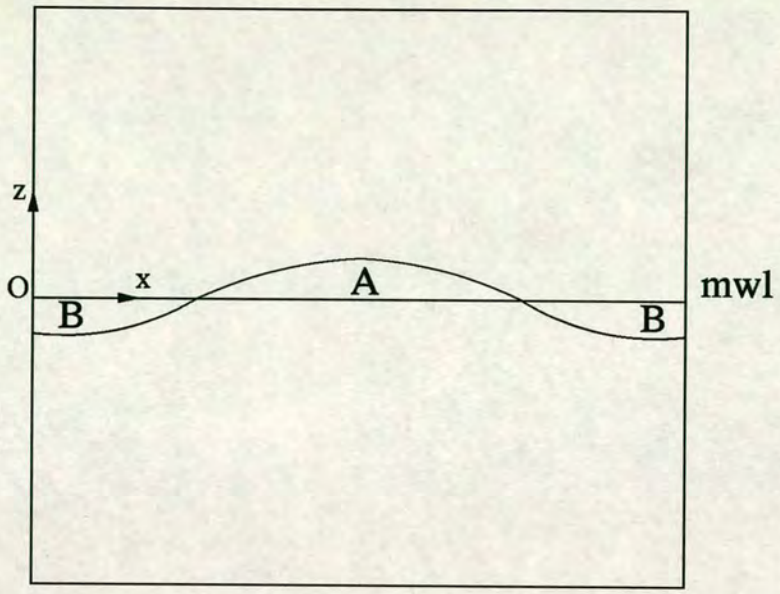

FIGURE 7–1: The Initialisation of a Standing Wave

the interface in the horizontal direction is sharp with width one grid space. The form of the interface changes to the expected shape, shown in figures 4–5 and 4–6, within a few time steps. There is also a slight reduction in the density around the wml mark of less than 1% which is only detectable for the first few time-steps after initialisation. For a square l by l grid with the mwl directly in the middle $\lambda = l$ and $h_1 = h_2 = \sqrt{3}l/4$. Thus $\tanh(kh_1) = \tanh(kh_2) = 0.99$ and so the wave can be considered as being in deep water [67].

7.3 Standing Wave Simulations

A velocity map and the position of the interface, seen through the value of the order parameter, is shown at times $t \simeq iT/8$, $i = 1, 2, ..., 7$ in figures 7–2 – 7–15 for a typical interfacial wave on a 256 by 256 grid with $g_1 = 2.5 \times 10^{-4}$, $g_2 = 3.5 \times 10^{-4}$, $\kappa = 0.001$, $\lambda = 256$ and $\nu = 0.05$. The interface is seen to be sharp since the interfacial energy κ is set to 0.001. Comparing, for example, the velocity and interface at $t \simeq T/8$, figures 7–2 and 7–3, with those at $t \simeq 7T/8$, figures 7–14 and 7–15, it is obvious that the wave is being damped at a considerable rate. The

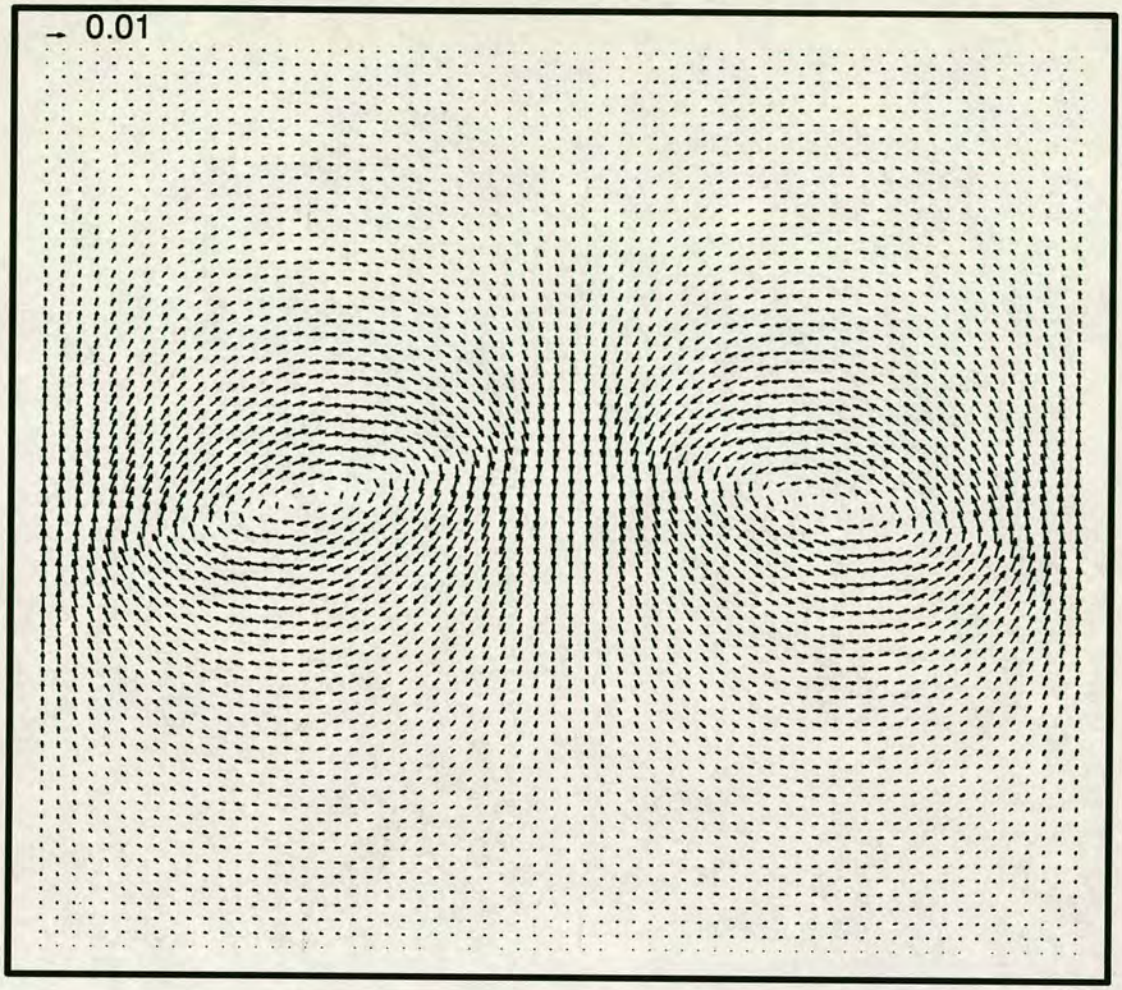

FIGURE 7–2: Velocity vector plot at $t \simeq T/8$ of an interfacial standing wave on a 256 by 256 grid with $g_1 = 2.5 \times 10^{-4}$, $g_2 = 3.5 \times 10^{-4}$, $\kappa = 0.001$, $\lambda = 256$ and $\nu = 0.05$.

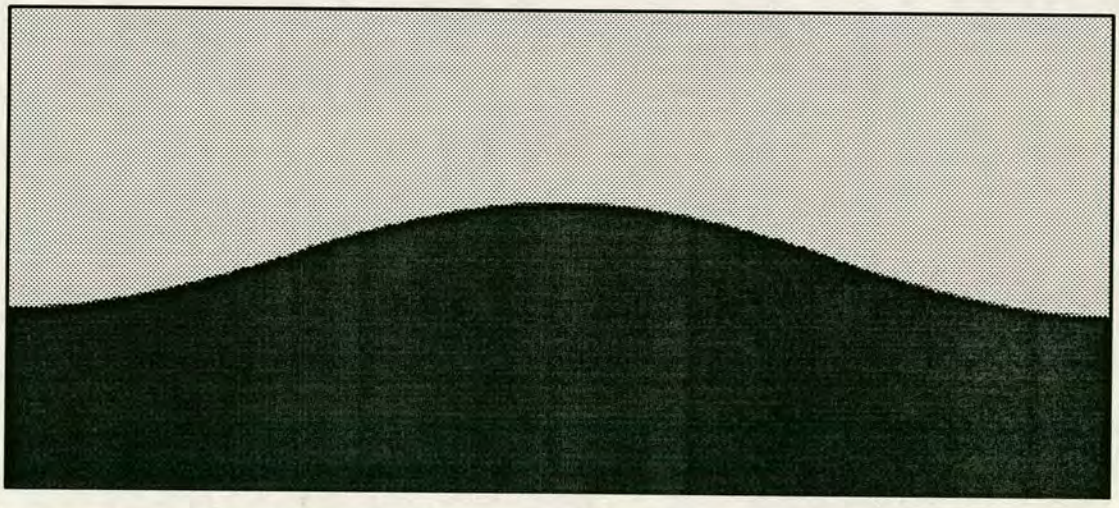

FIGURE 7–3: The order parameter at $t \simeq T/8$ of an interfacial standing wave on a 256 by 256 grid with $g_1 = 2.5 \times 10^{-4}$, $g_2 = 3.5 \times 10^{-4}$, $\kappa = 0.001$, $\lambda = 256$ and $\nu = 0.05$. Only halve the grid, centred on the interface, is shown.

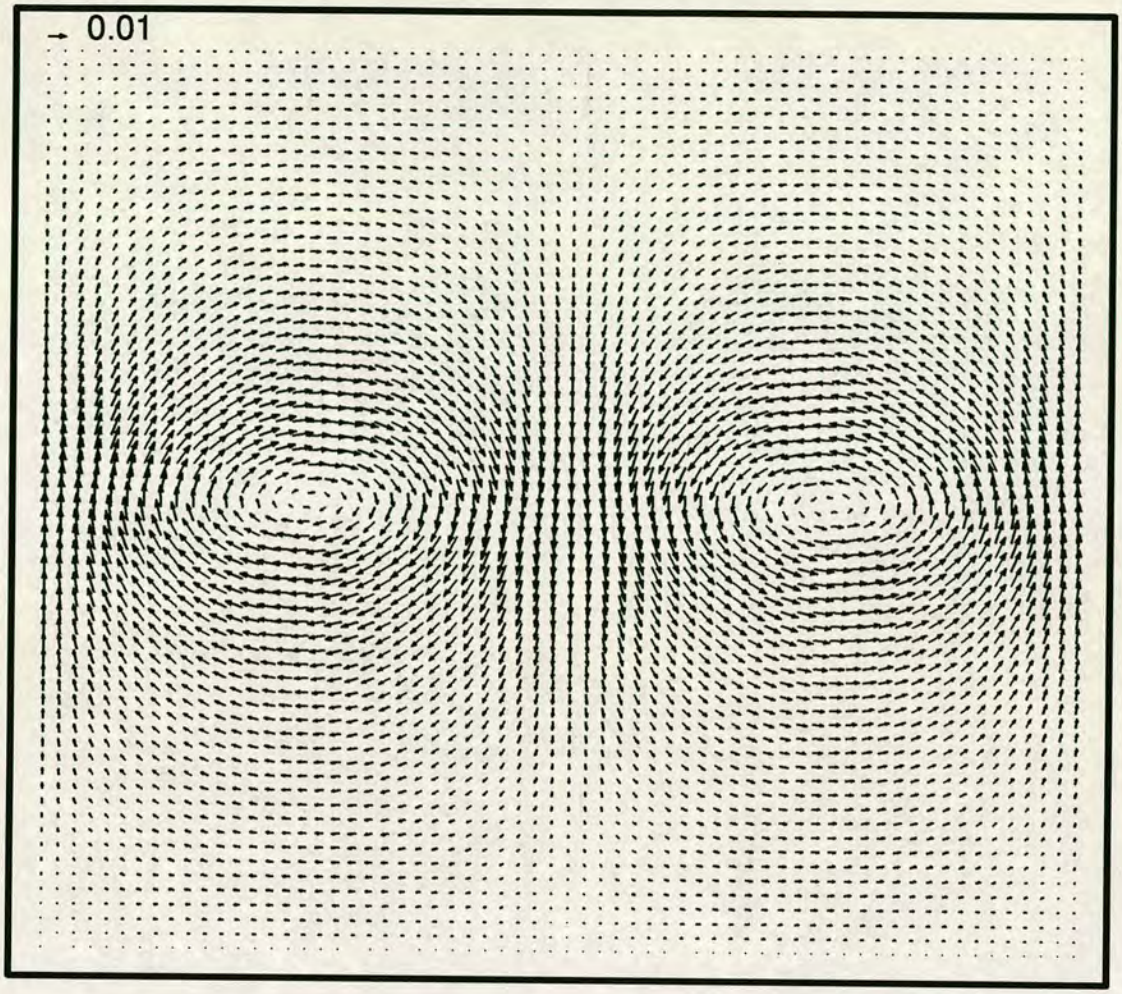

FIGURE 7–4: Velocity vector plot at $t \simeq 2T/8$ of an interfacial standing wave on a 256 by 256 grid with $g_1 = 2.5 \times 10^{-4}$, $g_2 = 3.5 \times 10^{-4}$, $\kappa = 0.001$, $\lambda = 256$ and $\nu = 0.05$.

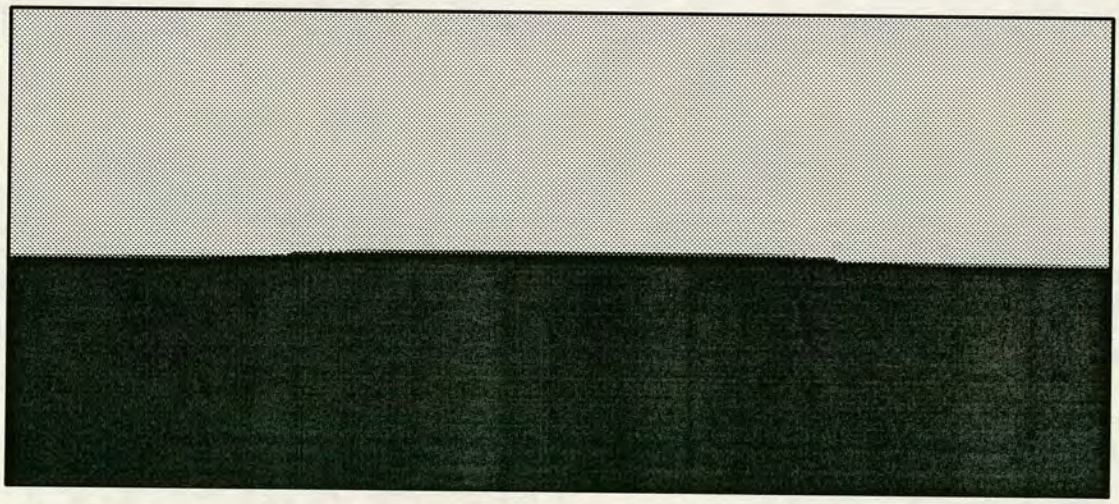

FIGURE 7–5: The order parameter at $t \simeq 2T/8$ of an interfacial standing wave on a 256 by 256 grid with $g_1 = 2.5 \times 10^{-4}$, $g_2 = 3.5 \times 10^{-4}$, $\kappa = 0.001$, $\lambda = 256$ and $\nu = 0.05$. Only halve the grid, centred on the interface, is shown.

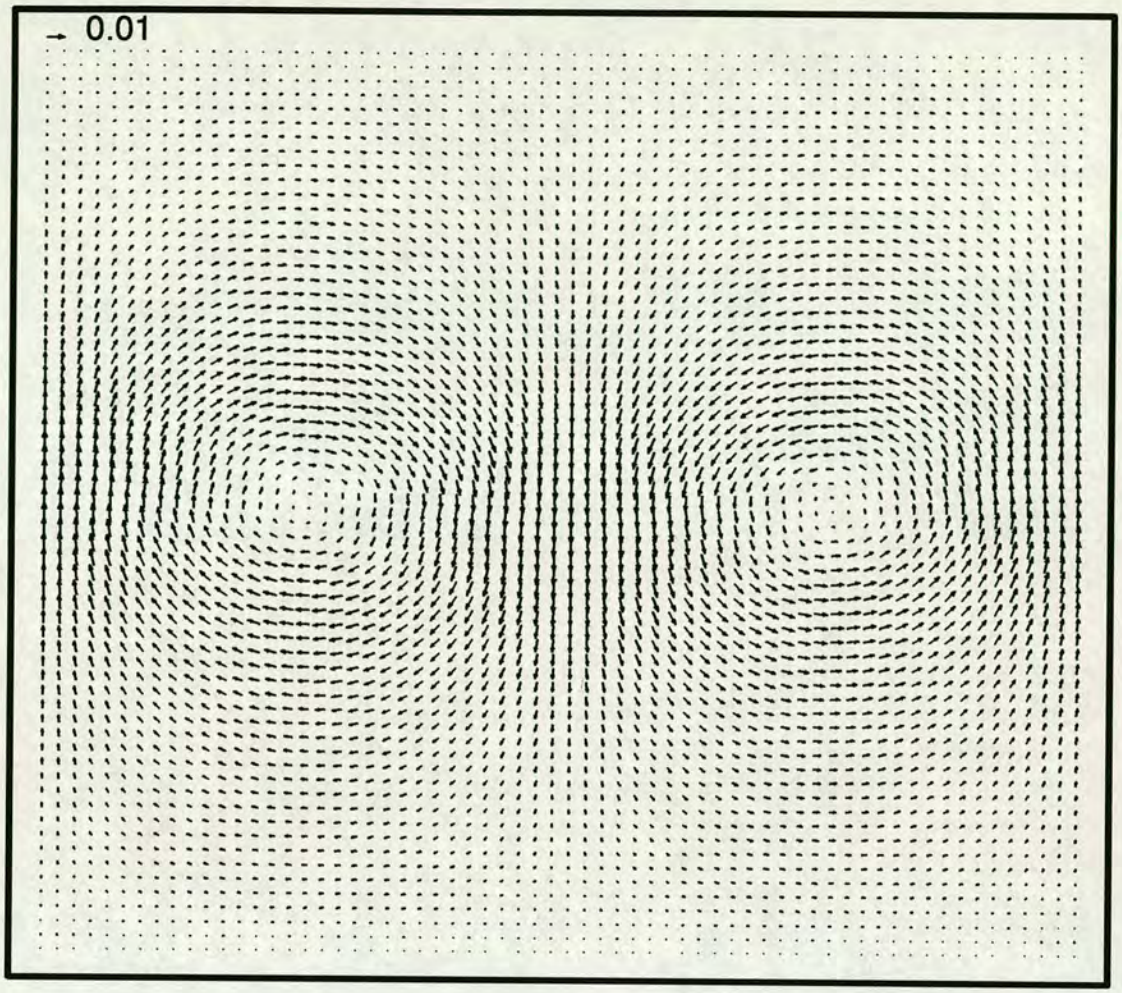

FIGURE 7–6: Velocity vector plot at $t \simeq 3T/8$ of an interfacial standing wave on a 256 by 256 grid with $g_1 = 2.5 \times 10^{-4}$, $g_2 = 3.5 \times 10^{-4}$, $\kappa = 0.001$, $\lambda = 256$ and $\nu = 0.05$.

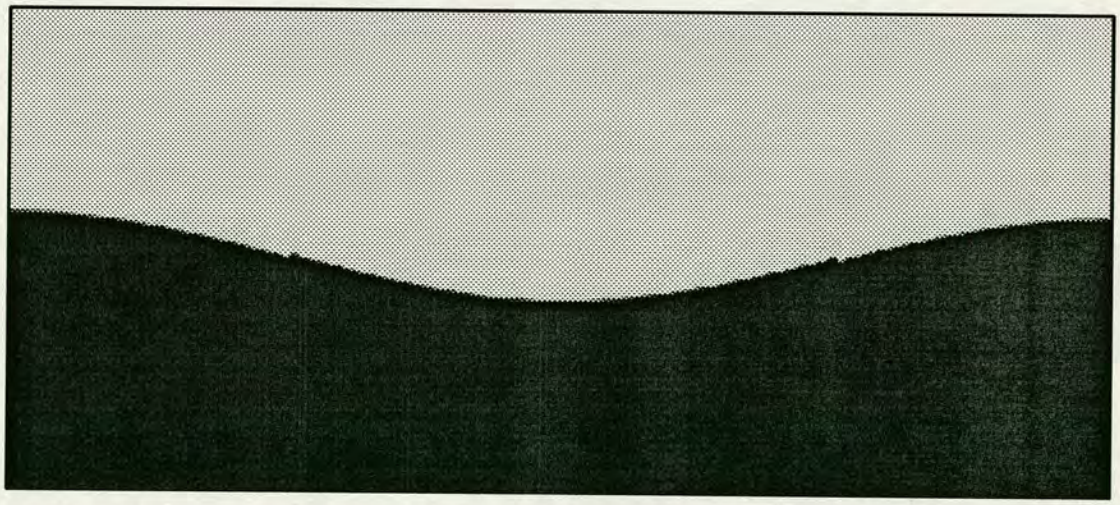

FIGURE 7–7: The order parameter at $t \simeq 3T/8$ of an interfacial standing wave on a 256 by 256 grid with $g_1 = 2.5 \times 10^{-4}$, $g_2 = 3.5 \times 10^{-4}$, $\kappa = 0.001$, $\lambda = 256$ and $\nu = 0.05$. Only halve the grid, centred on the interface, is shown.

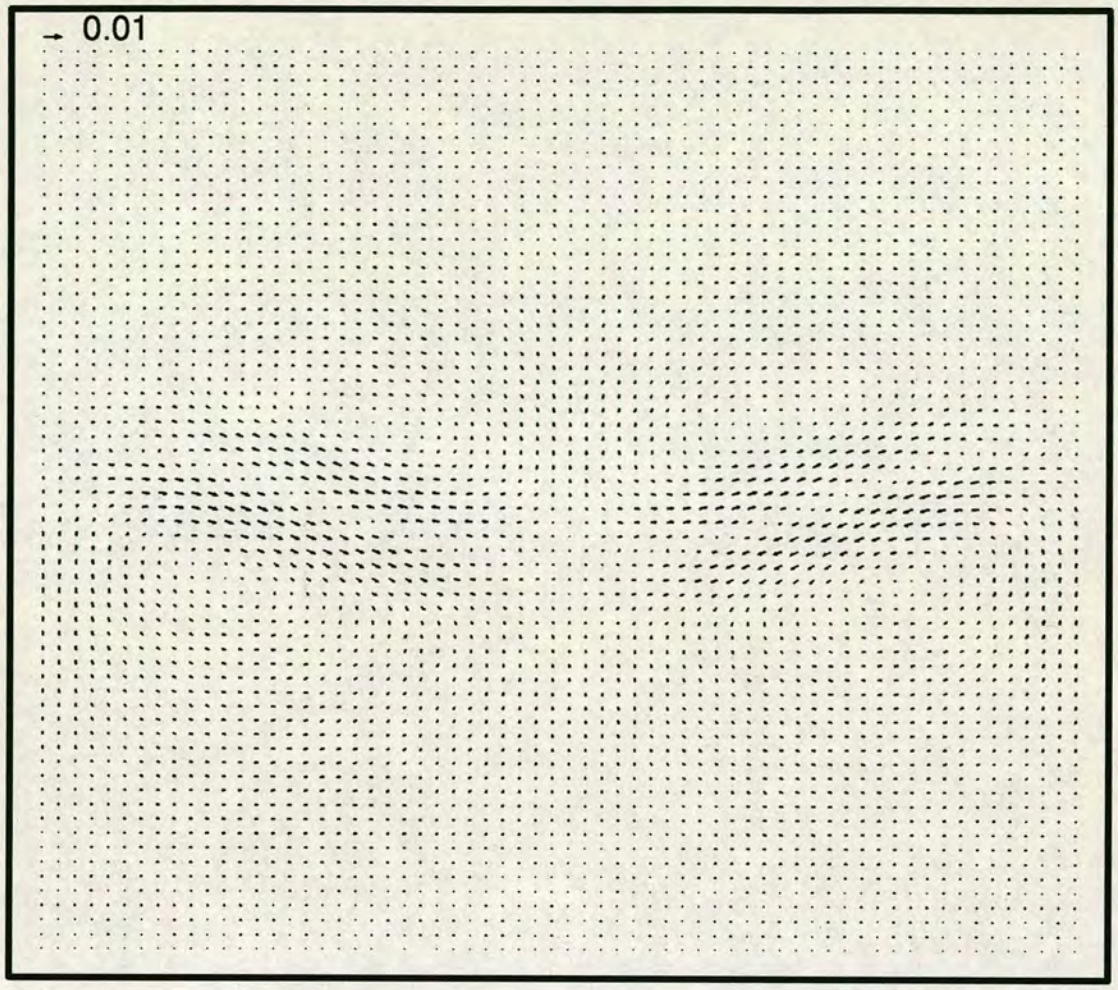

FIGURE 7–8: Velocity vector plot at $t \simeq 4T/8$ of an interfacial standing wave on a 256 by 256 grid with $g_1 = 2.5 \times 10^{-4}$, $g_2 = 3.5 \times 10^{-4}$, $\kappa = 0.001$, $\lambda = 256$ and $\nu = 0.05$.

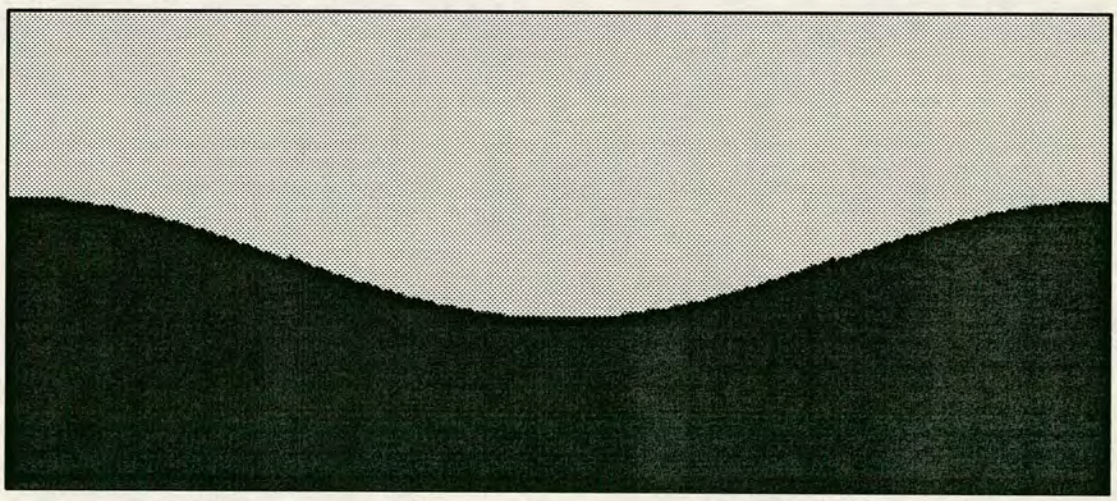

FIGURE 7–9: The order parameter at $t \simeq 4T/8$ of an interfacial standing wave on a 256 by 256 grid with $g_1 = 2.5 \times 10^{-4}$, $g_2 = 3.5 \times 10^{-4}$, $\kappa = 0.001$, $\lambda = 256$ and $\nu = 0.05$. Only halve the grid, centred on the interface, is shown.

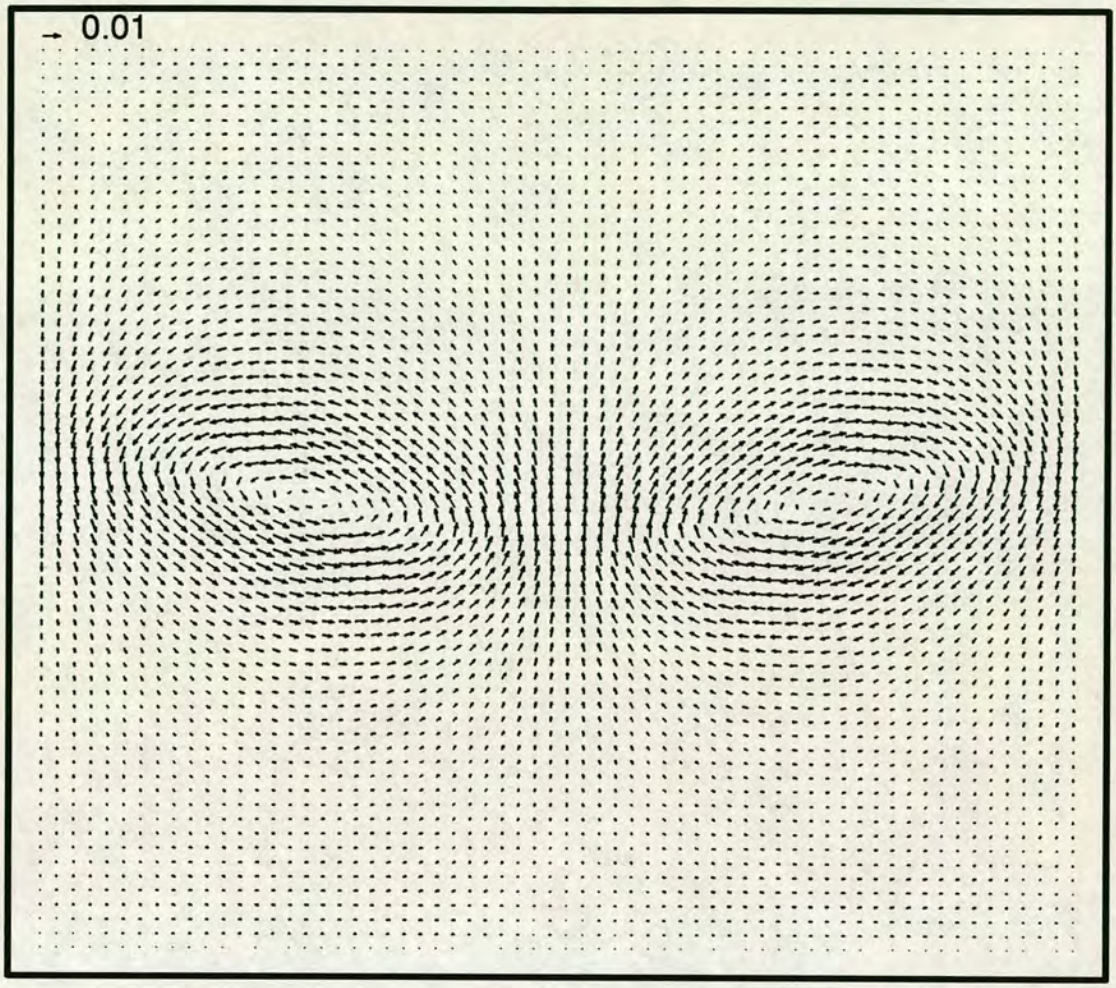

FIGURE 7–10: Velocity vector plot at $t \simeq 5T/8$ of an interfacial standing wave on a 256 by 256 grid with $g_1 = 2.5 \times 10^{-4}$, $g_2 = 3.5 \times 10^{-4}$, $\kappa = 0.001$, $\lambda = 256$ and $\nu = 0.05$.

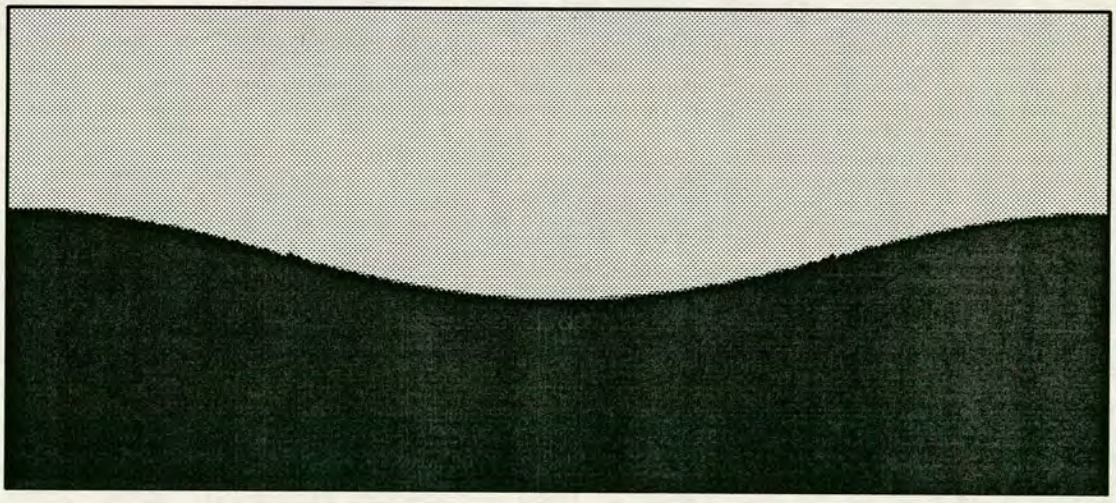

FIGURE 7–11: The order parameter at $t \simeq 5T/8$ of an interfacial standing wave on a 256 by 256 grid with $g_1 = 2.5 \times 10^{-4}$, $g_2 = 3.5 \times 10^{-4}$, $\kappa = 0.001$, $\lambda = 256$ and $\nu = 0.05$. Only halve the grid, centred on the interface, is shown.

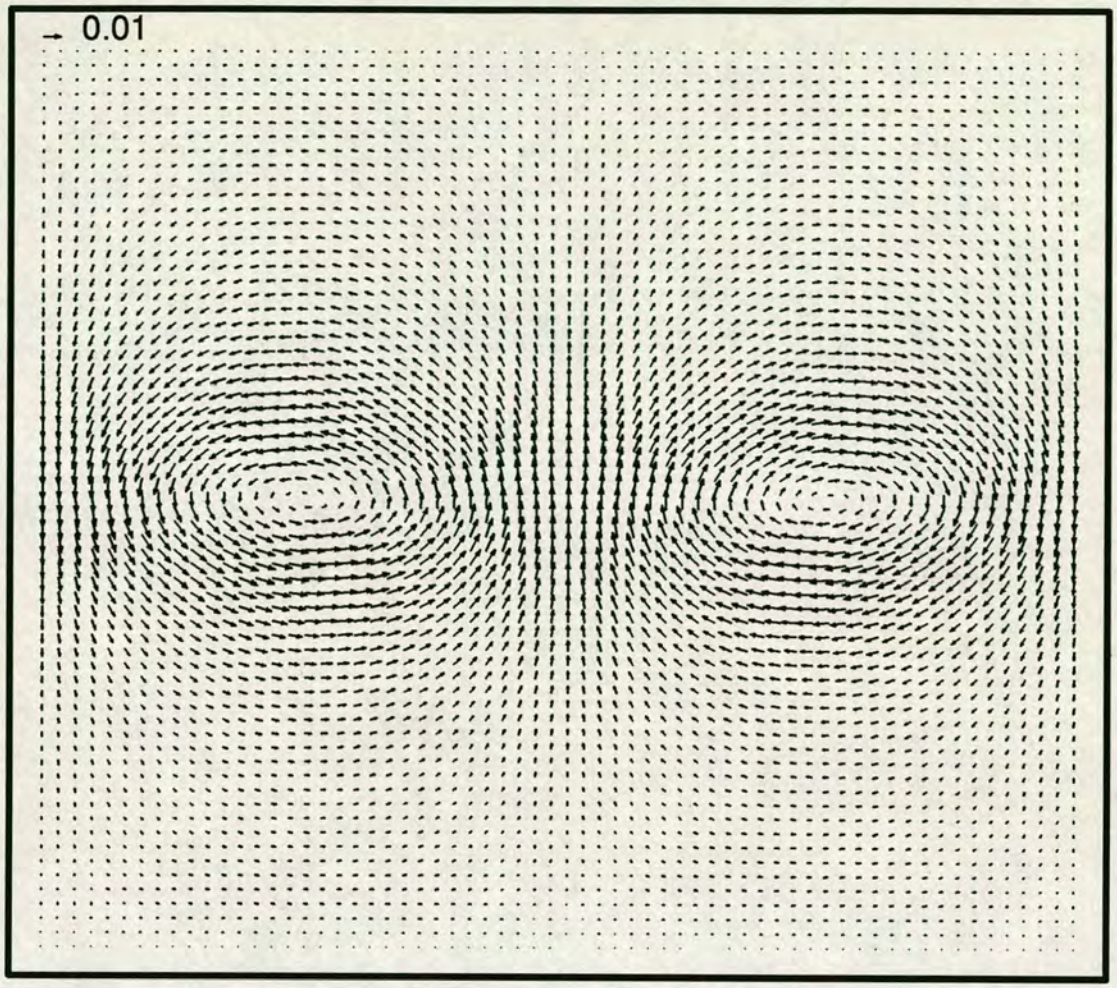

FIGURE 7–12: Velocity vector plot at $t \simeq 6T/8$ of an interfacial standing wave on a 256 by 256 grid with $g_1 = 2.5 \times 10^{-4}$, $g_2 = 3.5 \times 10^{-4}$, $\kappa = 0.001$, $\lambda = 256$ and $\nu = 0.05$.

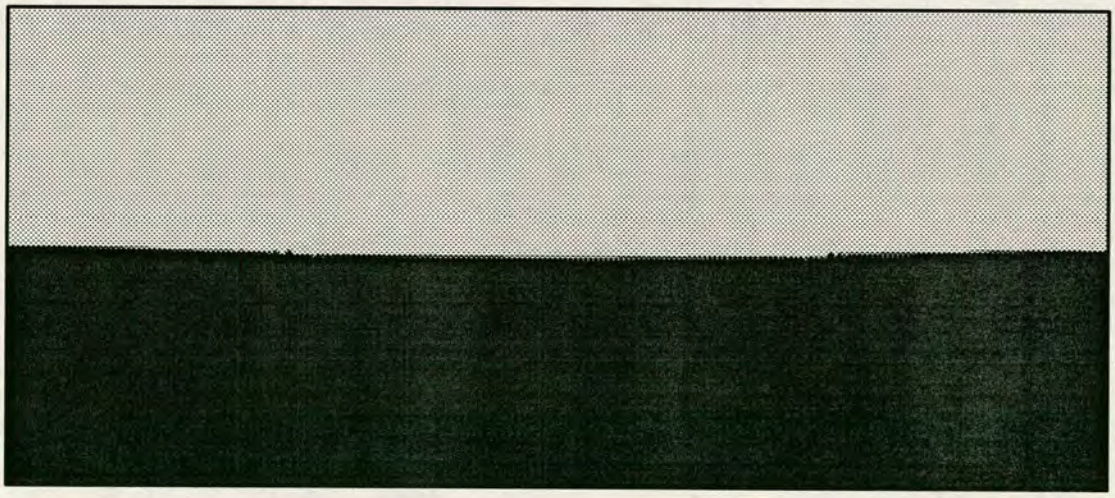

FIGURE 7–13: The order parameter at $t \simeq 6T/8$ of an interfacial standing wave on a 256 by 256 grid with $g_1 = 2.5 \times 10^{-4}$, $g_2 = 3.5 \times 10^{-4}$, $\kappa = 0.001$, $\lambda = 256$ and $\nu = 0.05$. Only halve the grid, centred on the interface, is shown.

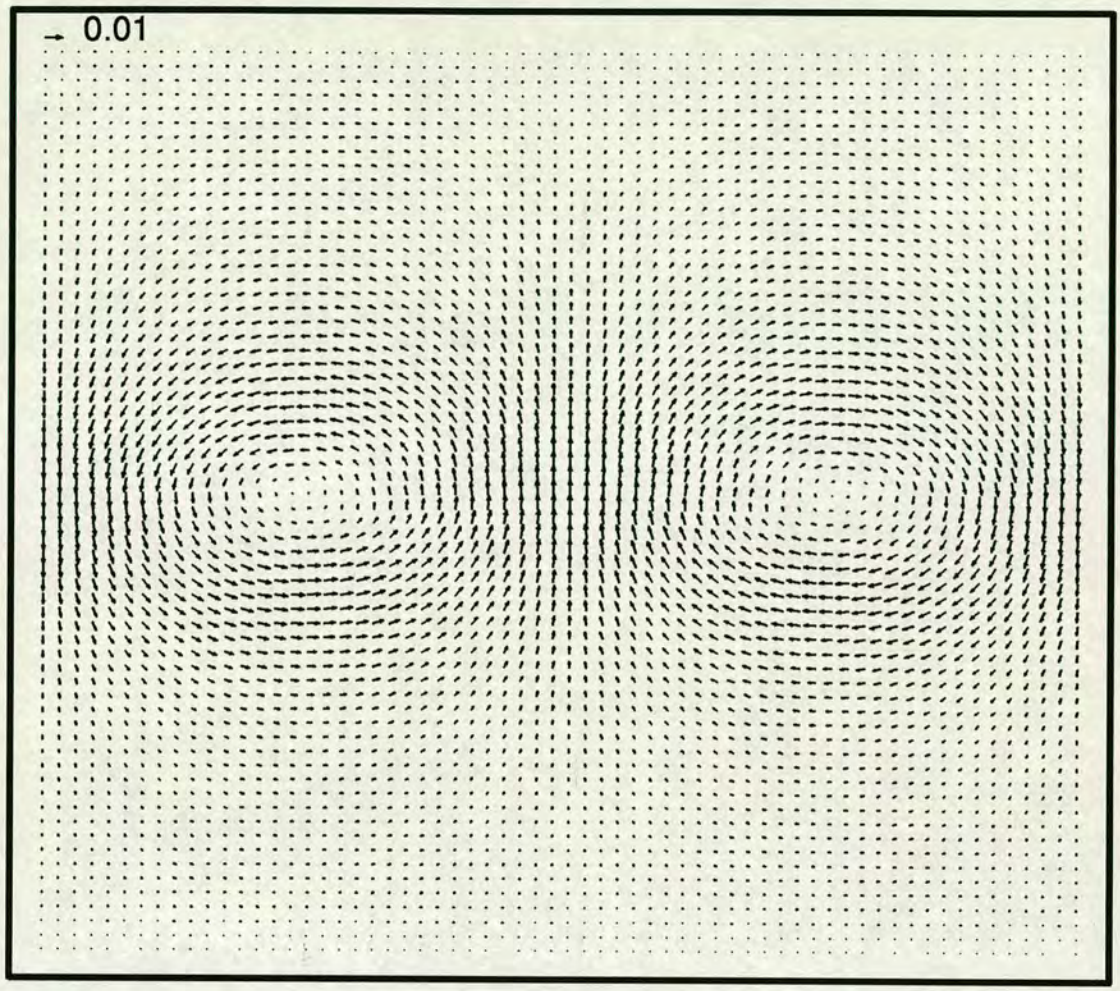

FIGURE 7–14: Velocity vector plot at $t \simeq 7T/8$ of an interfacial standing wave on a 256 by 256 grid with $g_1 = 2.5 \times 10^{-4}$, $g_2 = 3.5 \times 10^{-4}$, $\kappa = 0.001$, $\lambda = 256$ and $\nu = 0.05$.

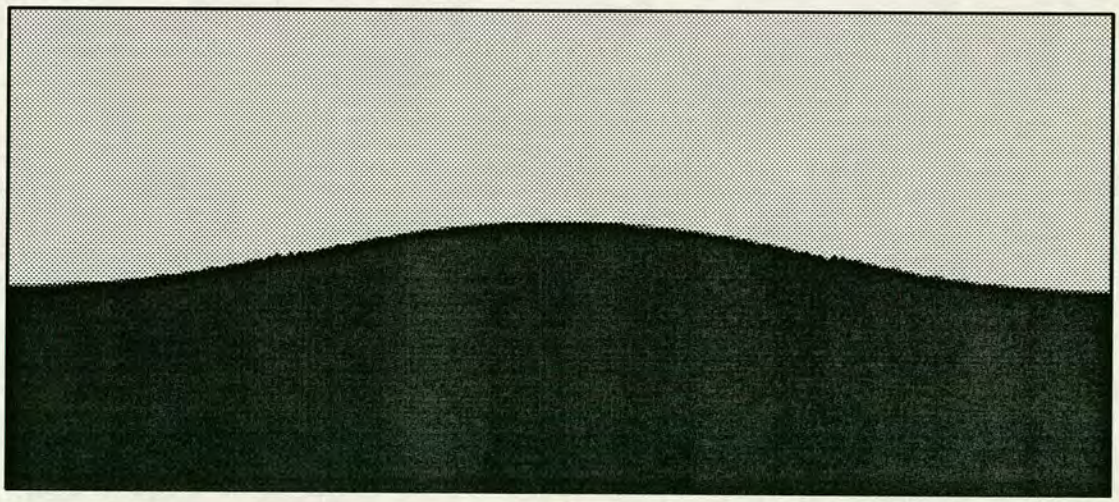

FIGURE 7–15: The order parameter at $t \simeq 7T/8$ of an interfacial standing wave on a 256 by 256 grid with $g_1 = 2.5 \times 10^{-4}$, $g_2 = 3.5 \times 10^{-4}$, $\kappa = 0.001$, $\lambda = 256$ and $\nu = 0.05$. Only halve the grid, centred on the interface, is shown.

wave velocities, the wave frequency and the damping rate will be examined in more detail in the rest of this chapter.

7.4 The Wave Period and the Damping Parameter

In this section we consider the period and damping parameter of the simulated waves. Their measurement is considered and they are compared with the theoretical expressions in chapter 6.

7.4.1 The Curve Fitting Process

During the simulations the height of the interface, above the bottom boundary, was found every forty time-steps at the centre of the wave, $x = \lambda/2$. The height of the wave was taken to be the height of the highest site containing the denser fluid. This gives a time series record of the wave height at the centre which was then fitted to a curve of the form

$$Ae^{-\alpha t}\cos(\omega t + \psi) + c. \tag{7.1}$$

This was done using a modified Gauss-Newton algorithm [82,83] where the parameters A, α, ω, ψ and c are the parameters found by the fitting process. The sum of the square of the deviation of the data from the fitted curve, e, was also computed and this gives a measure of the accuracy of the cure fitting process and the fitted parameters. The two parameters in which we are interested are the frequency ω and the damping parameter α. The fitted parameter c should correspond to the mwl h_2 which was used in initialising the wave. In practice it is shifted slightly, particularly when κ is large and the interface has a significant thickness. The curve fitting process was applied using an equation of the form

$$Ae^{-\alpha t}\cos(\omega t + \psi) + h_2. \tag{7.2}$$

where h_2 is fixed and the other parameters are found as before. The results obtained for ω and α were found to be within 1% of their previous values. The value of e was increased by $\sim N|h - c|$, where N is the number of points. This means that e is no longer a good measure of the goodness of fit of the other parameters. Thus it was decided to include c in the set of fitted parameters. Similarly the value of A should be related to the initial deformation amplitude. It is, however, slightly different, again due to the interface thickness. If A is fixed, in equation (7.1), to an incorrect value there is little effect on ω but a significant effect on α. If A is set too large the value found for α can be seen to be too large, the values of the fitted curve being greater then the data points for small times and smaller than the data points for large times. If A is set too small the value of α is correspondingly too small. Thus it is important that A has the correct value and this is best achieved by allowing it to be found by the fitting routine. A phase difference ψ is also included in equation (7.1). This accounts for any discrepancy in the initialisation procedure. The main error in the initialisation is the profile of the density and the order parameter at the interface. The values found for ψ were no larger then 1% of 2π suggesting that the initialisation method is adequate. The average value found for e from over a hundred different waves, each with either 1,000 or 900 data points, was found to be 85. This corresponds to an RMS difference between the data and the fitted curve of 0.31 lattice units.

The Contribution to e from the Discrete Lattice

To asses the size of this error the values of the curve in equation (7.1) were calculated, using the typical parameters: $A = 20\sqrt{3}/2$, $\alpha = 5 \times 10^{-5}$, $\omega = 2\pi/6000$, $\psi = 0$ and $c = 128$, at times $t_i = 40i$, $i = 1, 2, ..., 1000$. The sum of the square of the difference between these 1000 values and their nearest integer value was then calculated and found to be 60.2. This is the value of e produced solely by the spatially discrete nature of the model. The values of e obtained from the curve fitting process are not significantly larger suggesting that equation (7.1) correctly describes the interface and that the fitted parameters are reasonably accurate.

Relating the Error Parameter to an Error in the Fitted Parameters

To investigate how a small error in ω or α will affect the error parameter e, the values of the curve at each of the 1000 times calculated above was compared to the value calculated when either ω or α was varied by a small amount. The sum of the square of these differences, e, was calculated and is shown plotted against the percentage variation in either ω or α in figure 7–16. Thus the difference between

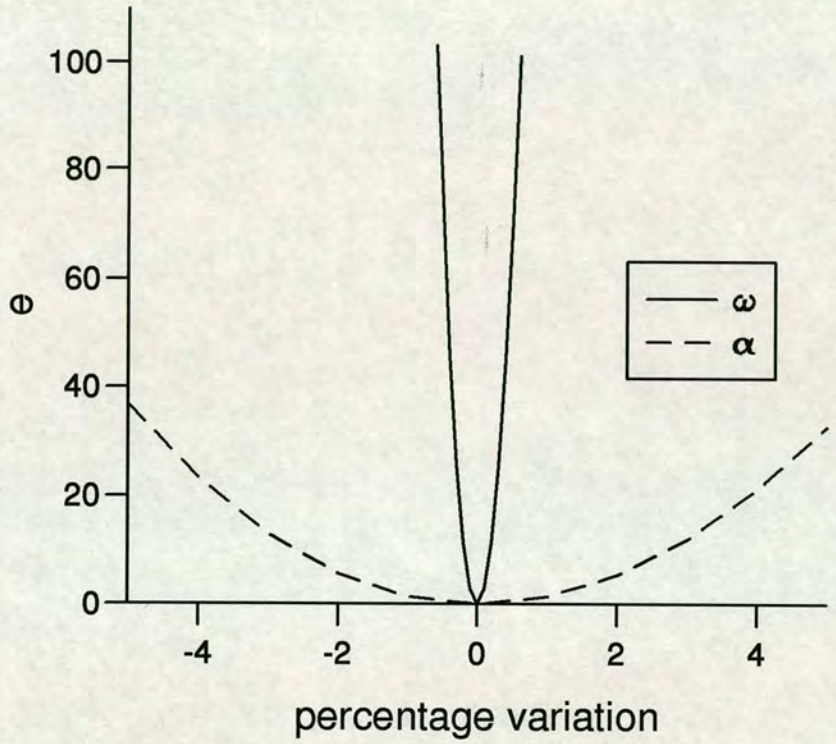

FIGURE 7–16: The sum of the square of the deviation between two curves of the form of equation (7.1) when the value of either ω or α has been varied, in one of the curves, by a small percentage from $2\pi/6000$ and 5×10^{-5} respectively. The sum is over 1000 different values taken at times $t = 40i$, $i = 1, 2, ..., 1000$. The values of the other parameters used are $A = 20\sqrt{3}/2, \psi = \pi$ and $c = 128$.

the average value of e found from curve fitting, 85, and the expected value of 60, due to the discrete nature of the grid, corresponds to an error in ω of about 0.3% or an error in α of about 4%.

Curve Fitting Results

A typical set of results is shown in figure 7–17 where only every tenth result has

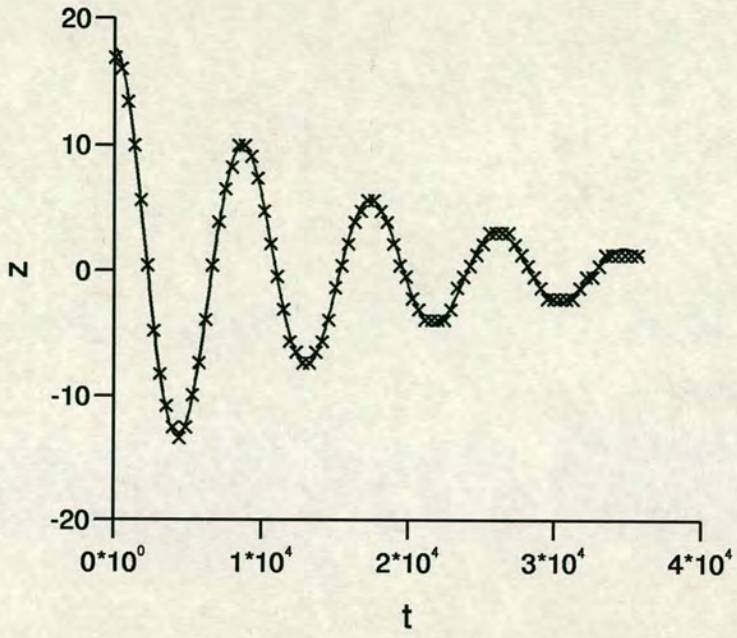

FIGURE 7–17: The wave's height, at $x = \lambda/2$, as a function of time for a standing wave with $\lambda = 256, \nu = 0.05, g_1 = 1.25 \times 10^{-4}$ and $g_2 = 1.75 \times 10^{-4}$. Only points every 400 time-steps have been marked. Also shown is the best fit curve through all the data points. This has the forms of equation (7.1) with $A = 17.7, \alpha = 6.52 \times 10^{-5}, \omega = 7.49 \times 10^{-4}, \psi = 3.14$ and $c = 110$.

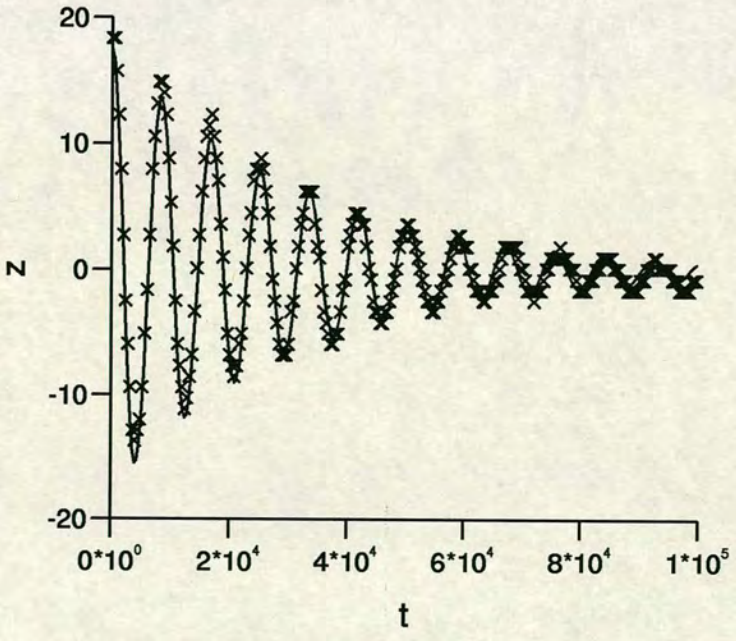

FIGURE 7–18: The wave's height, at its centre, as $x = \lambda/2$ of time for a standing wave with $\lambda = 512, \nu = 0.05, g_1 = 2.5 \times 10^{-4}$ and $g_2 = 3.5 \times 10^{-4}$. Only points every 400 time-steps have been marked. Also shown is the best fit curve through all the data points. This has the forms of equation (7.1) with $A = 17.6, \alpha = 3.22 \times 10^{-5}, \omega = 7.23 \times 10^{-4}, \psi = 3.07$ and $c = 237$.

been plotted. The wave was simulated using $g_1 = 1.25\times10^{-4}$, $g_2 = 1.75\times10^{-4}$, $\nu = 0.05$ and $\lambda = 256$. The best fit curve through all the data points is also shown. The close agreement between the data points and the fitted curve can clearly be seen. A number of longer simulations were also run. These simulations were generally performed on a larger grid because of the high rate of damping observed when a wavelength of 256 lu is used. A typical example is shown in figure 7–18 which was simulated on a 512 by 512 grid. Only points every 400 time-steps have been marked. The wave was simulated with $g_1 = 2.5 \times 10^{-4}$, $g_2 = 3.5 \times 10^{-4}$, $\nu = 0.05$ and $\lambda = 512$. The wave was allowed to evolve for 1×10^5 time-steps and was observed to oscillate for almost twelve periods in this time. The agreement between the results and the best fit curve through the points is good although the discrepancy becomes larger towards the end of the simulation when the amplitude of the waves is only a few lattice sites. The error is slightly larger than that found earlier when a shorter time period was considered. Here $e = 2531$ giving a root mean square deviation of 1.0 lu.

7.4.2 Comparison with Theory

The results shown in figures 7–19 – 7–28 are all for waves with $\tau_\Delta = \tau_*$, $\kappa = 0.001$ and $a = 20\sqrt{3}/2$. The solid lines are the theoretical values calculated from equations (6.15), (6.16), (6.43) and (6.44). In figures 7–19 and 7–20 the parameter sg_1 was fixed while sg_2 was varied to give different values of f. The viscosity and the wavelength were fixed at 0.05 and 256 respectively. The results are for $sg_1 = 0.0001(\times)$ and $sg_1 = 0.00005(+)$. The results in figures 7–21 and 7–22 are for $\nu = 0.05$ and $\lambda = 256$ with $g = 1.5 \times 10^{-4}(\times)$ and $g = 5 \times 10^{-5}(+)$ where the density ratio f is varied. Figures 7–23 and 7–24 have $g_2 - g_1 = 5 \times 10^{-5}$. The viscosity and the wavelength were again fixed at 0.05 and 256 respectively. Figures 7–25 and 7–26 are for $g_1 = 2.5\times10^{-4}$, $g_2 = 3.5\times10^{-4}(\times)$ and $g_1 = 1.025 \times 10^{-4}$, $g_2 = 1.075 \times 10^{-4}(+)$. The wavelength is $\lambda = 256$. Figures 7–27 and 7–28 are also for $g_1 = 2.5 \times 10^{-4}$, $g_2 = 3.5 \times 10^{-4}(\times)$ and $g_1 = 1.025 \times 10^{-4}$, $g_2 = 1.075 \times 10^{-4}(+)$ when the viscosity is fixed at $\nu = 0.05$.

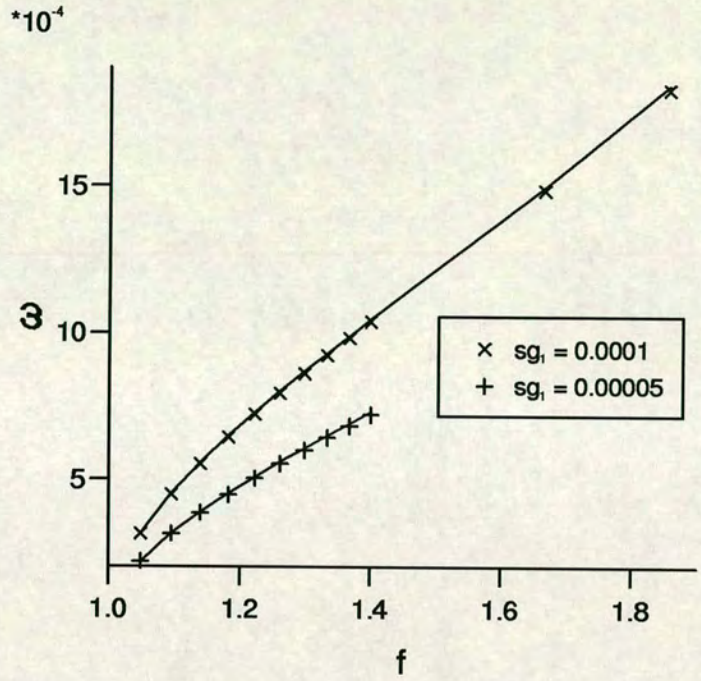

FIGURE 7–19: The frequency ω as a function of the density ratio f when sg_1 is fixed, $\lambda = 256$ and $\nu = 0.05$. The solid lines are the theoretical curves.

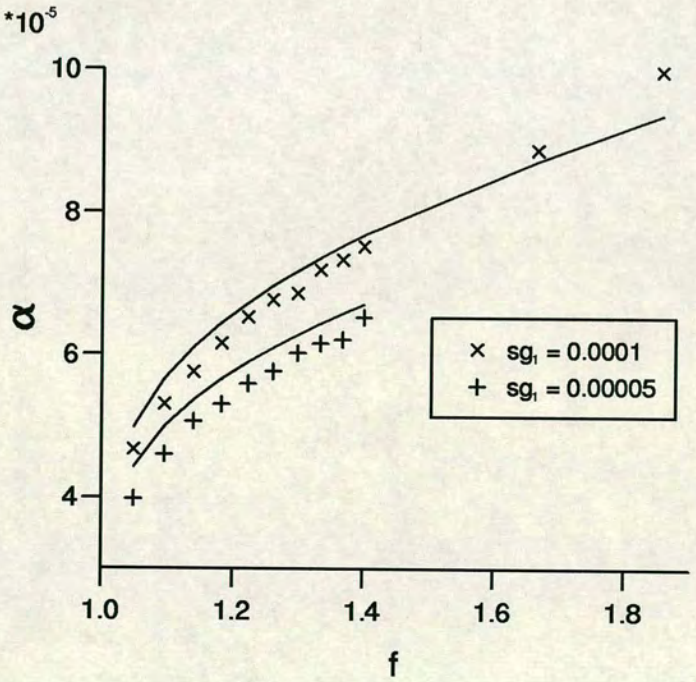

FIGURE 7–20: The damping parameter α as a function of the density ratio f when sg_1 is fixed, $\lambda = 256$ and $\nu = 0.05$. The solid lines are the theoretical curves.

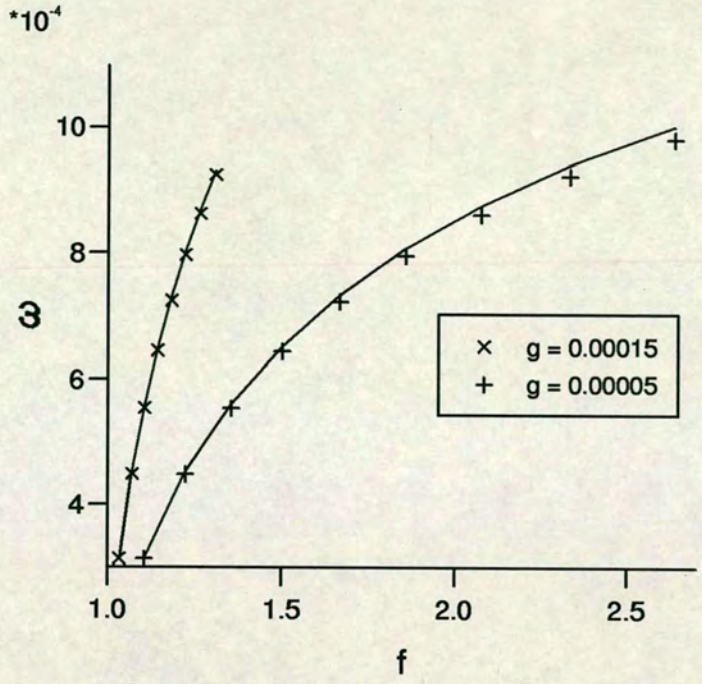

FIGURE 7–21: The frequency ω as a function of the density ratio f when the gravitational acceleration g is fixed, $\lambda = 256$ and $\nu = 0.05$. The solid lines are the theoretical curves.

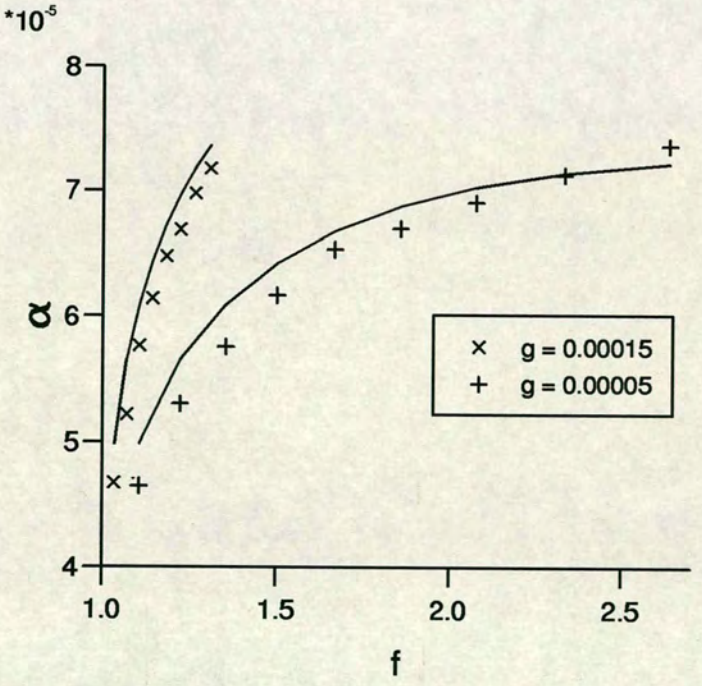

FIGURE 7–22: The damping parameter α as a function of the density ratio f when the gravitational acceleration g is fixed, $\lambda = 256$ and $\nu = 0.05$. The solid lines are the theoretical curves.

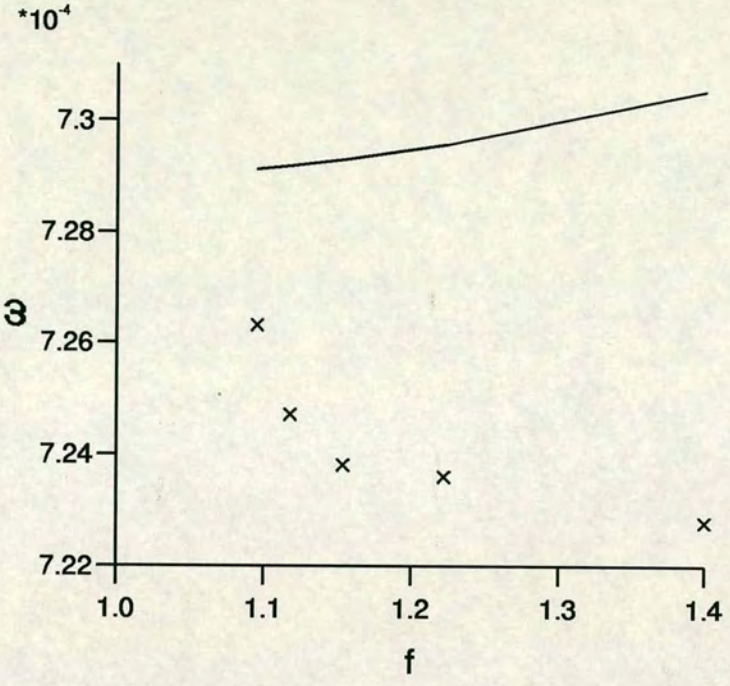

FIGURE 7–23: The frequency ω as a function of the density ratio f when the density difference is fixed by $g_2 - g_1 = 5 \times 10^{-5}, \lambda = 256$ and $\nu = 0.05$. The solid line is the theoretical curve.

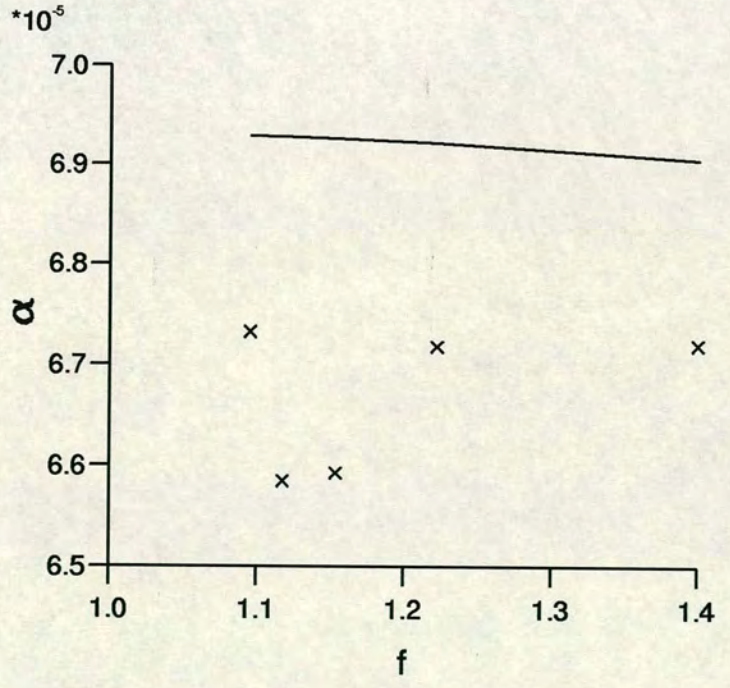

FIGURE 7–24: The damping parameter α as a function of the density ratio f when $g_2 - g_1 = 5 \times 10^{-5}, \lambda = 256$ and $\nu = 0.05$. The solid line is the theoretical curve.

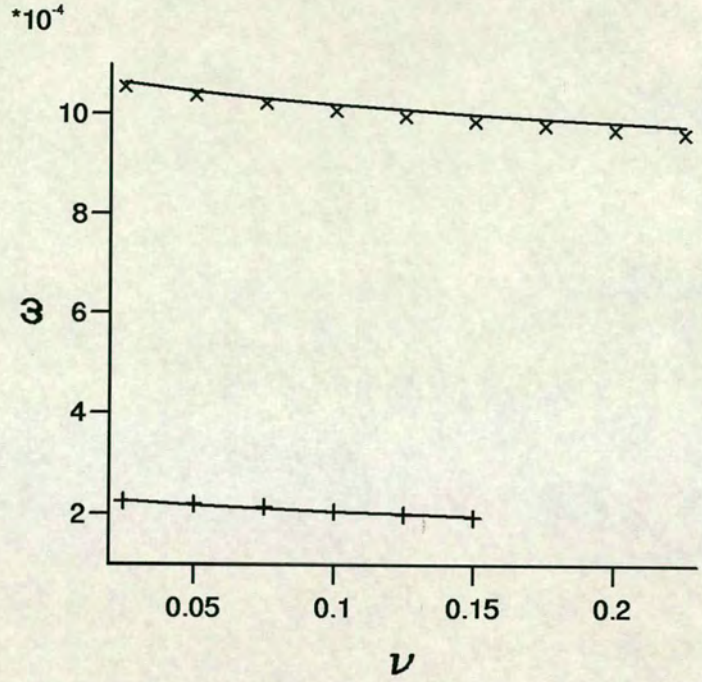

FIGURE 7–25: The frequency ω as a function of the viscosity ν. The results are for $g_1 = 2.5 \times 10^{-4}, g_2 = 3.5 \times 10^{-4}(\times)$ and $g_1 = 1.025 \times 10^{-4}, g_2 = 1.075 \times 10^{-4}(+)$. The wavelength is $\lambda = 256$. The solid lines are the theoretical curves.

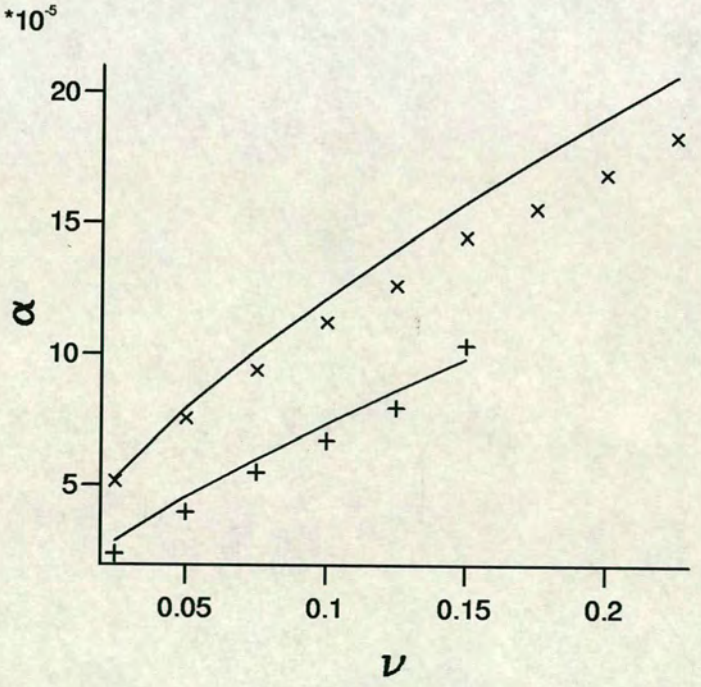

FIGURE 7–26: The damping parameter α as a function of the viscosity ν. The results are for $g_1 = 2.5 \times 10^{-4}, g_2 = 3.5 \times 10^{-4}(\times)$ and $g_1 = 1.025 \times 10^{-4}, g_2 = 1.075 \times 10^{-4}(+)$. The wavelength is $\lambda = 256$. The solid lines are the theoretical curves.

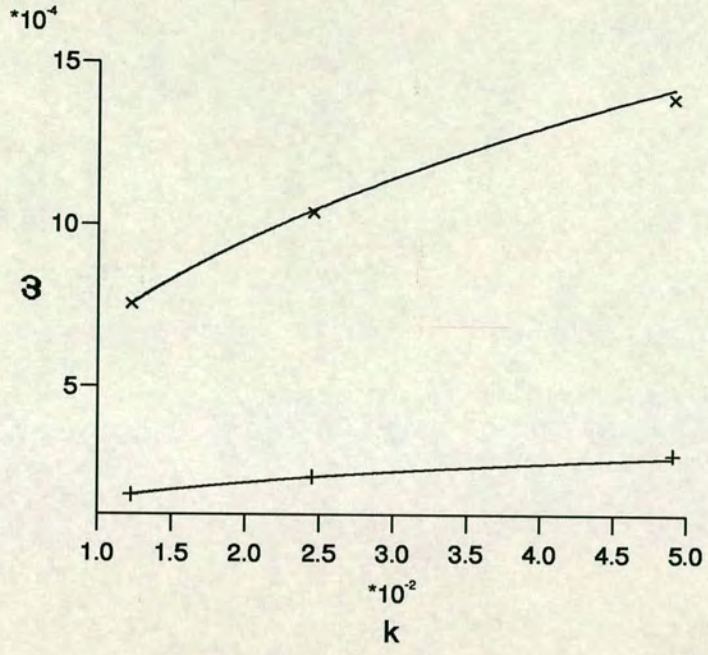

FIGURE 7–27: The frequency ω as a function of the wavenumber k. The results are for $g_1 = 2.5 \times 10^{-4}, g_2 = 3.5 \times 10^{-4}(\times)$ and $g_1 = 1.025 \times 10^{-4}, g_2 = 1.075 \times 10^{-4}(+)$. The viscosity is $\nu = 0.05$. The solid lines are the theoretical curves.

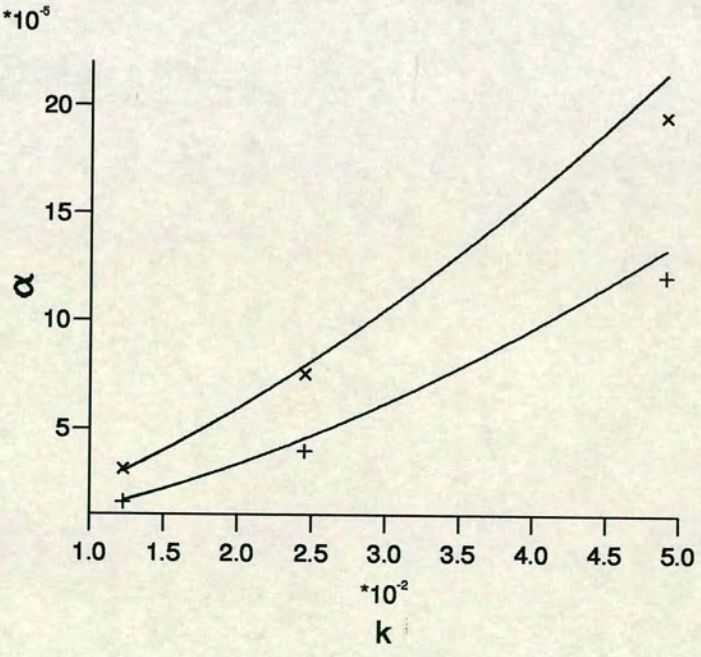

FIGURE 7–28: The damping parameter α as a function of the the wavenumber k. The results are for $g_1 = 2.5 \times 10^{-4}, g_2 = 3.5 \times 10^{-4}(\times)$ and $g_1 = 1.025 \times 10^{-4}, g_2 = 1.075 \times 10^{-4}(+)$. The viscosity is $\nu = 0.05$. The solid lines are the theoretical curves.

In each case there is reasonable agreement between the results and the theory. When $\nu = 0.05$ and $\lambda \geq 256$ the results found for the frequency are, in general, about 1% smaller than the theoretical predictions while the results for α are, on average, about 4% smaller. This is particularly noticeable in figures 7–23 and 7–24 where there is little variation in ω and α over the range of results. The results in figure 7–26 show a greater departure between the theory and the simulations for larger values of the viscosity, this can also be seen to a much lesser extent in figure 7–25. The results in figures 7–27 and 7–28 also show a larger difference between the theory and the simulations when $\lambda = 128$ ($k = 0.05$). As before the difference is greater for the damping parameter then it is for the frequency. Thus, for small ν and small k, the regime where equations (6.43) and (6.44) can be applied, there is good agreement between the results and the theory. For larger values of the viscosity and the wavenumber there are larger discrepancies however the theory is less accurate for these values since higher-order terms will become significant. The difference observed for ω and α between the computational results and the theory, where ν and k are small, was found to be about 1% and 4% respectively. These are slightly larger than the 0.3% and 4% errors predicted in section 7.4.1. Here, however, the fitted parameters are always smaller then their theoretical values. This might suggest that there is some bias in the fitting routine. No evidence of this was found when it was tested in section 7.4.1. The differences are nevertheless small and the comparison is good.

7.4.3 Continuously Varying Density at the Interface

A number of the simulations described above were repeated with the interfacial energy κ set to 0.1. This gives a much wider interface region in which the order parameter $\Delta\rho$ varies smoothly indicating that there is a mixture of both fluids in the interface region which is about 10 lattice units wide. The damping parameters found for the waves when $\kappa = 0.1$ were found to vary negligibly from the results for a sharp interface. A significant change was found in the wave frequency which noticeably increased when the interface was widened. This is shown in figures 7–29 and 7–30 where the solid lines and the $\times$ marks are the theoretical and ex-

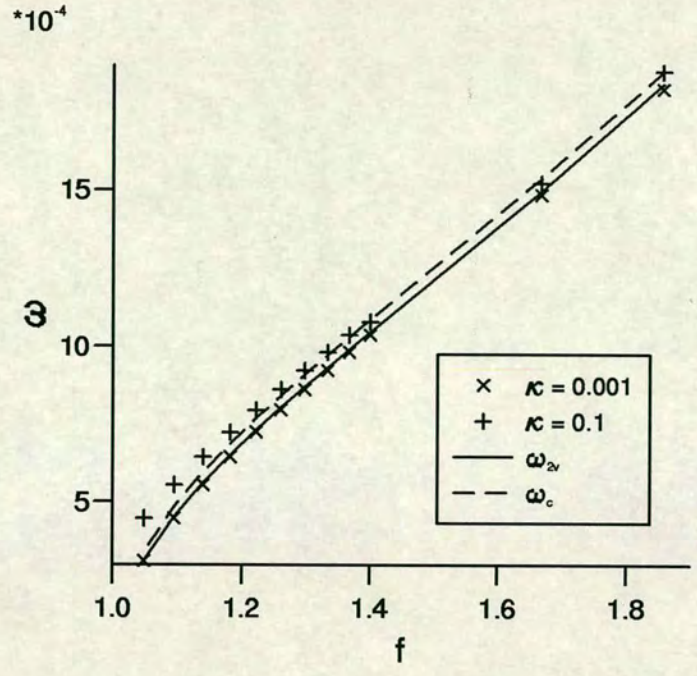

FIGURE 7–29: The frequency ω as a function of f for $\kappa = 0.001$ and $\kappa = 0.1$ when $sg_1 = 0.0001, \nu = 0.05$ and $\lambda = 256$. Also shown are the theoretical frequencies $\omega_{2\nu}$ and ω_c for a viscous two-layer model and an inviscid model with a continuous density change over an interface with width $l = 10$.

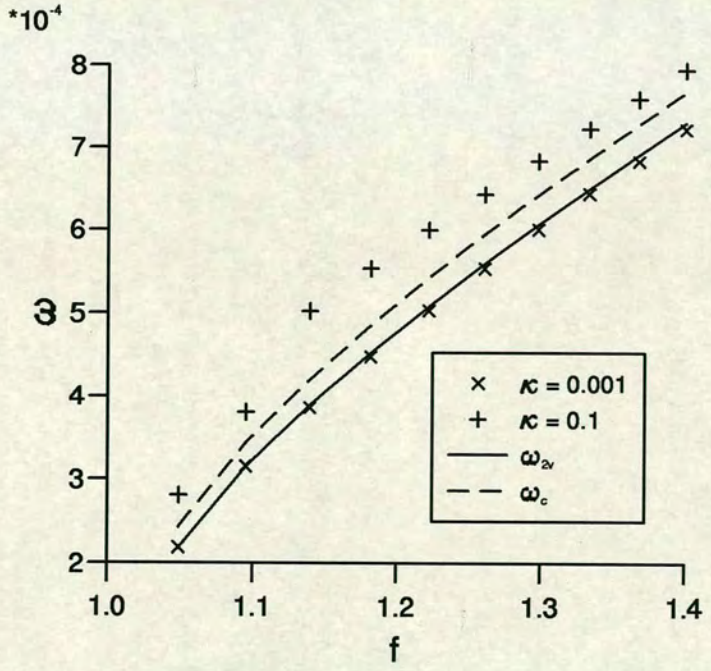

FIGURE 7–30: The frequency ω as a function of f for $\kappa = 0.001$ and $\kappa = 0.1$ when $sg_1 = 0.00005, \nu = 0.05$ and $\lambda = 256$. Also shown are the theoretical frequencies $\omega_{2\nu}$ and ω_c for a viscous two-layer model and an inviscid model with a continuous density change over an interface with width $l = 10$.

perimental values which were displayed in figure 7–19. The + marks represent the simulation results when $\kappa = 0.1$ and the dashed lines are the frequency calculated from the Sturm-Liouville equation for an interface width $l = 10$. It should be noted here that the solution of the Sturm-Liouville equation is only applicable to an inviscid fluid and so a close agreement between the results and the dotted line was not expected. In the two-layer problem the viscous frequency was seen to be modified only slightly from its inviscid value so in this similar problem it can be expected that the inviscid theory should at least give a rough estimate of the frequency in a viscous fluid. These results show that the wave frequency is sensitive to the size of the interface. When $\kappa = 0.001$ and the interface is no larger than 1 lu the results agree well with the viscous two-layer theory. When the interface has a larger width, 10 lu, there is a significant change in the frequency even when the interface is only 4% of the wavelength and 9% of depth of each fluid.

7.5 Velocities

The fluid velocity is shown in figures 7–31 – 7–38 at $t \simeq T/4$ for the four waves shown in table 7–1. All four waves have g in the range $1 \times 10^{-4} \rightarrow 5 \times 10^{-4}$. The

wave	λ	ν	g	f	ω	$(\nu/\omega)^{1/2}$
(1)	256	0.05	3×10^{-4}	1.40	1.04×10^{-3}	6.94
(2)	256	0.05	1.05×10^{-4}	1.05	2.19×10^{-4}	15.12
(3)	256	0.05	5×10^{-4}	1.86	1.82×10^{-3}	5.23
(4)	256	0.25	3×10^{-4}	1.40	9.59×10^{-4}	16.15

TABLE 7–1: The four waves in figures 7–31 – 7–38

value of g affects both the magnitude and the shape of the velocity profile since ω is a function of g. Wave (1) has a relatively low viscosity and the lower fluid is significantly denser than the top fluid. Wave (2) also has a relatively low viscosity and the two fluids are of similar densities varying by only 5%. Wave (3) has the

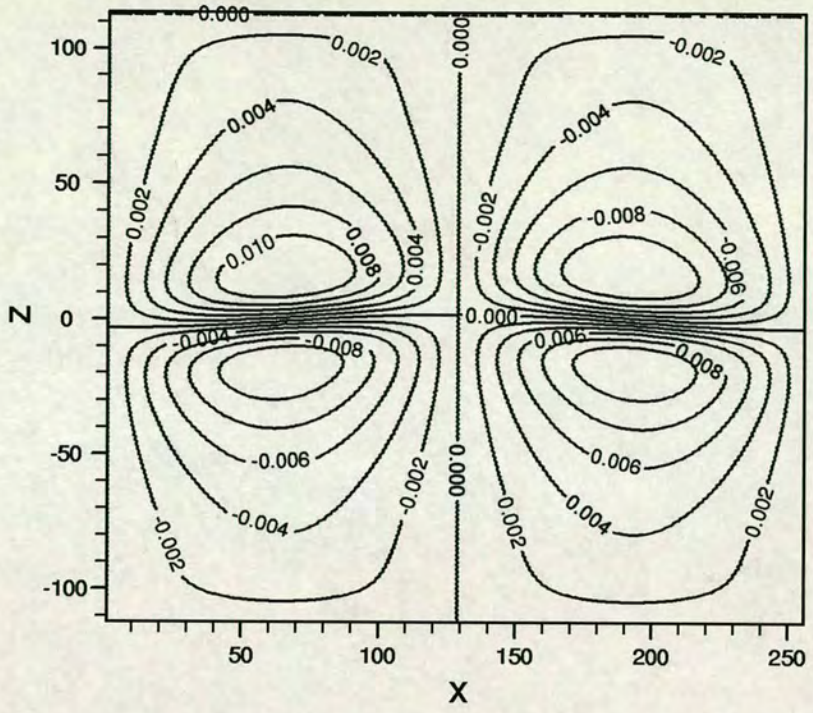

FIGURE 7–31: Horizontal velocity contour plot for wave (1) with $\lambda = 256$, $\nu = 0.05$, $g = 3 \times 10^{-4}$ and $f = 1.4$ at $t \simeq T/4$.

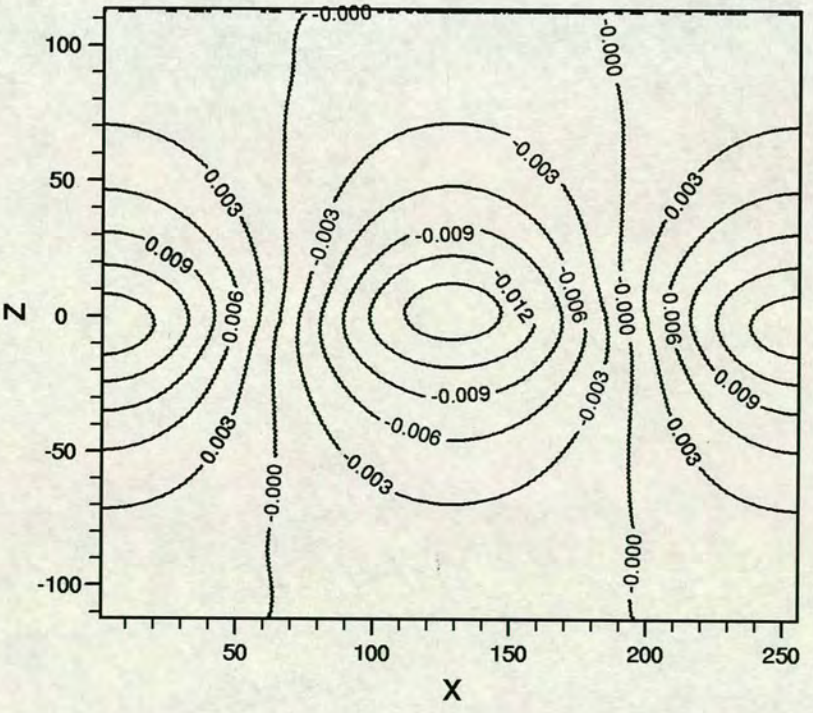

FIGURE 7–32: Vertical velocity contour plot for wave (1) with $\lambda = 256$, $\nu = 0.05$, $g = 3 \times 10^{-4}$ and $f = 1.4$ at $t \simeq T/4$.

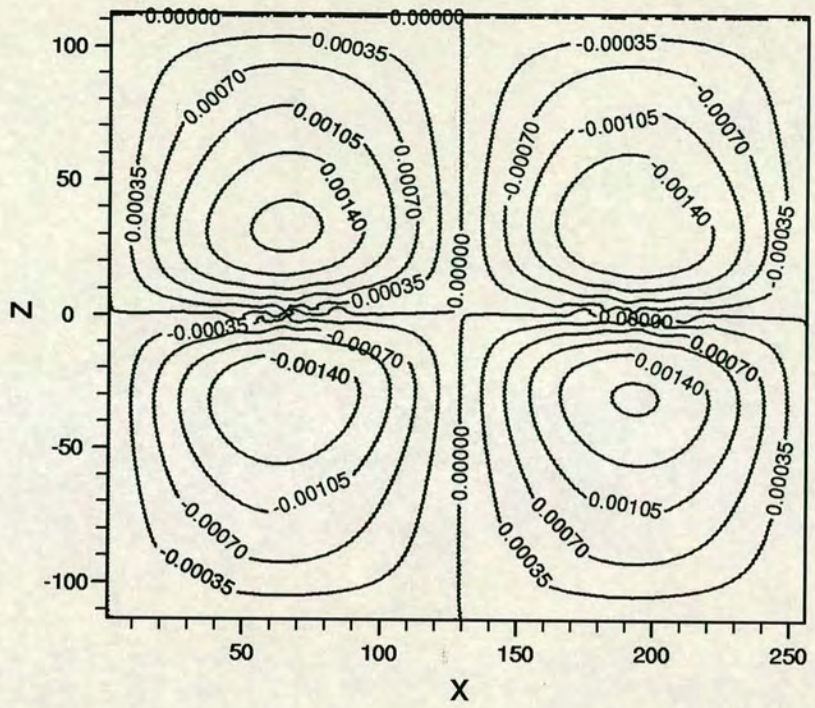

FIGURE 7–33: Horizontal velocity contour plot for wave (2) with $\lambda = 256$, $\nu = 0.05$, $g = 1.05 \times 10^{-4}$ and $f = 1.05$ at $t \simeq T/4$.

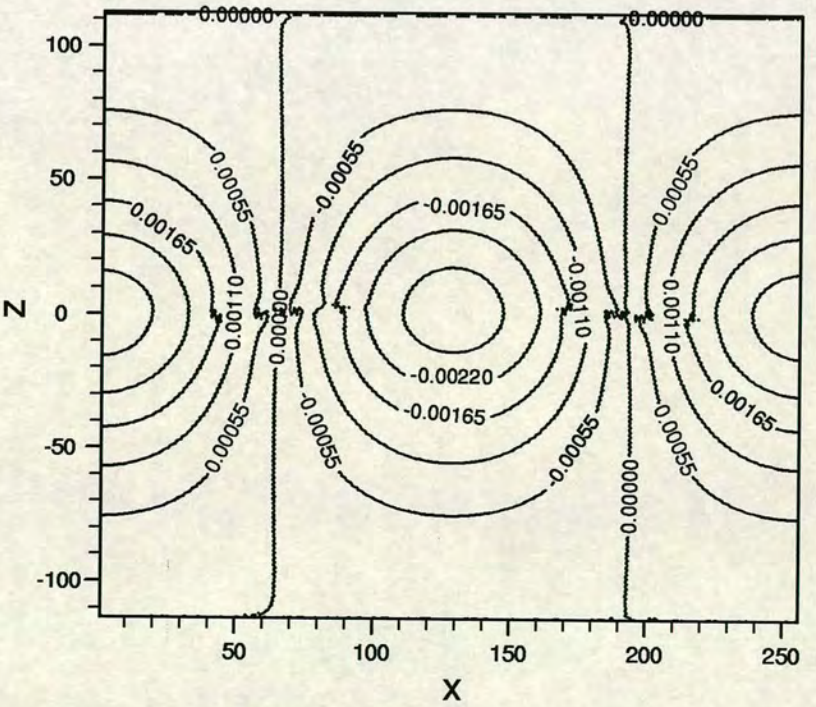

FIGURE 7–34: Vertical velocity contour plot for wave (2) with $\lambda = 256$, $\nu = 0.05$, $g = 1.05 \times 10^{-4}$ and $f = 1.05$ at $t \simeq T/4$.

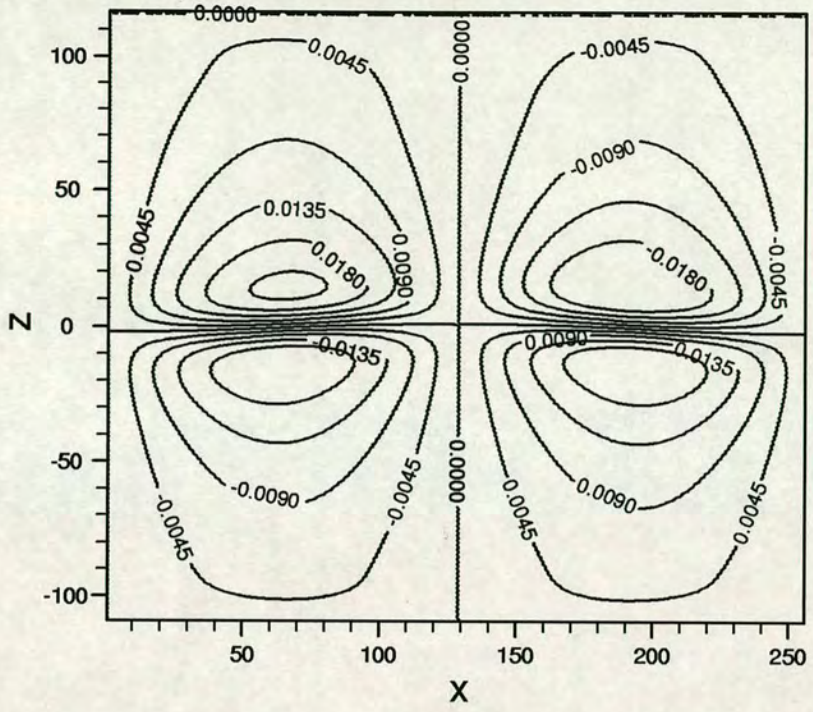

FIGURE 7–35: Horizontal velocity contour plot for wave (3) with $\lambda = 256$, $\nu = 0.05$, $g = 5 \times 10^{-4}$ and $f = 1.86$ at $t \simeq T/4$.

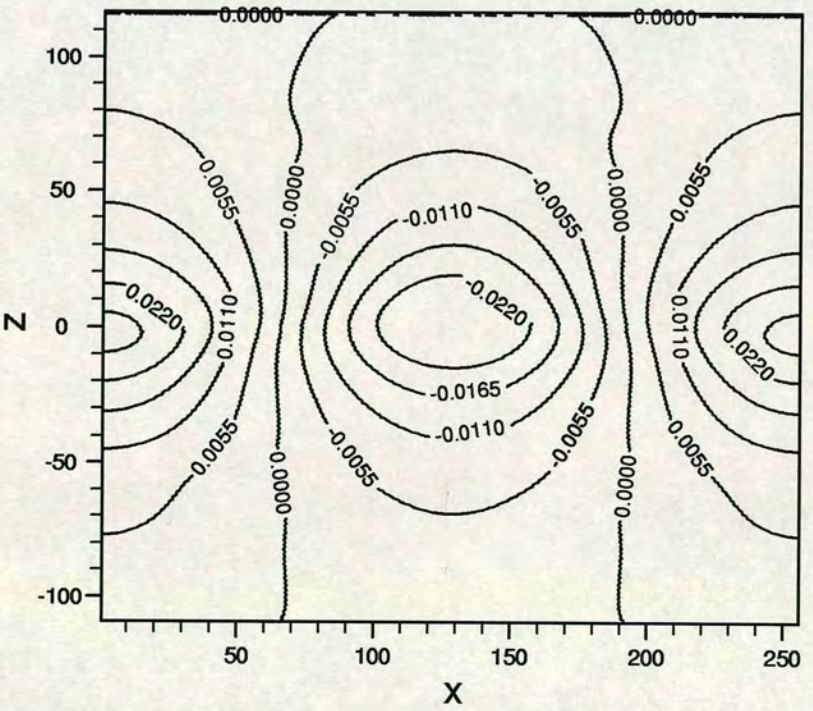

FIGURE 7–36: Vertical velocity contour plot for wave (3) with $\lambda = 256$, $\nu = 0.05$, $g = 5 \times 10^{-4}$ and $f = 1.86$ at $t \simeq T/4$.

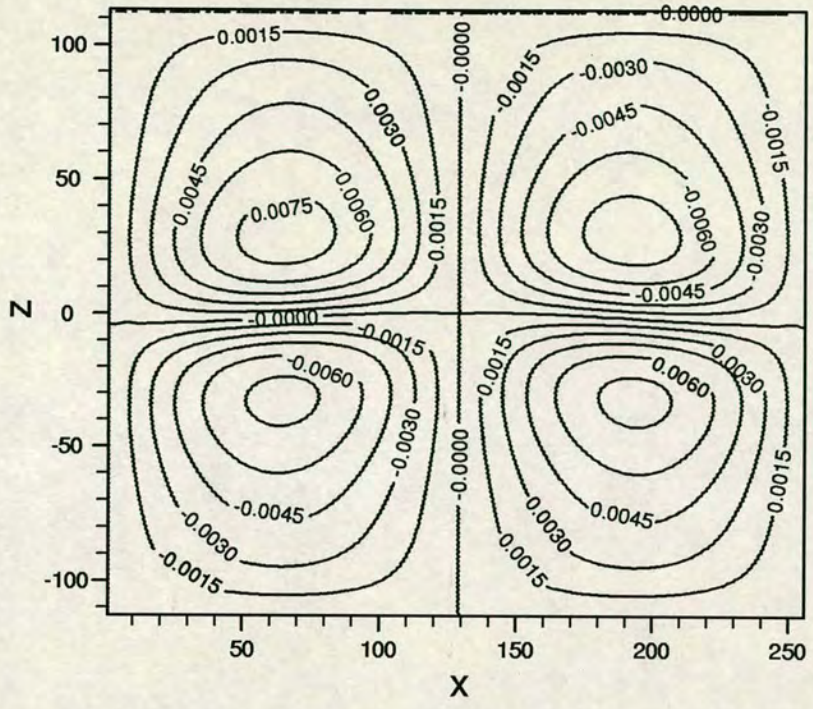

FIGURE 7–37: Horizontal velocity contour plot for wave (4) with $\lambda = 256$, $\nu = 0.25$, $g = 3 \times 10^{-4}$ and $f = 1.4$ at $t \simeq T/4$.

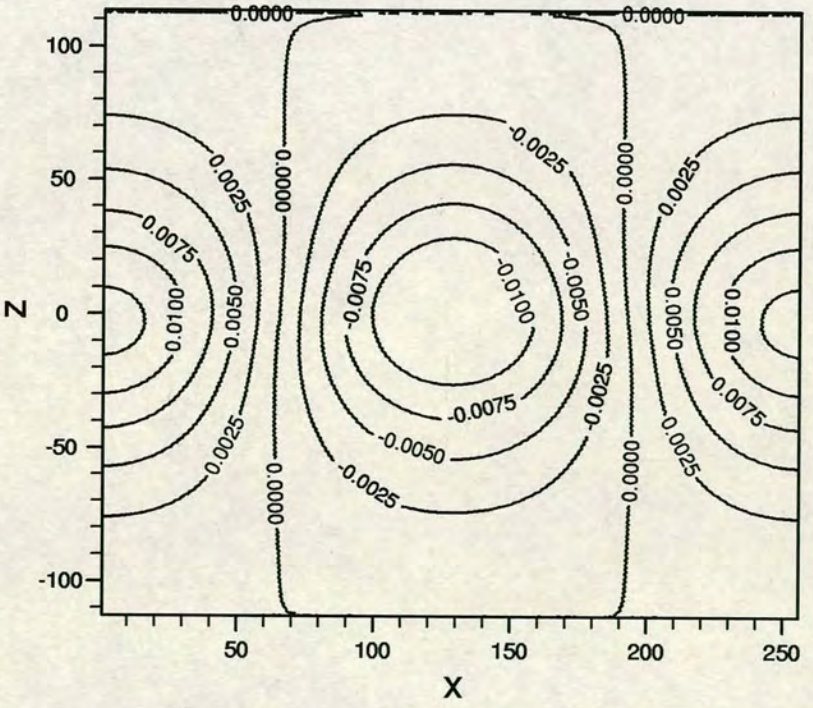

FIGURE 7–38: Vertical velocity contour plot for wave (4) with $\lambda = 256$, $\nu = 0.25$, $g = 3 \times 10^{-4}$ and $f = 1.4$ at $t \simeq T/4$.

same viscosity as the first two waves but the density difference is considerable, the ratio of the densities is 1.86. Wave (4) has the same density distribution as wave (1) but the viscosity is five times larger. For each wave the velocity is symmetric about and $x = \lambda/2$. The velocities are not symmetric about $x = 0$, although the contour plots are similar in both fluids. The difference is greatest when there is a large density difference corresponding to a large value of f. The magnitudes of the velocities are different for each wave. Wave (2) has velocities considerable smaller than the other waves. These lower velocities are shown in figures 7–33 and 7–34 where the contour lines are distorted slightly near the interface. This is due to small, spurious interface velocities which have been observed for the lattice Boltzmann model and which are due to the finite space and time steps [38]. This is not observed for the other waves where the velocities are higher. For each wave the magnitudes of u and w are similar. The vertical velocity peaks at $z = 0$ to a slightly higher value than the peak horizontal velocity, which occurs slightly above and below the interface. In wave (1) and wave (3) u peaks close to the interface, the contours for the higher magnitudes have an elliptical appearance, the semi-major axis parallel to the interface. The contours for the lower magnitudes appear more triangular in shape with the base near the interface and the opposite angle considerably rounded. Waves (2) and (4), on the other hand, have u peaking further from the interface. The high magnitude contours are much more circular and the lower magnitude contours are almost rectangular with curved corners. The lower magnitude contours for the vertical velocity are elliptical for all the waves, the semi-major axis is perpendicular to the interface. The higher magnitude contours for waves (2) and (4) are approximately circular while for waves (1) and (3) they are more elliptical in the same sense as the horizontal velocity.

7.5.1 Velocity Variation Across a Vertical Cross-Section

The velocities found from the four waves are compared with the theoretical expressions, equations (6.55), (6.56), (6.57) and (6.58), in figures 7–39 – 7–46 where the horizontal velocity is measured at $x = \lambda/4$, $t = T/4$ and the vertical velocity

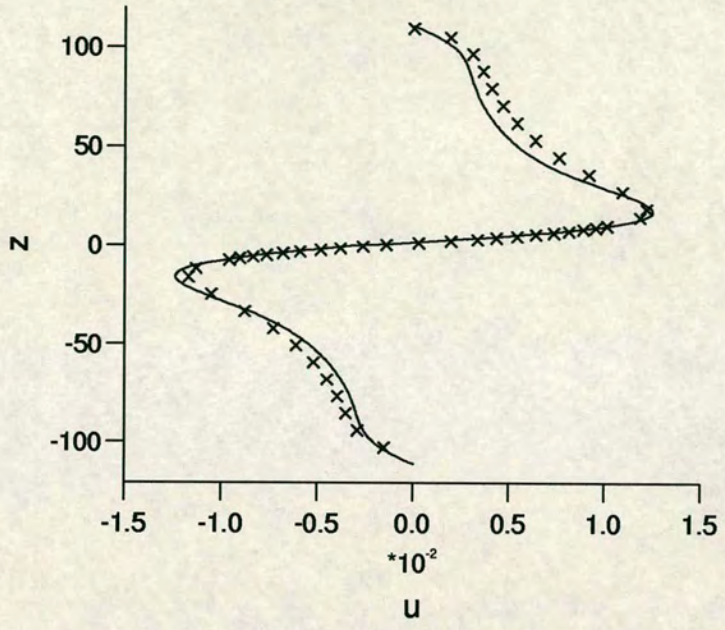

FIGURE 7–39: The horizontal velocity u as a function of z for wave (1) with $\lambda = 256$, $\nu = 0.05$, $g = 3 \times 10^{-4}$ and $f = 1.4$ at $x = \lambda/4, t \simeq T/4$. The solid line is the theoretical curve.

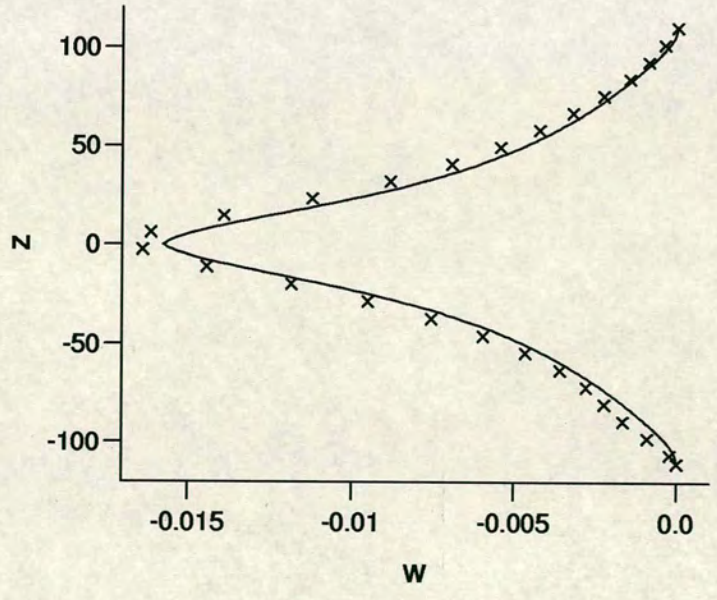

FIGURE 7–40: The vertical velocity w as a function of z for wave (1) with $\lambda = 256$, $\nu = 0.05$, $g = 3 \times 10^{-4}$ and $f = 1.4$ at $x = \lambda/2, t \simeq T/4$. The solid line is the theoretical curve.

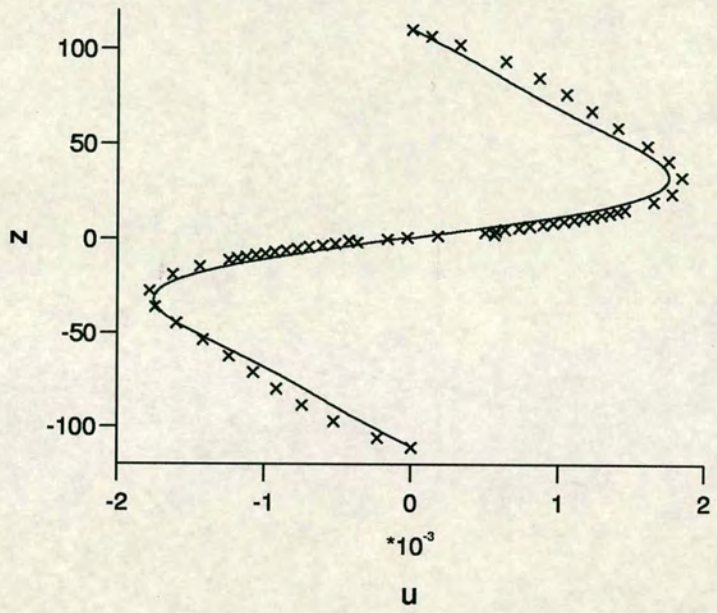

FIGURE 7–41: The horizontal velocity u as a function of z for wave (2) with $\lambda = 256$, $\nu = 0.05$, $g = 1.05 \times 10^{-4}$ and $f = 1.05$ at $x = \lambda/4, t \simeq T/4$. The solid line is the theoretical curve.

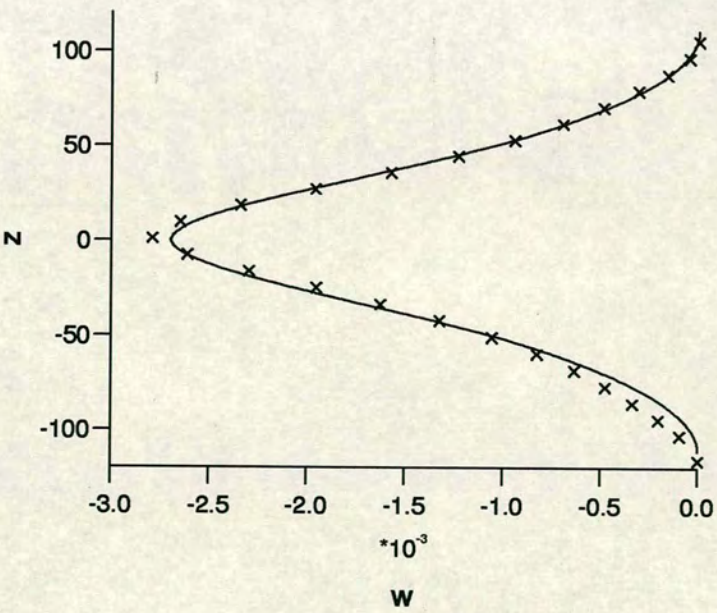

FIGURE 7–42: The vertical velocity w as a function of z for wave (2) with $\lambda = 256$, $\nu = 0.05$, $g = 1.05 \times 10^{-4}$ and $f = 1.05$ at $x = \lambda/2, t = \tau/4$. The solid line is the theoretical curve.

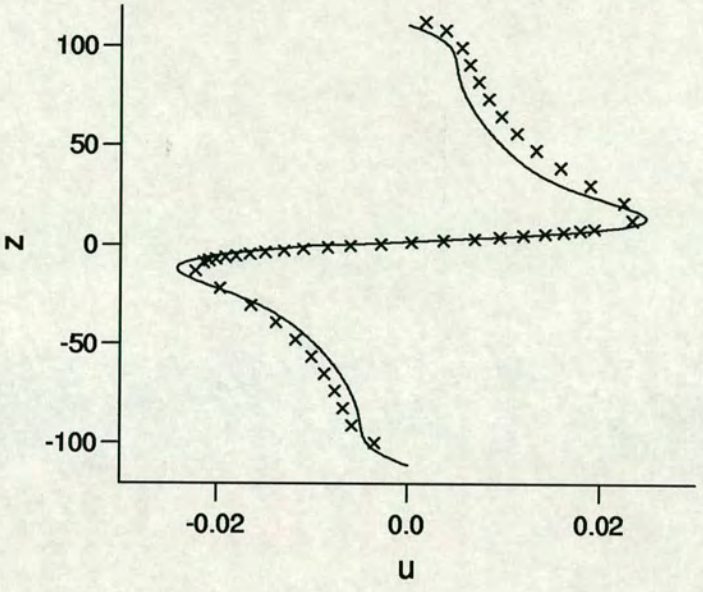

FIGURE 7–43: The horizontal velocity u as a function of z for wave (3) with $\lambda = 256$, $\nu = 0.05$, $g = 5 \times 10^{-4}$ and $f = 1.86$ at $x = \lambda/4, t \simeq T/4$. The solid line is the theoretical curve.

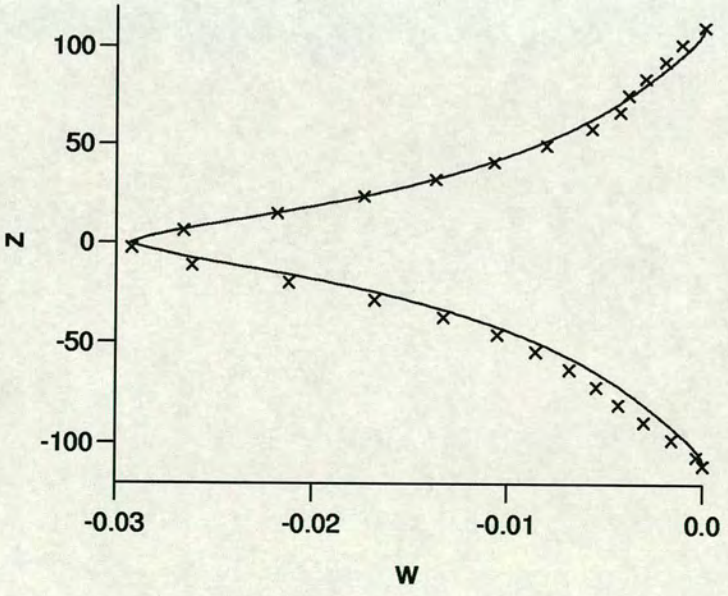

FIGURE 7–44: The vertical velocity w as a function of z for wave (3) with $\lambda = 256$, $\nu = 0.05$, $g = 5 \times 10^{-4}$ and $f = 1.86$ at $x = \lambda/2, t \simeq T/4$. The solid line is the theoretical curve.

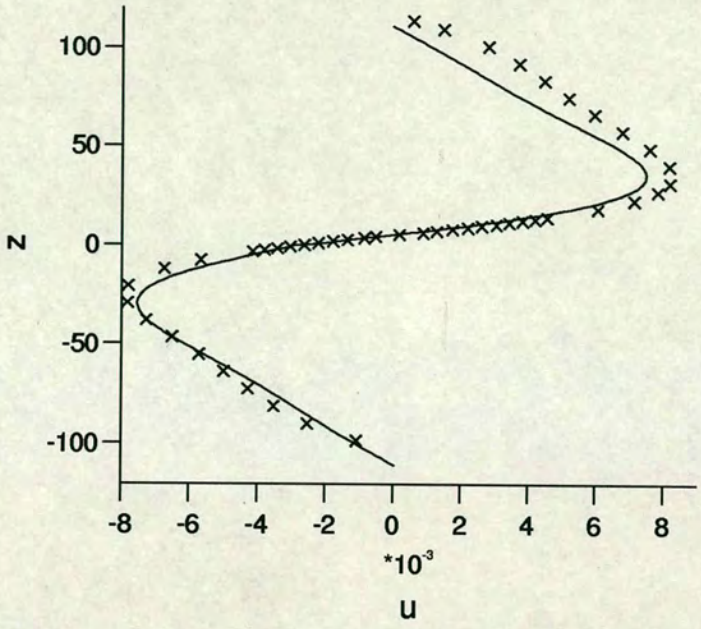

FIGURE 7–45: The horizontal velocity u as a function of z for wave (4) with $\lambda = 256$, $\nu = 0.25$, $g = 3 \times 10^{-4}$ and $f = 1.4$ at $x = \lambda/4, t \simeq T/4$. The solid line is the theoretical curve.

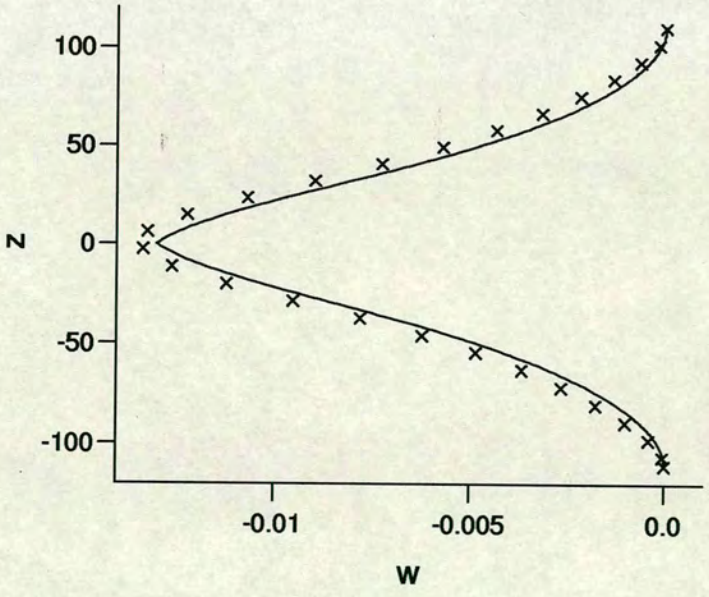

FIGURE 7–46: The vertical velocity w as a function of z for wave (4) with $\lambda = 256$, $\nu = 0.25$, $g = 3 \times 10^{-4}$ and $f = 1.4$ at $x = \lambda/2, t \simeq T/4$. The solid line is the theoretical curve.

at $x = \lambda/2$, $t = T/4$. This is where the magnitudes of the velocities are maximum. The solid lines are the theoretical values and the markers are the simulation results. For each wave there is a good agreement for both the magnitude and the shape of the velocity distributions. The poorest fit is for the horizontal velocity in wave (4) where the viscosity is at its largest. Despite the large viscosity ϵ in equation (6.46) is 0.05 which is still small so the theory should be applicable. The fit is good everywhere except outside the viscous interface region in the upper fluid. At its worst the discrepancy is about 1×10^{-3}, about 25%, however the difference is generally much smaller, only a few percent. As predicted in section 6.3.2 the viscosity has little affect on the shape of the vertical velocity distribution, the shape of the graphs in figures 7–40, 7–42, 7–44 and 7–46 all being similar. The difference in the velocity magnitude is due mainly to the different values of $\omega_0 \propto [(f-1)g/(1+f)]^{1/2}$ as would be the case for inviscid waves. The effect of the viscosity is much more evident in the horizontal velocity profiles shown in figures 7–39, 7–41, 7–43 and 7–45. Waves (1) and (3) both show a definite boundary layer, in both fluids, in the region of the solid boundary (at $z \simeq \pm 110$). The influence of the boundary layer is only obvious within about 10 lattice units of the boundary. Waves (2) and (4) both have very low velocities close to the boundary and there is no noticeable change in the velocity profile. At the interface ($z = 0$) the effect of the viscosity can be seen readily in each of the waves. The magnitude of the horizontal velocity peaks some distance from the interface and then decreases steadily to zero at the interface. The distance of the peak from the interface is $\simeq$ 10 lu for waves (1) and (3) and $\simeq$ 30 lattice units for waves (2) and (4). This is consistent with the values of $(\nu/\omega)^{1/2}$: 7, 15, 5 and 16 given in table 7–1. For waves (1) and (3) $(\nu/\omega)^{1/2}$ has a similar value, about a third of the value for waves (2) and (4). Twice this distance from the boundary the magnitude of the irrotational velocity will be reduced a factor of e^{-2} to about 14% of its value at the interface/boundary and its effect will become negligible at greater distances.

The results in figures 7–47 and 7–48 show the horizontal and the vertical velocity profile respectively at times $t \simeq T/4$, $3T/4$, $5T/4$, $7T/4$, $9T/4$ and $11T/4$ for

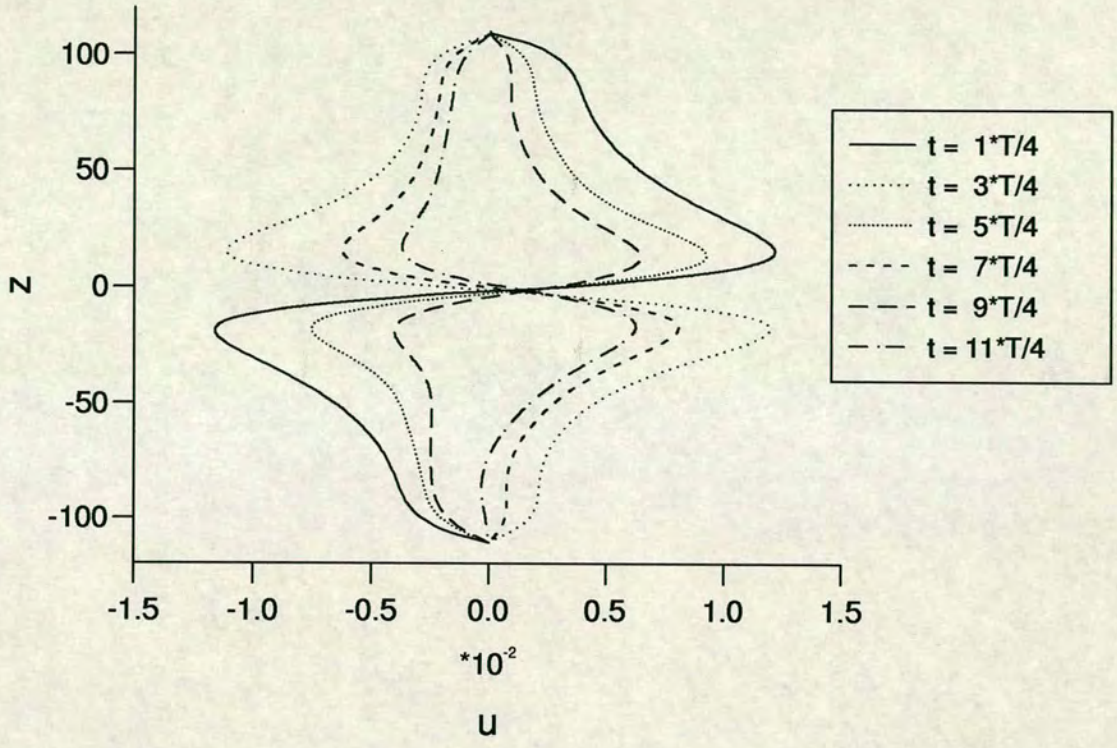

FIGURE 7–47: The horizontal velocity u as a function of z for wave (1) at $x = \lambda/4$ and at multiples of $T/4$.

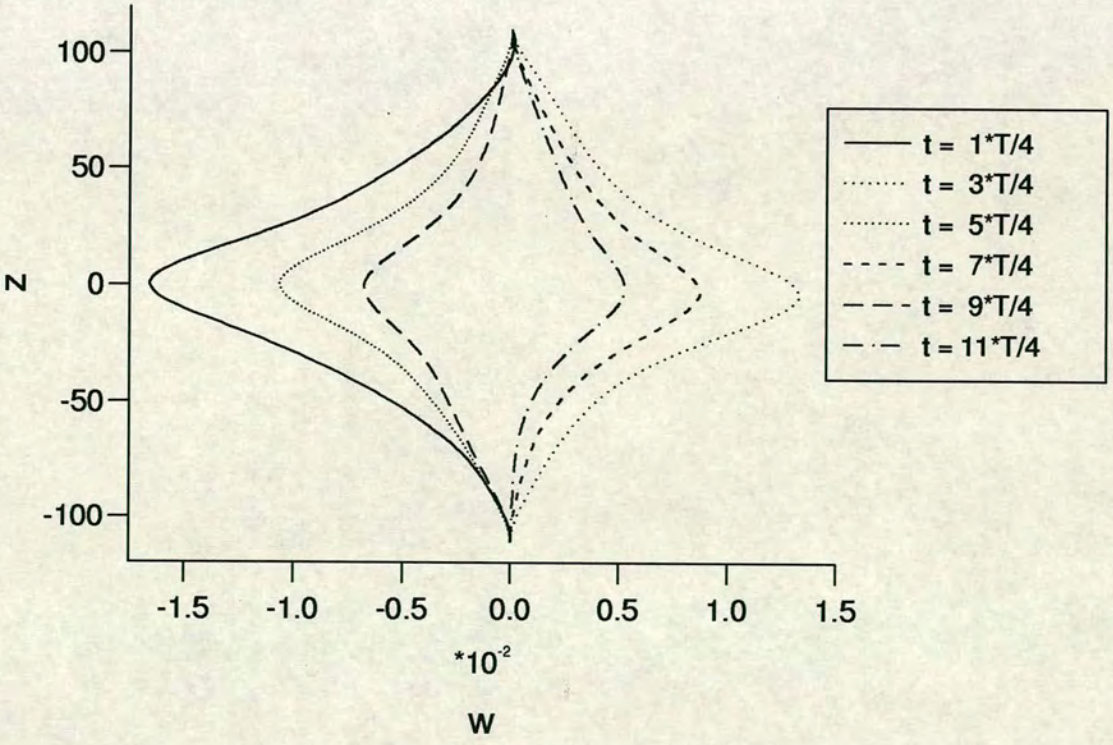

FIGURE 7–48: The vertical velocity w as a function of z for wave (1) at $x = \lambda/2$ and at multiples of $T/4$.

wave (1). The horizontal velocity is shown at $x = \lambda/4$ and the vertical velocity at $x = \lambda/2$. The decrease in both the horizontal and the vertical velocity with time can be seen over the three periods of oscillation. This is expected at the rate $\exp(-\alpha t)$ since this is the rate at which a, the interface amplitude, is decaying and the velocities are proportional to a. There is also a lack of symmetry about $z = 0$ which is particularly obvious in the horizontal velocity, see figure 7–47. This is expected since the ratio of the irrotational velocities $C1/C2$ is 1.4 here.

7.5.2 Velocity Variation Across a Horizontal Cross-Section

The velocity variation along horizontal cross-sections through the wave were also examined. These are shown in figures 7–49 – 7–52 for wave (1) at $t \simeq T/4$. Figures 7–49 and 7–50 show the horizontal and vertical velocities along cross-sections through the inviscid body of the fluid. Figures 7–51 and 7–52 show the horizontal velocity along cross-sections through the viscous boundary layers near the solid boundaries and the interfacial region respectively. Also plotted in the figures are sine and cosine curves with selected amplitudes, these are represented by the solid lines. The vertical velocity is very small within the boundary layer at the solid boundary. In the interfacial boundary layer the variation in w is the same as that shown in figure 7–50.

The results in figures 7–49 and 7–50 show very good agreement with the sine and cosine curves. Thus the wave velocities are seen to be following the expected variation with horizontal distance. Note that the amplitude of the sine and cosine curves in figures 7–49 and 7–50 (and in figures 7–51 and 7–52) have been picked arbitrarily to give a good fit to the results and are not the amplitudes predicted by theory. This was done because any small deviation of the velocity profile from a sinusoidal variation would not be obvious if the simulation results were being compared to a sine curve with a different amplitude. The difference between the amplitude of the results and the amplitude predicted by equations (6.55) – (6.58) is typically small and can be seen in figures 7–39 and 7–40. The results in figures

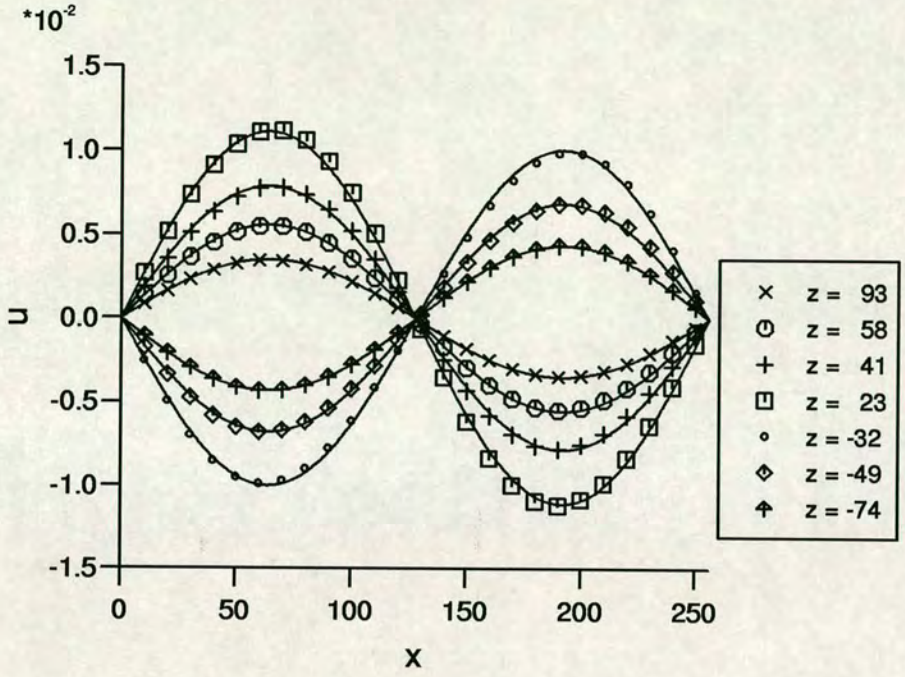

FIGURE 7–49: The horizontal velocity u as a function of x at $t \simeq T/4$. The results are for wave (1) at different heights z within the inviscid body of the wave. The solid lines are sine curves with an appropriate amplitude.

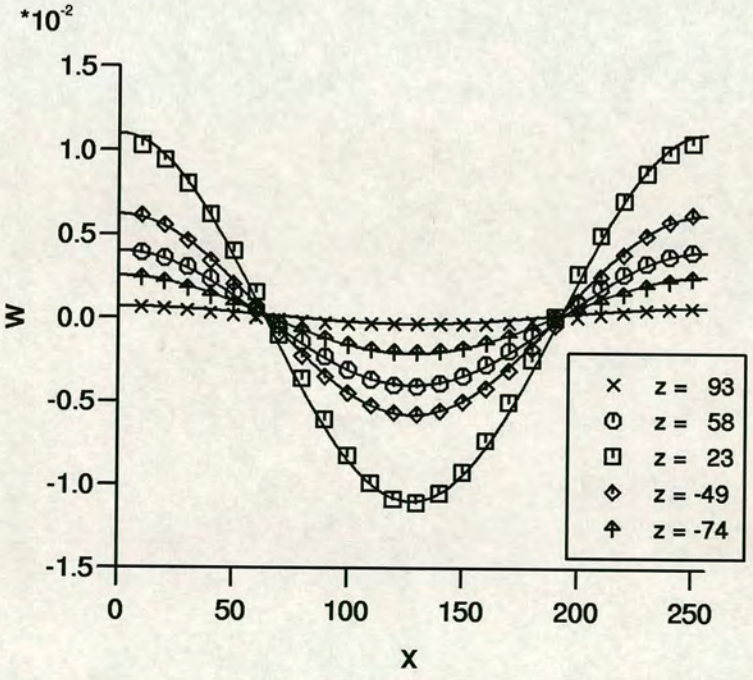

FIGURE 7–50: The vertical velocity w as a function of x at $t \simeq T/4$. The results are for wave (1) at different heights z within the inviscid body of the wave. The solid lines are cosine curves with an appropriate amplitude.

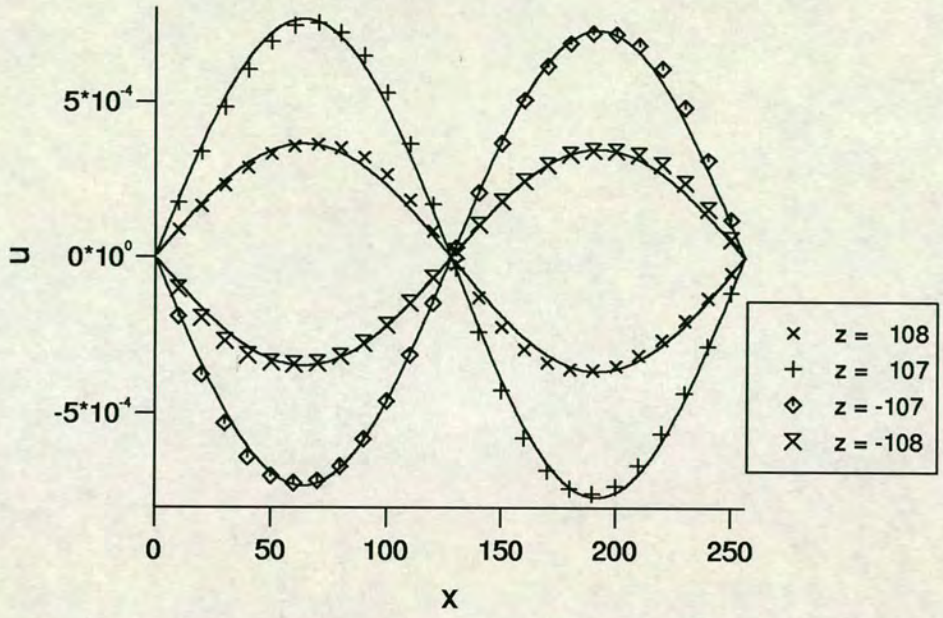

FIGURE 7–51: The horizontal velocity u as a function of x at $t \simeq T/4$. The results are for wave (1) at different heights z within the viscous boundary layer at the solid boundaries. The solid lines are sine curves with an appropriate amplitude.

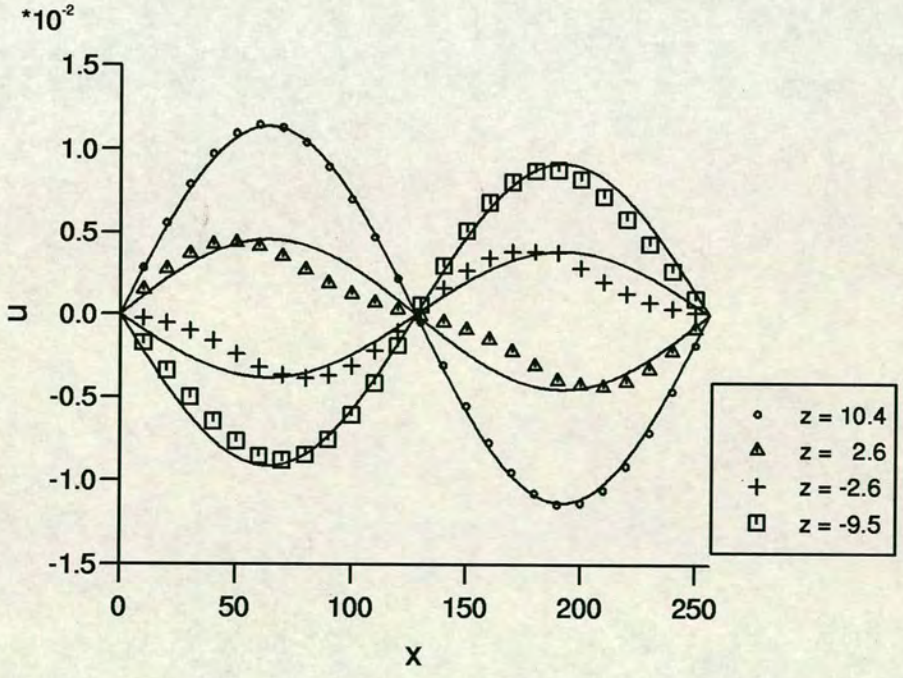

FIGURE 7–52: The horizontal velocity u as a function of x at $t \simeq T/4$. The results are for wave (1) at different heights z within the viscous boundary layer at the interface. The solid lines are sine curves with an appropriate amplitude.

7–51 show the comparison inside the boundary layer at the fixed boundaries. The fit here is not quite as good, the results vary slightly from the sine curves. Any small phase shift introduced by the irrotational part of the velocity will be the same at all points and so should not affect the shape of the curves. The results in figure 7–52 show a poorer fit close to the interface. This is because the interface is not completely flat, see figures 7–31 and 7–32. For z positive the results are closer to the interface, and hence smaller, at $x = \lambda/2$ than they are at $x = 0$ and $x = \lambda$. Conversely when z is negative the results for $x = 0$ and $x = \lambda$ are closer to the interface than the results for $x = \lambda/2$. This distorts the results from the plotted sine curves.

7.5.3 Boundary Layer at the Solid Boundaries

Most of the waves simulated have been on a square grid with the interface near the centre. This means that the depth of the two fluids h_1 and h_2 satisfy $kh_i \simeq \sqrt{3}\pi$. Thus $\tanh(kh_i) \simeq 0.99$ and the wave can be considered as being in deep water. There can, however, be a finite velocity close to the solid boundaries and a boundary layer is formed, see for example figure 7–39. A wave with the same parameters as wave (1), in table 7–1, was initialised on a grid with twice the height and with the interface at the centre so that $h1 = h2 = \sqrt{3}\lambda/2$. The wave was allowed to evolve and the velocity profiles and the frequency and damping parameter compared to those for wave (1). The fitted values found for the frequency and the damping parameter were not found to differ significantly. The velocity profiles for wave (1) and for the new wave on the larger grid are shown in figures 7–53 – 7–55. In the interface region the horizontal velocities, u_s and u_l of the wave on the small and large grid respectively, are consistent for the small and large grids. The horizontal velocity of the wave on the larger grid has become negligible within the inviscid region of the fluid and so there is no evidence of a boundary layer at the solid boundary. The boundary layer for the wave on the smaller grid can be observed, as before, and the horizontal velocity is zero on the solid boundary, as expected. Away from the solid boundary $|u_s|$ increases rapidly and becomes

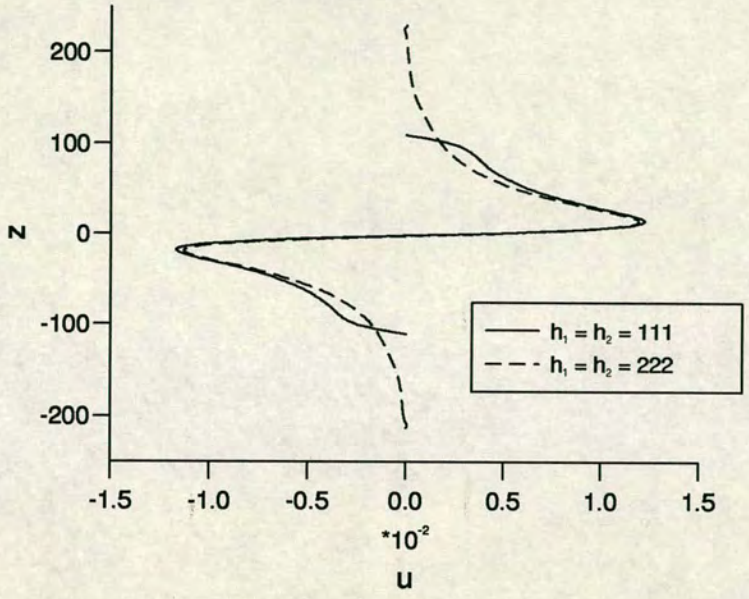

FIGURE 7–53: The horizontal velocity u at $x = \lambda/4$, $t \simeq T/4$ as a function of z for wave (1) using two different grid sizes.

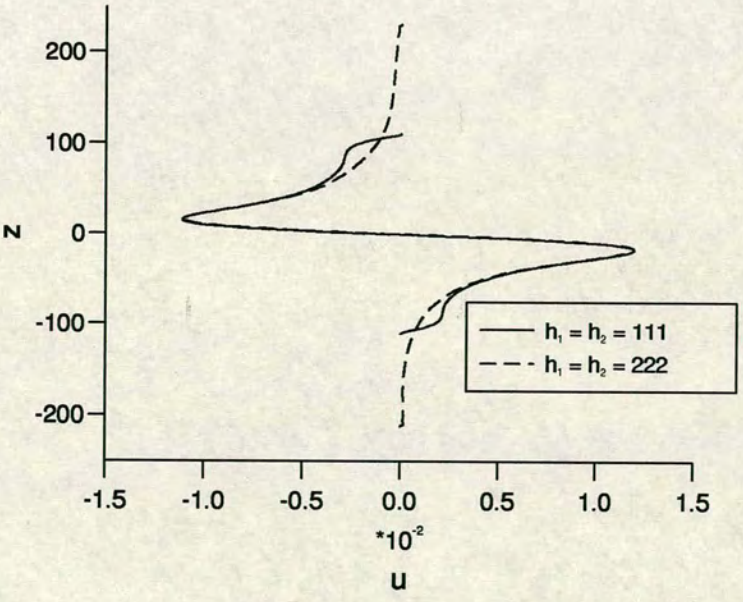

FIGURE 7–54: The horizontal velocity u at $x = \lambda/4$, $t \simeq 3T/4$ as a function of z for wave (1) using two different grid sizes.

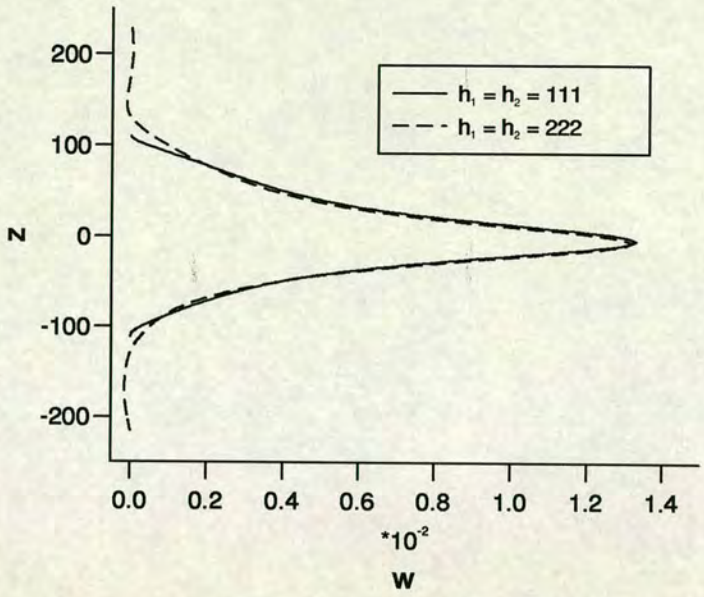

FIGURE 7–55: The vertical velocity w at $x = \lambda/2$, $t \simeq 3T/4$ as a function of z for wave (1) using two different grid sizes.

slightly larger then $|u_l|$ outside its boundary layer. This is due partly to the similar effect observed in figure 6–2 but mainly due to the different values of h_i for the two waves. This is seen in figures 7–53 and 7–54 at $t \simeq T/4$ and $t \simeq 3T/4$ respectively. The results in figure 7–55 show that w_s and w_l are very similar everywhere except within the boundary layer of the smaller grid where w_s approaches zero. The velocity w_l is also small in this region and reaches zero slightly further from the interface and no boundary layer is observed at the solid boundary of the larger grid. In the region between w_l approaching zero and $z = \pm 512\sqrt{3}/4$ we would expect w_l to be zero. In fact, there is a small variation observed. This is derived from a small vertical velocity which is produced at the interface at the beginning of the simulation when the density is very slightly reduced across the small interface region. The velocities produced are very small and are generally negligible, particularly when $\kappa = 0.001$ and the interface is sharp.

Thus we have seen that increasing the depth of both fluids has a negligible affect on the frequency and damping parameter. The velocities are similar near the interface were they are largest, away from the interface there is only a small difference

in the velocities mainly due to a boundary layer forming around the solid boundary.

7.5.4 Peak Horizontal Velocity

The results above all show that the magnitude of the horizontal velocity $|u|$ peaks above and below the interface within the boundary layer region. The height at which the peaks occur has been seen to depend on the $(\nu/\omega)^{1/2}$. Here we look more closely at the dependence of d, the vertical distance between the two peeks, on the simulation parameters, f, λ and ν. The values of d was found from the simulations when $t = T/4$ at $x = \lambda/4$ and are correct to within one lu. The theoretical values were obtained by finding the zeros of $\mathrm{d}u_1/\mathrm{d}z$ and $\mathrm{d}u_2/\mathrm{d}z$ [84] where u_1 and u_2 are given in equations (6.55) and (6.56). The results are shown in figures 7–56 – 7–58. The results in figure 7–56 are for three cases. Case (1) has

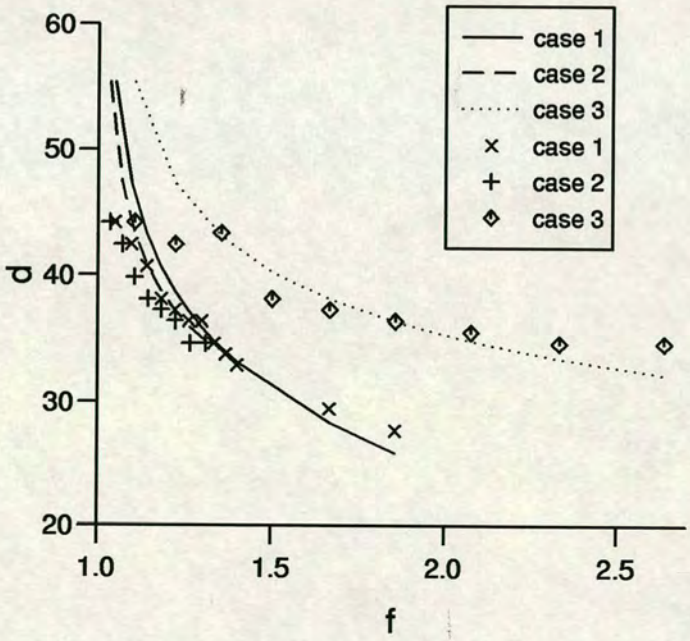

FIGURE 7–56: The vertical separation d of the horizontal velocity peaks as a function of f values of f for three cases. Case (1) has $sg_1 = 0.0001, \nu = 0.05, \lambda = 256$ and sg_2 varied. Case (2) has $g = 1.5 \times 10^{-4}, \nu = 0.05$ and $\lambda = 256$. The values of g_1 and g_2 are varied to give different values of f while keeping g fixed. Case (3) has $g_2 - g_1 = 5 \times 10^{-5}, \nu = 0.05$ and $\lambda = 256$. The marks represent the simulated data and the lines the theoretical separation.

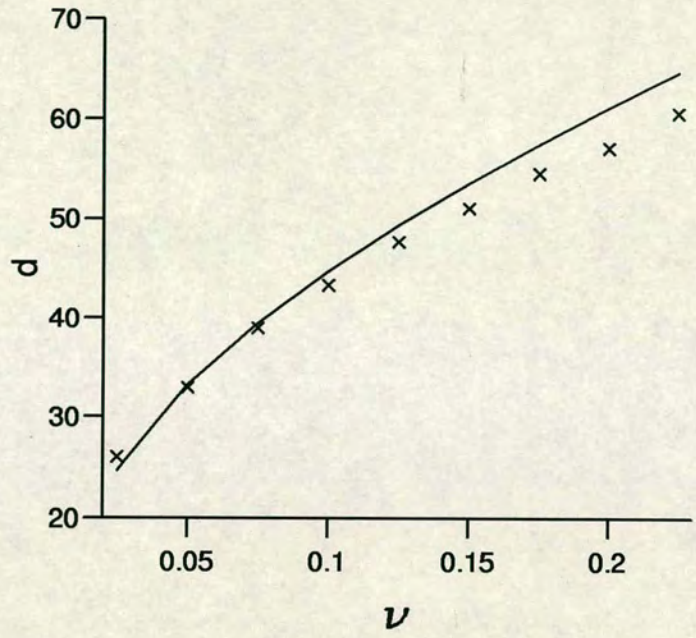

FIGURE 7–57: The vertical separation d of the horizontal velocity peaks as a function of the the viscosity ν when $g_1 = 2.5 \times 10^{-4}, g_2 = 3.5 \times 10^{-4}, f = 1.4$ and $\lambda = 256$.

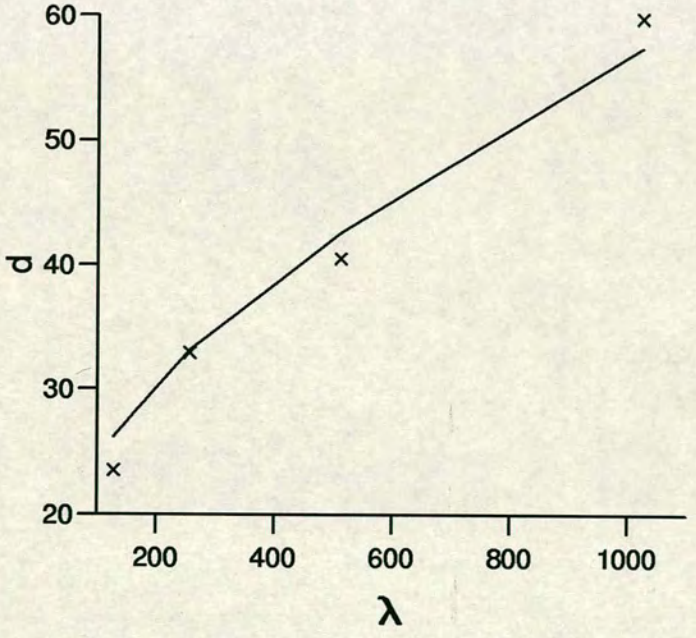

FIGURE 7–58: The vertical separation d of the horizontal velocity peaks as a function of the wavelength λ when $g_1 = 2.5 \times 10^{-4}, g_2 = 3.5 \times 10^{-4}, f = 1.4$ and $\nu = 0.005$.

$sg_1 = 0.0001, \nu = 0.05, \lambda = 256$ and sg_2 varied. Case (2) has $g = 1.5 \times 10^{-4}, \nu = 0.05$ and $\lambda = 256$. The values of g_1 and g_2 are varied to give different values of f while keeping g fixed. Case (3) has $g_2 - g_1 = 5 \times 10^{-5}, \nu = 0.05$ and $\lambda = 256$. There is good agreement with the theory except for the lowest values of f, the density ratio, where the theory predicts a value for d which is significantly larger than the one measured in the simulations. When the boundary layer is large compared to the wavelength the assumptions made in deriving the velocity expressions are no longer valid. The results in figure 7–57 show the variation in d for different values of the viscosity when $g_1 = 2.5 \times 10^{-4}$, $g_2 = 3.5 \times 10^{-4}$, $f = 1.4$ and $\lambda = 256$. Here the simulation results also show good agreement with the theory except at the highest values of the viscosity where, again, the size of the boundary layer is becoming significant compared to the wavelength. The results here suggest that, provided the size of the boundary layer (taken here to be $d/2$) is less than $\lambda/10$, there is good agreement between the expressions found from the theory and the simulation results. Figure 7–58 shows the value of d for different wavelengths when $g_1 = 2.5 \times 10^{-4}, g_2 = 3.5 \times 10^{-4}, f = 1.4$ and $\nu = 0.005$. A square grid was used here so $h_1 = h_2 = \sqrt{3}\lambda/2$ and $d \ll \lambda$ for each wavelength. Again a good fit is observed between the simulation points and the theory. The size of the boundary layer about the interface is seen, in figure 7–58, to increase with the wavelength when all other parameters are unchanged. Despite this increase in the size of the boundary layer the dimensionless size of the boundary layer d/λ, which is shown in figure 7–59, decreases with increasing λ. This is as expected since as λ, and hence the Reynolds number of the wave, is increased it is expected that the viscous effects become less significant. The profile of the vertical velocity at $t \simeq T/4$, $x = \lambda/2$ is also shown in figure 7–60 for the same waves. The viscosity has less affect on the vertical velocity and all the profiles have the same shape with a different amplitude. There is some small variations in w which can be observed near the solid boundaries of the waves with the larger wavelengths. These are similar to those observed in figure 7–55 and are also due to the initial separation of the interface. If it also possible that there may be a small residual oscillation from the initial settling of the density gradient. However, every care was taken to ensure this had damped out before the simulations were performed.

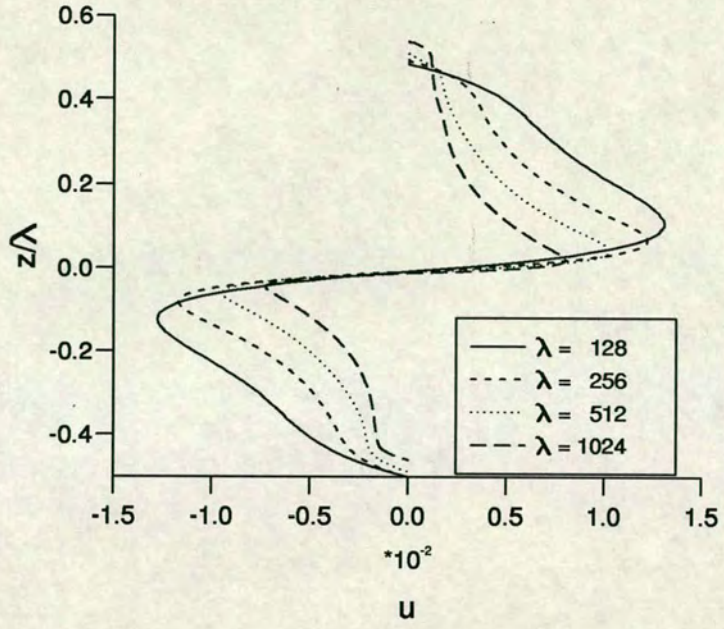

FIGURE 7–59: The horizontal velocity profile, at $x = \lambda/4$, $t \simeq T/4$, as a function of the dimensionless parameter z/λ. This is for waves with $g_1 = 2.5 \times 10^{-4}, g_2 = 2.5 \times 10^{-4}, f = 1.4$ and $\nu = 0.005$.

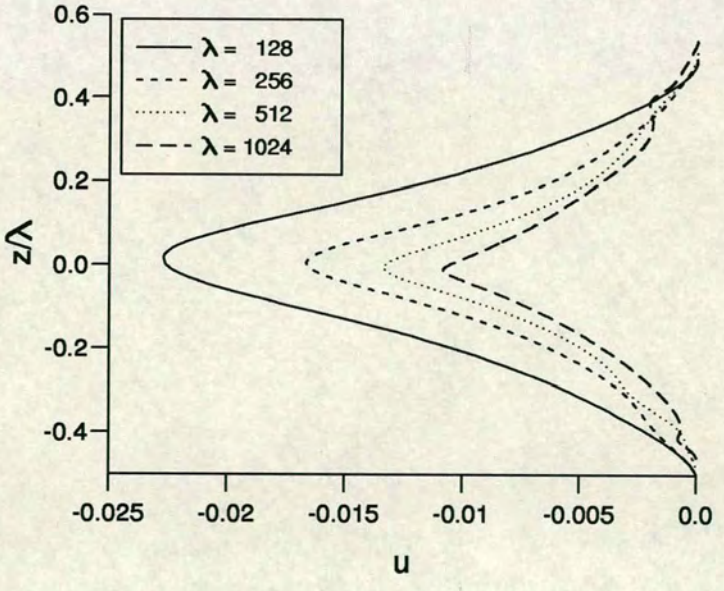

FIGURE 7–60: The vertical velocity profile, at $x = \lambda/2$, $t \simeq T/4$, as a function of the the dimensionless parameter z/λ. This is for waves with $g_1 = 2.5 \times 10^{-4}, g_2 = 2.5 \times 10^{-4}, f = 1.4$ and $\nu = 0.005$.

7.6 Summary

It has been seen that a standing wave can be initialised at the interface between two fluids. This can be done for a chosen wavelength and wave amplitude using the natural density gradient, correct for the values of g_i being used. This method of initialisation does not require that any velocities or a frequency are imposed on the wave. This means that any measured quantity has arisen solely from the wave motion. Many standing waves have been simulated for different values of the wavelength λ, the gravitational strengths g_1 and g_2, the density ratio f, the viscosity ν and the interface thicknesses l. The viscosity is varied through the relaxation time τ_ρ and the interface thickness is varied through the interfacial energy κ. The measured frequencies, damping constants and velocities were compared to the theoretical predictions. All the results for the frequency were found to be in good agreement with the theory; the damping constant was also seen to be in good agreement with the theory over a range of values where the theory is applicable. The measured velocities were also seen to agree well with theory.

Chapter 8

Interfacial Progressive Wave Simulations

In many situations it is progressive waves which are of interest, not the standing waves which were considered in the chapter 7. In this chapter we describe a method for initialising a progressive wave and present some simulation results. The progressive wave simulations are compared with the experimental interfacial waves of Martin *et al.* [10].

8.1 Progressive Wave Initialisation

It has been seen in chapter 6 that a progressive wave and a standing wave, with the same wavelength and amplitude, have the same z-dependence and a different x and t dependence. This means that we can use the results obtained in chapter 7 to initialise a progressive wave. This is done by first initialising a standing wave, as described in section 7.2, and allowing it to evolve for a quarter period. The magnitude of the horizontal velocity $\tilde{u}(z)$ is then found at $x = \lambda/4$ and the magnitude of the vertical velocity $\tilde{w}(z)$ at $x = \lambda/2$. The density profile $\rho(z)$ is found at any value of x. A progressive wave can then be initialised with density $\rho(x,z) = \rho(z)$ and velocities $u(x,z) = \tilde{u}(z)\sin(kx)$ and $w(x,z) = \tilde{w}(z)\cos(kx)$. The interface $\eta(x) = a\cos(kx)$ is imposed by shifting each column of sites by an amount $\eta(x)$ to produce the interface. Values shifted off the grid are discarded. Sites near the boundary which are not assigned a new value retain their original value.

8.2 Progressive Interfacial Waves

Progressive waves were simulated for some of the combinations of parameters used in chapter 7. Figures 8–1 – 8–10 show a progressive wave on a 256 by 256 site grid. The parameters used are $g_1 = 1.025 \times 10^{-4}$, $g_2 = 1.075 \times 10^{-4}, \kappa = 0.1, \lambda = 256$ and $\nu = 0.05$. The difference between the interface shown here where $\kappa = 0.1$ and the interface of the standing waves shown in, for example figure 7–3, where $\kappa = 0.001$ can be seen. Here there is a definite region around the interface where there is a mixture of the two fluids. This can be see in figures 8–1 – 8–10 as the grey region around the interface. This region is not there in figure 7–3 where the interface is much sharper.

8.3 Experimental Investigations into Progressive Interfacial Waves

The majority of experimental investigations into wave motion have been concerned with surface gravity waves rather than internal waves. This is because surface waves are easier to produce and measure in a wave tank and easier to measure in a field experiment. This is for a number of reasons.

1. It is easy to fill a tank, with a single fluid, in order to study surface waves. It is more complicated to produce a desired density distribution in the tank. The following methods can be used to produce a density difference.

   (a) Two different liquids can be used. This has the drawback that the surface tension between the two liquids can act to damp the waves. This does not happen in the ocean or the atmosphere where the density difference is produced by a thermocline or a salinity change.

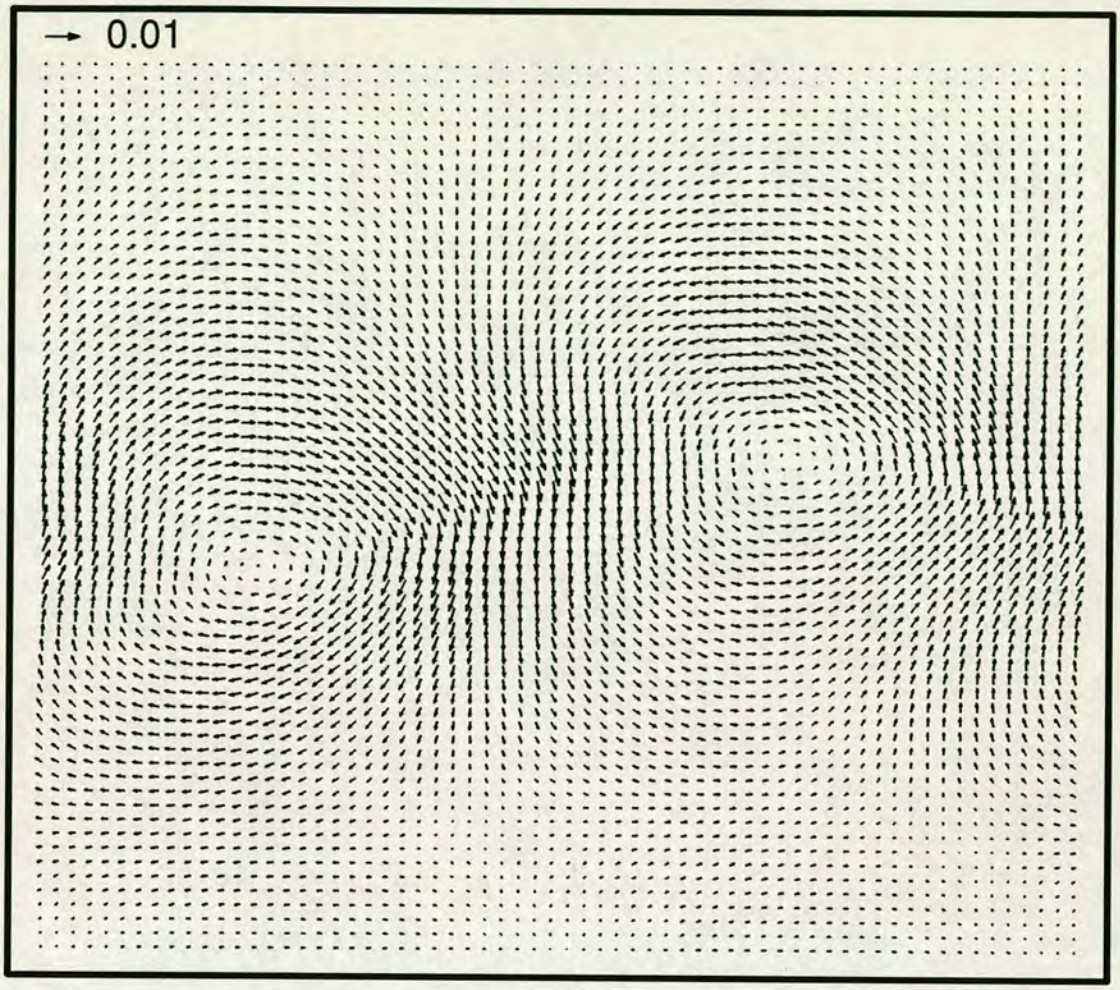

FIGURE 8–1: Velocity vector plot at $t \simeq T/5$ of an interfacial progressive wave on a 256 by 256 grid with $g_1 = 1.025 \times 10^{-4}$, $g_2 = 1.075 \times 10^{-4}$, $\kappa = 0.1$, $\lambda = 256$ and $\nu = 0.05$.

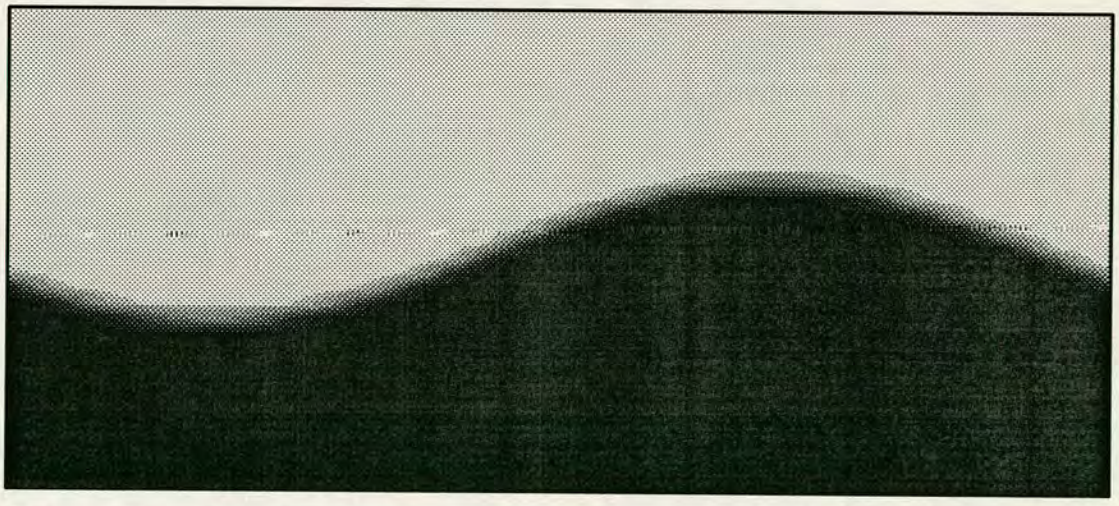

FIGURE 8–2: The order parameter at $t \simeq T/5$ of an interfacial progressive wave on a 256 by 256 grid with $g_1 = 1.025 \times 10^{-4}$, $g_2 = 1.075 \times 10^{-4}$, $\kappa = 0.1$, $\lambda = 256$ and $\nu = 0.05$. Only halve the grid, centred on the interface, is shown.

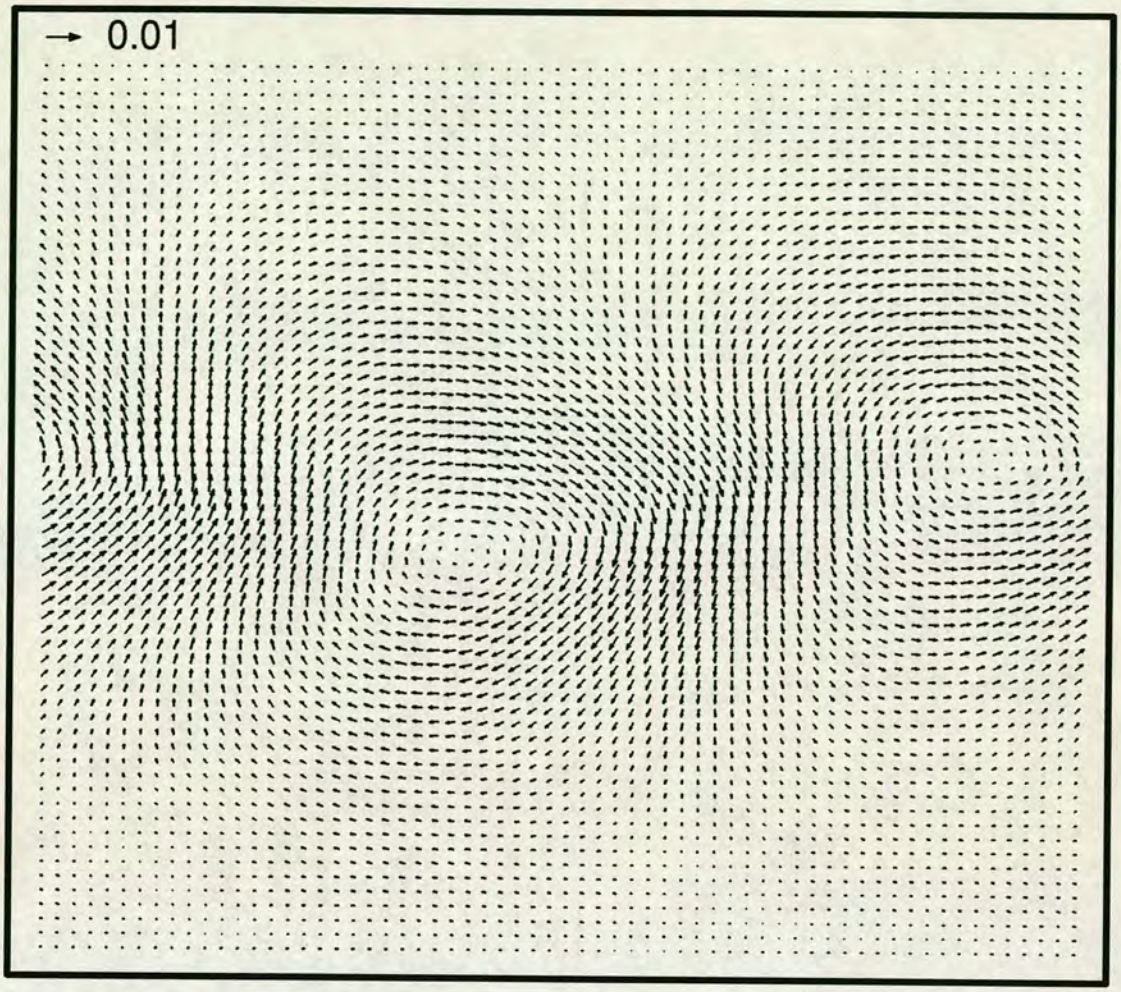

FIGURE 8–3: Velocity vector plot at $t \simeq 2T/5$ of an interfacial progressive on a 256 by 256 grid with $g_1 = 1.025 \times 10^{-4}$, $g_2 = 1.075 \times 10^{-4}, \kappa = 0.1, \lambda = 256$ and $\nu = 0.05$.

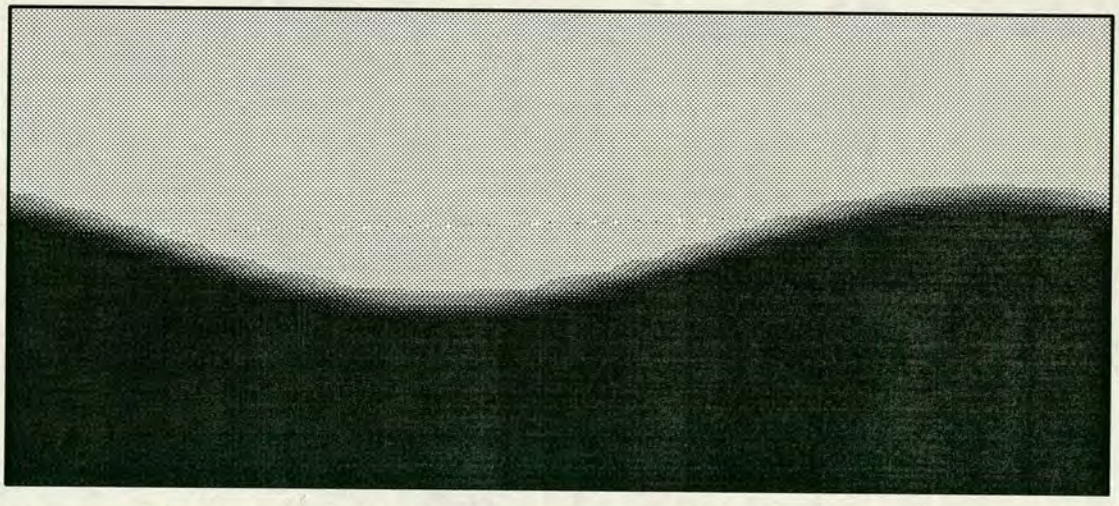

FIGURE 8–4: The order parameter at $t \simeq 2T/5$ of an interfacial progressive wave on a 256 by 256 grid with $g_1 = 1.025 \times 10^{-4}$, $g_2 = 1.075 \times 10^{-4}, \kappa = 0.1, \lambda = 256$ and $\nu = 0.05$. Only halve the grid, centred on the interface, is shown.

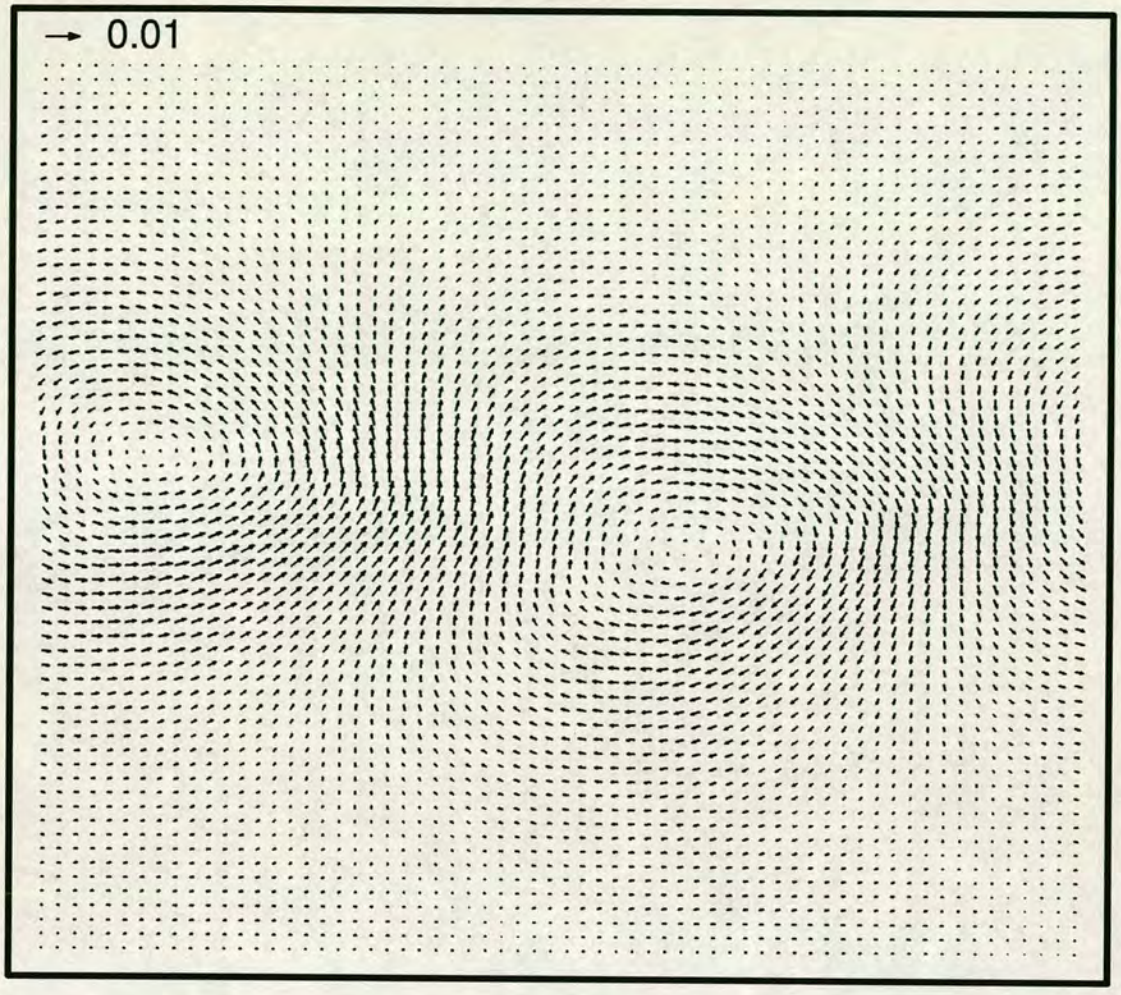

FIGURE 8–5: Velocity vector plot at $t \simeq 3T/5$ of an interfacial progressive wave on a 256 by 256 grid with $g_1 = 1.025 \times 10^{-4}$, $g_2 = 1.075 \times 10^{-4}$, $\kappa = 0.1$, $\lambda = 256$ and $\nu = 0.05$.

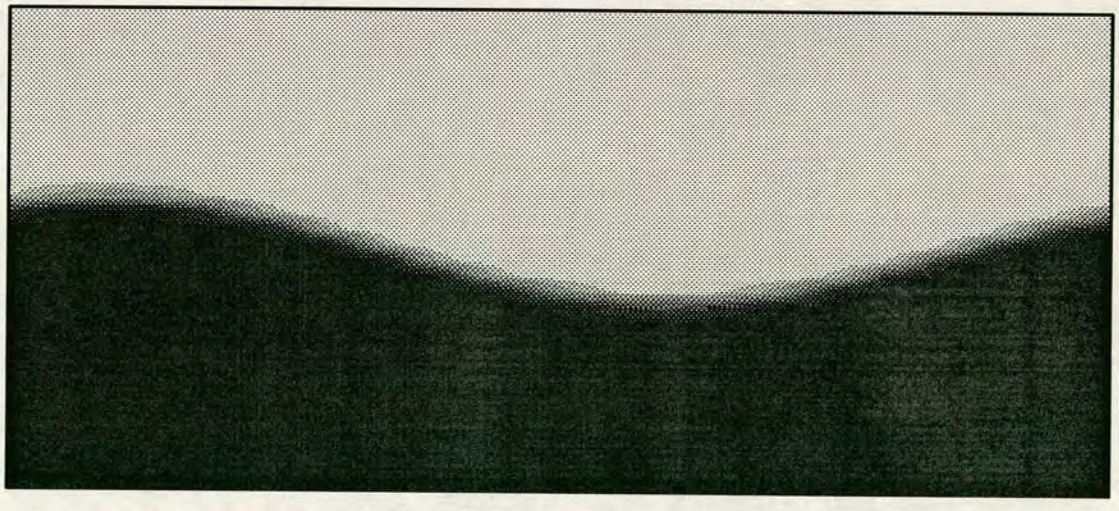

FIGURE 8–6: The order parameter at $t \simeq 3T/5$ of an interfacial progressive wave on a 256 by 256 grid with $g_1 = 1.025 \times 10^{-4}$, $g_2 = 1.075 \times 10^{-4}$, $\kappa = 0.1$, $\lambda = 256$ and $\nu = 0.05$. Only halve the grid, centred on the interface, is shown.

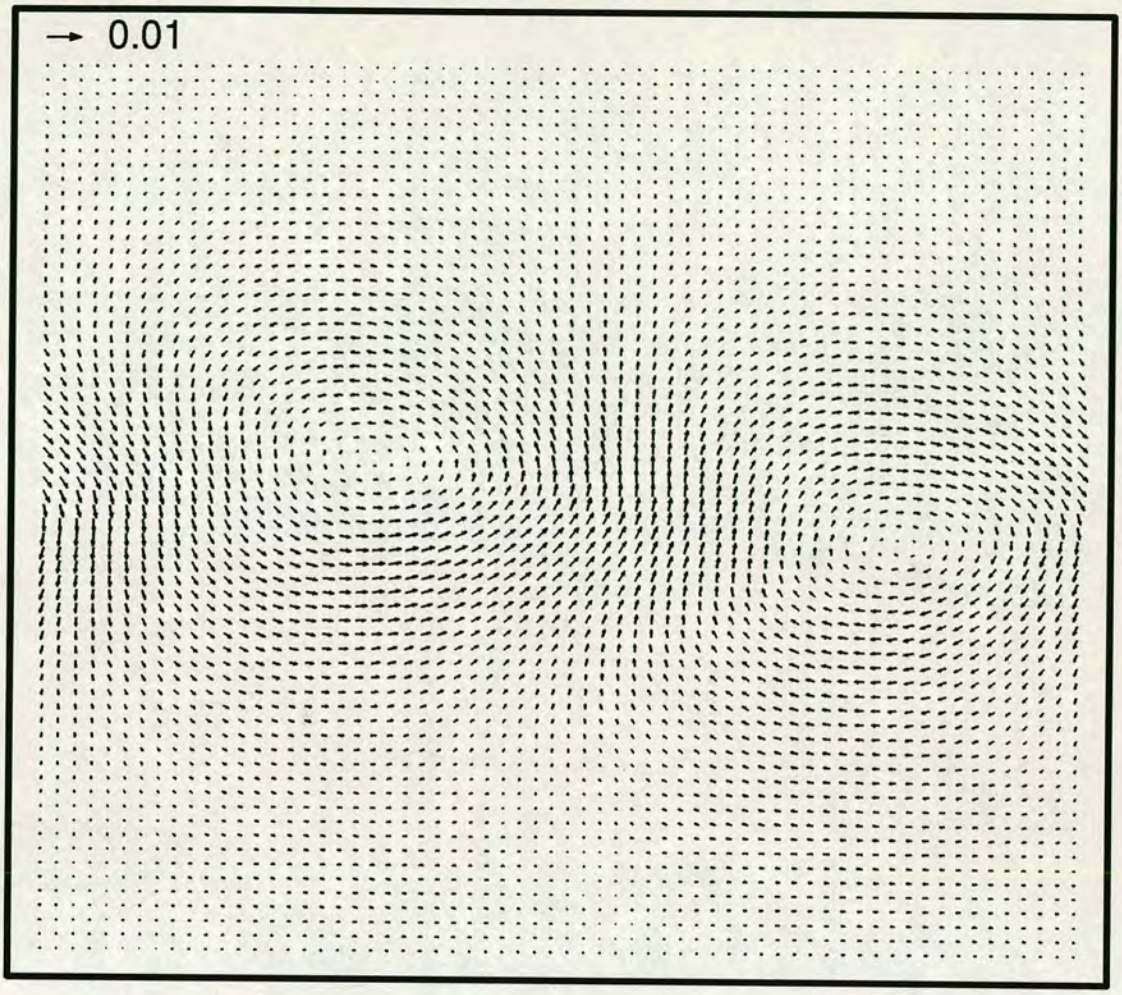

FIGURE 8–7: Velocity vector plot at $t \simeq 4T/5$ of an interfacial progressive wave on a 256 by 256 grid with $g_1 = 1.025 \times 10^{-4}$, $g_2 = 1.075 \times 10^{-4}$, $\kappa = 0.1$, $\lambda = 256$ and $\nu = 0.05$.

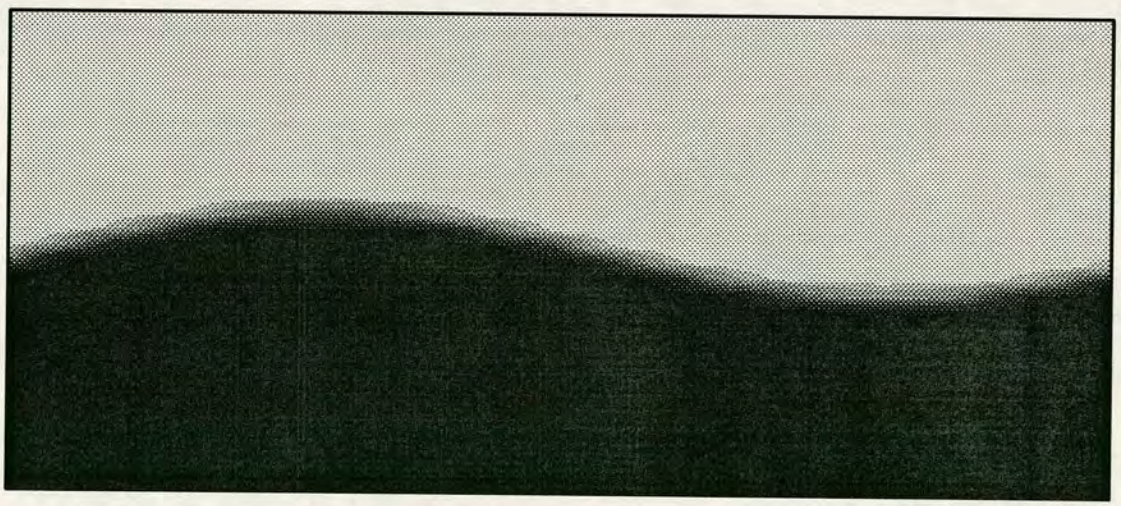

FIGURE 8–8: The order parameter at $t \simeq 4T/5$ of an interfacial progressive wave on a 256 by 256 grid with $g_1 = 1.025 \times 10^{-4}$, $g_2 = 1.075 \times 10^{-4}$, $\kappa = 0.1$, $\lambda = 256$ and $\nu = 0.05$. Only halve the grid, centred on the interface, is shown.

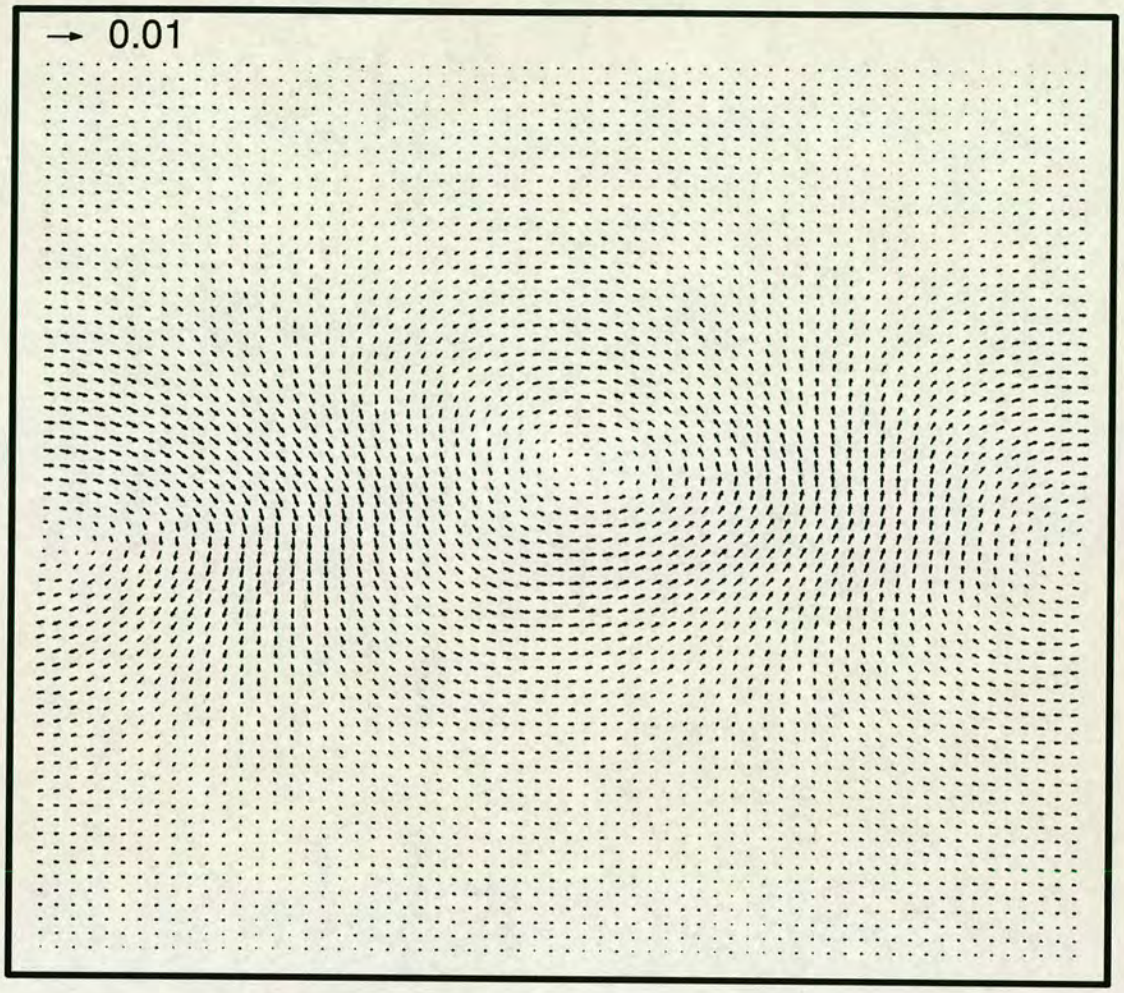

FIGURE 8–9: Velocity vector plot at $t \simeq T$ of an interfacial progressive wave on a 256 by 256 grid with $g_1 = 1.025 \times 10^{-4}$, $g_2 = 1.075 \times 10^{-4}$, $\kappa = 0.1$, $\lambda = 256$ and $\nu = 0.05$.

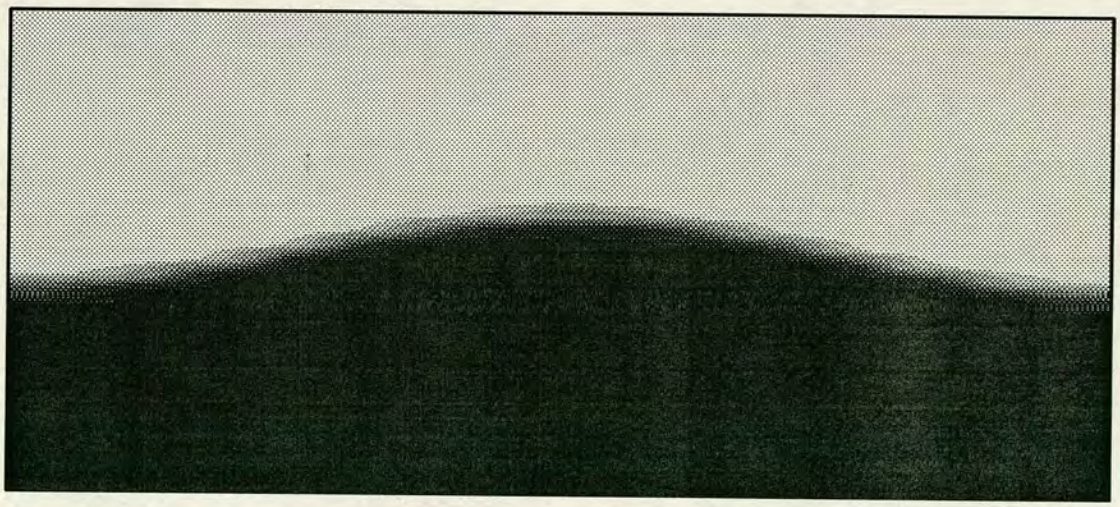

FIGURE 8–10: The order parameter at $t \simeq T$ of an interfacial progressive wave on a 256 by 256 grid with $g_1 = 1.025 \times 10^{-4}$, $g_2 = 1.075 \times 10^{-4}$, $\kappa = 0.1$, $\lambda = 256$ and $\nu = 0.05$. Only halve the grid, centred on the interface, is shown.

(b) A change in the density can be introduced by using a saline solution for the denser fluid and pure water for the less-dense fluid. Such a configuration is stable but the tank will need to be emptied and refilled at regular intervals. This can be very time consuming particularly if more than two layers are being used. Each layer, with its own salinity, must be allowed to settle before the next layer is added. The fluid must enter the tank at a slow speed so that it does not mix with the other layers.

2. Surface waves can be produced in the laboratory using a paddle system at one end of the tank, the movement of the paddle initialising the wave motion, which then propagates along the tank. If interfacial waves are to be produced the wavemaker normally moves in a vertical plane and the mean position of the wavemaker is matched to the interface height.

3. The high rate of damping observed in interfacial waves means that the measurement area must be close to the production area to prevent the wave being excessively damped. This is not a problem with surface waves.

4. Measurements of the wave amplitude can be made, in a laboratory or in a field experiment, either using a floating buoy or using a wave gauge which measures the resistance, or capacitance, between two metal probes and relates it to the immersed length of the probes. More complex methods need to be used for internal waves.

Early investigations were carried out [85,86] by dying one of the fluids and making photographic records of the waves in the tank. This allows the shape of the interface to be measured. The movement of the wave down the tank can also be found. To obtain information about the wave velocities it is preferable to use a non-intrusive measuring technique. Until relatively recently the main technique

for measuring the velocity in a multi-layer fluid has been laser Doppler anemometry (LDA) [87,88]. LDA can be used to measure the velocity of a fluid at a single point were two laser beams intersect. The main drawback of the LDA technique is that it can only make a measurement at one position in space. To record velocities at different positions the apparatus must be realigned to each position. The flow must be repeatable since each measurement is being taken at a different time. There are additional problems associated with LDA applied to a multi-layer systems because of the change in the refractive index within the flow [89]. This can be overcome, to some extent, if the density difference is small. Hannoun *et al.* [90,91] suggest that, provided a suitable solvent is used, the refractive indices can be matched between the layers of a two layer system for density differences of up to 2%. The matching technique allows LDA measurements to be made.

A recent development in measurement technology was the development of particle image velocimetry (PIV) [92]. This uses a pulsed bean laser or a continuous laser beam which is scanned across the fluid, illuminating a vertical plane. Small, neutrally buoyant particles are suspended in the fluid. The laser light reflected from the particles is recorded on film, each frame containing several images of each particle from successive pulses or scans of the laser. This information can then be analysed to produce a two-dimensional velocity map in the plane which was illuminated by the laser. PIV has been applied widely to surface gravity waves [93] but has only recently been applied to internal waves. One of the difficulties encountered in applying PIV to internal waves is the presence of zero and low velocities where the suspended particles move an insignificant distance, relative to their size, between exposures. This is overcome using an image shifting technique [94], this also eliminates any directional ambiguity in the velocity. Such a PIV system was employed at Edinburgh University to produce the experimental results [10] which will be compared with the simulations in the rest of this chapter.

8.4 Comparison Between Interfacial Wave Simulations and Experimental Results

The following comparison is between two interfacial waves: wave (a) which was generated in a wave tank [10] and wave (b) which was simulated using the lattice Boltzmann model described above.

8.4.1 Wave Parameters

Density Profile

Wave (a) has a density profile

$$\rho = \overline{\rho}\left[1 - \alpha \tanh\left(\frac{2z}{l}\right)\right] \tag{8.1}$$

where $\overline{\rho} = 1044$ kgm^{-3}, $\alpha = 0.044061$ and l, the interface thickness, is 0.0192m. Away from the interface the asymptotical densities are $\rho_1 = 998$ kgm^{-3} and $\rho_2 = 1090$ kgm^{-3}. The potential density can be considered as being the same as the fluid density here. Wave (b) has $\kappa = 0.1$ which gives an interface width of $l \simeq 10$lu. In the upper fluid the density is proportional to g_1 and in the lower fluid it is proportional to g_2. In the interface region we expect the density to vary in a smooth manner, similar to that shown in figure 4–6 for the order parameter. Away from the interface the ratio of the potential densities is $\rho_2/\rho_1 = 1.118$.

Dimensional Parameters

The wave parameters for the two waves and the units they are measured in are shown in table 8–1.

Dimensionless Parameters

There are a number of dimensionless parameters which can be derived from table 8–1. These are shown in table 8–2 and are an exhaustive set. Any other

	wave (a)		wave (b)	
parameter	value	unit	value	unit
h_1	0.245	m	414	lu
h_2	0.254	m	610	lu
λ	0.740	m	1024	lu
k	8.49	m^{-1}	6.14×10^{-3}	lu^{-1}
ω	1.88	s^{-1}	1.73×10^{-3}	$(\text{time-steps})^{-1}$
ν	1.0×10^{-6}	$m^2 s^{-1}$	0.05	$lu^2(\text{time-steps})^{-1}$
δ	7.28×10^{-4}	m	5.37	lu
g	9.80	ms^{-1}	9.0×10^{-3}	$lu\ (\text{time-steps})^{-1}$
a	0.0148	m	17.3	lu
c	0.222	ms^{-1}	0.282	$lu\ (\text{time-steps})^{-1}$
l	0.0881	m	10	lu

TABLE 8–1: The value of the parameters describing waves (a) and (b) and the units in which they are measured. The depth of the upper and lower fluids are h_1 and h_2 respectively, λ is the wavelength, k is the wavenumber, ω the frequency, ν the viscosity, δ is the boundary layer thickness $(\nu/\omega)^{1/2}$, g is the acceleration due to gravity, a is the wave amplitude, c is the wave celerity ω/k, and l is the interface thickness.

name	parameter	wave (a)	wave (b)	ratio a/b
	l/λ	0.119	9.77×10^{-3}	12.2
	a/λ	0.0200	0.0169	1.183
	kh_1	2.08	2.54	0.819
	kh_2	2.15	3.75	0.349
	f	1.09	1.12	0.977
Froude number (F)	$c\sqrt{k/g'}$	0.989	0.988	1.00
Reynolds number (Re)	$c/(k\nu)$	2.61×10^4	9.20×10^2	28.4

TABLE 8–2: The dimensionless parameters, derivable from the quantities in table 8–1, for the two waves being considered.

dimensionless parameter can be expressed in terms of these in table 8–2.

Comparison of Dimensionless Parameters

When comparing two waves, whether they are simulated results, experimental results from a wave tank, experimental results from a field experiment or theoretical predictions, the dimensionless parameters need to be matched. In practice it is not possible to have all the dimensionless parameters the same for both waves but they must be of a similar order. The ratios l/λ are not particularly well matched. The relative interface thickness is about twelve times larger for wave (a). This should affect the velocities near the interface, see figure 6–1. The different interface thicknesses should have little effect on the comparison since the experimental results are measured every 0.0125 m which is approximately $l/7$. The ratios a/λ are both small and of a similar size. This means that both waves can be considered to be linear waves. The values of kh_i are somewhat different for the two waves, however we are interested in $\tanh(kh_i)$. For both waves this is never smaller than 0.97 in either fluid so both waves can be considered as deep water waves. The values of f, the density ratio, are similar for both waves giving a density difference of about 10%. The internal Froude number [68] F is approximately unity for both waves. This is expected for deep waves through the dispersion relation. The Reynolds number Re, which can be taken to be $c/(k\nu)$, is different for both waves. The Reynolds number of wave (a), the experimental wave, is almost thirty times the Reynolds number of wave (b), the simulated wave. Both Reynolds numbers are however large. The Reynolds number appears in the Navier-Stokes equation as a measure of the balance between inertial and viscous terms. Since Re is large for both waves we expect viscous effects to be small in both waves but slightly larger in the simulated wave. The affect of the different Reynolds number on the two waves can most easily be seen through the ratio of the boundary layer thickness to the wavelength $\delta/\lambda = \sqrt{Re/(2\pi)}$. Wave (a) and wave (b) have $\delta/\lambda = 9.84 \times 10^{-4}$ and 5.24×10^{-3} respectively. Both are small, however the relative boundary layer thickness of the simulated waves is about five times larger. The boundary layer thickness is considerably smaller than the spacing of the experimental results.

8.4.2 Numerical Comparisons

The experimental results [10] are shown in figures 8–11 and 8–13 at two different times. The simulated results are shown in figures 8–12 and 8–14 for areas with the same dimensionless size. The separation between the simulated results plotted is 16lu. The results plotted are the dimensionless velocities, $\boldsymbol{u}/c$. The axis have been picked so that $z = 0$ is the mwl, as before, and $x = 0$ is at a trough. When comparing the simulation results and the experimental results it should be realised that the spacing between the vectors is different. The separation between the experimental results is 0.0125m, giving about 59 points per wavelength in both directions. The simulation results are plotted every 16 sites. That gives 64 vectors per wavelength in the x-direction and 74 vectors per wavelength in the z-direction. Thus, since the dimensionless areas are the same in both plots, the simulated results have slightly more vectors in the horizontal direction and considerably more in the vertical direction. This means that the length of the vectors should be compared and not the closeness of packing.

The velocity profile was found for the experimental and the simulation results. The horizontal profile is shown in figure 8–15 for the results at the wave trough and in figure 8–16 at the wave crest. The vertical velocity profile at $x = \lambda/4$, the midpoint between the crest and the trough, is shown in figure 8–17. The vertical velocities, displayed in figure 8–17, show good agreement between the simulation results and the experimental results. There is clearly some degree of uncertainty in the experimental results. The horizontal results, shown in figures 8–15 and 8–16, are qualitatively similar, however quantitatively there are some discrepancies. In each of the three sets of measurements the horizontal velocities in one of the fluids agree well, while in the other fluid the magnitude of the experimental results are somewhat smaller than the simulation results. As figure 8–15 demonstrates it is not always the same fluid which contains the discrepancy. This effect can also be seen in figures 8–11 and 8–13 where the magnitude of the horizontal velocity above and below the troughs and crest are different. The difference between the two sets of experimental results in figure 8–15 and the fact that theory predicts

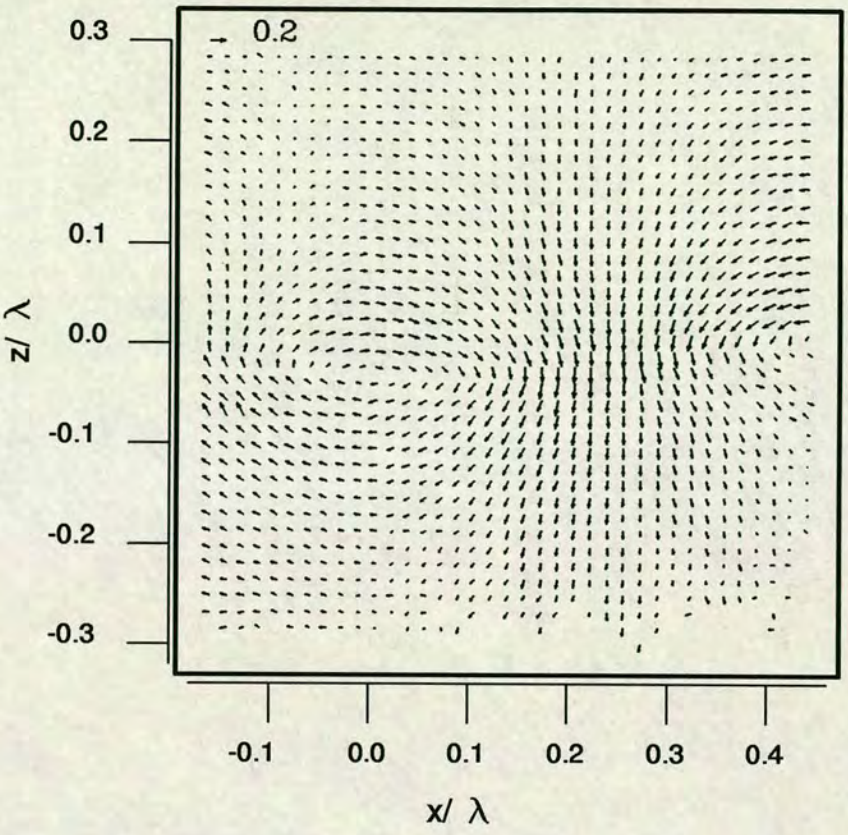

FIGURE 8–11: Vector plot of the dimensionless velocity $\boldsymbol{u}/c$ for wave (a).

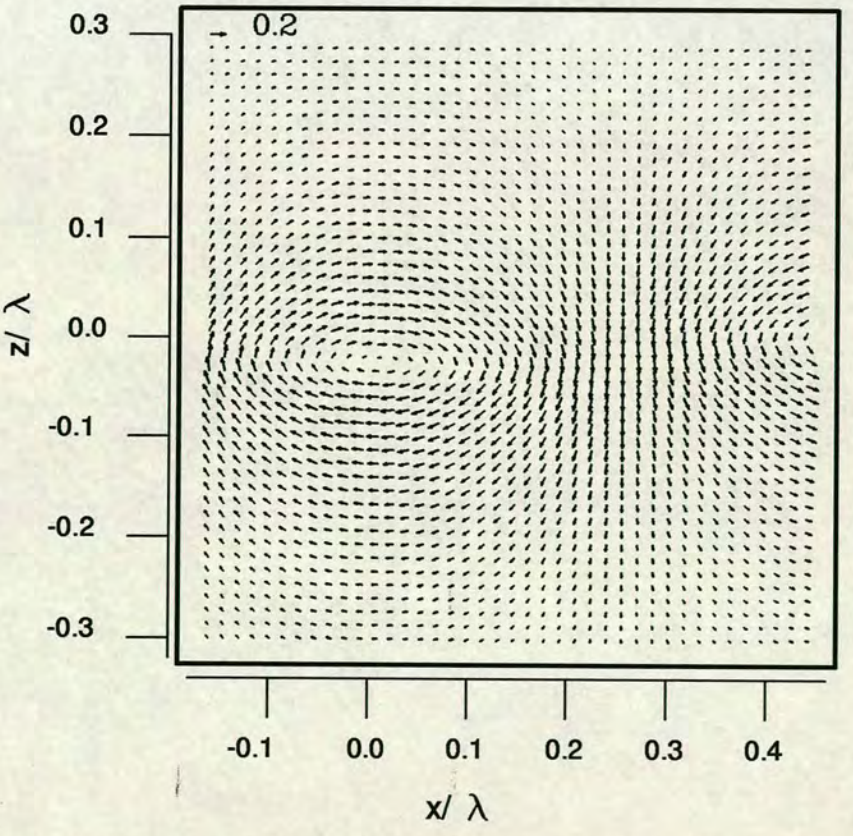

FIGURE 8–12: Vector plot of the dimensionless velocity $\boldsymbol{u}/c$ for wave (b).

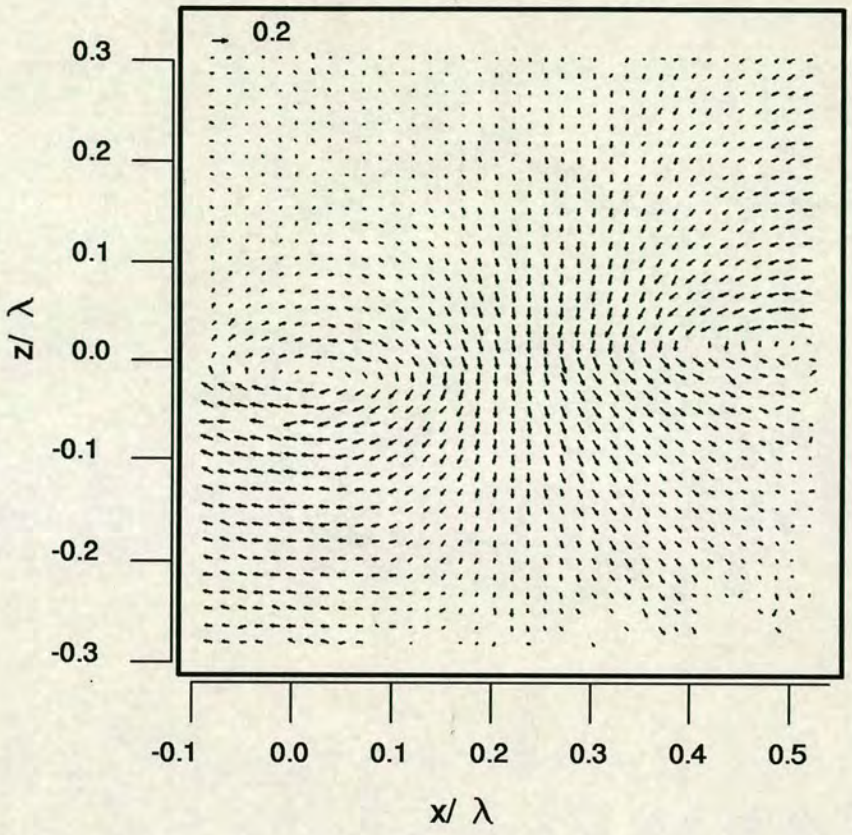

FIGURE 8–13: Vector plot of the dimensionless velocity $\boldsymbol{u}/c$ for wave (a).

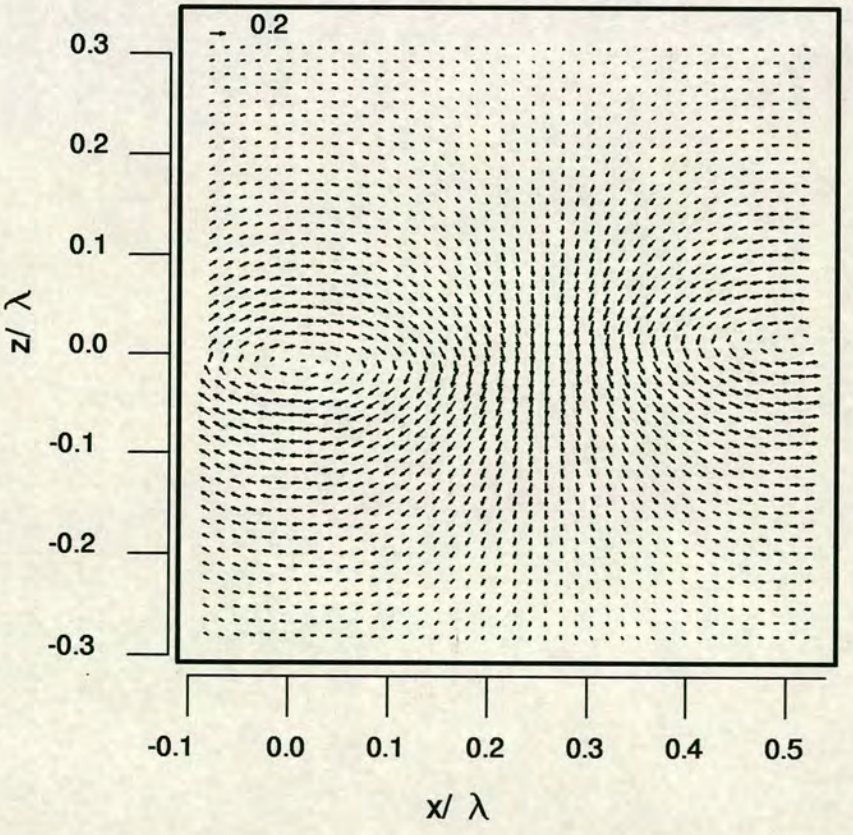

FIGURE 8–14: Vector plot of the dimensionless velocity $\boldsymbol{u}/c$ for wave (b).

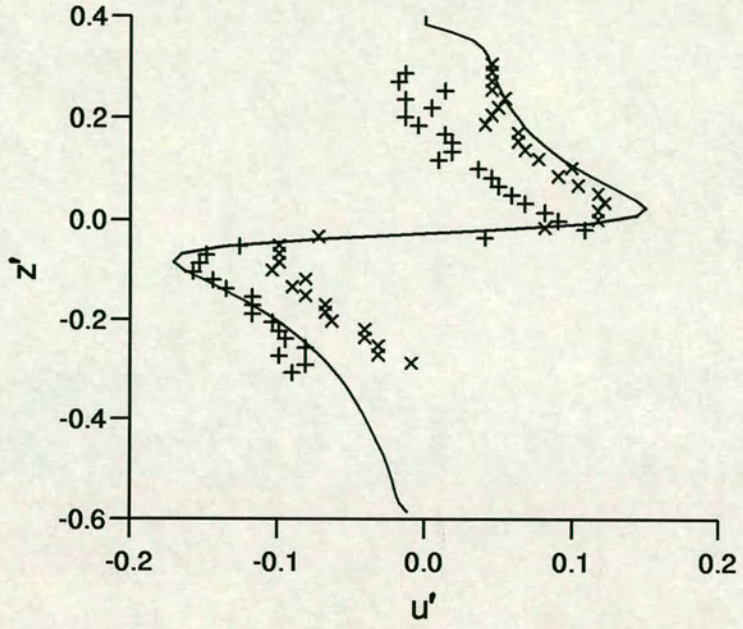

FIGURE 8–15: The horizontal component of the dimensionless velocity $u' = u/c$ as a function of the dimensionless length z/λ for the two troughs shown in figure 8–11 ($\times$) and figure 8–13 ($+$). The solid line represents the simulation results.

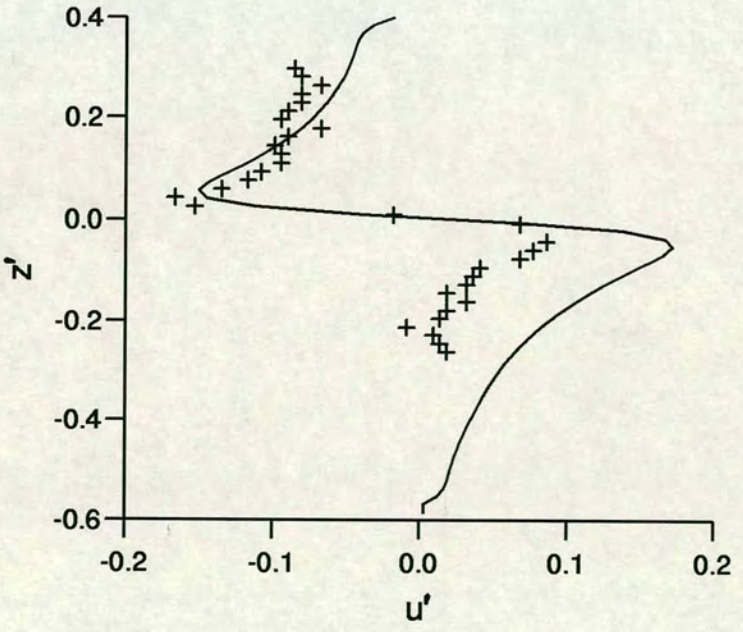

FIGURE 8–16: The horizontal component of the dimensionless velocity $u' = u/c$ as a function of the dimensionless length z/λ for the crest shown in figure 8–13 ($+$). The solid line represents the simulation results.

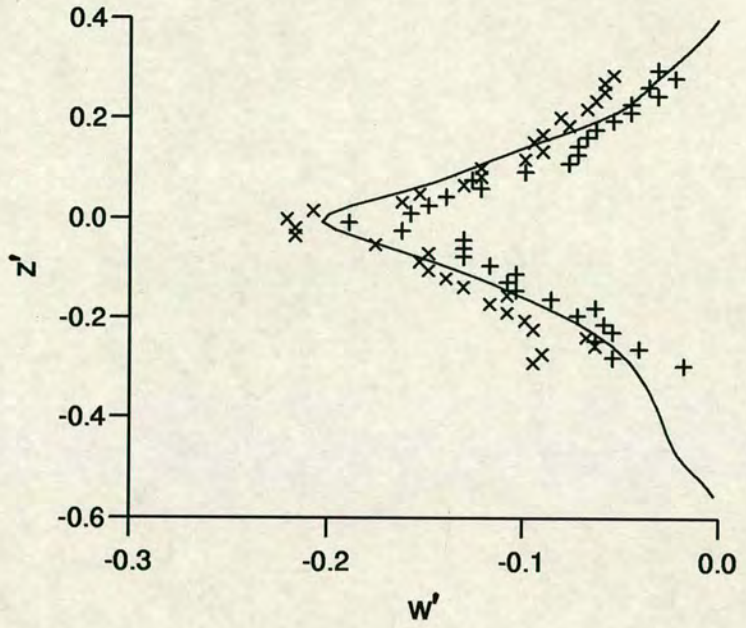

FIGURE 8–17: The vertical component of the dimensionless velocity $w' = w/c$ as a function of the dimensionless length z/λ at $x = \lambda/4$ shown in figure 8–11 ($\times$) and figure 8–13 ($+$). The solid line represents the simulation results.

only a small difference close to the interface, suggest that the discrepancy is due to some problem with the experimental results rather than the simulations. There are a number of sources which can introduce errors into the experimental results. The most likely cause is the image shifting system which is imposing a horizontal shift velocity onto the flow [94]. This velocity is considerably larger than the flow velocity and may be slightly irregular. Despite these errors the vertical profile is seen to fit well with the experimental results. The horizontal velocity shows the same qualitative features and the comparison is as good as can be expected, given the uncertainties in the experimental results. It is interesting to note that despite the difference in the Reynolds number there is little difference is the shape of the horizontal velocity close to the interface. This could be partly due to the difference in the interface thicknesses.

8.5 Summary

We have considered the initialisation of a progressive wave using the results which has previously been obtained from the standing wave simulations. Some results have been presented for the progressive waves. A comparison has been made between the simulated waves and experimental waves [10]. The results were seen to be in qualitative agreement. A quantitative comparison was less convincing, due to the large variation in some of the experimental horizontal velocities. The velocities were of a similar order.

Chapter 9

Conclusion

The relatively new numerical technique of lattice Boltzmann modelling has been applied to simulate interfacial internal waves. The model simulates two immiscible fluids, with the correct thermodynamical properties, separated by an interface. A body force can be incorporated in such a way that it can act with different strengths in the two fluids. The model is, at worst, very close to Galilean invariant and exhibits no dependence on the orientation of the lattice on which the model evolves. There are free parameters which allow the interface thickness, the fluid viscosity, the relative gravitational density of the two fluids and the strength of the gravitational body force to be altered. The technique has been used to simulate both standing and progressive interfacial waves for a range of the model parameters and also for different wavelengths. The main features of the work are discussed below.

Body Forces

The introduction of a body force into the lattice Boltzmann scheme has been studied. A number of techniques have been examined and a new method proposed which introduces a body force directly into the Boltzmann equation. The new method has been shown to act in a very similar way to an existing method and has been seen to have the expected effect on the fluid. The new method has been seen to be equally applicable to a single species and a two species fluid. The introduction of the body force has been shown to be independent of the orientation

of the lattice and has been shown to preserve the Galilean invariance of the lattice Boltzmann model.

Interfacial Wave Modelling

The body force was incorporated into the immiscible, binary fluid model of Orlandini *et al.* [9] and the combined model was used to simulate interfacial waves. The gravitational density of the two fluids can be changed by applying the body force with different strengths to each fluid. Standing waves were initialised at the fluid interface, with a given wavelength and amplitude, without any prior knowledge of the other properties of the wave. This means that measurements taken from the standing waves, at a later time, are in no way influenced by any velocity or oscillation imposed on the wave during the initialisation procedure. A large number of standing waves were simulated for a range of the available model and wave parameters. The frequency of the waves, the rate at which they are damped and the velocities produced by the wave motion were all recorded at selected times for each of the waves studied. Progressive waves were also simulated. These were initialised using the results obtain for standing waves under the same conditions. The frequency, damping parameter and velocities were measured for the progressive waves and found to be in agreement with those obtained for the standing wave simulations.

Comparison of Results with Theory and Experiment

The results obtained for the standing waves were compared with the theoretical values. Good agreement was found in all cases where the theory was applicable. The frequency results were found to be typically within 1% of the predicted values while the damping parameter was found to be about 4% different. The velocities were found to be in good agreement with the theoretical predictions, differing typically by only a few percent. The progressive waves were also compared with experimental results. Qualitatively the results matched well. The vertical velocities were found to compare well quantitatively; a quantitative comparison of the

horizontal velocities was not possible due to variations in the experimental results; the horizontal velocities were of a similar magnitude.

Model Strengths

The application of the lattice Boltzmann model to wave simulation has been successfully implemented. The algorithm, although complicated by the introduction of density and order parameter gradients needed to simulate the immiscible fluids, still has the underlying simplicity which allows it to be run efficiently on a parallel computer. This gives a high degree of performance. One of the main strengths of the model is that the boundary between the fluids appears naturally within the model. There is no need to keep track of the interface or to treat sites at the interface differently from the other fluid sites.

In summary, the application of the lattice Boltzmann technique to interfacial wave modelling has proved very successful. Interfacial internal waves have been simulated for a range of the model parameters and the measurements made from the simulations have been shown to agree well with the available wave theory. The waves have also been compared with experimental results and have shown good agreement within the limitations of the measurements.

Bibliography

[1] P. Roach. *Computational Fluid Dynamics.* Hermosa Publishing, 1972.

[2] J. Connor and C. Brebbia. *Finite Element Techniques for Fluid Flow.* Newnes-Butterworths, 1976.

[3] J. Dupuy and A. Dianoux. *Microscopic Structure and Dynamics of Liquids.* Plenum Press, 1978.

[4] J. Goodfellow. *Molecular Dynamics.* Macmillan Press, 1991.

[5] U. Frisch, B. Hasslacher, and Y. Pomeau. Lattice-gas automata for the Navier-Stokes equation. *Physical Review Letters*, 56:1505–1508, 1986.

[6] P. L. Bhatnagar, E. P. Gross, and M Krook. A model for collision processes in gases. I. Small amplitude processes in charged and neutral one-component systems. *Physical Review*, 94 (3):511–525, 1954.

[7] J. Buick, W. Easson, and C. Greated. Simulation of wave motion using a lattice gas model. *International Journal for Numberical Methods in Fluids*, 22:313–321, 1996.

[8] U. Frisch, D. d' Humières, B. Hasslacher, P. Lallemand, and Y. Pomeau. Lattice gas hydrodynamics in two and three dimensions. *Complex Systems*, 1:649–707, 1987.

[9] E. Orlandini, M. R. Swift, and J. M. Yeomans. A lattice Boltzmann model of binary-fluid mixtures. *Europhysics Letters*, 32 (6):463–468, 1995.

[10] A. J.. Martin, W. J. Easson, and C. A. Greated. Experimental study of oceanic internal waves using particle image velocimetry. In *ISOPE 95*, Delft, 1995.

[11] S. Chapman and T. G. Cowling. *The Mathematical Theory of Non-Uniform Gases.* Cambridge University Press, 1970.

[12] C. Cercignani. *Theory and Application of the Boltzmann Equation.* Scottish Academic Press, 1975.

[13] S. Harris. *An Introduction to the Theory of The Boltzmann Equation.* Holt, Rinehart and Winston INC., 1970.

[14] L. E. Reichl. *A Modern Course in Statistical Physics.* Edward Arnold (Publishing) LTD, 1980.

[15] E. G. D. Cohen. Fifty years of kinetic theory. *Physica A*, 194:229–257, 1993.

[16] J. Hardy, Y. Pomeau, and O. de Pazzis. Time evolution of two-dimensional model system I: invariant states and time correlation functions. *Journal of Mathematical Physics*, 14:1746–1759, 1973.

[17] J. Hardy, O. de Pazzis, and Y. Pomeau. Molecular dynamics of a classical lattice gas: Transport properties and time correlation functions. *Physics Review A*, 13:1949–1961, 1976.

[18] A. K. Gunstensen and D. H. Rothman. A Galilean-invariant immiscible lattice gas. *Physica D*, 47:53–63, 1991.

[19] D. d' Humières, P. Lallemand, and G. Searby. Numerical experiments on lattice gases: Mixtures and Galilean invariance. *Complex Systems*, 1:633–647, 1987.

[20] D. d' Humières, P. Lallemand, and U Frisch. Lattice gas models for 3D hydrodynamics. *Europhysics Letters*, 2:291–297, 1986.

[21] R. Cornubert, D. d' Humières, and D. Levermore. A Knudsen later theory for lattice gases. *Physica D*, 47:241–259, 1991.

[22] M. Hénon. In [8].

[23] M. Hénon. Viscosity of a lattice gas. *Complex Systems*, 1:763–789, 1987.

[24] S. Wolfram. Cellular automaton fluids 1: Basic theory. *Journal of Statistical Physics*, 45(3/4):471–529, 1986.

[25] P. Clavin, P. Lallemand, Y. Pomeau, and G. Searby. Simulations of free boundaries in flow systems by lattice-gas models. *Journal of Fluid Mechanics*, 188:437–464, 1988.

[26] A. K. Gunstensen and D. H. Rothman. A lattice-gas model for three immiscible fluids. *Physica D*, 47:47–52, 1991.

[27] V. Zehnlé and G Searby. Lattice gas experiments on a non-exothermic flame in a vortex field. *Le Journal De Physique France*, 50:1083–1097, 1989.

[28] D. H. Rothman and J. M. Keller. Immiscible cellular-automaton fluids. *Journal of Statistical Physics*, 52:1119–1127, 1988.

[29] C. Appert and S Zaleski. Lattice gas with a liquid-gas transition. *Physical Review Letters*, 64:1–4, 1990.

[30] C. Appert, D Rothman, and S Zaleski. A liquid-gas model on a lattice. *Physica D*, 47:85–96, 1991.

[31] D. d' Humières and P. Lallemand. Flow of a lattice gas between two parallel plates and development of the Poiseuille profile. *Computes Rendus de L'Académie des Sciences Paris*, 302:983, 1986.

[32] D. d' Humières, Y. Pomeau, and P. Lallemand. Simulation of 2-D Von Karman streets using a lattice gas. *Computes Rendus de L'Académie des Sciences Paris*, 301:423–426, 1985.

[33] D. d' Humières and P. Lallemand. Lattice gas automata for fluid mechanics. *Physica A*, 140:326–335, 1986.

[34] J. P. Boon and A. Noullez. Lattice gas hydrodynamics. In *Special Course on Modern Theoretical and Experimental Approaches to Turbulent Flow Structure and its Modelling.* AGARD (Advisory Group for Aerospace Research and Development) NATO, 1987.

[35] B. Wylie. *Application of Two-Dimensional Cellular Automaton Lattice-Gas Models to the Simulation of Hydrodynamics.* PhD thesis, The University of Edinburgh, 1990.

[36] R. Kenway, D. McComb, and B. Wylie. Results reproduced in [95].

[37] G. Searby, V Zenlé, and B Denet. Lattice gas mixtures and reactive flows. In *Discrete Kinetic Theory, Lattice Gas Dynamics and the Foundations of Hydrodynamics*, Torino, Italy, September 1988.

[38] M. R. Swift, E. Orlandini, W. R. Osborn, and J. M. Yeomans. Lattice Boltzmann simulation of liquid-gas and binary fluid systems. *Physical Review E*, 54 (5):5041–5052, 1996.

[39] G. R. McNamara and G. Zanetti. Use of the Boltzmann equation to simulate lattice-gas automata. *Physical Review Letters*, 61:2332–2335, 1988.

[40] F. J. Higuera and J. Liménez. Boltzmann approach to lattice gas simulations. *Europhysics Letters*, 9 (7):663–668, 1989.

[41] F. J. Higuera, S. Succi, and R. Benzi. Lattice gas dynamics with enhanced collisions. *Europhysics Letters*, 9 (4):345–349, 1989.

[42] M. Vergassola R. Benzi and S. Succi. On the hydrodynamic behaviour of the lattice Boltzmann equation. *Europhysics Letters*, 13 (5):411–416, 1990.

[43] S. Chen, H. Chen, D. Martinez, and W. Matthaues. Lattice Boltzmann model for simulation of magnetohydrodynamics. *Physical Review Letters*, 67 (27):3776–3779, 1991.

[44] Y. H. Qian, D. d' Humières, and P Lallemand. Lattice BGK models for Navier-Stokes equation. *Europhysics Letters*, 17 (6):479–484, 1992.

[45] H. Chen, S. Chen, and H. Matthaeus. Recovery of the Navier-Stokes equation using a lattice-gas Boltzmann method. *Physical Review A*, 45 (8):5339–5342, 1992.

[46] S. Chen, Z. Wang, X. Shan, and G. D. Doolen. Lattice Boltzmann computational fluid dynamics in three dimensions. *Journal of Statistical Physics*, 68 (3/4):379–400, 1992.

[47] R. D. Kingdon. A lattice BGK model for mimicking the Navier-Stokes equation for fluid flow in two dimensions. Technical Report AEA-InTec-1298, AEA Technology, 1993.

[48] l. D. Landau and E. M. Lifschitz. *Fluid Mechanics.* Pergamon, 1987.

[49] D. P. Ziegler. Boundary conditions for lattice Boltzmann simulations. *Journal of Statistical Physics*, 71 (5/6):1171–1177, 1993.

[50] D. R. Noble, J. G. Georgiadis, and R. O. Buckius. Direct assessment of lattice Boltzmann hydrodynamics and boundary conditions for recirculating flows. *Journal of Statistical Physics*, 81 (1/2):17–33, 1995.

[51] D. R. Noble, S. Chen, J. G. Georgiadis, and R. O. Buckius. A consistent hydrodynamic boundary condition for the lattice Boltzmann method. *Physics of Fluids*, 7 (1):203–209, 1995.

[52] P. A. Skordos. Initial and boundary conditions for the lattice Boltzmann method. *Physical Review E*, 48 (6):4823–4842, 1993.

[53] O. Behrand. Solid-fluid boundaries in particle suspension simulations via the lattice Boltzmann method. *Physical Review E*, 52 (1b):1164–1175, 1995.

[54] A. J. C. Ladd. Numerical simulations of particulate suspensions via a discretized Boltzmann equation. Part 1. Theoretical foundation. *Journal of Fluid Mechanics*, 271:285–309, 1994.

[55] A. J. C. Ladd. Numerical simulations of particulate suspensions via a discretized Boltzmann equation. Part 2. Numerical results. *Journal of Fluid Mechanics*, 271:311–339, 1994.

[56] A. K. Gunstensen, D. H. Rothman, A. Zaleski, and G. Zanetti. Lattice Boltzmann model of immiscible fluid. *Physical Review A*, 43 (8):4320–4327, 1991.

[57] D. Grunau, S. Chen, and K. Eggert. A lattice Boltzmann model for multiphase fluid flow. *Physics of Fluids A*, 5 (10):2557–2562, 1993.

[58] I. Halliday and C. M. Care. Steady state hydrodynamics of a lattice Boltzmann immiscible lattice gas. *Physical Review E*, 53 (2):1602–1612, 1996.

[59] E. G. Flekkøy. Lattice Bhatnagar-Gross-Krook models for miscible fluids. *Physical Review E*, 47 (6):4247–4257, 1993.

[60] X. Shan and H. Chen. Lattice Boltzmann model for simulating flows with multiple phases and components. *Physical Review E*, 47:1815–1819, 1993.

[61] X. Shan and H. Chen. Simulation of non-ideal gases and liquid-gas phase transitions by a lattice Boltzmann equation. *Physical Review E*, 49 (4A):2941–2948, 1994.

[62] X. Shan and G. Doolen. Multi-component lattice-Boltzmann model with interparticle interactions. *Journal of Statistical Physics*, 81 (1-2):379–393, 1995.

[63] M. R. Swift, W. R. Osborn, and J. M. Yeomans. Lattice Boltzmann simulation of nonideal fluids. *Physical Review Letters*, 75 (5):830–833, 1995.

[64] J. P. Gunton, M. San Miguel, and P. S. Sahni. The dynamics of first-order phase transitions. In Phase Transitions and Critical Phenomena, editors, *C. Domb and J. L. Lebowitz*, volume 8. Academic Press New York, 1983.

[65] J. S. Rowlinson and B. Widom. *Molecular Theory of Capillarity.* Clarendon Press, Oxford, 1982.

[66] N. S. Martys and H. Chen. Simulation of multicomponent fluids in complex three-dimensional geometries by the lattice Boltzmann method. *Physical Review E*, 53 (1):743–750, 1996.

[67] J. Lighthill. *Waves In Fluids.* Cambridge University Press, 1978.

[68] J. S. Turner. *Buoyancy Effects in Fluids.* Cambridge University Press, 1973.

[69] O. M. Phillips. *The Dynamics of the Upper Ocean.* Cambridge University Press, 1969.

[70] J. Turner. *Buoyancy Effects In Fluids.* Cambridge University Press, 1973.

[71] Ø. Arnsten. *Uniform Stratified Flow Interaction with a Submerged Horizontal Cylinder - a Revisit of 'deadwater' in a Norwegian Fjord.* PhD thesis, University of Trondheim (Norwegian Institute of Technology), 1990.

[72] R. Courant and D. Hilbert. *Methods in Mathematical Physics.* Interscience, 1953.

[73] Routine D02KEF. The NAG Fortran Library, Mark 14, 1990.

[74] W. J. Harrison. The influence of viscosity on the oscillations of superposed fluids. *Proceedings of the London Mathematical Society*, (2) 6:396–405, 1908.

[75] H. Lamb. *Hydrodynamics.* Cambridge University Press, 1962.

[76] J. N. Hunt. The viscous damping of gravity waves in shallow water. *La Houille Blanche*, 6:345–349, 1964.

[77] B. Johns. A boundary layer method for the determination of the viscous damping of small amplitude gravity waves. *Quarterly Journal of Mechanics and Applied Mathematics*, 21 (1):93–103, 1968.

[78] R. G. Dean and R. A. Dalrymple. *Water Wave Mechanics for Engineers and Scientists.* Prentice-Hall Inc., New Jersey, 1984.

[79] C. C. Mei and L.-F. Liu. The damping of surface gravity waves in a bounded liquid. *Journal of Fluid Mechanics*, 59 (2):239–256, 1973.

[80] R. A. Dalrymple and P. L.-F. Liu. Waves over soft muds: A two-layer fluid model. *Journal of Physical Oceanography*, 8:1121–1131, 1978.

[81] P. L-F. Liu. Damping of water waves over porous bed. *Journal of the Hydraulics Division*, 99:2263–2271, 1973.

[82] Routine E04HFF. The NAG Fortran Library, Mark 14, 1990.

[83] P. E. Gill and W. Murry. Algorithms for the solution of the nonlinear least-squares problem. *SIAM Journal of Numerical Analysis*, 15:977–992, 1978.

[84] Routine C04ADF. The NAG Fortran Library, Mark 14, 1990.

[85] S. A. Thorpe. On standing internal gravity waves of finite amplitude. *Journal of Fluid Mechanics*, 32(3):489–528, 1968.

[86] S. A. Thorpe. On the shape of progressive internal waves. *Philosophical Transactions A*, 263:563–614, 1968.

[87] Y. Yeh and H. Z. Cummins. Localized fluid flow measurements with an He-Ne laser spectrometer. *Applied Physics Letters*, 4(10):176–178, 1964.

[88] T. S. Durrani and C. A. Greated. *Laser Systems in Flow Measurement.* Plenum Press, 1977.

[89] T. J. McDougall. On the elimination of refractive index variations in turbulent density stratified flows. *Journal of Fluid Mechanics*, 93:83–93, 1979.

[90] I. A. Hannoun, H. J. S. Fernando, and E. J. List. Turbulent structure near a sharp density interface. *Journal of Fluid Mechanics*, 189:189–209, 1988.

[91] I. A. Hannoun and E. J. List. Turbulent mixing at a shear free density interface. *Journal of Fluid Mechanics*, 189:211–234, 1988.

[92] C. Gray and C. A. Greated. The application of particle image velocimetry to the study of water waves. *Optics and Lasers in Engineering*, 9:265–276, 1988.

[93] C. Gray, C. A. Greated, D. R. McClusky, and W. J. Easson. An analysis of the scanning beam PIV illumination system. *Journal of Physics E*, 2:717–724, 1991.

[94] C. Gray and C. A. Greated. Evolution of the particle image velocimetry flow measuring technique. *Strain*, pages 3–8, 1995.

[95] D. Wallace. Scientific computation on simd and mimd machines. *Philosophical Transactions of the Royal Society of London A*, 326:481–498, 1988.

[96] D. d' Humières and P. Lallemand. Numerical simulations of hydrodynamics with lattice gas automata in two dimensions. *Complex Systems*, 1:599, 1987.

Appendix A

Notation

α	damping parameter
α	half of the ratio density difference/ mean density
α_i	constants in a linear sum of the collision invariants
Γ	fluid mobility
$\Delta\rho$	density difference between two fluids, also known as the order parameter
$\mathit{\Delta}_i$	distribution function for $\Delta\rho$
$\overline{\mathit{\Delta}}_i$	equilibrium distribution function for $\Delta\rho$
$\mathit{\Delta}_i^{(a)}$	ath order approximation to $\mathit{\Delta}_i$
Δ_i	collision function for link i
$\Delta\mu$	chemical potential
$\Delta\boldsymbol{P}$	change in momentum
$\delta\rho$	density relative to a constant density
$\delta\rho$	density difference between simulations performed using different models
ϵ	Knudsen number
ϵ	small number
ξ	function of the deviation of the density from its equilibrium value
ξ	small displacement
η	displacement at interface
θ	scattering angle
θ	angle between velocity and x-axis
θ	angle between x-axis and x'-axis

θ_f	angle of the colour gradient
θ_i	angle between $\boldsymbol{e}_i$ and x-axis
κ	interfacial energy
Λ	strength of free energy, binary fluid interaction
λ	wavelength
λ	mean free path
λ	eigenvalue of the enhanced collision matrix
ν	kinematic shear viscosity
ζ	kinematic bulk viscosity
$\Pi_{\alpha\beta}$	momentum flux tensor
ρ	density
$\overline{\rho}$	mean density
ρ'	density fluctuation about mean
ρ_{pot}	potential density
ρ_0	initial density
ρ_0	constant density
σ	complex time scale of a wave in a viscous fluid
σ	differential cross section
σ	eigenvalue of the enhanced collision matrix
τ	relaxation time
τ_*	value of the order parameter relaxation time which gives Galilean invariance
τ	eigenvalue of the enhanced collision matrix
Φ	gravitational potential
ϕ	irrotational velocity potential
ϕ	azimuthal angle
χ	salinity
Ψ	free energy
ψ	bulk free energy
ψ_a	effective mass of ath component
ψ_i	collision invariant

ψ	rotational part of velocity solution
ψ	phase factor
Ω	collision function
$\mathrm{d}\Omega$	solid angle
ω	wave frequency
ω_0	wave frequency in an inviscid fluid
ω'	viscous correction to the inviscid frequency
ω_c	frequency of a wave in an inviscid fluid at a continuous density change
$\omega_{2\nu}$	frequency of a wave in a viscous fluid at a sharp interface
A	initial amplitude of wave
A	constant determining strength of surface tension
A	coefficient of the equilibrium distribution function
A	amplitude term of the velocity potential
A_0	coefficient of the equilibrium distribution function
$A(s \to s')$	probability of $s \to s'$ in a collision
$\mathcal{A}$	amplitude term
A	constant
a	amplitude of inviscid interfacial perturbation
a	coefficient of the equilibrium distribution function
a_0	coefficient of the equilibrium distribution function
a_θ	component of the enhanced collision function Ω_{ij}
a	constant determining strength of free energy liquid-gas interaction
a_i	bubble diameter in direction i
B	blue particle
B	coefficient of the equilibrium distribution function
$\mathcal{B}$	amplitude term
b	number of links
b	component of the enhanced collision function Ω_{ij}
b	impact parameter
b	coefficient of the equilibrium distribution function
b	constant determining strength of free energy liquid-gas interaction

$\mathcal{C}$	collision operator
$C(\boldsymbol{r}, t)$	colour density
C	coefficient of the equilibrium distribution function
C_0	coefficient of the equilibrium distribution function
C_i	constant
C_i'	constant
$\mathcal{C}$	amplitude term
$\boldsymbol{c}$	particle velocity
c	wave celerity
c	mean depth of lower fluid, found from curve fitting
c_s	speed of sound
c	coefficient of the equilibrium distribution function
c_0	coefficient of the equilibrium distribution function
c	component of the enhanced collision function Ω_{ij}
D	dimension of space
D	diffusion coefficient
D	coefficient of the equilibrium distribution function
$\mathcal{D}$	phase term
D	distance OP
d	mean density per link
d	vertical distance between the peaks of $\|u\|$
d_0	constant
d	coefficient of the equilibrium distribution function
d	distance of a point from the origin
E	equilibrium distribution
$\mathcal{E}$	evolution operator
E	$1/c^2$ in the Strum-Liouville equation
$\boldsymbol{e}_i$	unit vector in the direction of link i
$\boldsymbol{e}_z$	unit vector in the vertical direction
e	internal energy
e	sum of the squares of the deviation between the data points and the

	fitted curve, also known as the error parameter
$\boldsymbol{F}(\boldsymbol{r},t)$	body force per unit mass
$\boldsymbol{F}_a$	force on ath component in local interaction model
F	Froude number
F	coefficient of the equilibrium distribution function
$f(\boldsymbol{r},\boldsymbol{c},t)$	distribution function
$\overline{f}$	equilibrium distribution function
f^*	non-equilibrium component of the distribution function
$f^{(a)}$	ath order approximation to f
$f^{(r)}$	distribution function for 'red' fluid
$f^{(b)}$	distribution function for 'blue' fluid
$\overline{f}_i(0)$	distribution function of link i when $\boldsymbol{u}=0$
$\overline{f}_i^*(0)$	distribution function of link $1-6$ when $\boldsymbol{u}=0$
$\overline{f}_i^0(0)$	distribution function of link 0 when $\boldsymbol{u}=0$
f	ratio of fluid densities, ρ_2/ρ_1
f'	above ratio multiplied by $\sqrt{\nu_2/\nu_1}$
$\boldsymbol{f}$	colour gradient
f	coefficient of the equilibrium distribution function
f	Fermi-Dirac function
G	Galilean invariance factor
$G_{a\bar{a}}$	Greens function
$\mathcal{G}_{a\bar{a}}$	local component of Greens function
G	coefficient of the equilibrium distribution function
g	acceleration due to gravity
g'	reduced gravity
g_i	strength of gravity in fluid i
$g(\rho)$	Galilean invariance term
g	magnitude of particles relative velocity before a binary collision
g	coefficient of the equilibrium distribution function
H	function of the distribution function
H	amplitude term

H	constant
h_i	depth of fluid i
$h(\rho, \boldsymbol{u})$	Lagrange multiplier
$\mathcal{I}$	identity operator
$\boldsymbol{J}$	mean mass current
$\mathcal{J}$	implementation operator for the long range interaction
k	wavenumber
k_B	Boltzmann's constant
L	representative length scale
l	interface thickness
l	typical microscopic length
l	size of the grid
M_i	the ith moment of the equilibrium distribution
M	number of particles in an averaging cell
M_i	number of particles on link i in an averaging cell
m	particle mass
m_i	exponential vertical decay factor for the viscous part of the fluid velocity
m	number of links including rest links
m	gradient of line
N_i	mean population of link i
$\overline{N}_i$	equilibrium mean population of link i
$N_i^{(a)}$	ath order approximation to N_i
$N(z)$	Brunt-Väisälä frequency
N	total number of points considered
N	number of points considered in curve fitting
n_i	occupation number of link i
O	origin
$P_{\alpha\beta}$	pressure tensor
$\boldsymbol{P}$	momentum
P	function in the Strum-Liouville equation
P	point just within the boundary

P	pressure incorporating a gravitational potential
p	pressure
p_0	isotropic part of $P_{\alpha\beta}$
p_0	reference pressure
$p_{\alpha\beta}$	stress tensor
$Q_{\alpha\beta}$	tensor
Q	function in the Strum-Liouville equation
$\boldsymbol{q}$	heat flux
q	concentration of particles
$\boldsymbol{q}$	local colour flux
$q(\rho, \boldsymbol{u})$	Lagrange multiplier
Re	Reynolds number
R	red particle
R	function in the Strum-Liouville equation
R	separation of sites participating in the long range interaction
$\boldsymbol{r}$	position vector
$\mathcal{S}$	streaming operator
$S_{\alpha\beta}$	tensor containing the viscous terms in the lattice gas Navier-Stokes equation
S	number of fluid components
S	entropy
sg_i	gravitational strength parameter in fluid i
s	in-state of a collision
s'	out-state of a collision
s_i	ith component of in-state
s'_i	ith component of out-state
$\mathrm{d}\boldsymbol{s}$	infinitesimal surface
T	wave period
T	temperature
$T_{i\alpha\beta\gamma\delta}$	four-dimensional tensor
t	time

$\boldsymbol{U}$	rotational velocity
U	horizontal component of $\boldsymbol{U}$
$\mathcal{U}$	amplitude of the horizontal velocity for a wave on a continuous density gradient
U	representative velocity scale
$\boldsymbol{u}$	fluid velocity
u	horizontal component of $\boldsymbol{u}$
$\boldsymbol{u}_0$	inviscid velocity
u_0	horizontal component of $\boldsymbol{u}_0$
$\boldsymbol{u}_0$	peculiar velocity
$\tilde{u}$	horizontal velocity magnitude
$\boldsymbol{u}'$	dimensionless horizontal velocity, $\boldsymbol{u}/c$
u'	dimensionless horizontal velocity, u/c
$\boldsymbol{u}^*$	equilibrium velocity
$\boldsymbol{u}'$	common equilibrium velocity
$\boldsymbol{u}$	mean velocity
u_x	velocity component parallel to x-axis
u_y	velocity component parallel to y-axis
u_l	horizontal velocity for a wave on a large grid
u_s	horizontal velocity for a wave on a small grid
V	interaction potential
$\boldsymbol{v}$	fluid velocity when the introduction of a body force is being considered
W	vertical component of $\boldsymbol{U}$
$\mathcal{W}$	amplitude of the vertical velocity for a wave on a continuous density gradient
W	work done by colour flux on colour gradient
w	vertical component of $\boldsymbol{u}$
w_0	vertical component of $\boldsymbol{u}_0$
$\tilde{w}$	vertical velocity magnitude
w'	dimensionless vertical velocity, w/c
w_l	vertical velocity for a wave on a large grid

w_s	vertical velocity for a wave on a small grid
x	coordinate of the lattice
x	horizontal coordinate
x'	coordinate at an angle to the standard x axis
y	coordinate of the lattice
y'	coordinate at an angle to the standard y axis
$Z(z)$	z-dependence of the velocity potential
z	vertical coordinate
z'	dimensionless vertical displacement, z/λ

Appendix B

FHP-III Collisions

The FHP-III collisions can be computed either using Boolean algebra [96], or using a lookup table. The Boolean equations used to calculate the new out-state and the lookup tables used are shown below.

B.1 Boolean Equations

If a_i, $i = \{0, ..., 6\}$ are boolean variables representing the presence or absence of particles in the links $\boldsymbol{e}_i$ then we can define:

$$\begin{aligned}
t_i &\stackrel{\text{def}}{=} a_i \oplus a_{i+1} \quad i = \{1, ..., 6\}, \\
u_i &\stackrel{\text{def}}{=} t_i \cdot t_{i+3} \quad i = \{1, 2, 3\}, \\
\gamma_i &\stackrel{\text{def}}{=} u_i \cdot (a_{i+1} \oplus a_{i+3}) \quad i = \{1, 2, 3\}, \\
\delta &\stackrel{\text{def}}{=} u_1 \cdot u_2 \cdot u_3, \\
\epsilon &\stackrel{\text{def}}{=} t_i \cdot t_{i+5} \cdot (a_o \oplus a_{i+1}) \quad i = \{1, ..., 6\}
\end{aligned} \tag{B.1}$$

where $a \cdot b$, $a + b$, $a \oplus b$ and $\overline{a}$ correspond to the *and*, *or*, *exclusive-or* and *not* operators respectively. Then c_i, the boolean variables representing the out-state, are given by [96]

$$\begin{aligned}
c_o &= \overline{\delta + (\gamma_1 + (\epsilon_1 \oplus \overline{\epsilon}_4)) \cdot (\gamma_2 + (\epsilon_2 \oplus \overline{\epsilon}_5)) \cdot (\gamma_3 + (\epsilon_3 \oplus \overline{\epsilon}_6))}, \\
c_i &= \delta + \overline{c}_0 \cdot (\gamma_i + \gamma_{i+2} \cdot \overline{\gamma}_{i+1}) + c_0 \cdot (\epsilon_{i+5} \oplus \epsilon_i \cdot \overline{\epsilon}_{i+2} + \epsilon_{i+1} \cdot \overline{\epsilon}_{i+3}) \quad i = \{1, 2, 3\}, \\
c_{i+3} &= \delta + \overline{c}_0 \cdot (\gamma_i + \gamma_{i+2} \cdot \overline{\gamma}_{i+1}) + c_0 \cdot (\epsilon_{i+2} \oplus \epsilon_{i+3} \cdot \overline{\epsilon}_{i+5} + \epsilon_{i+4} \cdot \overline{\epsilon}_i) \quad i = \{1, 2, 3\}
\end{aligned} \tag{B.2}$$

or

$$
\begin{aligned}
c_o &= \overline{\delta + (\gamma_1 + (\epsilon_2 \oplus \overline{\epsilon}_5)) \cdot (\gamma_2 + (\epsilon_3 \oplus \overline{\epsilon}_6)) \cdot (\gamma_3 + (\epsilon_1 \oplus \overline{\epsilon}_4))}, \\
c_i &= \delta + \overline{c}_0 \cdot (\gamma_{i+2} + \gamma_i \cdot \overline{\gamma}_{i+1}) + c_0 \cdot (\epsilon_{i+1} \oplus \epsilon_i \cdot \overline{\epsilon}_{i+4} + \epsilon_{i+5} \cdot \overline{\epsilon}_{i+3}) \quad i = \{1,2,3\}, \\
c_{i+3} &= \delta + \overline{c}_0 \cdot (\gamma_{i+2} + \gamma_i \cdot \overline{\gamma}_{i+1}) + c_0 \cdot (\epsilon_{i+4} \oplus \epsilon_{i+3} \cdot \overline{\epsilon}_{i+1} + \epsilon_{i+2} \cdot \overline{\epsilon}_i) \quad i = \{1,2,3\}.
\end{aligned}
\tag{B.3}
$$

B.2 Lookup Tables

Table B–1 shows the lookup tables used to calculate the collisions. Both the integer representation of the state and the particles present are shown. The first out-state is the one found from equation B.2 and the second from equation B.3.

in-state	out-state		in-state	out-state	
0	0	0	32	32	32
1	1	1	33	33	33
2	2	2	34	65	65
3	3	3	35	35	35
4	4	4	36	18	9
5	66	66	37	19	98
6	6	6	38	69	11
7	7	7	39	39	39
8	8	8	40	80	80
9	36	18	41	81	50
10	68	68	42	21	21
11	38	69	43	83	101
12	12	12	44	26	84
13	74	22	45	54	27
14	14	14	46	77	86
15	15	15	47	87	87
16	16	16	48	48	48
17	96	96	49	49	49
18	9	36	50	41	81
19	98	37	51	51	51
20	72	72	52	104	25
21	42	42	53	105	114
22	13	74	54	27	45
23	102	75	55	107	107
24	24	24	56	56	56
25	52	104	57	57	57
26	84	44	58	116	89
27	45	54	59	117	117
28	28	28	60	60	60
29	90	108	61	122	122
30	30	30	62	93	93
31	110	110	63	63	63

in-state	out-state		in-state	out-state	
64 	64 	64 	96 	17 	17 
65	34 	34	97 	97 	97
66 	5	5 	98	37 	19 
67 	67 	67 	99 	99 	99 
68 	10 	10 	100 	82 	73 
69 	11 	38	101 	43 	83 
70	70	70 	102	75	23
71	71	71	103	103	103
72	20	20	104	25	52
73	100	82	105	114	53
74	22	13	106	85	85
75	23	102	107	55	55
76	76	76	108	29	90
77	86	46	109	118	91
78	78	78	110	31	31
79	79	79	111	111	111
80	40	40	112	112	112
81	50	41	113	113	113
82	73	100	114	53	105
83	101	43	115	115	115
84	44	26	116	89	58
85	106	106	117	59	59
86	46	77	118	91	109
87	47	47	119	119	119
88	88	88	120	120	120
89	58	116	121	121	121
90	108	29	122	61	61
91	109	118	123	123	123
92	92	92	124	124	124
93	62	62	125	125	125
94	94	94	126	126	126
95	95	95	127	127	127

TABLE B–1: Collisions for the FHP-III model

Appendix C

Publications

The following paper [7] has been published in the International Journal for Numerical Methods in Fluids and is reproduced below.

INTERNATIONAL JOURNAL FOR NUMERICAL METHODS IN FLUIDS, VOL. 22, 313–321 (1996)

SIMULATION OF WAVE MOTION USING A LATTICE GAS MODEL

J. BUICK,* W. EASSON† AND C. GREATED*

*Department of Physics and Astronomy, † Department of Mechanical Engineering, The University of Edinburgh, James Clerk Maxwell Building, The King's Buildings, Mayfield Road, Edinburgh EH9 3JZ, U.K.

SUMMARY

The lattice gas model for simulating two-phase flow, proposed by Appert and Zaleski, has been modified by the introduction of gravitational interactions and the new model has been used to simulate standing wave patterns on the free surface of a fluid. The results compare well with linear theory.

KEY WORDS: lattice gas; cellular automata, wave modelling; standing waves

1. INTRODUCTION

1.1. Lattice gas modelling

In recent years lattice gas models have been used to model a variety of fluid phenomena such as flow round plates[1] and also more complicated simulations involving two or more fluids such as the Kelvin–Helmholtz instability[2] and the combustion of two gases to produce a third.[3]

Although less well developed than techniques such as finite difference and finite element solutions of the Navier–Stokes equation, the lattice gas approach has inherent advantages in the solution of complex phenomena such as wave motion through media with density gradients and in simulations where mixing or phase changes may occur.

The lattice gas model was first introduced by Frisch, Hasslacher and Pomeau (FHP).[4] Their formulation is the basis for the model used in our simulations and is described below. The FHP model consists of an ensemble of fluid 'particles' which move on an underlying hexagonal grid. Each particle moves along one of the six link directions d_α ($\alpha = 1, \ldots, 6$), where the direction d_α is given by $\cos(\pi\alpha/3 - \pi/6)\mathbf{i} + \sin(\pi\alpha/3 - \pi/6)\mathbf{j}$, as shown in Figure 1. The particles travel at unit speed, moving from one intersection point or site to a neighbouring site in each time step. Only one particle can travel along any one link at any time. At the end of each time step all the particles coming into a particular site are allowed to collide in such a way that the momentum and number of particles at that site are conserved. Particles then move off in their new directions at the beginning of the next time step. The general lattice gas model can be expanded to allow any number of rest particles to be present at each of the sites (d_0). In the following simulations the FHPIII model is used, which allows a maximum of one rest particle at each site.

The basic FHP collisions[5] are shown in Figure 2, where the left-hand column shows the incoming configurations and the righ-hand column shows the possible outcomes. Rest particles are represented by a solid sphere. When there is more than one possible outcome, one of these is selected at random.

CCC 0271–2091/96/040313–09

Received September 1993
Revised May 1995

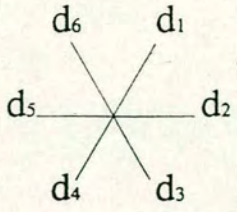

Figure 1. The six directions of the hexagonal lattice

The FHPIII collision rules are formed from the basic collisions, the basic collisions with a spectator particle (moving or at rest) and the dual of these collisions formed by swapping particles and empty links. Free slip conditions can be produced at a solid boundary by flipping all incoming particles in such a way that the particle momentum parallel to the boundary is conserved and the particle momentum perpendicular to the boundary is reversed.[6] Thus a particle approaching a horizontal free slip boundary along link d_6, see Figure 1 (travelling towards the site), will leave the site travelling along link d_1. Macroscopic fluid quantities such as velocity and density can be found by averaging the microscopic quantities over a cell typically no smaller than 16 sites by 16 sites.[5]

It can be shown[4,5] that for the FHPIII model the macroscopic collision rules satisfy the equations

$$\partial_t \rho + \sum_\alpha \partial_\alpha(\rho u_\alpha) = 0,$$

$$\partial_t(\rho u_\alpha) + \sum_\beta \partial_{x_\beta}[\rho g(d) u_\alpha u_\beta] = -\partial_{x_\alpha} P + \sum_\beta \partial_{x_\beta}[\nu(\rho)\partial_\beta u_\alpha],$$

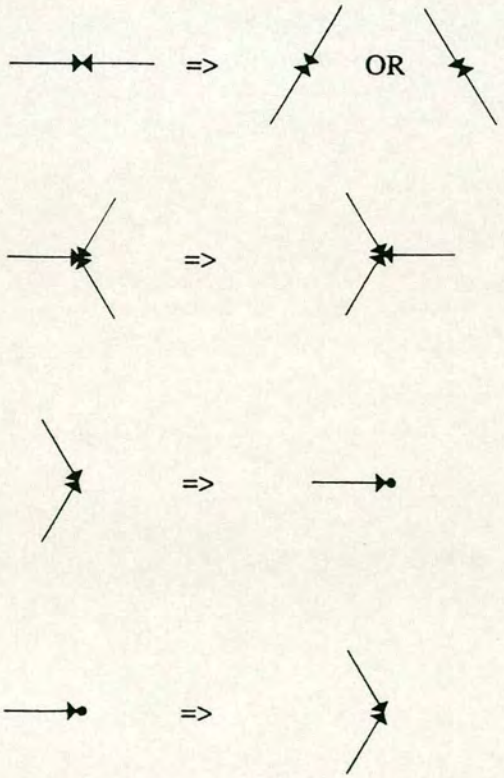

Figure 2. The basic FHP collision rules

where ρ is the density, P is the pressure, d is the density per link, $d = \rho/7$, ν is the bulk viscosity and $g(d) = 7(1 - 2d)/12(1 - d)$. These are the continuity equation and the Navier–Stokes equation with an extra factor g. The Navier–Stokes equation can be recovered by rescaling time, pressure and viscosity by g: $t' \to tg$, $P' \to P/g$, $\nu' \to \nu/g$.

1.2. Gravitational interactions

Gravitational interactions can be simulated by flipping a small number of particles after the collision from link d_1 to d_3 and from link d_6 to d_4, provided that there is not already a particle travelling in that direction. This interaction was introduced into the FHP model by allowing particles to be flipped every time step. The gravitational interaction is performed after the particles have collided and has the effect of decreasing the momentum in the y-direction while leaving the momentum in the x-direction unchanged. This interaction produces a density gradient across the fluid; however, this will not be particularly large provided that the number of gravitational interactions is small.[6] Here we restrict the number of such flips to be 0·5% of the total number of flips. This gives an average of $2{\cdot}5 \times 10^{-3}$ flips per site per time step. This is significantly smaller than the number of FHP collisions taking place: in a 25,000-time-step simulation there will only be on average 62·5 gravity flips perfomed at each site compared with an average of 15,000 FHP collisions.[1]

1.3 Liquid–gas model

A liquid–gas (LG) model is a lattice gas model which undergoes a phase separation producing separate light and dense phases. This phase separation is produced using interaction rules which were first introduced by Appert and Zaleski[7,8] and are shown in Figure 3. The interaction operates on two sites a distance IL apart in one of the directions d_1, d_2 or d_3 (Figure 3 shows the interaction rules acting in the direction d_2). Particles travelling along the links represented by the full arrows are flipped into the directions shown by the broken arrows provided that there are particles in both the initial links and no particles in either of the destination links. These interaction rules clearly conserve overall

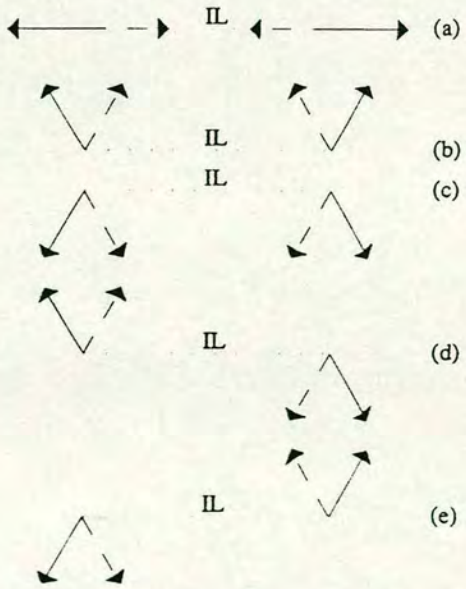

Figure 3. The long-range interaction

momentum, although they do not conserve the momentum at each site. The value of IL used in the following simulations was three lattice units.

1.4. Implementation of the model

The model was implemented on the Connection Machine (CM) 200 at The University of Edinburgh, the different interactions described above being implemented in the following order:

(1) FHPIII collision rules
(2) gravitational interactions
(3) interaction (a) in direction (i), direction (ii), then direction (iii)
(4) interaction (b) in direction (i), direction (ii), then direction (iii)
(5) interaction (c) in direction (i), direction (ii), then direction (iii)
(6) interactions (d) and (e) combined in direction (i), direction (ii), then direction (iii).

where directions (i), (ii) and (iii) are a random ordering of d_1, d_2 and d_3, the ordering being different for each of the four implementations (3)–(6) above. Interactions (d) and (e) are combined to prevent a net clockwise or anticlockwise rotation being imposed on the fluid.

1.5. Numerical modelling

One of the main advantages of the FHP model is its simplicity.

1. The state of the particles on the lattice need only be known at discrete time intervals. There is no need to track the particles when they are moving from one site to a neighbouring site.
2. The state of each site at any time step can be expressed as a 7 bit integer, one bit for each link taking the value 1 or 0 in the presence or absence of a particle on the link.
3. The FHP collisions can be implemented using a look-up table taking the initial particle configuration at the site (an integer in the range 0–127) and returning the new configuration after the collision. This removes the need to calculate the outcome of each collision.
4. Updating the lattice between time steps requires only a knowledge of the particle states at each of the six neighbouring sites. This is done by shifting the lattice in each of the six link directions.

When introducing the new interactions, it is important to try and keep the underlying simplicity of the FHP model. The gravitational interaction is perfomed by first selecting all the sites where the interaction can take place and then selecting a percentage (we used 0·5%) of these at which the interaction is allowed to take place. The interaction can be modelled using simple addition and subtraction: a particle being flipped from link 1 (integer value 2^1) to link 3 (integer value 2^3) results in $2^3 - 2^1$ being added to the integer representing the particles at the site. In practice it was found best to consider the two possible gravity flips ($d_1 \rightarrow d_3$ and $d_6 \rightarrow d_4$) separately.

In principle the Appert and Zaleski interactions can be implemented simply by first shifting the world IL units in the chosen direction and comparing the shifted configuration with the original configuration to see whether an interaction can take place. If an interaction can take place, this is done again using simple arithmetic, to the shifted lattice. Finally the grid is shifted back to its original position and the inverse arithmetic operation applied. Thus, for example, if interaction (a) of Figure 3 is to be applied to the sites (1, 1) and (1, 4), then site (1, 1) is first shifted three units to the right to position (1, 4). The two grids are then considered at the point (1, 4) to see whether the interaction can take place. This can only happen if bit5 = 1 and bit2 = 0 on the shifted grid and bit5 = 0 and bit2 = 1 on the original grid. The integer $2^5 - 2^2$ is then subtracted from the integer representation at the point (1, 4) on the shifted grid. The altered point (1, 4) is then shifted back to its original position (1, 1) and finally $2^5 - 2^2$ must be added to the integer representing the point (1, 4). This is done in parallel to all

points on the grid at the same time. If no interaction can take place, the integers at the points (1, 1) and (1, 4) remain unchanged. They may, however, be changed by one of the subsequent interactions.

The implementation of this interaction is complicated slightly by the need to randomize the order in which the interactions (a)–(e) are performed and also the order in which each interaction is perfomed along the three possible directions.

2. STANDING WAVE SIMULATIONS

The modified LG model was used to simulate standing waves on a 4096 × 256 grid. Continuous boundary conditions were used, with a solid free slip boundary placed at the bottom of the grid. Initially a standing wave was set up with wavelength 4096 units and depth 180 units. This was done by first allowing the fluid to settle, with a horizontal interface between the two phases at the mean water level (MWL). Area A shown in Figure 4 was then filled with stationary fluid of the same density as the fluid just below the MWL, while areas B were filled with stationary fluid of the same density as the fluid just above the MWL. The standing wave was then allowed to oscillate under the effect of the gravitational interactions. This was repeated six times, starting from the same initial conditions but using a different set of random numbers during the simulations. The velocity results shown below are averaged over the six simulations.

3. RESULTS AND DISCUSSION

The wave height at its centre was measured every 40 time steps; this is shown in Figure 5 for one of the six simulations along with the best-fit curve of the form $Ae^{-\alpha t}\cos(2\pi t/\tau + \psi) + h$, where $A = 15{\cdot}0$, $\alpha = 5{\cdot}16 \times 10^{-5}$, $\tau = 10{,}100$, $\psi = -0{\cdot}139$ and $h = 165$, all in units of time steps and lattice lengths. Although it is possible to initialize a wave with a density gradient which is a good approximation to its natural gradient, there will always be a short initial period during which the wave readjusts itself. The variable ψ is added to account for this and to allow for the wave not starting to oscillate at $t = 0$ from exactly the start of a period. It can be seen from the best-fit data that ψ is equivalent to approximately 200 time steps. The velocity field under the standing wave at $t = 3000$ time steps is shown in Figure 6(a). This can be compared with Figure 6(b) which shows the corresponding velocities computed for a wave with the same depth-to-wavelength ratio at time $t = \tau/4$ using the linear wave theory equations[9]

$$v_x = \frac{-a\omega\cosh(y+h)}{\sinh(kh)}\sin(kx)\sin(\omega t), \qquad v_y = \frac{a\omega\sinh(y+h)}{\sinh(kh)}\cos(kx)\sin(\omega t),$$

where h is the mean water depth and y is measured vertically upwards from the mean free surface. The plots in Figure 6(a) are in lattice units; the plots in Figure 6(b) have been normalized so that the peak x-velocity at the surface corresponds in magnitude to that found from the model. The linear theory y-velocities were normalized by the same factor. Figure 6 shows a vector plot of the velocities, Figure 7

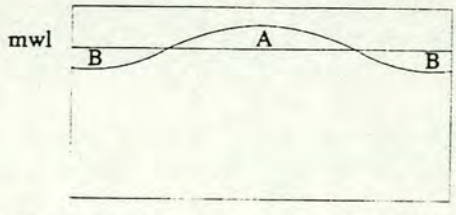

Figure 4. The construction of a standing wave from a flat surface. Note that this figure is not drawn to scale. The wave is in fact very shallow, with an amplitude of about 15 units and a wavelength of 4096 units

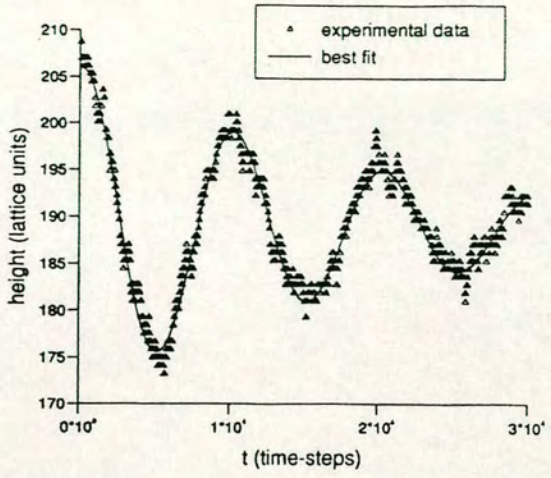

Figure 5. The height of the wave centre for one of the six runs plotted against time and the best-fit curve

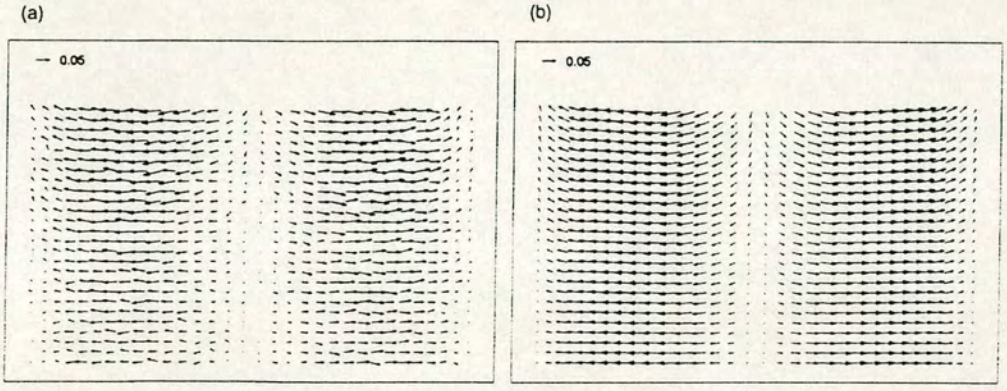

Figure 6. (a) Velocity vector plot. (b) Velocity vector plot from linear wave theory

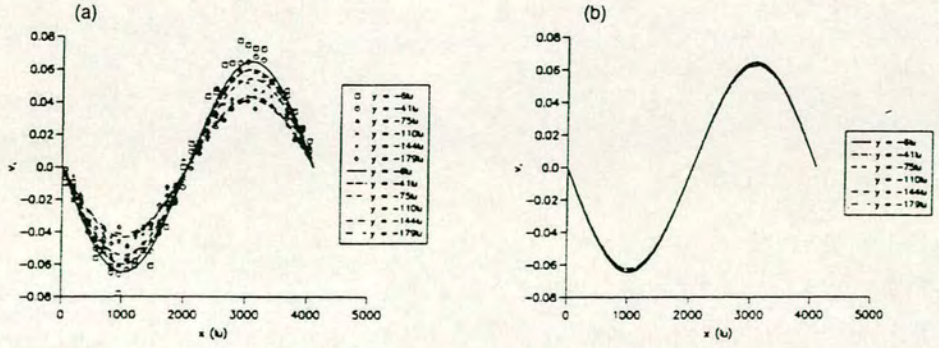

Figure 7. (a) x-Velocity profile. (b) x-Velocity profile from linear wave theory

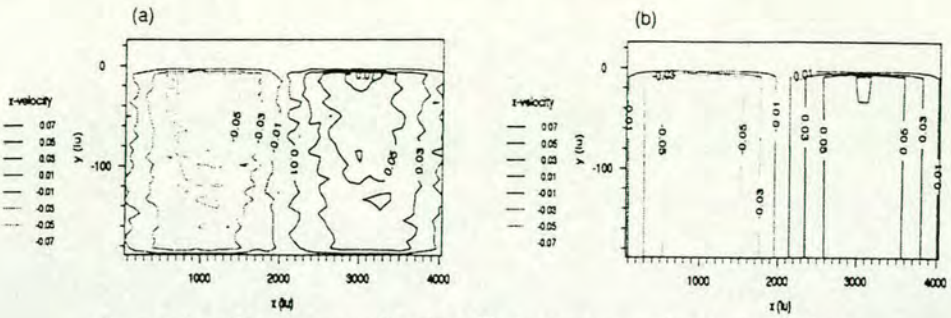

Figure 8. (a) x-Velocity contour plot. (b) x-Velocity contour map from linear wave theory

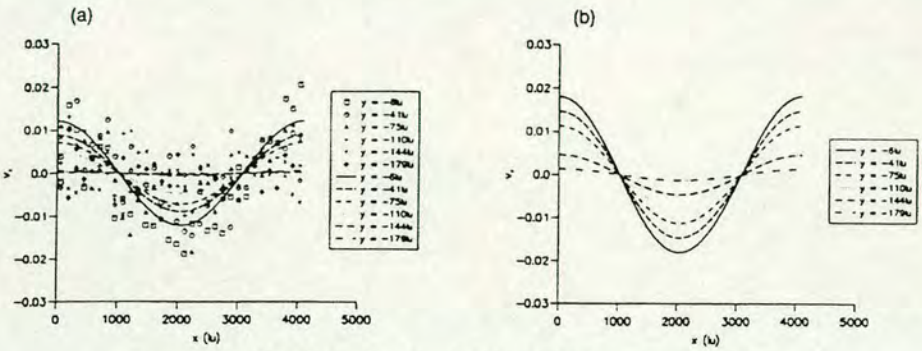

Figure 9. (a) y-Velocity profile. (b) y-Velocity profile from linear wave theory

shows the x-velocity profile across the phase of the wave at different heights (y), Figure 8 shows a contour plot of the x-velocity and Figure 9 shows the y-velocity profile. In Figures 7(a) and 9(a) the symbols are the experimental data points and the full curves are produced by filtering out the noise with a Fourier filter. It can be seen from Figures 7(a) and 9(a) that the y-velocities are significantly smaller than the x-velocities and the signal-to-noise ratio for the y-velocity is small. This causes a contour plot of the y-velocities to be particularly noisy and of little interest.

The results obtained compare well with the linear theory, except for two obvious differences. Firstly, the x-velocity decreases with the distance below the surface faster than predicted by the theory; this can be seen best when comparing figures 7(a) and 7(b). Secondly, the ratio of x-velocity to y-velocity is slightly larger than predicted by linear theory. The x-velocities from linear theory were scaled so that their magnitude would be as close as possible to the computed x-velocities; when the y-velocities are scaled by the same factor, the computed y-velocities are found to be smaller by a factor of about 0·8. Both differences are consistent with the simulated wave having an altered depth-to-wavelength ratio. The main cause of this effect is found to be the density gradient which is produced across the fluid by the gravitational interactions. This change in density with depth, which is not present in the linear theory, is seen to have the effect of changing the apparent depth of the fluid. The ratio of the real depth to the apparent depth can be accounted for in any simulation, since it is found to depend solely on the strength of the gravitational interaction. The strength of the gravitational interaction used here has the effect of causing the fluid to appear approximately twice its actual depth. Another factor which changes the depth of the fluid is the fact that the long-range interactions do not act at the bottom boundary. This affects the density of the fluid at the bottom three or four sites, which will change the effective depth only slightly, but significantly since we are dealing with shallow water waves. It is necessary that the long-range interaction does not act at the boundary to prevent particles becoming trapped in the boundary.

To investigate the effect of grid size on the model, another wave was initialized on a 2048 × 128 grid with a wavelength of 2048 lattice units and an MWL of 91 lattice units. The period of this wave was found to be 7423 time steps. This wave has half the wavelength and approximately half the depth of the wave already discussed. We can now compare the Reynolds numbers of the two waves: the Reynolds number is given by

$$Re = \frac{LUg(d)}{\nu},$$

where L and U are characteristic lengths and velocities respectively of the simulation and $\nu/g(d)$ is the scaled viscosity (see Section 1.1), which will be the same for both waves since the density is the same. In this comparison we will use a subscript '1' for the shorter wave and subscript '2' for the longer wave. For surface waves, Froude scaling applies with $\tau_2/\tau_1 = \sqrt{(\lambda_2/\lambda_1)}$; in this case $\tau_2 = \sqrt{2}\tau_1$.[10]

Comparing the ratio of the periods of the two waves, we see that $\tau_1/\tau_2 = 1{\cdot}46 \approx \sqrt{2}$ to within 3%. The characteristic velocity is taken to be the peak x-velocity of an undamped wave. This is given by

$$U = v_x(x = \lambda/4, y = 0, t = \tau/4)\exp(\alpha\tau/4).$$

The factor $\exp(\alpha\tau/4)$ compensates for the damping which occurs during the first quarter-period and is required because the velocity is damped at different rates for different waves. Using this characteristic velocity, we get $U_1/U_2 = 0{\cdot}75 \approx \sqrt{\frac{1}{2}}$ to within 6%, which is as expected since $U_i \propto \tau_i^{-1}$. Thus, comparing Reynolds numbers $Re_1 = Re_2$, we see that doubling the size of the wave has reduced the effective viscosity by a factor of $\sqrt{2}$.

A calculation of the Reynolds number requires the values of the scaling constant $g(d)$ and the viscosity ν. These have been found experimentally, but their measurement is beyond the scope of this paper. The values obtained for $g(d)$ and ν are 0·6 and 20 respectively, where both values are in lattice units. This gives a Reynolds number of about 10. The high viscosity present in the model is the main restraint on the Reynolds number which can be achieved. This is a common feature of lattice gas simulations which is increased in this model by the introduction of the additional interactions.

4. CONCLUSIONS

The close comparison between the results obtained and the linear theory suggests that an LG model is suitable for modelling surface waves. The waves produced are clearly highly viscous, which is one of the features of a lattice gas model. The viscous effect can be reduced by using a larger grid and increasing the wavelength of the wave. It may also be possible to alter the fluid density by changing the long-range interaction rules, which would change the viscosity of the model.

ACKNOWLEDGEMENTS

The authors would like to acknowledge the assistance of Paul Stansell who coded an original version of the program which was used in the simulations. The first author would like to acknowledge the support of the Science and Engineering Research Council.

REFERENCES

1. D. d'Humières and P. Lallemand, 'Numerical simulations of hydrodynamics with lattice gas automata in two dimensions', *Complex Syst.*, 1, 599 (1987).
2. D. d'Humières, P. Lallemand and G. Searby, 'Numerical experiments on lattice gasses: mixtures and galilean invariance', *Complex Syst.*, 1, 633 (1987).
3. G. Searby, V. Zenlé and B. Denet, 'Lattice gas mixtures and reactive flows', in *Discrete Kinetic Theory, Lattice Gas Dynamics and the Foundations of Hydrodynamics*, Torino, September 1988.

4. U. Frisch, B. Hasslacher and Y. Pomeau, 'Lattice-gas automata for the Navier–Stokes equation', *Phys. Rev. Lett.*, **56**, 1505 (1986).
5. U. Frisch, D. d'Humières, B. Hasslacher, P. Lallemand, Y. Pomeau and J.-P. Rivet, 'Lattice gas hydrodynamics in two and three dimensions', *Complex Syst.*, **1**, 649 (1987).
6. J. P. Boon and A. Noullez, 'Lattice gas hydrodynamics', in *Special Course on Modern Theoretical and Experimental Approaches to Turbulent Flow Structure and its Modelling*, AGARD, 1987.
7. C. Appert and S. Zaleski, 'Lattice gas with a liquid–gas transition', *Phys. Rev. Lett.*, **64**, 1 (1990).
8. C. Appert, D. Rothman and S. Zaleski, 'A liquid–gas model on a lattice', *Physica D*, **47**, 85 (1991).
9. G. D. Crapper, *Introduction to Water Waves*, Ellis Horwood, Chichester, 1984.
10. B. Le Méhauté, *An Introduction to Hydrodynamics and Water Waves*, Springer, Berlin, 1976.